Transversity
in two-hadron fragmentation

This thesis was reviewed by:

dr. A. Bacchetta	Deutsches Elektronen-Synchroton DESY, Germany
prof.dr. K. Griffioen	College of William & Mary, USA
prof.dr. P. Mulders	Vrije Universiteit Amsterdam
dr. G. Schnell	Ghent University, Belgium

Cover artwork by W. Zwarthoed (willem.zwarthoed@gmail.com)

The work described in this thesis is part of the research program of the 'Nationaal Instituut voor Kernfysica en Hoge-Energie Fysica' (NIKHEF) in Amsterdam, the Netherlands. The author was financially supported by the 'Stichting Fundamenteel Onderzoek der Materie' (FOM).

VRIJE UNIVERSITEIT

Transversity
in two-hadron fragmentation

ACADEMISCH PROEFSCHRIFT

ter verkrijging van de graad Doctor aan
de Vrije Universiteit Amsterdam,
op gezag van de rector magnificus
prof.dr. L.M. Bouter,
in het openbaar te verdedigen
ten overstaan van de promotiecommissie
van de faculteit der Exacte Wetenschappen
op woensdag 5 september 2007 om 15.45 uur
in het auditorium van de universiteit,
De Boelelaan 1105

door

Paul Bastiaan van der Nat

geboren te Amsterdam

promotor: prof.dr. G. van der Steenhoven
copromotor: dr. L. Lapikás

Contents

1

Introduction

1.1 Scattering experiments

In 1909, Geiger and Marsden fired a beam of α particles at a thin sheet of gold and noticed that 1 out of 20000 α particles scattered over huge angles, with an average scattering angle of 90° [1]. This led Rutherford to conclude that "the atom contains a central charge distributed through a very small volume" [2], which marks the discovery of the atomic nucleus. At the same time, it was one of the first scattering experiments ever. The setup of the original experiment is shown in Fig. 1.1.

Although experiments in high-energy physics have become more and more complex, the recipe for probing the structure of matter at the smallest possible scales has remained basically unchanged over the last hundred years. All the essential ingredients are contained in the relatively simple setup of the experiment performed by Geiger and Marsden shown in Fig. 1.1: a source of energetic particles (the beam of α particles coming out of the glass tube AB), a target (the gold foil RR) and particle detectors (the zinc sulfide screen S and the microscope M)[1]. In 1969, conceptually similar ingredients were used in a famous experiment at the Stanford Linear Accelerator Center (SLAC) [4] in California. Here, the source of energetic particles was a 7–18 GeV electron beam from a linear accelerator, the target was a thin-walled vessel containing liquid hydrogen and for particle detection a magnetic spectrometer was used, placed at scattering angles of $6–10^{\circ}$, consisting of several components for particle identification and determination of the particle trajectories.

[1] See [3] for a detailed historic overview on the discovery of subatomic particles.

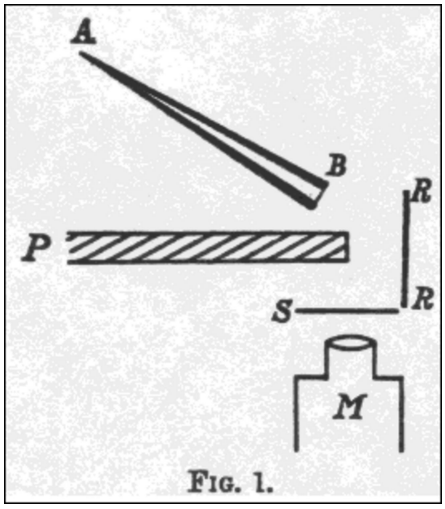

Figure 1.1: *The setup of the 1909 scattering experiment that led to the discovery of the atomic nucleus [1, 2]. A glass tube (AB) contains radioactive radium from which α particles are radiated (with a speed of* 2×10^7 *m/s [3]), A lead plate (P) is placed in between the source and a zinc sulfide screen (S), such that the α particles can only reach S if they scatter over large angles off the thin gold foil (RR). When struck by an α particle, the zinc sulfide emits light, which can be observed by a microscope (M). Note the relatively simple setup in comparison to present-day scattering experiments like HERMES (see Figs. 3.1, 3.2 and 3.3).*

Nobel laureates Taylor, Kendall, and Friedman together with their collaborators observed that the electron colliding with the proton sometimes scattered over relatively large angles, similar to what Geiger and Marsden observed when scattering α particles off gold atoms. The conclusions were comparable as well, i.e., that the proton itself is also made up of tiny electrically-charged particles, which were named *quarks*[2].

In another SLAC experiment [6], similar to the one of 1969 mentioned above, it was shown that the interaction of a virtual photon with the struck quark[3] only depends on a dimensionless scaling variable x (cf. Sec. 2.1.1) and not on any energy or length scale. This phenomenon is referred to as scale invariance (or Bjorken scaling, after the prediction of Bjorken in 1969 [7]) and it implies that quarks behave as point-like particles in these experiments, i.e., particles without any apparent internal structure at the energy scales accessible to present-day experiments.

The scattering experiments by Geiger and Marsden in 1909 and at SLAC in 1969 and 1972 represent major breakthroughs in our understanding of matter at the subatomic level. Nowadays, scattering experiments are still our dominant source of information in subatomic physics and are still used to deepen our understanding of the internal structure of the nucleon. The HERMES

[2] See for instance [5] (the Nobel lecture of J. Friedman, who received the 1990 Nobel Prize for the discovery of quarks) for a discussion on the discovery and the acceptance within the physics community of quarks as elementary constituents of hadrons.

[3] According to the theory of Quantum Electrodynamics, the interaction of an electron with a quark occurs through the exchange of a virtual photon.

collaboration at the German research center DESY in Hamburg, for instance, is devoted to the study of the origin of the nucleon spin, one of the nucleon's fundamental properties, and how it is related to the dynamics of the quark constituents. In this thesis, results are presented from the HERMES experiment.

1.2 Spin physics

The year 1987 marks the discovery by the EMC experiment at CERN that only a small fraction of the spin of the nucleon can be attributed to the spin of the quarks [8, 9]. This totally unexpected result has been confirmed by many experiments at CERN, SLAC and DESY [10–19]: the spin of quarks accounts for about 30% of the nucleon spin. With this discovery, the field of QCD spin physics was born, which to this day tries to identify the carriers of angular momentum in the nucleon and tries to map their contribution to the dynamical spin structure of the nucleon.

These dedicated spin experiments scatter polarized leptons off polarized nucleons. Because a lepton almost exclusively interacts with a quark that has the opposite direction of polarization, such experiments can be used to study the spin orientation of the quarks inside the nucleon. In particular, these experiments determined the cross section asymmetry A_1:

$$A_1 = \frac{\sigma_{1/2} - \sigma_{3/2}}{\sigma_{1/2} + \sigma_{3/2}}, \tag{1.1}$$

where $\sigma_{1/2}$ and $\sigma_{3/2}$ are the virtual-photon absorption cross sections when the projection of the total angular momentum of the photon-nucleon system along the incident photon direction is 1/2 or 3/2, respectively. In Fig. 1.2, this asymmetry is shown as obtained by the experiments mentioned above, as a function of the Bjorken scaling variable x. In the infinite-momentum frame, Bjorken x can be interpreted as the fraction of the momentum of the proton carried by the struck quark. In the limit $x \to 1$, the asymmetry almost reaches its theoretical maximum value of $A_1 = 1$, implying that the spin of the proton is almost exclusively carried by the struck quark. The asymmetry A_1 is related to the structure function g_1. In the quark parton model (QPM), g_1 has a probabilistic interpretation in the infinite-momentum frame; it probes the helicity distribution of the quarks inside a longitudinally polarized nucleon. At present, g_1 cannot be calculated from the QCD Lagrangian, because it involves the 'confinement problem', which requires highly non-perturbative QCD calculations.

Measurements of g_1 are shown in the right panel in Fig. 1.2. These values are obtained from the asymmetry measurements shown in the panel on the left. The integral of g_1 over x is directly related to $\Delta\Sigma$, the fraction of the helicity of the nucleon that can be attributed to the helicity of its quarks (see for instance Ref. [20]). It is the quantity $\Delta\Sigma$ that the spin exeriments found to be only about 30%.

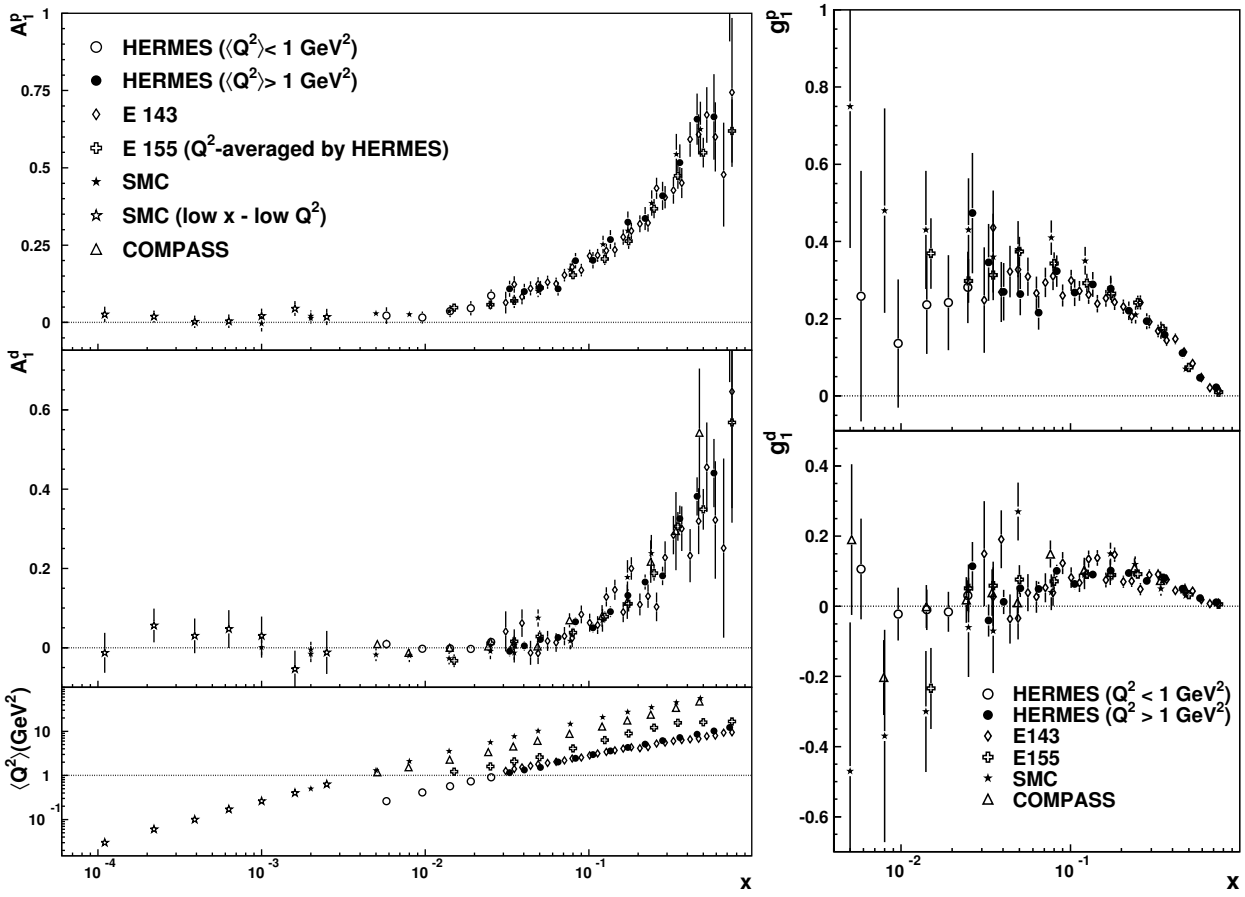

Figure 1.2: *HERMES results on A_1 (left) and the structure function g_1 (right) for the proton (A_1^p,g_1^p) and the deuteron (A_1^d,g_1^d) [18], both vs. x and compared to data from SMC [12–14], E143 [15], E155 [16] and COMPASS [17]. The bottom panel on the left shows the average value of Q^2 for each of the data points shown in the upper left panels. The value of Q^2 is a measure of the resolution with which the virtual photon probes the nucleon (cf. Sec. 2.1.1).*

Nowadays, it is understood that there can be various contributions to the total nucleon spin, expressed by the helicity sum rule [20]:

$$\frac{1}{2} = \frac{1}{2}\Delta\Sigma + L_z^q + \Delta G + L_z^g, \tag{1.2}$$

where ΔG denotes the contribution from gluon helicity, and L_z^q and L_z^g represent the contributions from the orbital angular momenta of quarks and gluons, respectively. Little information is available yet on the contributions from L_z^q and L_z^g. However, Ji has shown [21] that the total angular momentum of quarks, $J_z = \frac{1}{2}\Delta\Sigma + L_z^q$, is related to the second moment of certain generalized parton distributions (GPDs) and that these moments can be accessed in hard exclusive electroproduction processes. Several experiments are currently studying these processes [22–27]. Recently, the HERMES collaboration reported measurements of a cross-section asymmetry that can be related to such GPDs [28, 29]. These measurements provide a first model-dependent approach to obtain values of $J_z^{u,d}$. However, at present, the data do not (yet) constrain the value of $J_z^{u,d}$ significantly.

More information is available on the contribution from the gluon spin ΔG. At present, experimental data indicate that the gluon polarization is quite small. A combined analysis of first measurements by the HERMES [30], SMC [31] and COMPASS [32, 33] collaborations gives a net value of $\Delta G \sim 0.5$ [34, 35] (whereas model predictions up to $\Delta G \sim 5$ have been reported [36]).

In order to access $\Delta\Sigma$ and ΔG, the above mentioned experiments used *longitudinally* polarized targets, i.e., targets that are polarized along the beam direction. Different and complementary aspects of the spin structure of the nucleon can be studied by polarizing the nucleon *transversely*, i.e., transverse with respect to the beam direction. This subject forms the main topic of the present thesis and is introduced in the following section.

1.3 Transverse spin physics

Usually, the structure of the nucleon is described in terms of the four structure functions F_1, F_2, g_1 and g_2. The first two functions F_1 and F_2 describe the density of quarks in the nucleon and g_1 represents the helicity distribution of quarks in the longitudinally polarized nucleon (see Fig. 1.2). The fourth function g_2 is needed to describe the structure of the nucleon when it is transversely polarized.

All four structure functions have been measured in inclusive deep-inelastic scattering (DIS) experiments. Several ongoing experiments extend these measurements over a larger kinematic range and determine the structure functions with improved accuracy. An up-to-date overview of the existing experimental data can be found in Ref. [19].

The structure functions mentioned above can be related to parton distribution functions. These functions give the distribution inside the nucleon for each individual quark species and thus provide a more detailed picture of the internal structure of the nucleon. At leading twist[4], only three

[4] *Leading twist* refers to the order in M/Q at which the distribution functions contribute to the cross section, where

such functions are required for a complete description of the distribution of the quarks in the nucleon, i.e., f_1^q, g_1^q and h_1^q, where the superscript q represents the quark flavor. These functions can be interpreted as the number density of unpolarized quarks in an unpolarized nucleon (f_1^q), the number density of longitudinally polarized quarks in a longitudinally polarized nucleon (the helicity distribution g_1^q), and the number density of transversely polarized quarks in a transversely polarized nucleon (the transversity distribution h_1^q). The functions f_1^q and g_1^q can be related to the corresponding structure functions, according to:

$$F_1(x) = \frac{1}{2}\sum_q e_q^2\, f_1^q(x), \qquad g_1(x) = \frac{1}{2}\sum_q e_q^2\, g_1^q(x), \tag{1.3}$$

where e_q represents the fractional electric charge for quarks of flavor q. However, no such expression exists relating h_1^q to g_2, because h_1^q is a chiral-odd function while g_2 is chiral-even (and thus can be measured in inclusive DIS experiments). The distribution function f_1^q has been determined with high accuracy [19]. The helicity distribution g_1^q is less well determined. To date, the HERMES experiment has provided the most precise data for 5 different quark flavors [38]. The transversity distribution function h_1^q is practically unknown, as only very few experimental data exist that can be used to extract its value.

The transversity distribution function, or in short *transversity*, is the only missing ingredient to complete the picture of the nucleon at leading-twist. For that reason, many different experiments are devoted to contribute to its determination. In the following section, some brief comments will be made on the properties of the transversity distribution function, after which in Sec. 1.5 an overview is given of the different processes that can be used to access transversity experimentally. One of these processes, two-hadron semi-inclusive deep-inelastic scattering, has been measured for the first time ever by the HERMES experiment. In this thesis the data analysis and the results are presented.

1.4 Transversity – theoretical considerations

Although theoretical model predictions for transversity are available (see for instance Ref. [39]), there is a lack of experimental data to (in)validate these predictions. The reason that there are hardly any experimental data available relating to transversity is that such measurements are rather difficult to perform. This is largely due to the fact that h_1^q is a chiral-odd function (see Fig. 1.3a). As a consequence, it cannot be probed in *inclusive* deep-inelastic scattering processes, as is indicated by the handbag diagram in Fig. 1.3b. In order to access transversity an experimental observable needs to be identified in which h_1^q is coupled to another chiral-odd object. This object can be another distribution function, but for most cases presently being studied this is a fragmentation function. This complicates the determination of transversity in two ways. Firstly, it implies that

M is the nucleon mass. See Ref. [37] for a detailed discussion of the concept twist.

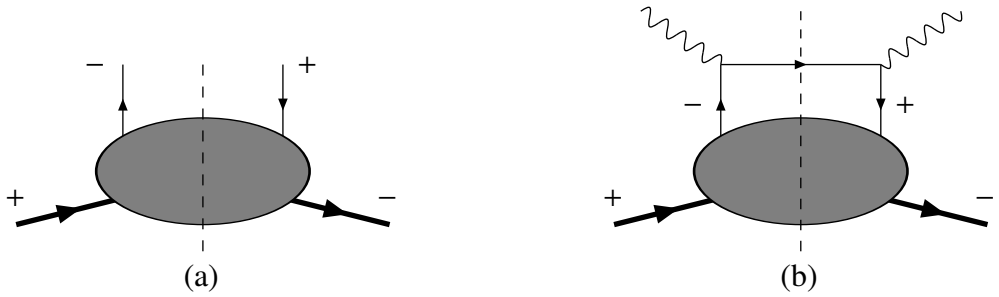

Figure 1.3: *Schematic representation of the chiral-odd distribution function h_1^q (a). The labels represent the spin of the corresponding particle. A characteristic of h_1^q is that it involves a simultaneous spin flip of parton and target. In panel (b) a handbag diagram for inclusive deep-inelastic scattering is shown assuming the characteristics of transversity, which is forbidden by chirality conservation (picture from Ref. [39]).*

experiments need to detect (and identify) one or more of the fragmenting hadrons, i.e., one needs to carry out *semi-inclusive* deep-inelastic scattering experiments, which are much more involved than inclusive scattering experiments. Secondly, the cross section for semi-inclusive scattering not only contains the unknown transversity distribution function, but an unknown chiral-odd fragmentation function as well.

The chiral-odd nature of transversity has some remarkable consequences. When transversity is probed in inelastic scattering, its chiral-odd nature implies that when the struck quark absorbs the virtual photon, both the quark and the target nucleon flip their helicity. Because a spin-1/2 nucleon can only absorb one unit of helicity, a simultaneous helicity flip of the gluons inside the nucleon is not possible, since that would involve a helicity flip of two units. Therefore, at leading twist, there is no contribution from gluons to transversity [40]. This has as a further consequence that the Q^2 evolution of transversity is much weaker than that of the helicity distribution [41].

Recently, the following transverse-spin sum rule was proposed [42]:

$$\frac{1}{2} = \frac{1}{2}\sum_{a=q,\bar{q}} \int \mathrm{d}x\, h_1^a(x) + \sum_{a=q,\bar{q},g} \langle L_T \rangle^a, \tag{1.4}$$

where L_T is the component of the orbital angular momentum L along the transverse polarization direction and the sums run over quark and antiquark flavors (including gluons as well for the second term). This sum rule is similar to the helicity sum rule expressed by Eq. 1.2, but differs in that Eq. 1.4 contains no contribution of gluon transversity[5]. Note that the first term in Eq. 1.4 is not equal to the tensor charge $\delta q = \int_0^1 \mathrm{d}x \left[h_1^q - h_1^{\bar{q}}\right]$, which involves the difference instead of the

[5]It should be mentioned that the interpretation of Eq. 1.4 has been discussed during a dedicated workshop [43]. Here, Mulders argued that the sum rule of Eq. 1.4 is model dependent and that a more fundamental transverse spin sum rule is the one given in Ref. [44, 45], in which the distribution function g_T appears instead of h_1.

sum of quark and antiquark distribution functions. It would be of interest to measure δq, since predictions are available for the tensor charge from Lattice QCD calculations (see e.g. [46, 47]). In the absence of such measurements, and as mentioned in Ref. [42], the combination of Eq. 1.4 with predictions for the tensor charge might therefore help to disentangle the quark and anti-quark transversity distributions.

Many models exist for the transversity distribution function (see for instance Ref. [39] for a review) and await verification or falsification by measurements. Although these models contain large inherent uncertainties, some basic relations exist between the three leading-twist distribution functions, which help to constrain transversity [48]:

$$|g_1(x)| \leq f_1(x), \tag{1.5}$$

$$|h_1(x)| \leq f_1(x), \tag{1.6}$$

$$|h_1(x)| \leq \frac{1}{2}\left[f_1(x) + g_1(x)\right]. \tag{1.7}$$

These relations are valid for the quark distribution function and similar inequalities hold for the antiquark distribution functions (see also Ref. [48]). The last inequality, Eq. 1.7, is known as the Soffer inequality [49].

1.5 Transversity – experiments

There are many different processes that can be used to access transversity. All these processes involve at least two hadrons of which at least one is transversely polarized. The processes can be divided into two groups: hadron-hadron scattering and lepton-hadron scattering. Below, a short overview is given of each group separately.

1.5.1 Hadron-hadron scattering

***h N*$^\uparrow$ → *h X*.** Single-spin asymmetries (SSAs) have been measured in several experiments for this type of process (with a transversely polarized nucleon). Starting from the 70s, nonzero asymmetries were reported [50–54]. However, these experiments were performed at relatively low energies ($\sqrt{s} \leq 6$ GeV), such that it is not apparent that the cross sections can be factorized in terms of distribution and fragmentation functions. In the 1990s these kind of measurements were also performed at higher energies ($\sqrt{s} = 19.4$ GeV) by the E704 experiment at FNAL [55, 56]. They measured surprisingly large asymmetries of up to 40% (see Fig. 1.4), which triggered a lot of new developments in the field. More recently, nonzero single-spin asymmetries were also observed at RHIC ($\sqrt{s} = 200$ GeV) by the STAR [57] and BRAHMS [58] experiments (whereas at mid-rapidity the PHENIX collaboration measures transverse SSAs consistent with zero [59]).

The asymmetry for the process $h\,N^\uparrow \rightarrow h\,X$ might be the result of a convolution of transversity with the so-called Collins fragmentation function [60] (the Collins mechanism). A disadvantage

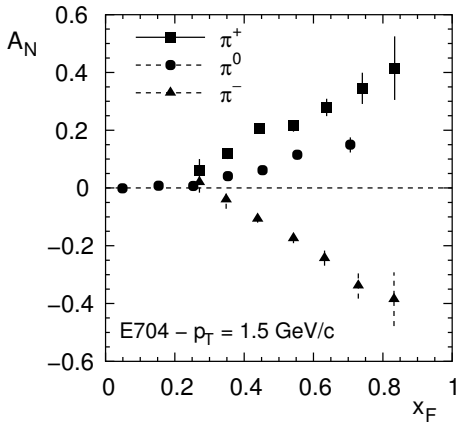

Figure 1.4: *The single-spin asymmetry A_N versus Feynman x ($x_F \equiv p_\parallel/p$) as measured by the E704 experiment at FNAL [55, 56] for the process $p^\uparrow\, p \to h\, X$, with $h = \pi^+, \pi^-$ and π^0.*

of this type of experiment (as a probe of transversity) is that various possible contributions to the asymmetry, like the Sivers [61] and Collins mechanisms, cannot be disentangled. Recently, it was shown that the measured asymmetries cannot be attributed to the Collins mechanism alone [62]. As a consequence, several unknown distribution and fragmentation functions need to be evaluated in order to reach a full understanding of these asymmetries. An eventual extraction of transversity from these measurement requires input from other experiments (for instance to obtain the Collins fragmentation function and the Sivers distribution function).

$N^\uparrow N^\uparrow \to l^+\, l^-\, X$. The tranversity distribution function was introduced in 1979 by Ralston and Soper in order to describe this polarized Drell-Yan process [63]. No data are available yet (with *both* nucleons transversely polarized), but it has been proposed to study this process using colliding polarized protons at RHIC [64]. The advantage of this process is that no fragmentation functions are involved, as the production of the lepton pair from the quark annihilation ($q\bar{q} \to l^+l^-$) is described by QED and can be precisely calculated. The double-spin asymmetry for this process is sensitive to the product of the quark and antiquark transversity distribution functions.

It is expected that transverse double-spin asymmetries are quite small for RHIC kinematic conditions, i.e., on the order of 1–2% only [65, 66]. This is partially due to the fact that the asymmetry is evaluated at low values of $\tau = x_1 x_2 \simeq 10^{-3}$, such that one mainly probes the transversity distributions of the sea quarks, which are expected to be small (here x_1 and x_2 are the values of Bjorken x for the two interacting quarks). Partially, transversity is also likely to be small in the kinematic region of the RHIC experiment as a consequence of its QCD evolution. In addition, the transversity distributions for antiquarks in the proton are presumably small. The latter is no problem when colliding polarized protons with polarized *antiprotons*. This is what the PAX collaboration is planning to do at the HESR (High Energy Storage Ring) at GSI [67]. In this case, the double-spin asymmetry is sensitive to the product of two quark transversity distribution functions. The kinematic region of the PAX experiment ($5.5 \lesssim \sqrt{s} \lesssim 14.5$ GeV, $\tau \simeq 0.2$–0.3) also favors a large double-spin

asymmetry. Model calculations predict values for this asymmetry of 30–40% [68, 69]. The biggest challenge for the PAX collaboration, however, will be to reach the intended transverse polarization for the antiproton beam of $P_{\bar{p}} = 0.2$–0.3 [70, 71].

$N\,N^{\uparrow} \rightarrow l^{+}\,l^{-}\,X$. Of all hadron-hadron scattering experiments, the double-spin asymmetries in Drell-Yan, described above, provide the cleanest access to transversity. However, the Drell-Yan process with only one of the two colliding hadrons polarized might also be used to study transversity. Nonzero *single*-spin asymmetries for this process could be related to the product of the transversity distribution function with the Boer-Mulders function, which describes the distribution of transversely polarized quarks in an unpolarized nucleon [72]. Transversity can then be extracted from the asymmetry in combination with measurements of the unpolarized Drell-Yan process, which can be used to obtain the Boer-Mulders distribution function. This process could be measured by the PAX experiment or one of the RHIC experiments

1.5.2 Lepton-hadron scattering

$l\,N^{\uparrow} \rightarrow l\,h\,X$. This process, one-hadron semi-inclusive deep-inelastic scattering, is a very good candidate for studying transversity. The interaction between the beam lepton and the struck quark in the nucleon can be calculated very accurately in QED. The remaining unknowns that describe this scattering process are distribution and fragmentation functions. The single-spin asymmetry for this process is related to the product of the transversity distribution function and the Collins fragmentation function. The Sivers function can also contribute to this asymmetry in a product with the unpolarized fragmentation function, as is the case for hadron production in polarized proton-proton scattering experiments. However for semi-inclusive DIS, these two contributions to the asymmetry can be separated because the azimuthal distributions of the produced pions are different. First preliminary results for measurements of this type appeared in conference proceedings by the SMC collaboration [73]. These data carried large margins of uncertainty and are consistent with zero. Results published in 2005 by the HERMES collaboration for charged pion production on a transversely polarized hydrogen target showed significantly nonzero SSAs both for the contribution related to the transversity distribution function and for the contribution related to the Sivers distribution function [74].

Shortly after this HERMES publication, the COMPASS collaboration at CERN published results for the SSA of unidentified charged hadrons on a transversely polarized ^{6}LiD target [75, 76] and later reported results for identified charged pions as well [77]. They measured very small asymmetries that are consistent with zero within the statistical uncertainty. The difference with the HERMES results can be due to cancellation effects between the SSAs on a proton and a neutron target.

Whereas the HERMES and COMPASS collaborations measure transversity of the proton and the deuteron, respectively, the E06-010/E06-011 experiment in Hall A at JLab is planning to mea-

sure transversity of the neutron, using a transversely polarized ^{3}He target [78]. An important issue for this experiment is the applicability of factorization in the interpretation of the measured SSAs. This question is especially relevant for this experiment, because it uses a beam energy of 6 GeV, which is much lower than the beam energies used by the HERMES (27.5 GeV) and COMPASS (160 GeV) experiments. The discussion on the applicability of factorization for low-energy semi-inclusive DIS is similar to the discussion on the applicability of factorization for hadron production in low-energy proton-proton scattering experiments, mentioned in Sec. 1.5.1. However, preliminary results on the cross section in semi-inclusive DIS (measured in Hall C at JLab; 6 GeV beam energy) are consistent with Monte-Carlo simulations that assume factorization to hold (see the discussion in Ref. [78]). This can be seen as an indication that in semi-inclusive DIS factorization holds even in the low-energy domain accessed by the JLab experiments. Apart from the E06-010/E06-011 experiment by the Hall A collaboration at JLab , the CLAS collaboration in Hall B is planning to study transversity as well [79], using the upgraded 12 GeV CEBAF accelerator [80].

In order to extract transversity from the SSAs in one-hadron semi-inclusive DIS a separate measurement of the Collins fragmentation function is needed. This function can be obtained from e^+e^- scattering ($e^+e^- \to h_1h_2X$), as was recently accomplished by the BELLE collaboration at KEK [81]. It enabled Anselmino et al. [82] to extract for the first time the transversity distribution function for u and d quarks from a global analysis of the results from the HERMES [74], COMPASS [75, 76] and BELLE [81] collaborations. The one-hadron semi-inclusive DIS process will be discussed in more detail in Chapter 2.

l N↑ → l h h X. Two-hadron semi-inclusive DIS was first suggested as a promising alternative to the one-hadron semi-inclusive DIS process for measuring transversity in 1994 by Collins, Heppelmann and Ladinsky [83, 84]. It can be measured by the same experiments that are used to study transversity in one-hadron semi-inclusive DIS, i.e., the HERMES and COMPASS experiments as well as experiments at JLab. Similar to the one-hadron process, transversity appears in the SSA coupled to an unknown fragmentation function, in the literature often called the *interference* fragmentation function. Also this fragmentation function can be measured by the BELLE collaboration [85]. The key advantage of two-hadron over one-hadron SSA measurements for accessing transversity is that in the two-hadron case transversity contributes to the SSA through a direct product with the interference fragmentation function, whereas in the one-hadron case transversity and the Collins fragmentation function appear in the SSA within a convolution integral over quark transverse momentum.

The measurement of two-hadron semi-inclusive DIS by the HERMES experiment and the extraction of the corresponding SSAs is the main topic of this thesis. The theoretical framework is covered in Chapter 2.

l N↑ → l h↑X. Transversity can be accessed through this type of process if the transverse spin of the struck quark is transferred to the produced hadron. The polarization of the produced hadron

can then be directly related to transversity times an unknown fragmentation function [86–88]. The specific process that has been suggested as the most promising candidate is: $l\ p^{\uparrow} \rightarrow l\ \Lambda^{\uparrow} X \rightarrow l\ p\ \pi\ X$. The advantage of the Λ is that its polarization can be directly derived from the decay products, i.e., the detected proton and pion. Any other hyperons are typically too rare to be useful for transversity measurements. First preliminary results have recently been obtained both by the COMPASS collaboration [89, 90] and the HERMES collaboration [91][6]. Both experiments find values for the transverse Λ polarization that are consistent with zero, which mainly reflects the rather large uncertainty of those measurements. Higher precision results are needed in order to conclude whether or not this process can be used to access transversity.

l N*$^{\uparrow}$ *→ l h*$^{J=1}$ *X. The production of spin-one hadrons, like the ρ, ϕ and K^* vector mesons, was first considered as a possible probe of the transversity distribution function by Ji in 1994 [92] and later discussed in more detail in Refs. [93–95]. The transverse polarization of the struck quark is transferred to a certain polarization state (described by the vector and tensor polarization), which can be analyzed by polarimetry of the decay products. This process has not been studied yet by any of the DIS experiments. It should be noted though that this process is closely related to the process of two-hadron leptoproduction (see f.i. Ref. [96]).

In conclusion, it should be noted that for each of the processes in lepton-hadron scattering that is considered as a possible candidate to study transversity, in principle the analogue process in hadron-hadron scattering can be used as well. For instance, dihadron fragmentation can be studied in polarized hadron-hadron scattering ($h\ h^{\uparrow} \rightarrow h\ h\ X$) at RHIC [64, 83, 97] as well as in lepton-hadron scattering. However, the extraction of transversity from measurements of these hadron-hadron scattering processes is more involved, because one more distribution function has to be accounted for.

1.6 Conclusions and outline of the thesis

The topic of this thesis is the extraction of single-spin asymmetries from measurements of two-hadron semi-inclusive deep-inelastic scattering by the HERMES experiment at DESY. This process has been proposed in the literature as a promising candidate for studying transversity. There are several reasons why this distribution function is of interest.

Firstly, transversity is the only missing distribution function that is needed to describe the structure of the nucleon at leading twist. Secondly, by polarizing the nucleon transversely, it is prepared in a way that no gluon distribution functions contribute to the total nucleon spin. This makes it easier to disentangle the various sources that do contribute to this total spin, as is expressed by Eq. 1.4. A third reason to investigate the transversity distribution function is that a weaker Q^2

[6] Note however that in Ref [91] quasi-real photoproduction is studied, with $\langle Q^2 \rangle \approx 0$.

evolution is predicted for this function, h_1, compared to the evolution of both f_1 and g_1. The experimental verification of this prediction can be seen as a novel test of QCD. Finally, the transversity distribution function is of interest, because its first moment gives the tensor charge of the nucleon. It is one of the few properties of the nucleon that are predicted by lattice QCD that can be measured experimentally.

The initial results obtained from measurements aimed at extracting transversity indicate that it will be difficult to obtain precise data, as the observed asymmetries are small and only a convoluted quantity is probed. In view of these first results it is concluded that it is very important to study various approaches to transversity. This thesis intends to contribute to this effort by discussing first results obtained for two-hadron transversity measurements.

The main questions that are addressed in this thesis are: is it feasible to measure two-hadron interference fragmentation at an electron-proton scattering experiment like HERMES and, if so, is it possible to use this process to study transversity?

The layout of this thesis is as follows. First, the theoretical framework is treated in some detail in Chapter 2. Then, in Chapter 3 the setup of the HERMES experiment is discussed, focussing on those parts of the experiments that are needed for the measurement of two-hadron semi-inclusive DIS. Chapter 4 covers in detail the analysis of those measurements, starting from the raw data up to the final results, which are finally discussed and interpreted in Chapter 5.

2

Transversity in deep-inelastic scattering

In this chapter the transversity distribution function is formally introduced. It is explained how this function can be measured, with the focus on those processes that are accessible by the HERMES experiment.

The chapter starts in Sec. 2.1 with a general discussion of inclusive deep-inelastic scattering (DIS), a process that can be used to probe the internal structure of the nucleon. The relevant kinematic variables used to describe inclusive scattering are introduced in Sec. 2.1.1. In Secs. 2.1.2–2.1.3 the cross section for this process is given including its spin dependence and expressed in terms of distribution functions. The meaning of these functions is discussed and it is explained why the transversity distribution function h_1 does not appear in the inclusive cross section. The Sections 2.2–2.3 discuss two processes, one-hadron and two-hadron semi-inclusive deep-inelastic scattering, which, in contrast to inclusive scattering, can be used to access transversity. A more detailed derivation of the formula's presented in Secs. 2.1–2.3 can be found in Ref. [96]. The actual observables in which the transversity results obtained in this thesis are expressed, are introduced in Secs. 2.4–2.5. Existing results on transversity obtained by the HERMES experiment with the one-hadron semi-inclusive deep-inelastic scattering process are presented in Sec. 2.6. Finally, Sec. 2.7 discusses in more detail how the two-hadron semi-inclusive deep-inelastic scattering process can be used to access transversity. This is also discussed in the context of some theoretical models. As

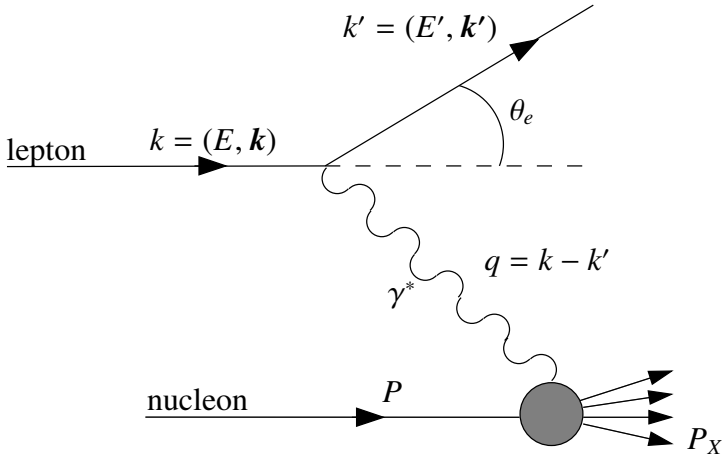

Figure 2.1: *Schematic representation of the deep-inelastic scattering process in lowest-order QED.*

transversity in two-hadron fragmentation is the main topic of this thesis the experimental results obtained by identifying this process in the data are discussed separately in Chapter 5.

2.1 Inclusive deep-inelastic scattering

In deep-inelastic scattering a lepton (l) and a nucleon (N) hit each other with such high energies that the nucleon breaks up. The interaction occurs through the exchange of a virtual neutral boson (γ or Z^0) between the lepton and one or more electrically charged constituents of the nucleon. As a consequence, this process can be used to probe the internal structure of the nucleon. The struck nucleon fragments into hadrons, which can be detected in a spectrometer. A lepton scattering process is called *inclusive* if only the scattered lepton (l') is considered. The hadronic final state (X) might be detected, partially or completely, but is ignored in inclusive DIS:

$$\mathrm{l}(k) + \mathrm{N}(P) \rightarrow \mathrm{l}'(k') + \mathrm{X}(P_X), \tag{2.1}$$

where the quantities in parentheses refer to the four-momenta shown in Fig. 2.1. In the remainder of this chapter it is always assumed that the exchanged boson is a γ. Since the total center-of-mass energy in the HERMES experiment ($\sqrt{s} = 7$ GeV) is so much lower than that of a Z^0 boson ($m_{Z^0} = 91$ GeV), the contribution of Z^0 exchange can be neglected.

2.1.1 Kinematics

The kinematics for scattering unpolarized leptons off unpolarized nucleons can be described by three independent four-vectors, e.g., k, P and q, which represent the momenta of the lepton, the nucleon and the exchanged virtual photon, respectively. They are illustrated in Fig. 2.1. Six independent Lorentz-invariant quantities can be constructed from these three four-vectors: k^2, P^2, q^2, $k \cdot P$, $k \cdot q$ and $P \cdot q$. Two of them represent the masses of the colliding particles ($k^2 = m_e^2$ and

$P^2 = M^2$, the mass of the lepton and nucleon, respectively), and two others depend on the energy of the lepton-nucleon system and the scattering angle ($k \cdot P$ and $k \cdot q$). Two invariants are left to describe the interaction of the virtual photon with the target:

$$Q^2 \equiv -q^2 \overset{\text{LAB}}{=} 4EE' \sin^2(\theta_e/2), \tag{2.2}$$

$$\frac{P \cdot q}{M} \equiv \nu \overset{\text{LAB}}{=} E - E', \tag{2.3}$$

with θ_e the lepton scattering angle, q^2 the virtuality of the virtual photon, ν its energy in the lab frame and E and E' the energy of the lepton before and after scattering off the nucleon, respectively. In Eq. 2.2, the lepton mass m_e is neglected, which is valid for the case $EE' \sin^2(\theta_e/2) \gg m_e^2$. As $q^2 \leq 0$, one usually works with Q^2, which is always positive. These equations are valid within the lab frame.

Alternatively, the two dimensionless variables x (called x-Bjorken) and y can be used:

$$x \equiv \frac{-q^2}{2P \cdot q} = \frac{Q^2}{2M\nu}, \tag{2.4}$$

$$y = \frac{P \cdot q}{P \cdot k} \overset{\text{LAB}}{=} \frac{E - E'}{E}, \tag{2.5}$$

where x can be interpreted as the momentum fraction of the nucleon carried by the struck quark and y as the fractional energy loss of the incident lepton. In the present work, also the Lorentz-invariant Mandelstam variable s is used, which can be written in terms of the above defined variables (again, neglecting the lepton mass) as

$$s \equiv (P + k)^2 \overset{\text{LAB}}{=} M^2 + 2ME = \frac{Q^2}{xy} + M^2. \tag{2.6}$$

The invariant mass squared of the final hadronic state is given by:

$$W^2 \equiv (P + q)^2 = M^2 + 2M\nu - Q^2. \tag{2.7}$$

An additional vector is needed to describe the inclusive scattering process when the target nucleon is polarized, i.e., the vector $\boldsymbol{S}$ describing the polarization direction. This vector is often decomposed in the two components $\boldsymbol{S_L}$ and $\boldsymbol{S_T}$, which are the longitudinal and transverse projections of $\boldsymbol{S}$ with respect to the virtual-photon direction $\boldsymbol{q}$, respectively. The azimuthal orientation of $\boldsymbol{S_T}$ around the virtual-photon direction is specified by the angle ϕ_S (see Fig. 2.2) so that $\boldsymbol{S} = (S_T \cos\phi_S, S_T \sin\phi_S, S_L)$, where S_T has values in between 0 and 1, and S_L has values between[1] -1 and 1. The angle ϕ_S can be calculated as

$$\phi_S = \frac{\boldsymbol{q} \times \boldsymbol{k} \cdot \boldsymbol{S}}{|\boldsymbol{q} \times \boldsymbol{k} \cdot \boldsymbol{S}|} \cos^{-1} \frac{\boldsymbol{q} \times \boldsymbol{k} \cdot \boldsymbol{q} \times \boldsymbol{S}}{|\boldsymbol{q} \times \boldsymbol{k}||\boldsymbol{q} \times \boldsymbol{S}|}. \tag{2.8}$$

[1]The sign convention is such that $S_L = +1$ corresponds to a right-handed proton in the $\gamma^* p$ center-of-mass frame (see Ref. [98]).

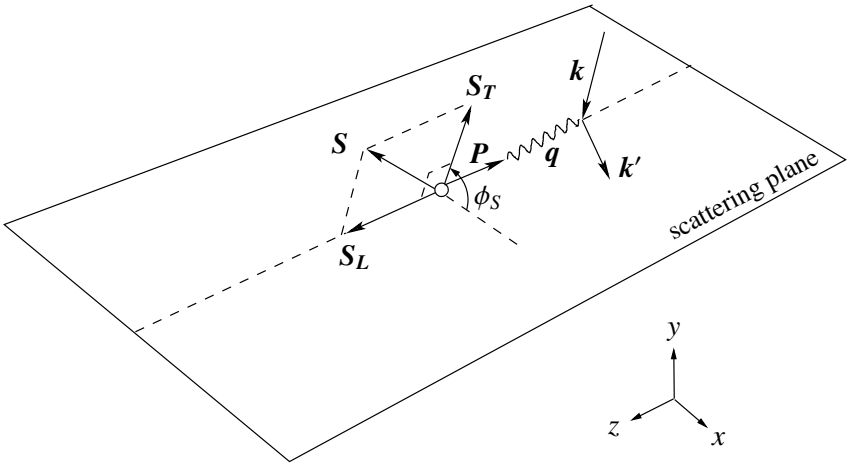

Figure 2.2: *Schematic configuration of an inclusive scattering event showing the azimuthal angle ϕ_S (drawn in the virtual-photon-nucleon center-of-mass frame). The vector $\boldsymbol{S}$ indicates the polarization direction of the target and $\boldsymbol{S_L}$ and $\boldsymbol{S_T}$ are the projections of $\boldsymbol{S}$ along and perpendicular to the virtual-photon direction $\boldsymbol{q}$. (Here, $\boldsymbol{S_L}$ is pointing in the negative direction.)*

2.1.2 Cross section

The cross section for inclusive deep-inelastic scattering can be written as a product of a leptonic tensor $L_{\mu\nu}$ and a hadronic tensor $W^{\mu\nu}$. Within the approximation of single-photon exchange the cross section is given by

$$\frac{\mathrm{d}^3\sigma}{\mathrm{d}x\,\mathrm{d}y\,\mathrm{d}\phi_S} = \frac{\alpha^2}{2(s-M^2)xQ^2} L_{\mu\nu}\, 2MW^{\mu\nu} \approx \frac{\alpha^2}{2sxQ^2} L_{\mu\nu}\, 2MW^{\mu\nu}, \tag{2.9}$$

where $\alpha \equiv \frac{e^2}{4\pi\hbar c}$ is the coupling constant of Quantum Electrodynamics (QED)[2]. The leptonic tensor $L_{\mu\nu}$ describes the emission of a virtual photon by the incident lepton and can be calculated in perturbative QED. It is given by [99]

$$L_{\mu\nu} = \sum_{\lambda_e'} \Big(\bar{u}(l',\lambda_e')\gamma_\mu u(l,\lambda_e)\Big)^* \Big(\bar{u}(l',\lambda_e')\gamma_\nu u(l,\lambda_e)\Big), \tag{2.10}$$

$$= 2(l_\mu l'_\nu + l'_\mu l_\nu - l\cdot l' g_{\mu\nu}) + 2i\lambda_e \epsilon_{\mu\nu\rho\sigma} l^\rho l'^\sigma, \tag{2.11}$$

where $u(l,\lambda_e)$ is the Dirac spinor for spin-$\frac{1}{2}$ particles with four-momentum l and helicity λ_e, $g_{\mu\nu}$ is the metric tensor and $\epsilon_{\mu\nu\rho\sigma}$ is the Levi-Civita tensor (cf. Sec. A).

The hadronic tensor $W_{\mu\nu}$ describes the interaction between the virtual photon and the nucleon, which is in principle given by Quantum Chromodynamics (QCD). Written in terms of the electroweak transition currents of the nucleon J^μ, it is given by

$$2MW_{\mu\nu} = \frac{1}{2\pi}\sum_X \int \frac{\mathrm{d}^3\boldsymbol{P_x}}{(2\pi)^3 2E_x} \langle P,S|J^\mu(0)|X\rangle\langle X|J^\nu(0)|P,S\rangle \delta^4(q+P-P_x), \tag{2.12}$$

[2] In the second part of Eq. 2.9, the approximation is made that $s = M^2 + 2ME \approx 2ME$ (at HERMES $s = 52\ \mathrm{GeV}^2$). For conciseness and for consistency with Ref. [96], this approximation is always made in the present work.

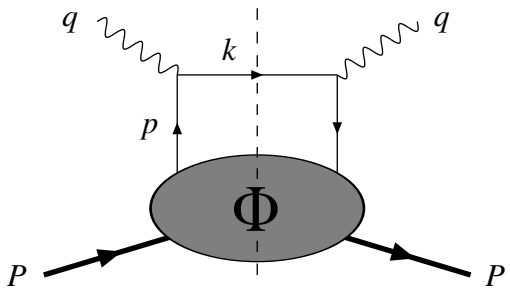

Figure 2.3: *The handbag diagram for inclusive deep-inelastic scattering at leading order. The quantity* Φ *represents the distribution correlator.*

where the summation runs over all possible undetected hadronic final states X, and $\langle X|J^\nu(0)|P,S\rangle$ is the matrix element of the transition between a nucleon with momentum P and spin S and the undetected hadronic final state X. However, this tensor cannot be calculated using perturbative techniques, since QCD is infrared divergent, i.e., if relatively large distances between the quarks are involved, as in a hadron, the interaction between the quarks is so strong that the perturbation expansion of pQCD does not converge anymore. How this situation is dealt with in practice is discussed in the following subsection.

2.1.3 Distribution functions

Although the hadronic tensor cannot be calculated in pQCD, it can be expanded in terms of *structure functions*, which can be measured in deep-inelastic scattering experiments. Examples of structure functions are the spin-independent functions F_1 and F_2 and the spin-dependent functions g_1 and g_2.

However, the expansion in terms of structure functions does not take into account our further knowledge of the substructure of the nucleon. Within the quark-parton model (QPM) the virtual photon scatters off point-like, spin-$\frac{1}{2}$ quarks. Using the optical theorem, the hadronic tensor can then be represented by the so-called handbag diagram shown in Fig. 2.3 which can be calculated to give [96]

$$2MW^{\mu\nu}(q,P,S) = \sum_q e_q^2 \int \frac{\mathrm{d}^4p}{(2\pi)^4}\delta\Big((p+q)^2\Big)\,\mathrm{Tr}\left[\Phi(p,P,S)\gamma^\mu(\not{k}+\not{q})\gamma^\nu\right], \tag{2.13}$$

where e_q is the fractional charge for a quark of flavor q and Φ is the distribution correlator, which represents the nonperturbative part of the hadronic tensor. The distribution correlator is a density matrix that contains information on the distribution of the quarks in the nucleon. It can be written

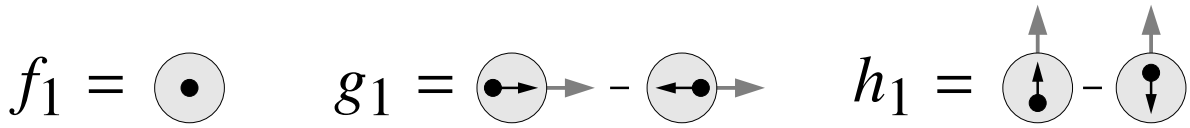

Figure 2.4: *Schematic representation of the three leading-twist distribution functions $f_1(x)$, $g_1(x)$ and $h_1(x)$ (from P.J. Mulders, see e.g. Ref. [101]). Grey arrows indicate the nucleon polarization, black arrows indicate the quark polarization. With respect to the shown configurations, the exchanged virtual-photon moves horizontally.*

as

$$\Phi_{ij}(p,P,S) = \sum_X \int \frac{\mathrm{d}^3\boldsymbol{P_x}}{(2\pi)^3 2E_x} \langle P,S|\bar{\psi}_j(0)|X\rangle\langle X|\psi_i(0)|P,S\rangle \delta^4(P-p-P_x), \tag{2.14}$$

where the summation runs over all possible undetected hadronic final states X and ψ_i is the quark field with spinor index i (compare with Eq. 2.12)[3]. This correlator can be expanded on a basis of Dirac matrices multiplied by *distribution functions*:

$$\Phi(x,S) = \int \mathrm{d}^2\boldsymbol{p_T}\,\mathrm{d}p^-\,\Phi(p,P,S)\Big|_{p^+=xP^+} \tag{2.15}$$

$$= \frac{1}{2}\{f_1(x) + S_L\, g_1(x)\,\gamma_5 + h_1(x)\,\gamma_5 \not{S}_T\}\not{P}, \tag{2.16}$$

where it was used that Φ needs to satisfy hermeticity, parity and time-reversal invariance. Equation 2.16 is a *leading-twist* expression, which refers to the order in M/Q at which the operator matrix elements contribute to the cross section[4]. Here, x is the "+" component of the light-cone momentum fraction of the nucleon carried by the struck quark, defined as $x \equiv p^+/P^+$. Bjorken-x, defined in Eq. 2.4, is equal to p^+/P^+ in the Bjorken limit ($Q^2 \to \infty$, $\nu \to \infty$; see Ref. [100, Appendix] for a discussion of this scaling variable).

The distribution functions are probability densities for finding a quark with a certain momentum fraction x inside the nucleon. They can be distinguished by the relative polarization of the quarks and the nucleon. The three distribution functions in Eq. 2.16 are called the unpolarized distribution function $f_1(x)$, the helicity distribution $g_1(x)$, and the transversity distribution $h_1(x)$. The meaning of the functions $f_1(x)$, $g_1(x)$ and $h_1(x)$ can be understood in the infinite-momentum frame of the nucleon. In this frame, the function $f_1(x)$ gives the probability for finding an unpolarized quark with momentum fraction x inside an unpolarized nucleon. The function $g_1(x)$ gives the probability for finding a quark with its polarization aligned with the polarization of the nucleon minus the probability for finding a quark with its polarization anti-aligned with the polarization of the nucleon, when the nucleon is polarized along its direction of motion[5]. The meaning of the

[3] In principle, a link operator (called a gauge link or Wilson line) is needed to make this expression color gauge-invariant (see e.g. Ref. [99]). For conciseness, here and in the following, this operator is assumed to be unity.

[4] See Ref. [37] for a detailed discussion of the concept twist.

[5] For distribution and fragmentation functions the notation of Ref. [99] is used. According to this scheme both

function $h_1(x)$ is the same, except for the nucleon now being polarized perpendicular to the direction of motion. This is shown schematically in Fig. 2.4, which indicates for each of the three distribution functions the relative orientation of the polarization of the quark and the nucleon.

Using Eqs. 2.13 and 2.16 for the hadronic tensor and the distribution correlator, respectively, an expression can be derived [96, 102] for the inclusive cross section at leading twist in terms of the distribution functions introduced above:

$$\frac{\mathrm{d}\sigma}{\mathrm{d}x\,\mathrm{d}y\,\mathrm{d}\phi_S} = \frac{\alpha^2}{sx(1-\epsilon)} \sum_q e_q^2 \left[f_1^q(x) + \lambda_e S_L \sqrt{1-\epsilon^2}\, g_1^q(x) \right], \tag{2.17}$$

where λ_e is the helicity of the electron and ϵ is the ratio of longitudinal and transverse photon flux given by

$$\epsilon = \frac{1 - y - \frac{1}{4}\gamma^2 y^2}{1 - y + \frac{1}{2}y^2 + \frac{1}{4}\gamma^2 y^2}, \qquad \gamma = \frac{2Mx}{Q}. \tag{2.18}$$

It is important to note that the transversity distribution function does not appear in Eq. 2.17. Transversity cannot be measured in inclusive DIS due to the fact that it is a chiral-odd function. In order to measure the transversity distribution function, it needs to be coupled to another chiral-odd object (see also Sec. 1.5). This can be realized in semi-inclusive DIS, where the second chiral-odd object is a fragmentation function. In this way, it is possible to conserve chirality for the scattering process as a whole. The semi-inclusive DIS process and the way it can be used to access transversity is discussed in Secs. 2.2–2.7.

2.2 One-hadron semi-inclusive deep-inelastic scattering

A deep-inelastic scattering process is called semi-inclusive if besides the scattered lepton, at least one final hadron (h) is also detected. In the case of one-hadron semi-inclusive DIS the reaction is written as

$$l(k) + N(P) \to l'(k') + h(P_h) + X(P_X), \tag{2.19}$$

where N represents the target nucleon, h the produced hadron, X the target remnant and the quantities in parentheses their four-momenta. Below, this process is discussed in some detail.

2.2.1 Kinematics

Apart from the inclusive variables x, y and ϕ_S, a new kinematic variable needs to be introduced to describe the one-hadron semi-inclusive process. This is the variable $\boldsymbol{P_h}$, the three-momentum of the detected hadron (see Fig. 2.5 for a picture of the vectors and angles used to describe this process). Alternatively, one can consider the variables z and $\boldsymbol{P_{h\perp}}$. In the lab frame, the dimension-

the helicity structure function and the helicity distribution function are called g_1. Then, in the quark parton model $g_1(x) = \sum_{q,\bar{q}} e_q^2 g_1^q(x)$. In Ref. [38] the distribution function $g_1^q(x)$ is referred to as $\Delta q(x)$.

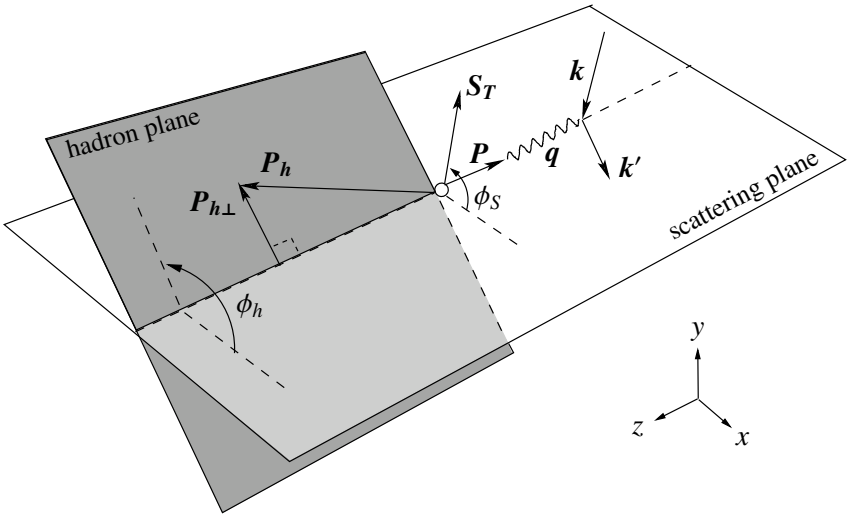

Figure 2.5: *Kinematic variables describing the one-hadron semi-inclusive deep-inelastic scattering process.*

less variable z represents the fraction of the virtual photon energy transferred to the hadron. It is defined as

$$z \equiv \frac{P \cdot P_h}{P \cdot q} \overset{\text{LAB}}{=} \frac{E_h}{E - E'} = \frac{E_h}{\nu}. \tag{2.20}$$

The variable $\boldsymbol{P_{h\perp}}$ is the component of $\boldsymbol{P_h}$ perpendicular to the virtual-photon direction. Under the assumption that $|\boldsymbol{P_{h\perp}}| \ll E_h$, one can relate $\mathrm{d}^3\boldsymbol{P_h}$ to $\mathrm{d}z$ and $\mathrm{d}^2\boldsymbol{P_{h\perp}}$ as:

$$\frac{\mathrm{d}^3\boldsymbol{P_h}}{E_h} = \frac{1}{z}\,\mathrm{d}z\,\mathrm{d}^2\boldsymbol{P_{h\perp}}. \tag{2.21}$$

The differential $\mathrm{d}^2\boldsymbol{P_{h\perp}}$ is often also rewritten as:

$$\mathrm{d}^2\boldsymbol{P_{h\perp}} = |\boldsymbol{P_{h\perp}}|\,\mathrm{d}|\boldsymbol{P_{h\perp}}|\,\mathrm{d}\phi_h, \tag{2.22}$$

where the azimuthal angle ϕ_h of the hadron direction around the virtual-photon direction has been introduced. It can be calculated, analogously to the calculation of ϕ_S (Eq. 2.8) as

$$\phi_h = \frac{\boldsymbol{q}\times\boldsymbol{k}\cdot\boldsymbol{P_h}}{|\boldsymbol{q}\times\boldsymbol{k}\cdot\boldsymbol{P_h}|}\cos^{-1}\frac{\boldsymbol{q}\times\boldsymbol{k}\cdot\boldsymbol{q}\times\boldsymbol{P_h}}{|\boldsymbol{q}\times\boldsymbol{k}||\boldsymbol{q}\times\boldsymbol{P_h}|}. \tag{2.23}$$

2.2.2 Cross section

With the newly defined variables, the cross section for one-hadron semi-inclusive DIS can now be written as

$$\frac{2E_h\,\mathrm{d}^6\sigma}{\mathrm{d}x\,\mathrm{d}y\,\mathrm{d}\phi_S\,\mathrm{d}^3\boldsymbol{P_h}} = \frac{2z\,\mathrm{d}^6\sigma}{\mathrm{d}x\,\mathrm{d}y\,\mathrm{d}\phi_S\,\mathrm{d}z\,\mathrm{d}^2\boldsymbol{P_{h\perp}}} = \frac{\alpha^2}{2sxQ^2}L_{\mu\nu}2MW^{\mu\nu}, \tag{2.24}$$

where the left hand side was rewritten using Eq. 2.21. The difference with respect to the inclusive DIS process is that the hadronic tensor now not only contains the distribution correlator Φ, but

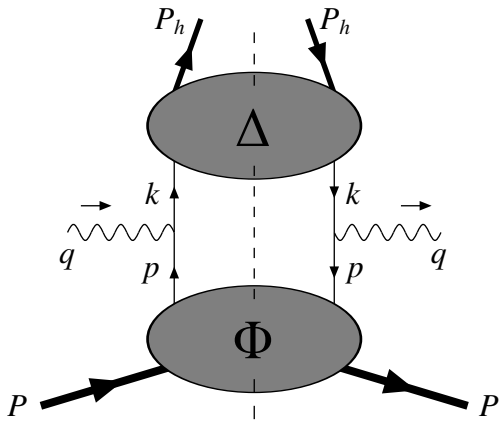

Figure 2.6: *Diagram describing semi-inclusive DIS at leading order.*

also the fragmentation correlator Δ, which describes the fragmentation of the struck quark into a hadron. In the case that the hadron h is unpolarized, the fragmentation correlator Δ can be written as

$$\Delta_{ij}(k, P_h) = \sum_X \int \frac{\mathrm{d}^3 \boldsymbol{P_x}}{(2\pi)^3 2E_x} \langle 0|\psi_i(0)|P_h, X\rangle\langle P_h, X|\bar{\psi}_j(0)|0\rangle \delta^4(k - P_h - P_x), \tag{2.25}$$

where $|P_h, X\rangle$ represents the hadronic final state and the summation runs over all possible undetected hadronic states X.

Figure 2.6 shows the leading-order diagram contributing to the semi-inclusive DIS process, where the distribution correlator Φ and the fragmentation correlator Δ account for the parts of the scattering process that cannot be calculated in pQCD. The hadronic tensor for this diagram can be written as:

$$2MW^{\mu\nu}(q, P, S, P_h) = 2z\mathcal{I}\left[\mathrm{Tr}(\Phi(x, \boldsymbol{p_T}, S)\gamma^\mu \Delta(z, \boldsymbol{k_T}\gamma^\nu))\right]. \tag{2.26}$$

Here, $\mathcal{I}$ denotes an integral over the transverse momenta, which convolutes the distribution correlator Φ and the fragmentation correlator Δ:

$$\mathcal{I}[\cdots] \equiv \int \mathrm{d}^2\boldsymbol{p_T}\, \mathrm{d}^2\boldsymbol{k_T} \delta^{(2)}(\boldsymbol{p_T} - \frac{\boldsymbol{P_{h\perp}}}{z} - \boldsymbol{k_T})[\cdots], \tag{2.27}$$

with $\boldsymbol{p_T}$ and $\boldsymbol{k_T}$ the transverse momenta of the struck quark before and after the interaction with the virtual photon, respectively. The convolution integral relates the transverse-momentum dependence of the quarks in the nucleon and the transverse-momentum dependence of the fragmentation process to the (observable) transverse-momentum dependence of the produced hadron.

These momenta are transverse with respect to the z axis in a frame where the nucleon N and the hadron h are collinear, i.e., antiparallel to the z axis. The integrated correlation functions

Figure 2.7: *Schematic representation of the two leading-twist fragmentation functions* $D_1(z, z^2\boldsymbol{k_T^2})$ *and* $H_1^\perp(z, z^2\boldsymbol{k_T^2})$*. The struck quark (produced hadron) is indicated as a black (light grey) circle.*

introduced in Eq. 2.26 are defined by

$$\Phi(x, \boldsymbol{p_T}, S) \equiv \int \mathrm{d}p^- \Phi(p, P, S)\Big|_{p^+=xP^+}, \tag{2.28}$$

$$\Delta(z, \boldsymbol{k_T}) \equiv \frac{1}{2z}\int \mathrm{d}k^+ \Delta(k, P_h)\Big|_{k^-=P_h^-/z}. \tag{2.29}$$

Eqs. 2.26–2.29 explicitly take the transverse-momentum dependence into account, in contrast to what was presented in Sec. 2.1.3 for inclusive DIS (see Eq. 2.15). The reason for this is that the transverse-momentum dependence of the detected hadron has to be measured in order to access the transversity distribution function. This will become apparent in the next subsection, in which the structure of the fragmentation correlator Δ is discussed.

2.2.3 One-hadron fragmentation functions

In a similar fashion as was done for the distribution correlator Φ, the fragmentation correlator Δ can be expanded on a basis of Dirac matrices, which in this case are multiplied by *fragmentation functions*. In general, a fragmentation function gives the probability for a quark to fragment into a hadron with a certain fraction z of the energy of the virtual photon. At leading twist and by requiring that the correlator satisfies hermiticity and parity invariance, the correlator can be written as:

$$\Delta(z, \boldsymbol{k_T}) = \frac{1}{2}\left(D_1(z, z^2\boldsymbol{k_T^2}) + iH_1^\perp(z, z^2\boldsymbol{k_T^2})\frac{\not{k}_T}{M_h}\right)\gamma^+. \tag{2.30}$$

Here, D_1 is the unpolarized fragmentation function, which describes the probability for an unpolarized quark to fragment into an unpolarized hadron. The function $H_1^\perp$, called the Collins fragmentation function, is a chiral-odd function, which gives the probability for a transversely polarized quark to fragment into an unpolarized hadron. This is shown schematically in Fig. 2.7. The cross section in terms of the distribution and fragmentation functions can be obtained by combining Eqs. 2.16, 2.26 and 2.30 into Eq. 2.24. The full (large) expression can be found for instance in Ref. [102, 103], which contains several terms that are characterized by Fourier components of the azimuthal angles ϕ_h and ϕ_S. The transversity distribution appears in this expression coupled to the Collins fragmentation function:

$$\frac{\mathrm{d}^6\sigma_{\text{Collins}}}{\mathrm{d}x\,\mathrm{d}y\,\mathrm{d}z\,\mathrm{d}\phi_S\,\mathrm{d}^2\boldsymbol{P_{h\perp}}} = -\sum_q \frac{2\alpha^2 e_q^2}{sxy^2} S_T(1-y)\sin(\phi_h+\phi_S)\mathcal{I}\left[\frac{\boldsymbol{k_T}\cdot\hat{\boldsymbol{P}}_{\boldsymbol{h\perp}}}{M_h}h_1^q H_1^{\perp q}\right], \tag{2.31}$$

which shows only that part of the cross section that depends on h_1. The summation is over the quark flavors. From this expression it is clear that in order to access transversity in one-hadron semi-inclusive DIS the target nucleon has to be polarized, with a transverse component S_T. Characteristic for this term in the cross section is the $\sin(\phi_h + \phi_S)$ modulation. Due to this modulation, this term can be distinguished from other terms in the cross section, which enables the extraction of transversity from measurements of the one-hadron semi-inclusive DIS process. The transversity distribution function h_1 and the Collins fragmentation function $H_1^\perp$ are convoluted in transverse momentum through the integral $\mathcal{I}$. In order to disentangle the contribution from the two unknown functions, one can either use a model prediction for their transverse-momentum dependence, or one can weight the cross section with $P_{h\perp}$ [96, 104]. Note also that the part of the cross section, given in Eq. 2.31, vanishes upon integration over $\boldsymbol{P_{h\perp}}$ (cf. Eq. 2.22).

Eq 2.31 shows that only a value of the convolution of h_1 and $H_1^\perp$ can be derived from measurements of one-hadron semi-inclusive DIS. In order to obtain h_1 an independent measurement of $H_1^\perp$ is needed, as was mentioned in Sec. 1.5.2. Recently, azimuthal asymmetries related to the product of the quark and antiquark Collins fragmentation functions were measured for the first time by the BELLE collaboration and found to be nonzero [81].

2.3 Two-hadron semi-inclusive deep-inelastic scattering

For two-hadron semi-inclusive deep-inelastic scattering it is required that besides the scattered lepton at least two hadrons (h_1 and h_2) are detected

$$l(k) + N(P) \rightarrow l'(k') + h_1(P_1) + h_2(P_2) + X(P_X), \tag{2.32}$$

where apart from h_1 (with mass M_1) and h_2 (with mass M_2), the symbols are similar to those used in Eq. 2.19.

2.3.1 Kinematics

In addition to the inclusive DIS variables, two additional independent kinematic variables appear: the momenta $\boldsymbol{P_1}$ and $\boldsymbol{P_2}$ of the two hadrons. In practice, several new variables can be introduced [105, 106] derived from $\boldsymbol{P_1}$ and $\boldsymbol{P_2}$, which are used to describe the two-hadron semi-inclusive deep-inelastic scattering process. They are the center-of-mass and relative momenta

$$P_h \equiv P_1 + P_2, \qquad R \equiv \frac{1}{2}(P_1 - P_2), \tag{2.33}$$

and the dimensionless variables

$$z_1 = \frac{P\cdot P_1}{P\cdot q}, \qquad z = z_1 + z_2 = \frac{P\cdot P_h}{P\cdot q}, \tag{2.34a}$$

$$z_2 = \frac{P\cdot P_2}{P\cdot q}, \qquad \zeta = 2\frac{R^-}{P_h^-} = 2\frac{z_1}{z} - 1, \tag{2.34b}$$

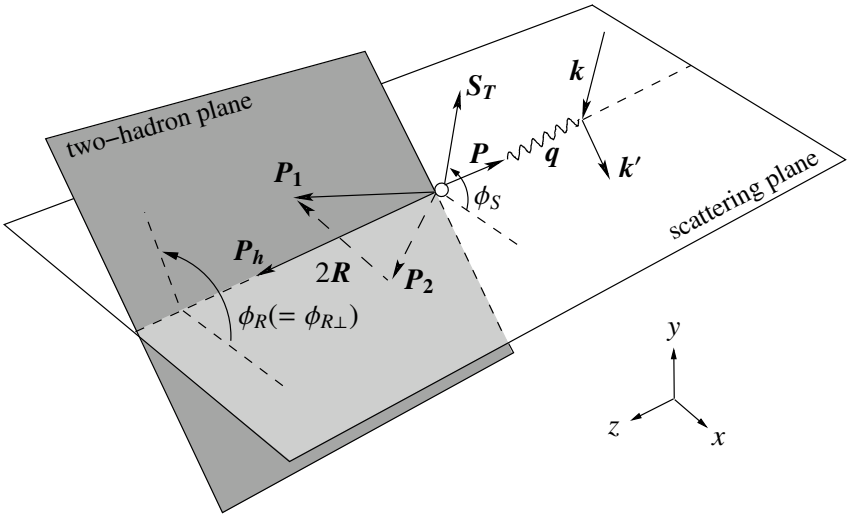

Figure 2.8: *Depiction of the azimuthal angles ϕ_R ($\phi_{R\perp}$) and ϕ_S (in the virtual-photon-nucleon center-of-mass frame). Shown here is the configuration, $P_{h\perp} = 0$, in which ϕ_R and $\phi_{R\perp}$ coincide.*

where R^- and P_h^- are light-cone components of R and P_h, respectively. The difference between $\boldsymbol{R}$ and $-\boldsymbol{R}$ is not defined if h_1 and h_2 are identical particles. In the present work, the specific process is considered where h_1 and h_2 are two oppositely charged pions. For this process, the sign of $\boldsymbol{R}$ can be defined: in the present work P_1 is defined as the momentum of the positive pion, consistent with the literature on the subject (as first defined in Ref. [107]).

Similar to the one-hadron case, P_h can be written in terms of its component $\boldsymbol{P_{h\perp}}$ perpendicular to the virtual-photon direction (cf. Eq. 2.21), which also introduces the two-hadron analogue of ϕ_h (cf. Eqs. 2.22 and 2.23). Also $\mathrm{d}^3\boldsymbol{R}$ can be written in terms of a transverse component:

$$\mathrm{d}^3\boldsymbol{R} = \frac{1}{2} E_h \,\mathrm{d}\zeta \,\mathrm{d}^2\boldsymbol{R_T}, \tag{2.35}$$

$$\mathrm{d}^2\boldsymbol{R_T} = |\boldsymbol{R_T}|\,\mathrm{d}|\boldsymbol{R_T}|\,\mathrm{d}\phi_R, \tag{2.36}$$

where $\boldsymbol{R_T}$ is the component transverse to $\boldsymbol{P_h}$ in the hadronic center-of-mass system and ϕ_R is the azimuthal angle around $\boldsymbol{P_h}$. In Fig. 2.8, the azimuthal angles ϕ_R and ϕ_S as well as the involved vectors are shown, for the special case that $\boldsymbol{P_{h\perp}} = 0$.

For the calculation of the cross section of semi-inclusive deep-inelastic scattering, one considers often two different Lorentz frames [108]. For the distribution part of the cross section it is common to use a frame ($\perp$-frame) where the z-axis is aligned with the virtual-photon direction, such that the virtual photon does not have a transverse momentum component (with respect to the z-axis in this frame), whereas the outgoing hadrons then do have transverse momentum components. For the fragmentation part of the cross section it is more common to resort to a frame (T-frame) where the outgoing hadron (or the sum of two outgoing hadrons, as is the case here) does not have a transverse momentum component and consequently the virtual photon does obtain a transverse momentum component. The difference between these two frames can be ignored for

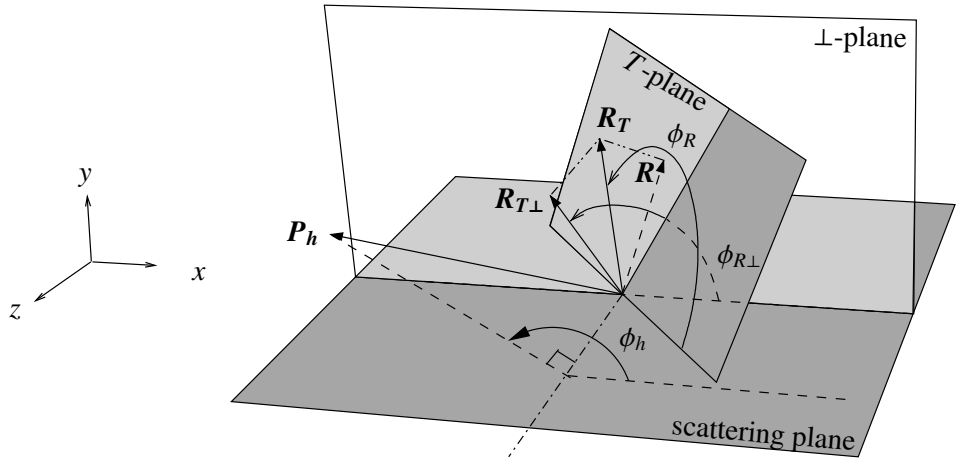

Figure 2.9: *Explanation of the angles ϕ_R, $\phi_{R\perp}$ and ϕ_h (see text).*

leading-twist analyses [108].

In Fig. 2.8, $\boldsymbol{P_h}$ is shown aligned with $\boldsymbol{q}$, an example of a configuration in which the $\perp$-frame and T-frame coincide. If the frames do not coincide, one can consider two different angles for the azimuthal orientation of $\boldsymbol{R}$. One can consider either the azimuthal angle of $\boldsymbol{R_T}$ around $\boldsymbol{P_h}$ (ϕ_R) or the azimuthal angle of $\boldsymbol{R_T}$ around $\boldsymbol{q}$ ($\phi_{R\perp}$). The difference between the two frames and these two angles is illustrated in Fig. 2.9. Here, the vector $\boldsymbol{R_{T\perp}}$ is the projection of $\boldsymbol{R_T}$ onto the $\perp$-plane.

The difference between these two angles can be ignored up to subleading-twist analyses [108]. For the configuration shown in Fig. 2.8 these two angles are the same. The angles ϕ_R and $\phi_{R\perp}$ can be calculated from the involved vectors as

$$\phi_R = \frac{\hat{\boldsymbol{n}} \cdot \boldsymbol{R_T}}{|\boldsymbol{R_T}|} \cos^{-1} \frac{\hat{\boldsymbol{n}} \cdot (\boldsymbol{P_h} \times \boldsymbol{R_T})}{|\boldsymbol{P_h} \times \boldsymbol{R_T}|}, \tag{2.37}$$

and

$$\phi_{R\perp} = \frac{\boldsymbol{q} \times \boldsymbol{k} \cdot \boldsymbol{R_T}}{|\boldsymbol{q} \times \boldsymbol{k} \cdot \boldsymbol{R_T}|} \cos^{-1} \frac{\boldsymbol{q} \times \boldsymbol{k} \cdot \boldsymbol{q} \times \boldsymbol{R_T}}{|\boldsymbol{q} \times \boldsymbol{k}||\boldsymbol{q} \times \boldsymbol{R_T}|}, \tag{2.38}$$

where $\hat{\boldsymbol{n}}$ is a unit vector defined by the line of intersection of the T-plane with the plane defined by $(\boldsymbol{k} \times \boldsymbol{q})$ and $\boldsymbol{P_h}$. In appendix D the calculation of $\hat{\boldsymbol{n}}$ is described.

2.3.2 Cross section

The cross section for the two-hadron semi-inclusive DIS process can be written as:

$$\frac{2E_1 2E_2\, \mathrm{d}^9\sigma}{\mathrm{d}^3\boldsymbol{P_1}\, \mathrm{d}^3\boldsymbol{P_2}\, \mathrm{d}x\, \mathrm{d}y\, \mathrm{d}\phi_S} = \frac{16z\, \mathrm{d}^9\sigma}{\mathrm{d}\zeta\, \mathrm{d}M_h^2\, \mathrm{d}\phi_R\, \mathrm{d}z\, \mathrm{d}^2P_{h\perp}\, \mathrm{d}x\, \mathrm{d}y\, \mathrm{d}\phi_S} = \frac{\alpha^2}{2sxQ^2} L_{\mu\nu} 2MW^{\mu\nu}. \tag{2.39}$$

At leading order in $1/Q$, the hadronic tensor can be written in terms of correlation functions, similar to what was done for the one-hadron case (see Eq. 2.26):

$$2MW^{\mu\nu}(q, P, S, P_1, P_2) = 32z\mathcal{I}\left[\mathrm{Tr}\left(\Phi(x, \boldsymbol{p_T}, S)\gamma^\mu \Delta(z, \boldsymbol{k_T}, \zeta, M_h^2, \phi_R)\gamma^\nu\right)\right], \tag{2.40}$$

where the distribution correlator Φ is the same function as the one appearing in Eq. 2.26, but the fragmentation correlator Δ is different, as it describes the fragmentation of the struck quark into a hadron pair. In this case it is defined as:

$$\Delta(z, \boldsymbol{k_T}, \zeta, M_h^2, \phi_R) \equiv \frac{1}{32z} \int \mathrm{d}k^+ \Delta(k, P_h, R)\Big|_{k^- = P^-/z}. \tag{2.41}$$

2.3.3 Two-hadron fragmentation functions

After defining the two-hadron fragmentation correlator, Eq. 2.41, a natural next step would be to expand this correlator in terms of two-hadron fragmentation functions, analogous to the procedure followed for the one-hadron semi-inclusive DIS process. In this case, we would end up with more fragmentation functions than for the one-hadron case. However, the situation can be simplified by considering the cross section integrated over the transverse momentum $\boldsymbol{P_{h\perp}}$ of the hadron pair. The hadronic tensor then becomes [106]:

$$2MW^{\mu\nu}(q, P, S, P_1, P_2) = 32z\mathrm{Tr}\left(\Phi(x, S)\gamma^\mu \Delta(z, \zeta, M_h^2, \phi_R)\gamma^\nu\right), \tag{2.42}$$

with

$$\Delta(z, \zeta, M_h^2, \phi_R) \equiv \frac{z}{32} \int \mathrm{d}k^+ \, \mathrm{d}^2\boldsymbol{k_T} \Delta(k, P_h, R)\Big|_{k^- = P^-/z}. \tag{2.43}$$

This simplification has the advantage that the fragmentation correlator, integrated over $\boldsymbol{P_{h\perp}}$, can now be expanded at leading-twist in terms of two fragmentation functions, D_1 and $H_1^\sphericalangle$:

$$\Delta(z, \zeta, M_h^2, \phi_R) = \frac{1}{16\pi}\left(D_1(z, \zeta, M_h^2) + iH_1^\sphericalangle(z, \zeta, M_h^2)\frac{\not{R}_T}{M_h}\right)\gamma^+. \tag{2.44}$$

These two-hadron fragmentation functions $D_1(z, \zeta, M_h^2)$ and $H_1^\sphericalangle(z, \zeta, M_h^2)$ have similar probabilistic interpretations as their one-hadron analogues $D_1(z, z^2\boldsymbol{k_T^2})$ and the Collins function $H_1^\perp(z, z^2\boldsymbol{k_T^2})$ (as shown in Fig. 2.7), only now producing two hadrons instead of one. The full transverse momentum-dependent expansion of Eq. 2.41 [105] introduces the two-hadron fragmentation function $H_1^\perp$ as well, i.e., the same symbols are used for the one-hadron and two-hadron Collins function. Both two-hadron fragmentation functions $H_1^\perp$ and $H_1^\sphericalangle$ describe the fragmentation of a transversely polarized quark into a pair of unpolarized hadrons. They are also both chiral-odd functions. The difference between them is the direction in which the two fragmenting hadrons move. The function $H_1^\perp$ is sensitive to the transverse momentum $\boldsymbol{P_{h\perp}}$ of the hadron pair relative to the virtual-photon direction whereas $H_1^\sphericalangle$ is sensitive to the relative transverse momentum $\boldsymbol{R_T}$ of the two hadrons.

By inserting the expressions for the distribution and fragmentation correlators, Eq. 2.16 and Eq. 2.44, into the expression for the hadronic tensor, Eq. 2.42, the cross section for two-hadron

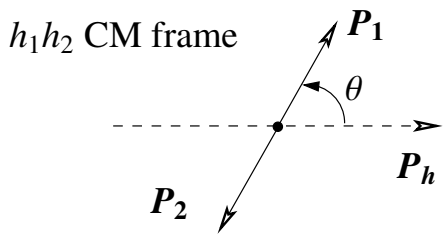

Figure 2.10: *Description of the polar angle θ, between the positive hadron in the hadron pair's center-of-mass frame and $\boldsymbol{P_h}$ in the γ^*N center-of-mass frame. In the present work $\boldsymbol{P_1}$ represents the momentum of the positively charged pion, in agreement with Ref. [107].*

production expressed in terms of quark distribution and fragmentation functions is obtained [106]

$$\frac{\mathrm{d}^7\sigma}{\mathrm{d}\zeta\,\mathrm{d}M_h^2\,\mathrm{d}\phi_R\,\mathrm{d}z\,\mathrm{d}x\,\mathrm{d}y\,\mathrm{d}\phi_S} = \frac{2\alpha^2}{4\pi s x y^2}\sum_q e_q^2\Big[A(y)f_1^q(x)D_1^q(z,\zeta,M_h^2) + \lambda_e S_L C(y) g_1^q(x) D_1^q(z,\zeta,M_h^2) - B(y) S_T \frac{|\boldsymbol{R_T}|}{M_h}\sin(\phi_R+\phi_S) h_1^q(x) H_1^{\sphericalangle,q}(z,\zeta,M_h^2)\Big], \quad (2.45)$$

with λ_e the helicity of the electron. The summation is over the quark flavours q and

$$A(y) = 1 - y + \frac{y^2}{2}, \qquad B(y) = (1-y), \qquad C(y) = y(1-\frac{y}{2}) \quad (2.46)$$

are purely kinematic functions. Eq. 2.45 is a leading-twist expression. The sub-leading twist expression can be found in Ref. [108]. The importance of Eq. 2.45 is that the dependence of the two-hadron semi-inclusive DIS cross section on the three leading-twist distribution functions f_1, g_1 and h_1 and the corresponding two-hadron fragmentation functions is made explicit. From Eq. 2.45 it is seen that information on transversity can be extracted from a two-hadron semi-inclusive DIS experiment, if a transversely polarized target is used and the amplitude of the $\sin(\phi_R+\phi_S)$ dependence is isolated.

2.3.4 Partial wave expansion

According to Ref. [106], the dihadron fragmentation functions introduced in the previous section can be expanded in terms of Legendre polynomials. In this subsection the work of Ref. [106] is briefly discussed.

The partial wave expansion allows to separate different possible contributions to these fragmentation functions like, for instance, the interference between a pion pair in a relative s-wave and a pion pair in a relative p-wave. The expansion is made in terms of the polar angle θ between the positive hadron in the center-of-mass of the pair and P_h in the target rest frame as shown in Fig. 2.10. The angle is related to the variable ζ as:

$$\zeta \equiv \frac{2R^-}{P_h^-} \overset{\mathrm{CM}}{=} \frac{1}{M_h}\left(\sqrt{M_1^2+|\boldsymbol{R}|^2} - \sqrt{M_2^2+|\boldsymbol{R}|^2} - 2|\boldsymbol{R}|\cos\theta\right), \quad (2.47)$$

with

$$|\boldsymbol{R}| = \frac{1}{2}\sqrt{M_h^2 - 2\left(M_1^2 + M_2^2\right) + \left(M_1^2 - M_2^2\right)\Big/M_h^2}. \tag{2.48}$$

At low invariant mass, the expansion can be truncated to include only the lowest order terms as in this mass region only contributions are expected from the pion pair in a relative s- or p-wave. Typically, in the literature the invariant-mass region below $M_h \approx 1$ GeV is considered, which includes the ρ^0 resonance ($M_h = 0.78$ GeV). The expansion can then be written as:

$$\begin{aligned}\frac{2|\boldsymbol{R}|}{M_h}D_1(z,\zeta(\cos\theta),M_h^2) &= D_{1,oo}(z,M_h^2) + D_{1,ol}^{sp}(z,M_h^2)\cos\theta \\ &\quad + D_{1,ll}^{pp}(z,M_h^2)\frac{1}{4}(3\cos^2\theta - 1), \end{aligned}\tag{2.49}$$

$$\frac{2|\boldsymbol{R}|}{M_h}H_1^{\sphericalangle}(z,\zeta(\cos\theta),M_h^2) = H_{1,ot}^{\sphericalangle,sp}(z,M_h^2) + H_{1,lt}^{\sphericalangle,pp}(z,M_h^2)\cos\theta. \tag{2.50}$$

The subscripts o, l and t refer, respectively, to the hadron pair being unpolarized, longitudinally polarized and transversely polarized. This polarization refers directly to the θ-dependent factors, which appear in Eqs. 2.49 and 2.50. The function $H_{1,ot}^{\sphericalangle,sp}$ describes the interference between a pion pair produced in a relative s-wave and a pion pair in a relative p-wave. The function $H_{1,lt}^{\sphericalangle,pp}$ relates to the interference between two pion pairs which are both in relative p-waves, but which are polarized differently. The fragmentation functions in Eqs. 2.49 and 2.50 are often also written without the superscript or the subscript, as they are directly related. In the present work only the superscripts are kept.

In principle, both fragmentation functions $H_1^{\sphericalangle,sp}$ and $H_1^{\sphericalangle,pp}$ can be used to access transversity, as was first mentioned in Ref. [106]. However, up to this moment in the literature the focus has been on the contribution to the cross section from $H_1^{\sphericalangle,sp}$ and model predictions, discussed in Sec. 2.7, are only available for $H_1^{\sphericalangle,sp}$. Therefore, also in this work transversity will be accessed through $H_1^{\sphericalangle,sp}$. A different reason for this choice, of a more technical nature, is discussed in Sec. 4.5.4.

2.4 Single-spin asymmetries

In Sec. 2.3.3 an expression was derived for the spin-dependent cross section of two-hadron semi-inclusive DIS (Eq. 2.45). Here, we are interested specifically in the transversity distribution, which is contained in the transversely polarized part of the cross section, i.e., the part sensitive to $|\boldsymbol{S_T}|$. In this section it is discussed how this polarized part of the cross section can be isolated experimentally.

The cross section for semi-inclusive deep-inelastic electron-proton scattering using an unpolarized lepton beam and a polarized target can generally be written as[6]:

$$\mathrm{d}\sigma(\phi_S) = \mathrm{d}\sigma_{UU} + \mathrm{d}\sigma_{UT}(\phi_S) + \mathrm{d}\sigma_{UL}, \tag{2.51}$$

[6]Here, $\mathrm{d}\sigma$ is short for $\mathrm{d}\sigma/(\,\mathrm{d}x\,\mathrm{d}y\,\mathrm{d}\phi_S\,\mathrm{d}\boldsymbol{P_h})$ in case of one-hadron DIS and for $\mathrm{d}\sigma/(\,\mathrm{d}x\,\mathrm{d}y\,\mathrm{d}\phi_S\,\mathrm{d}\boldsymbol{P_1}\,\mathrm{d}\boldsymbol{P_2})$ in case of two-hadron DIS (the same is true for $\mathrm{d}\sigma_{UU}$, $\mathrm{d}\sigma_{UT}$ and $\mathrm{d}\sigma_{UL}$).

with

$$\mathrm{d}\sigma_{UT} = S_T \cos\phi_S a_1 + S_T \sin\phi_S a_2, \qquad \mathrm{d}\sigma_{UL} = -S_L a_3, \tag{2.52}$$

where only the dependence on ϕ_S is explicitly shown and with S_L and S_T the target polarization along and perpendicular to the virtual-photon direction, respectively. The subscripts U, T and L refer to unpolarized beam, transversely polarized target and longitudinally polarized target, respectively. The quantities a_i are independent of ϕ_S.

A common method to analyze the spin-dependent part of the cross section is through cross-section asymmetries. The part dependent on S_T can be accessed by the single-spin asymmetry (SSA) $A_{UT}^{\gamma^*}$:

$$A_{UT}^{\gamma^*} = \left.\frac{\mathrm{d}\sigma(\phi_S) - \mathrm{d}\sigma(\phi_S+\pi)}{\mathrm{d}\sigma(\phi_S) + \mathrm{d}\sigma(\phi_S+\pi)}\right|_{S_T=1,S_L=0} = \frac{\mathrm{d}\sigma_{UT}}{\mathrm{d}\sigma_{UU}}, \tag{2.53}$$

where the superscript γ^* indicates that the target is polarized transversely with respect to the virtual-photon direction. The part of the cross section dependent on S_L can be accessed by $A_{UL}^{\gamma^*}$:

$$A_{UL}^{\gamma^*} = \left.\frac{\mathrm{d}\sigma(S_L=+1) - \mathrm{d}\sigma(S_L=-1)}{\mathrm{d}\sigma(S_L=+1) + \mathrm{d}\sigma(S_L=-1)}\right|_{S_T=0} = \frac{\mathrm{d}\sigma_{UL}}{\mathrm{d}\sigma_{UU}}. \tag{2.54}$$

Asymmetries have a big advantage from the experimental point of view compared to cross sections. In case of asymmetries many systematic uncertainties cancel to a large extent because they appear in the same way in the numerator of the expression for the asymmetry as in the denominator. Also, it is not needed to measure absolute cross sections, as long as the two cross sections in the asymmetry are properly normalized with respect to each other.

For both one-hadron and two-hadron semi-inclusive deep-inelastic scattering, the asymmetry $A_{UT}^{\gamma^*}$ provides access to transversity. Eq. 2.53 indicates that in order to measure this asymmetry, one needs a target that is polarized transversely with respect to the virtual-photon direction. However, polarized experiments like HERMES can only measure the following asymmetries:

$$A_{UT}^{\ell} = \left.\frac{\mathrm{d}\sigma(\phi_S) - \mathrm{d}\sigma(\phi_S+\pi)}{\mathrm{d}\sigma(\phi_S) + \mathrm{d}\sigma(\phi_S+\pi)}\right|_{P_T=1,P_L=0} \tag{2.55}$$

and

$$A_{UL}^{\ell} = \left.\frac{\mathrm{d}\sigma(P_L=+1) - \mathrm{d}\sigma(P_L=-1)}{\mathrm{d}\sigma(P_L=+1) + \mathrm{d}\sigma(P_L=-1)}\right|_{P_T=0}, \tag{2.56}$$

where P_T and P_L are the target polarization components transversely and longitudinally oriented *with respect to the beam*. The difference between the polarization $\boldsymbol{P}$ and $\boldsymbol{S}$ is shown in Fig. 2.11. The experimentally accessible asymmetries A_{UT}^{ℓ} and A_{UL}^{ℓ} can be rewritten in terms of the asymmetries $A_{UT}^{\gamma^*}$ and $A_{UL}^{\gamma^*}$ defined in Eq. 2.53 and Eq. 2.54 [98]:

$$A_{UL}^{\ell} = \cos\theta_\gamma A_{UL}^{\gamma^*} - \sin\theta_\gamma A_{UT}^{\gamma^*}(0), \tag{2.57}$$

$$A_{UT}^{\ell}(\phi_S) = \frac{\cos\theta_\gamma A_{UT}^{\gamma^*}(\phi_S) + \sin\theta_\gamma \cos\phi_S A_{UL}^{\gamma^*}}{\sqrt{1-\sin^2\theta_\gamma \sin^2\phi_S}}. \tag{2.58}$$

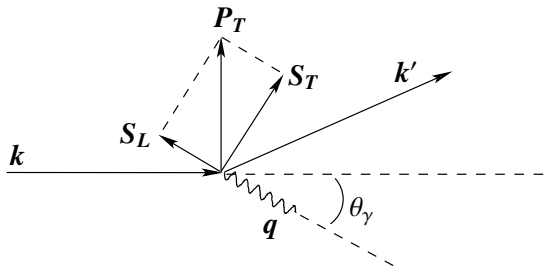

Figure 2.11: *Schematic explanation of the difference between the polarization vectors* $\boldsymbol{P}$ *and* $\boldsymbol{S}$ *(here for the situation that* $\phi_S = 0$*,* $P_T = 1$ *and* $P_L = 0$*).*

Here, θ_γ is the angle between the lepton direction $\boldsymbol{k}$ and the virtual-photon direction $\boldsymbol{q}$ and

$$\sin\theta_\gamma = \gamma\sqrt{\frac{1 - y - \frac{1}{4}y^2\gamma^2}{1+\gamma^2}}. \tag{2.59}$$

For two-hadron semi-inclusive DIS at HERMES, $\sin\theta_\gamma$ is quite small, i.e. $\langle\sin\theta_\gamma\rangle = 0.05$ (within the kinematical region used for the extraction of the SSA, as discussed in Sec. 4.2.3).

Eqs. 2.57 and 2.58 indicate that A_{UL}^{ℓ} contains a small contribution from $A_{UT}^{\gamma^*}$ and A_{UT}^{ℓ} contains a small contribution from $A_{UL}^{\gamma^*}$. From here on, the superscripts γ^* and ℓ are not shown, as it will be clear from the context which one is referred to.

2.5 Azimuthal moments and amplitudes

The asymmetries as defined in the previous section provide a way to extract the part of the cross section that depends on the polarization of the target in a convenient way. For both one- and two-hadron semi-inclusive deep-inelastic scattering, this part of the cross section can contain several different terms, which all contain a product or a convolution of a distribution function and a fragmentation function. Many of these terms have a unique dependence on the azimuthal angles, i.e., ϕ_h and ϕ_S for one-hadron semi-inclusive deep-inelastic scattering and ϕ_h, ϕ_S and $\phi_{R\perp}$ for two-hadron semi-inclusive deep-inelastic scattering. Typically, this dependence takes the form of Fourier components of these angles or combinations of these angles. To single out one or more specific terms of the cross section, with a distinct angular dependence, one can use *azimuthal moments* of the asymmetry. As an example, the azimuthal moment $\langle\sin(\phi_h+\phi_S)\rangle_{UT}$ is defined as

$$\langle\sin(\phi_h+\phi_S)\rangle_{UT} \equiv \left.\frac{\int \mathrm{d}\phi_h\,\mathrm{d}\phi_S\,\sin(\phi_h+\phi_S)[\,\mathrm{d}\sigma(\phi_h,\phi_S) - \mathrm{d}\sigma(\phi_h,\phi_S+\pi)]}{\int \mathrm{d}\phi_h\,\mathrm{d}\phi_S[\,\mathrm{d}\sigma(\phi_h,\phi_S) + \mathrm{d}\sigma(\phi_h,\phi_S+\pi)]}\right|_{|\boldsymbol{S_T}|=1,|\boldsymbol{S_L}|=0}. \tag{2.60}$$

Then, if the cross section is given by

$$\mathrm{d}\sigma(\phi_h,\phi_S) = b_0 + S_L b_1 + S_T[b_2\sin(\phi_h+\phi_S) + \ldots], \tag{2.61}$$

the azimuthal moment becomes $\langle \sin(\phi_h + \phi_S) \rangle_{UT} = b_2/(2b_0)$ (where the b_i are arbitrary parameters, independent of ϕ_h and ϕ_S). In this thesis, instead of the azimuthal moments like $\langle \sin(\phi_h + \phi_S) \rangle_{UT}$ the *amplitudes* $A_{UT}^{\sin(\phi_h+\phi_S)}$ are often used, which are related to each other as $A_{UT}^{\sin(\phi_h+\phi_S)} = 2\langle \sin(\phi_h + \phi_S \rangle_{UT}$. These amplitudes have values in the range [-1,1] like the asymmetries themselves.

Now that the theoretical framework for transversity studies in one-hadron and two-hadron semi-inclusive DIS has been discussed in Secs. 2.1– 2.3 and the method that is used to access transversity experimentally has been discussed in Secs. 2.4– 2.5, in the remaining sections of this chapter some existing experimental results and models for these processes are discussed.

2.6 Transversity studies in one-hadron semi-inclusive DIS

The HERMES experiment has taken data with a transversely polarized hydrogen target from the year 2002 until 2005. First measurements by the HERMES collaboration of the transverse single-spin asymmetry A_{UT}, based on the data taking period 2002-2003, were published in 2005 [74]. It contains the first direct measurement ever of the azimuthal moment $\langle \sin(\phi_h + \phi_S) \rangle$, i.e., the so-called Collins moment, which is sensitive to the transversity distribution function $h_1(x)$ and the Collins fragmentation function $H_1^\perp$ [96] (cf. Eq. 2.31):

$$\langle \sin(\phi_h + \phi_S) \rangle_{UT} = -S_T \frac{B(y) \sum_q e_q^2 \int \mathrm{d}^2 \boldsymbol{P}_{h\perp} \mathcal{I}\left[\frac{\boldsymbol{k_T} \cdot \hat{\boldsymbol{P}}_{h\perp}}{M_h} h_1^q(x, \boldsymbol{p_T^2}) H_1^{\perp q}(z, z^2 \boldsymbol{k_T^2})\right]}{2A(y) \sum_q e_q^2 f_1^q(x) D_1^q(z)}, \tag{2.62}$$

where all functions were introduced in Sec. 2.2–2.3. Recently, preliminary results appeared of measurements of the Collins moment with higher statistical precision, obtained from the longer data taking period 2002–2004 [109]. These results are shown in Fig. 2.12 [7]. Here, the Collins moments are divided by the kinematic factor $B(y)/2A(y)$, also referred to as the virtual-photon depolarization factor[8]. The advantage of taking this factor into account is that the presented observable $(2A/B)\langle \sin(\phi_h + \phi_S) \rangle_{UT}$, called the *virtual-photon* Collins moment, is independent of y, which simplifies comparisons to model predictions.

The measured azimuthal moments are positive for positive pions and negative for negative pions. The averaged values are $\langle \sin(\phi_h + \phi_S) \rangle^{\pi^+} = 0.0373 \pm 0.0075 \pm 0.0018$ and $\langle \sin(\phi_h + \phi_S) \rangle^{\pi^-} = -0.0423 \pm 0.0089 \pm 0.0024$. This sign difference is consistent with $h_1^u > 0$ and $h_1^d < 0$, which is also in agreement with model predictions [39] and resembles the helicity densities. However, the fact that the moments were found to be of about the same size for positive and negative pions was quite unexpected. The azimuthal moments relate to the following combinations of distribution and

[7] See Ref. [110] for the Collins moments including the HERMES data from 2005 (without curves from model predictions or fits to the data).

[8] For the calculation of this kinematic factor, higher order α_s corrections were taken into account (see Ref. [74]).

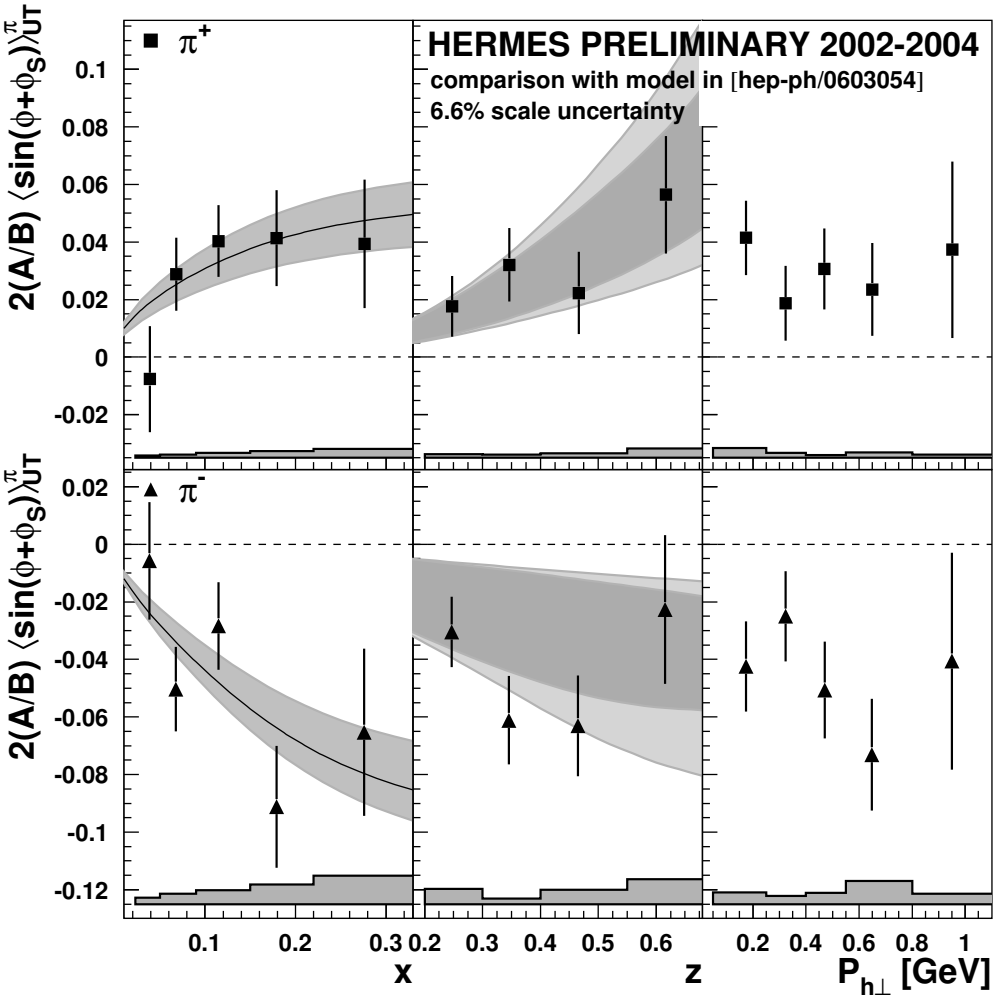

Figure 2.12: *Collins moments for semi-inclusively produced charged pions as a function of x, z and $P_{h\perp}$ as measured by HERMES [109]. The error bars represent the statistical uncertainty. The systematic uncertainty is indicated separately as a dark grey histogram in the lower part of each panel. In Ref. [111], the Collins fragmentation function was extracted from a fit to the x dependence of the data. The curve and the dark grey error band in the left panel indicate the result from the fit and the corresponding uncertainty, respectively. The middle panel shows predictions from Ref. [111] based on an extraction of the Collins function from a fit to the BELLE data [81] The dark grey error band in the middle panel represents the uncertainty of the fit and the light grey error band indicates the uncertainty related to the unknown transverse-momentum dependence of $h_1(x, \boldsymbol{p}_T^2)$ and $H_1^\perp(z, z^2\boldsymbol{k}_T^2)$.*

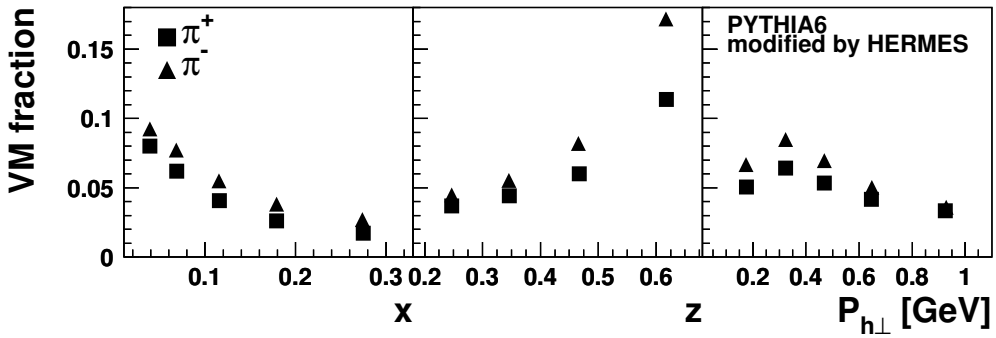

Figure 2.13: *The fraction of exclusively produced vector mesons contributing to the pion yield as determined using the Pythia Monte-Carlo simulation, tuned for the HERMES kinematics.*

fragmentation functions: (with fav=favored and dis=disfavored) [112]:

$$\langle \sin(\phi_h + \phi_S) \rangle^{\pi^+} : \quad 4h_1^u H_1^{\perp \mathrm{fav}} + h_1^d H_1^{\perp \mathrm{dis}}, \tag{2.63}$$

$$\langle \sin(\phi_h + \phi_S) \rangle^{\pi^-} : \quad 4h_1^u H_1^{\perp \mathrm{dis}} + h_1^d H_1^{\perp \mathrm{fav}}. \tag{2.64}$$

Taking into account that one expects from model predictions $|h_1^d| < |h_1^u|$, this would imply that the data require a large disfavored Collins functions, with $H_1^{\perp \mathrm{dis}} \approx -H_1^{\perp \mathrm{fav}}$. The opposite sign of the favored and disfavored Collins function can be understood within the context of the string model of fragmentation (see e.g. [113]). If a favored pion is formed from the first string break, the second string break will result in a disfavored pion. Due to momentum conservation, this second disfavored pion will have transverse momentum in the opposite direction compared to the favored pion. As a consequence the Collins fragmentation function gets the opposite sign [114] (see also [115]).

The data sample of semi-inclusive DIS events, used to obtain the results that are shown in Fig. 2.12 is slightly contaminated with pions that result from the decay of exclusively produced vector mesons. In Fig. 2.13, the fraction of exclusively produced vector mesons is shown as determined using the Pythia Monte-Carlo simulation [109]. Recent studies [116] indicate that the asymmetry produced by this contribution is small and does not bias the results presented in Fig 2.12. This implies that the exclusively produced vector mesons only give rise to a dilution of the measured asymmetries, which can be corrected for. The corrections were found to be very small in all kinematic bins except for the highest z bins. For the results shown here, the correction was not implemented.

Also shown in Fig. 2.12 are the results of a simultaneous analysis of the HERMES and BELLE data from Ref. [111]. For the x-dependence, the HERMES data are fitted using a chiral quark-soliton model (cQSM) parametrization for the transversity distribution function [117] and a Gaussian ansatz for the transverse momentum dependence of both the transversity distribution function and the Collins fragmentation function. The dark shaded area indicates the uncertainty associated with the fit. This fit is used to extract the Collins fragmentation function from the HERMES data.

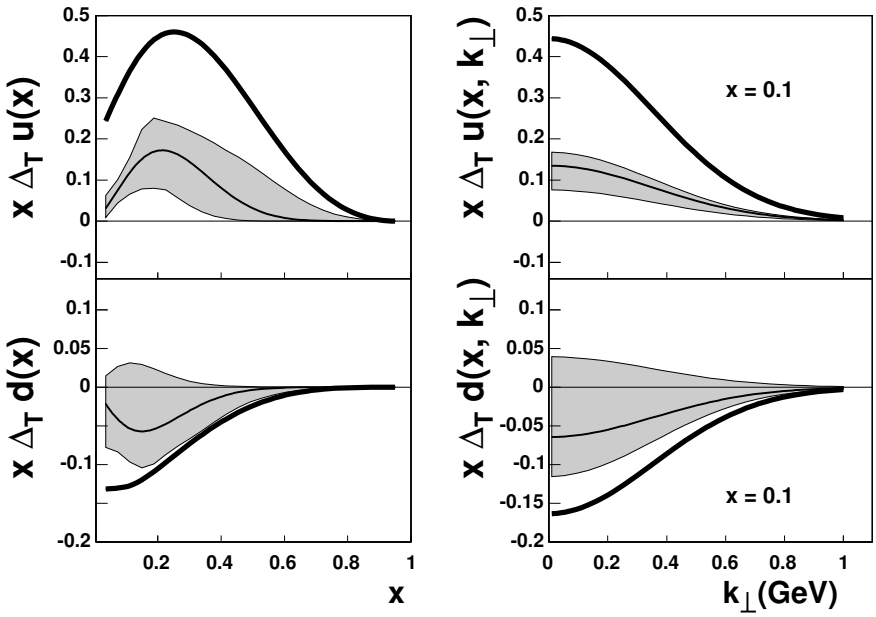

Figure 2.14: *The transversity distribution for u and d quarks from a global analysis presented in Ref. [82] of the HERMES [74], COMPASS [76] and BELLE data [81]. The thick curve represents the Soffer bound [49] for the value of the tranversity distribution function (here indicated as Δ_T instead of h_1). The x dependence shown on the left is a result from a fit to the data, the $k_\perp$ dependence on the right is chosen to be the same as that of the unpolarized distribution functions. The shaded area represents the uncertainty of the fit.*

Within the model assumptions, indeed opposite values are obtained for the favored and disfavored Collins fragmentation function integrated over z [111]:

$$\langle 2B_{\text{Gauss}} H_1^{\perp(1/2)\text{fav}} \rangle = (3.5 \pm 0.8)\%, \tag{2.65}$$

$$\langle 2B_{\text{Gauss}} H_1^{\perp(1/2)\text{dis}} \rangle = -(3.8 \pm 0.7)\%, \tag{2.66}$$

where B_{Gauss} is a factor depending on the Gaussian widths used in the Gaussian ansatz, and $H_1^{\perp(1/2)}$ is the (1/2)-moment of the Collins function (see Ref. [111] for details.).

In contrast, for the z dependence the curves are predictions for the azimuthal moment, based on an extraction of the Collins function from a fit to the BELLE data [81] and on the same cQSM for the transversity function. Here, the dark shaded area indicates the uncertainty related to the fit to the BELLE data and the light shaded area indicates the sensitivity of the SSA to the unknown ratio of the Gaussian widths of h_1 and $H_1^\perp$. These curves for the z dependence indicate that within the model assumption of Ref. [111], the transverse SSA's as measured by the HERMES collaboration, shown in Fig. 2.12, and the measurement of the Collins fragmentation function by the BELLE collaboration are consistent. This result supports the fact that the measurements by the HERMES and BELLE collaborations are both related to the same effect, that is, the Collins effect, which indicates that their combined measurements can be used to extract transversity. Although such an extraction was not performed in Ref. [111], it was concluded from the comparison of the HERMES and BELLE data, that the transversity distribution for d quarks, $h_1^d(x)$, is practically un-

constrained by the data, meaning that it can vary within the limits of the Soffer bound [49], but that the transversity distribution for u quarks, $h_1^u(x)$, is positive and within 30% of the Soffer bound.

Using the published HERMES results [74], combined with the transverse single-spin asymmetries measured by the COMPASS collaboration [76] and the results on the Collins function from the BELLE collaboration [81], in Ref. [82] for the first time a value has been extracted for the transversity distribution function of u and d quarks. This is shown in Fig. 2.14. Although it is mentioned in Ref. [82] that the extracted Collins fragmentation functions are consistent with the values found in Ref. [111], this is not the case for the transversity distribution function of d quarks. As shown in Fig. 2.14, the analysis performed in Ref. [82] contrains both the $h_1^d(x)$ and $h_1^u(x)$ quite well. The value that is found for $h_1^u(x)$ is considerably smaller than the Soffer bound, also indicated in the figure, which is inconsistent with the prediction of Ref. [111]. However, this could well be just an indication that the uncertainties in the analyses of Refs. [82, 111] are larger than the values quoted in these papers.

2.7 Transversity studies in two-hadron semi-inclusive DIS

The two-hadron semi-inclusive DIS process was first suggested as an alternative to the one-hadron semi-inclusive DIS process for measuring transversity in 1994 by Collins, Heppelmann and Ladinsky [83, 84]. Since that time, several publications appeared on this subject [97, 105, 107, 108, 118–120]. A detailed description of the formalism used to describe this process in terms of distribution and fragmentation functions (at leading twist), as well as an introduction to the subject can be found in Ref. [96].

2.7.1 The asymmetry

According to Eq. 2.53, the transverse single-spin asymmetry for two-hadron semi-inclusive DIS can be written as

$$A_{UT} = \frac{1}{S_T}\frac{\mathrm{d}^7\sigma_{UT}}{\mathrm{d}^7\sigma_{UU}}, \tag{2.67}$$

with the cross section difference $\mathrm{d}\sigma_{UT}$ and the spin-independent total cross section $\mathrm{d}\sigma_{UU}$ (cf. Eqs. 2.51 and 2.53) at leading twist derived from Eq. 2.45, 2.49 and 2.50 given by

$$\begin{aligned}\frac{\mathrm{d}^7\sigma_{UT}}{\mathrm{d}\cos\theta\,\mathrm{d}M_h^2\,\mathrm{d}\phi_R\,\mathrm{d}z\,\mathrm{d}x\,\mathrm{d}y\,\mathrm{d}\phi_S} &= -\frac{\alpha^2}{2\pi s x y^2}\sum_q e_q^2 B(y) S_T \frac{|\boldsymbol{R}|}{M_h}\sin(\phi_R+\phi_S)\,h_1(x)\\ &\times\left(H_1^{\sphericalangle,sp}(z,M_h^2)\sin\theta+\frac{1}{2}H_1^{\sphericalangle,pp}(z,M_h^2)\sin 2\theta\right),\end{aligned} \tag{2.68}$$

and

$$\frac{\mathrm{d}^7\sigma_{UU}}{\mathrm{d}\cos\theta\,\mathrm{d}M_h^2\,\mathrm{d}\phi_R\,\mathrm{d}z\,\mathrm{d}x\,\mathrm{d}y\,\mathrm{d}\phi_S} = \frac{\alpha^2}{2\pi s x y^2}\sum_q e_q^2 A(y) f_1(x) \times\left(D_1(z,M_h^2) + D_1^{sp}(z,M_h^2)\cos\theta + D_1^{pp}(z,M_h^2)\frac{1}{4}(3\cos^2\theta - 1)\right), \tag{2.69}$$

where the various symbols were introduced in Secs. 2.3.3–2.3.4 and where it was used that $|\boldsymbol{R_T}| = \sin\theta|\boldsymbol{R}|$. The superscripts on the distribution and fragmentation functions indicating the quark flavor are not indicated for conciseness.

From Eq. 2.68 it is clear that by measuring the amplitude $A_{UT}^{\sin(\phi_R+\phi_S)}$ one can access transversity. This amplitude, defined equivalently to Eq. 2.60, is given by:

$$A_{UT}^{\sin(\phi_R+\phi_S)} \equiv 2\langle\sin(\phi_R+\phi_S)\rangle \equiv \frac{1}{S_T}\frac{\int \mathrm{d}\phi_R\,\mathrm{d}\phi_S\,\sin(\phi_R+\phi_S)\,\mathrm{d}^7\sigma_{UT}}{\int \mathrm{d}\phi_R\,\mathrm{d}\phi_S\,\mathrm{d}^7\sigma_{UU}}, \tag{2.70}$$

$$= \frac{1}{S_T}\frac{1}{\sin(\phi_R+\phi_S)}\frac{\mathrm{d}^7\sigma_{UT}}{\mathrm{d}^7\sigma_{UU}}. \tag{2.71}$$

From Eqs. 2.68–2.71 it can be seen that this amplitude can get contributions from both fragmentation functions $H_1^{\sphericalangle,sp}$ and $H_1^{\sphericalangle,pp}$. In order to select the contributions from $H_1^{\sphericalangle,sp}$ and $H_1^{\sphericalangle,pp}$ separately, one can use the orthogonality of Legendre polynomials to define the following two amplitudes:

$$A_{UT}^{\sin(\phi_R+\phi_S)\sin\theta} \equiv \frac{2}{S_T}\frac{\int \mathrm{d}\cos\theta\,\mathrm{d}\phi_R\,\mathrm{d}\phi_S\,\sin(\phi_R+\phi_S)(\,\mathrm{d}^7\sigma_{UT}/\sin\theta)}{\int \mathrm{d}\cos\theta\,\mathrm{d}\phi_R\,\mathrm{d}\phi_S\,\mathrm{d}^7\sigma_{UU}} = -\frac{B(y)}{A(y)}\frac{|\boldsymbol{R}|}{M_h}\frac{\sum_q e_q^2 h_1(x) H_1^{\sphericalangle,sp}(z,M_h^2)}{\sum_q e_q^2 f_1(x) D_1(z,M_h^2)}, \tag{2.72}$$

and

$$A_{UT}^{\sin(\phi_R+\phi_S)\sin 2\theta} \equiv \frac{3}{S_T}\frac{\int \mathrm{d}\cos\theta\,\mathrm{d}\phi_R\,\mathrm{d}\phi_S\,\sin(\phi_R+\phi_S)\cos\theta(\,\mathrm{d}^7\sigma_{UT}/\sin\theta)}{\int \mathrm{d}\cos\theta\,\mathrm{d}\phi_R\,\mathrm{d}\phi_S\,\mathrm{d}^7\sigma_{UU}} = -\frac{B(y)}{A(y)}\frac{|\boldsymbol{R}|}{M_h}\frac{\sum_q e_q^2 h_1(x) H_1^{\sphericalangle,pp}(z,M_h^2)}{\sum_q e_q^2 f_1(x) D_1(z,M_h^2)}, \tag{2.73}$$

where the factors 2 and 3 are implemented such that the amplitudes have values in between −1 and 1, in agreement with the Trento Conventions [121]. These amplitudes are directly proportional to $h_1(x)$ and thus shows the potential for transversity determinations through two-hadron semi-inclusive DIS measurements. Experimental data for the amplitude $A_{UT}^{\sin(\phi_R+\phi_S)\sin\theta}$ obtained with the HERMES experiment represent the main result of this thesis, and are described in detail in Chapter 4.

In Ref. [122], the contribution of $h_1 H_1^{\sphericalangle,sp}$ to the asymmetry A_{UT} is selected in a slightly different way. There, the numerator and denominator of the amplitude $A_{UT}^{\sin(\phi_R+\phi_S)}$ are integrated over $\cos\theta$,

which gives the same result up to a constant factor:

$$A_{UT}^{\sin(\phi_R+\phi_S)}(x,y,z,M_h^2) = \frac{1}{\sin(\phi_R+\phi_S)}\frac{1}{S_T}\frac{\mathrm{d}^6\sigma_{UT}}{\mathrm{d}^6\sigma_{UU}} \tag{2.74}$$

$$= \frac{\pi}{4}A_{UT}^{\sin(\phi_R+\phi_S)\sin\theta}(x,y,z,M_h^2). \tag{2.75}$$

2.7.2 One-hadron versus two-hadron fragmentation

The similarity between using one-hadron fragmentation and two-hadron fragmentation as a probe for transversity is that in both cases the transversity distribution function is coupled to a *naively* T-odd fragmentation function[9]. These fragmentation functions can exist due to the interference of different probability amplitudes with a nonvanising interaction phase [124]. Such interferences can occur for instance in final-state interactions. In case of one-hadron semi-inclusive DIS, final-state interactions between the hadron and the rest of the hadronic final state X could give rise to a nonzero SSA through the Collins fragmentation function [60]. Also, in two-hadron semi-inclusive DIS, final-state interactions could give rise to a nonzero SSA through a T-odd fragmentation function. However, the difference is that, in case of the interference fragmentation function, the relevant final-state interaction can occur between the two hadrons themselves. Initially, this difference was seen as an advantage of the latter process, as Jaffe argued that for one-hadron semi-inclusive DIS the interaction phase might vanish when all unobserved states X are summed over [118]. However, the HERMES measurements of a nonzero Collins asymmetry [74] demonstrated that this is not the case[10].

In both processes, one looks for correlations between the transverse spin of the fragmenting quark and the momentum of the outgoing hadron(s). Specifically, the Collins fragmentation function describes the correlation between the transverse momentum $\boldsymbol{k_T}$ of the fragmenting quark, its spins $\boldsymbol{s}$ and the momentum $\boldsymbol{P_h}$ of the produced hadron, i.e.,

$$\boldsymbol{k_T} \times \boldsymbol{P_h} \cdot \boldsymbol{s}, \tag{2.76}$$

whereas the two-hadron interference fragmentation function describes the correlation between the orientation $\boldsymbol{P_1} \times \boldsymbol{P_2}$ of the two-hadron plane and the transverse spin $\boldsymbol{s}$ of the fragmenting quark [123], i.e.,

$$\boldsymbol{P_1} \times \boldsymbol{P_2} \cdot \boldsymbol{s}. \tag{2.77}$$

There are several reasons why the two-hadron semi-inclusive DIS process is seen as a good alternative to the one-hadron process. Firstly, if one compares equations 2.31 and 2.45 one can see that transversity appears in a direct product with the dihadron fragmentation function $H_1^{\sphericalangle}$ in

[9] See for instance Ref. [123] for a discussion of naive T-odd distribution and fragmentation functions.

[10] It should be noted, though, that not only final-state interactions can give rise to nonzero T-odd fragmentation functions. In Ref [125], for instance, a discussion of four different model calculations of the Collins fragmentation function is presented.

Eq. 2.45, while it appears coupled to the Collins fragmentation function $H_1^\perp$ within a convolution integral over transverse momentum in Eq. 2.31. This convolution integral complicates the extraction of transversity from the measured azimuthal moments in one-hadron semi-inclusive DIS. This can be dealt with by using a model for the transverse momentum dependence of the transversity distribution function and the Collins fragmentation function, such that the convolution integral can be evaluated, typically assuming Gaussian dependencies [96]. A different solution is to deconvolute the convolution integral by weighting the azimuthal moments with an appropriate $|\boldsymbol{P}_{h\perp}|$ dependent factor [96, 116]. The latter solution is complicated in practice for an experiment not having a full acceptance in $|\boldsymbol{P}_{h\perp}|$ (cf. Sec. 4.5). Secondly, the dependence on $|\boldsymbol{P}_{h\perp}|$ in the one-hadron case also makes it more difficult to handle color gauge invariance correctly and to calculate the evolution equations (see f.i. [108]).

Another important reason to study two-hadron fragmentation as well as one-hadron fragmentation is that most likely a detailed understanding of transversity can only be obtained from a combined analysis of several different processes involving this distribution function $h_1(x)$ (see Sec. 1.5).

Apart from the interpretational advantages of determining the transversity distribution function using two-hadron semi-inclusive DIS, there is also an obvious experimental disadvantage. This is that the cross section for two-hadron semi-inclusive DIS (for which usually two oppositely charged pions are taken) is smaller than for one-hadron semi-inclusive DIS, resulting in larger statistical uncertainties. Moreover, the two-hadron semi-inclusive cross section is more complicated as it depends on 9 kinematic variables instead of 6. Luckily, the fact that one can integrate the cross section over $\boldsymbol{P}_{h\perp}$ (and still remain sensitive to transversity) reduces this dependency from 9 to 7 variables.

2.7.3 Model predictions

Most model predictions for transverse single-spin asymmetries in semi-inclusive production of two pions consider the interference between a pion pair produced in a relative s-wave and a pion-pair produced in a relative p-wave, which is described by the interference fragmentation function $H_1^{\sphericalangle,sp}$.

A first model calculation of this fragmentation process was made in 1994 by Collins and Ladinsky [84] within the context of the Linear Sigma model (modified in order to use pions and quarks instead of pions and nucleons). In this model the interfering channels are a narrow s-wave σ resonance and a p-wave background as shown in Fig. 2.15. This is a qualitative model, showing for the first time that, within the model assumptions, a nonzero asymmetry A_{UT} (see Eq. 2.67) can exist, relating the transverse polarization of quarks in a transversely polarized nucleon to the relative distribution of the two pions.

In 1998, Jaffe, Jin and Tang [118, 119] made a different model describing the interference fragmentation using a more realistic choice for the interfering channels. Here the interference occurs between the ρ^0 (resonant p-wave, $m = 0.78$ GeV) and a nonresonant s-wave background.

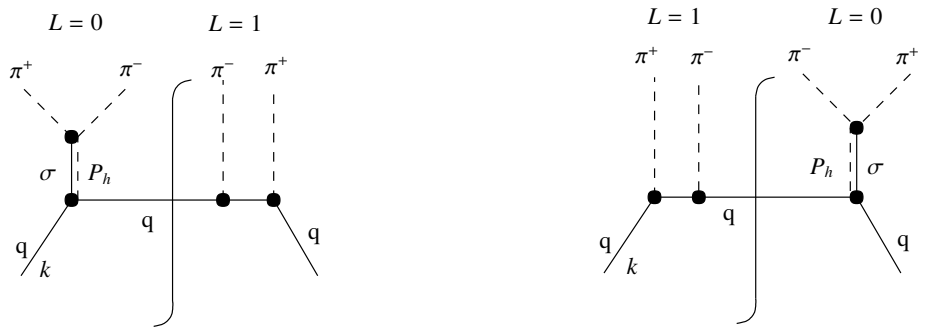

Figure 2.15: *The diagrams evaluated in the model of Ref. [84]. In this model the interference occurs between a σ resonance (s-wave) and a p-wave background.*

Writing the final state $|h_1h_2\rangle$ as a superposition of the s-wave $|h\rangle$ and the p-wave $|h'\rangle$, with relative phases δ_0 and δ_1, respectively, i.e.,

$$|h_1h_2, X\rangle = e^{i\delta_0}|h, X\rangle + e^{i\delta_1}|h', X\rangle, \tag{2.78}$$

they showed that the fragmentation function $H_1^{\sphericalangle,sp}$ can be written as

$$H_1^{\sphericalangle,sp}(z, M_h^2) = \sin\delta_0 \sin\delta_1 \sin(\delta_0 - \delta_1) H_1^{\sphericalangle,sp'}(z, M_h^2), \tag{2.79}$$

where the phases δ_0 and δ_1 depend on the invariant mass M_h. These phases (or phase shifts) were measured [126] in a pion-nucleon scattering experiment ($\pi N \rightarrow \pi\pi N$). The phase factor $\sin\delta_0 \sin\delta_1 \sin(\delta_0 - \delta_1)$ as obtained from this experiment is shown in Fig. 2.16(a). Although this model does not predict the size (or sign) of the asymmetry, according to this model the asymmetry will exhibit a strong invariant-mass dependence in the vicinity of the ρ^0 resonance, changing it's sign approximately at the ρ^0 mass.

In 2002, a model prediction by Radici, Jakob and Bianconi [107] was published. This model also considered the interference between the ρ^0 resonance and an s-wave background. Here, the interference diagrams shown in Fig. 2.17 are calculated within the context of a spectator model[11]. The resulting amplitude $A_{UT}^{\sin(\phi_R+\phi_S)}$ as a function of the invariant mass of the two-pion system M_h is shown in Fig. 2.16(b). A striking difference between the two model predictions shown in Fig. 2.16 is that whereas the model of Ref. [118] predicts a sign change of the asymmetry approximately at the ρ^0 mass, the model of Ref. [107] does not.

A new model calculation, close to the model of Ref. [107], was performed by Bacchetta and Radici [122] in 2006. They were able to fix many free parameters in their model for the unpolarized dihadron fragmentation functions using a Pythia Monte-Carlo simulation (tuned for HERMES kinematics, see Sec. 4.5.1) of the two-hadron semi-inclusive DIS process. The model predicts the amplitude $A_{UT}^{\sin(\phi_R+\phi_S)}$ in a much broader invariant-mass range compared to the model of Ref. [107],

[11] Earlier they already calculated interference fragmentation for proton-pion pair production [120], also within the context of a spectator model.

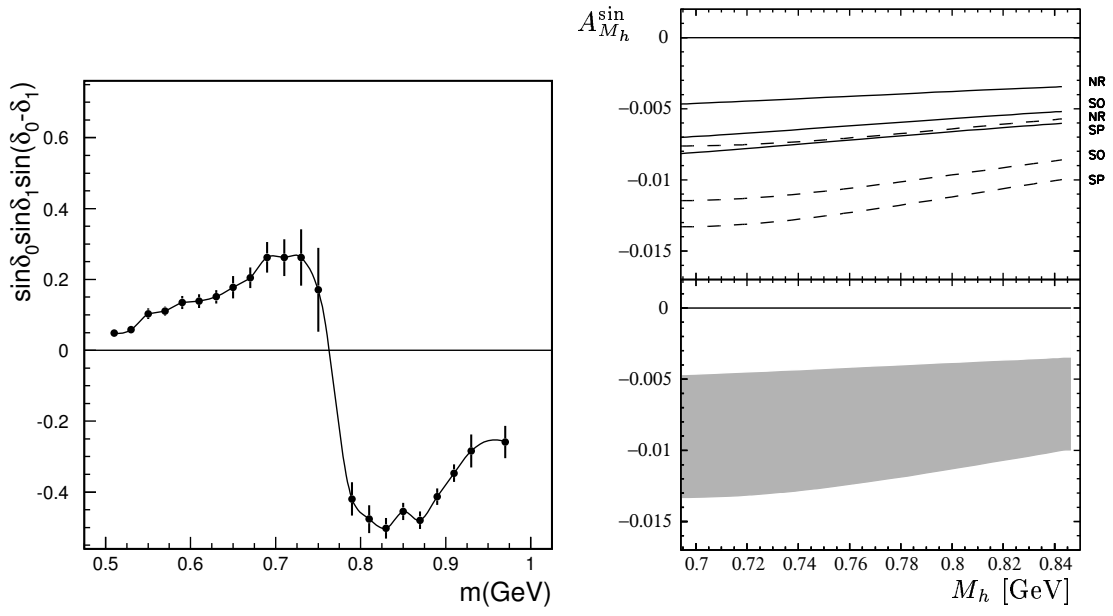

(a) (b)

Figure 2.16: *In Fig. 2.16(a) the phase factor* $\sin\delta_0 \sin\delta_1 \sin(\delta_0 - \delta_1)$ *as obtained from Ref. [126] is shown. This phase factor relates directly to the invariant-mass dependence of the amplitude* $A_{UT}^{\sin(\phi_R+\phi_S)}$ *according to the model of Ref. [118]. Fig. 2.16(b) shows the amplitude* $A_{UT}^{\sin(\phi_R+\phi_S)}$ *itself as a function of the invariant mass* M_h *in the region of the* ρ^0 *mass (*$M = 0.78$ *GeV) according to the model of Ref. [107]. The different curves correspond to different assumptions for the distribution functions* $f_1(x)$*,* $g_1(x)$ *and* $h_1(x)$ *and the fragmentation functions* $D_1(z, M_h^2)$ *and* $H_1^{\sphericalangle}(z, M_h^2)$*. The bottom panel shows the full spread of the model due to variations in the input functions. This amplitude needs to be multiplied by* -1 *in order to be consistent with the Trento Conventions [121].*

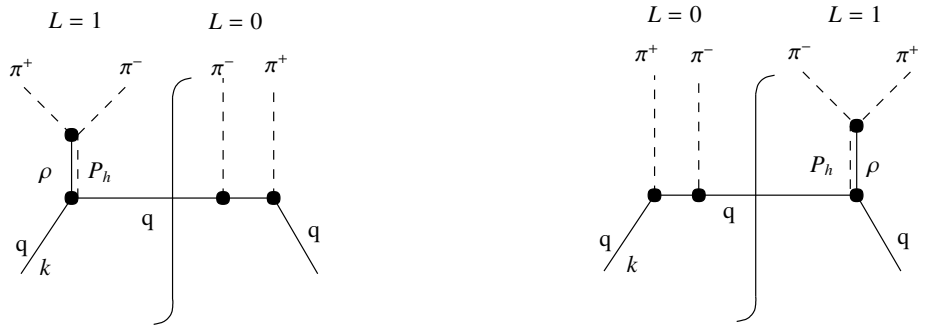

Figure 2.17: *The diagrams calculated in the model of Ref. [107]. In this model the interference occurs between the* ρ^0 *resonance (p-wave) and an s-wave background.*

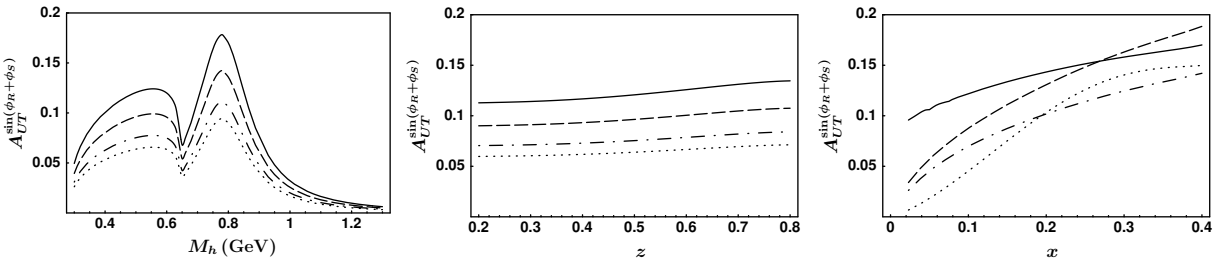

Figure 2.18: *The amplitude $A_{UT}^{\sin(\phi_R+\phi_S)}$ as calculated in Ref. [122] versus $M_{\pi\pi}$, x and z. calculated for HERMES kinematics. The different lines correspond to different models of the transversity distribution function: dotted lines from Ref. [127], dash-dotted line from Ref. [128], dashed line from Ref [117], and solid line from Ref. [129].*

as shown in Fig. 2.18. The figure shows the invariant-mass dependence as well as the x and z dependence of the amplitude $A_{UT}^{\sin(\phi_R+\phi_S)}$. In this model, the fragmentation function is almost proportional to the imaginary part of the ρ^0 and ω ($M_{\pi\pi} \approx 0.5$ GeV) resonances, which explains the strong dependence on the invariant mass. This model does not predict the sign of the amplitude and uses the sign of the HERMES data as presented in Chapter 4 as input. Note that the ω resonance does not show up in this figure around its invariant mass of $M = 0.783$ GeV, because only two of the three pions of the dominant decay channel $\omega \to \pi^+\pi^-\pi^0$ (branching ratio 89%) are considered.

2.8 Summary

In this chapter the theoretical framework describing the processes of one-hadron and two-hadron semi-inclusive DIS in terms of distribution functions and fragmentation functions has been discussed in considerable detail. The advantages and disadvantages of the two approaches to transversity have been compared. Several model predictions have been presented for $A_{UT}^{\sin(\phi_R+\phi_S)\sin\theta}$, the amplitude of the transverse single-spin asymmetry A_{UT}, which demonstrates that substantial nonzero effects can be expected and that large differences exist between the models.

In the following chapter the experimental setup to measure this process is discussed: the accelerator HERA, the HERMES spectrometer, the transversely-polarized gas target and how these three main parts combine. The extraction of the amplitude $A_{UT}^{\sin(\phi_R+\phi_S)\sin\theta}$ from the HERMES measurements is discussed in Chapter 4. In that chapter it will become clear that it is essential to understand the full kinematic dependence of the transverse single-spin asymmetry, as was presented in this chapter, in order to extract the amplitude. In Chapter 5, the data are compared to the model predictions discussed in the previous section.

3

The HERMES experiment

The HERMES experiment is one of the four experiments at the HERA accelerator in Hamburg at the German national research center DESY. The other experiments at HERA are the *ep* collider experiments ZEUS and H1 and the fixed target *pp* experiment HERA-B, as indicated in Fig. 3.1. HERMES is a fixed target experiment as well, which uses the 27.5 GeV positron beam[1] of HERA. It can be operated with polarized gas targets as well as with high-density unpolarized gas targets. The initially unpolarized positron beam becomes transversely polarized with respect to the magnetic bending field due to a small asymmetric spin-flip amplitude in the synchrotron radiation process, the Sokolov-Ternov effect [130]. In practice, many depolarization effects are present and in order to obtain a polarized beam, appropriate beam tuning is required [131]. Upstream from the HERMES experiment the beam polarization direction is changed from transverse to longitudinal and back again downstream from the experiment, which is accomplished by two spin rotators. In the period 2002-2005, after the luminosity upgrade of HERA in 2001, longitudinal polarization values up to 55% were obtained.

The HERa MEasurement of Spin (HERMES) experiment was proposed in 1990 [132] to study the spin structure of nucleons in response to the recently discovered proton *spin puzzle*, i.e., the totally unexpected discovery by the EMC experiment in the 1980s [8, 9] that the spin of the valence quarks in the proton accounts for only a small fraction of the total proton spin. The HERMES

[1] For practical purposes, throughout this thesis we will always refer to the *positrons* of the HERA beam. During some data taking periods electrons were used instead. Statements related to the beam hold independently of whether positrons or electrons were involved, unless stated otherwise.

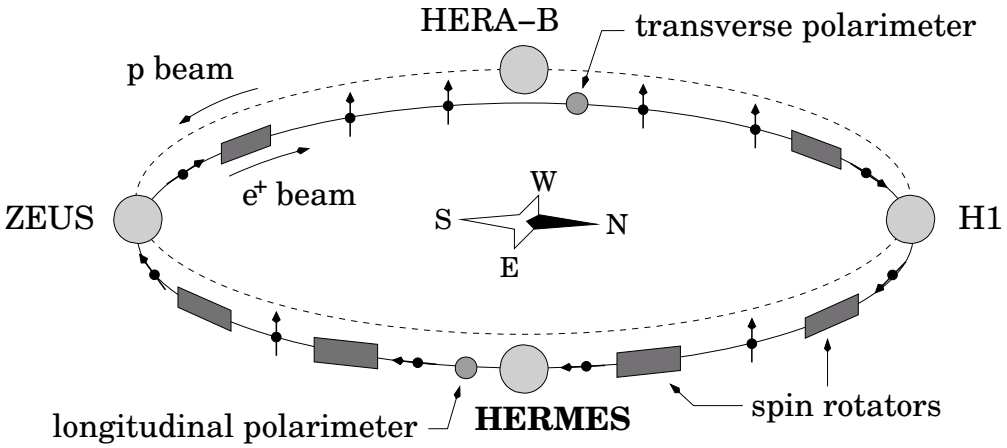

Figure 3.1: *The HERA storage ring with the four experiments in the setup since the end of 2001: the collider experiments ZEUS and H1 and the fixed-target experiments HERMES and HERA-B. The small arrows indicate the polarization direction of the positron beam.*

experiment was designed to measure spin asymmetries. It has made important contributions to the knowledge of the structure function g_1 [18, 133, 134] and was the first to measure the tensor structure function b_1 [135] of the deuteron, both through the measurement of *inclusive* spin asymmetries. However, the strength of the HERMES experiment is that it is able to identify hadrons in coincidence with the scattered lepton, that is, it can be used to study *semi-inclusive* deep-inelastic scattering. Therefore, with the HERMES experiment not only the nucleon structure functions can be measured, but also the distribution functions of quarks of a specific flavor and gluons inside the nucleons. This is possible as an identified hadron in semi-inclusive experiments serves as a flavor tag of the deep-inelastic scattering event. The HERMES collaboration was thus able to obtain precise information on the polarization and helicity distribution of u, $\bar{u}$, d, $\bar{d}$ and s quarks in the nucleon [38]. Many other interesting results have been obtained at HERMES on the spin structure of nucleons through semi-inclusive DIS. Examples include the measurement of a double-spin asymmetry related to the gluon helicity distribution [30, 136–138] and the measurement of single-spin asymmetries related to transversity, discussed in this thesis. Detailed overviews on the spin-physics results obtained by HERMES so-far are given in Refs. [139–142]. Besides its spin physics program, HERMES has a broad physics program using unpolarized gas targets. Examples are the investigation of hadron formation [143] and the search for exotic baryons like the pentaquark [144].

In this chapter, the setup of the HERMES experiment is briefly discussed, with a focus on those components that were used for the analysis of the two-hadron fragmentation processes presented in this thesis. The polarized gas target is discussed in Sec. 3.1, the spectrometer in Sec. 3.2, followed by two short sections on the trigger system and the data production chain, Secs. 3.3 and 3.4.

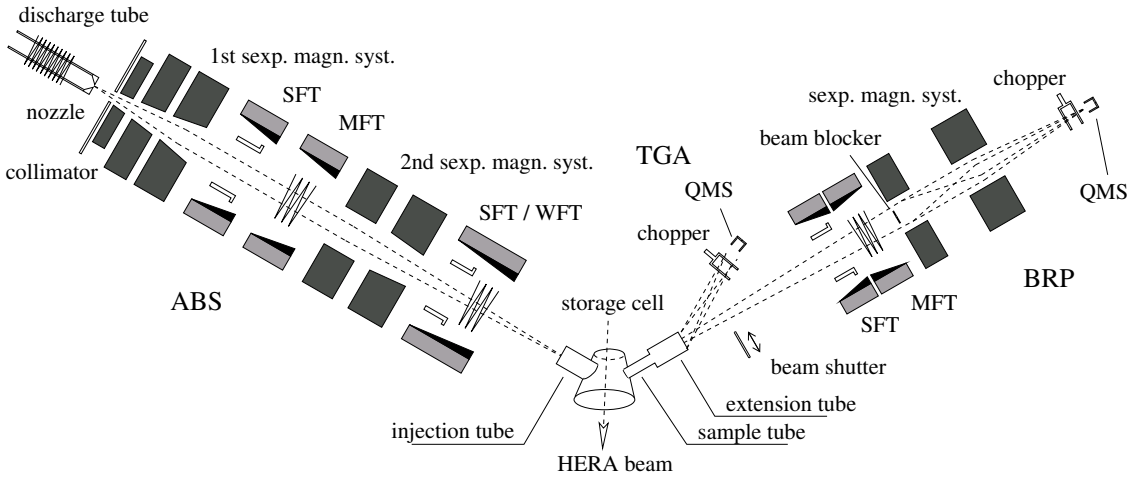

Figure 3.2: *Diagram of the polarized gas target with on the left the Atomic Beam Source (ABS) in the middle the target cell and on the right the Target Gas Analyzer (TGA) and the Breit-Rabi Polarimeter (BRP).*

3.1 The polarized gas target

The HERMES experiment has operated with polarized gas targets from 1995 until 2005. During the period from 1995 until 2000, helium, hydrogen and deuterium gas targets were polarized *longitudinally* with respect to the beam. In 2001, during a shutdown for a major luminosity upgrade of HERA [145], a new target magnet was installed in order to run with a *transversely* polarized hydrogen target. After this installation, the experiment operated with transverse polarization until 2005. At the end of 2005, the polarized target was removed to allow for the installation of a recoil detector [146, 147]. This ended a succesful decade of data taking with polarized targets for the HERMES experiment [148].

Below, a short overview is given of the various components that are used to polarize the target and to measure the degree of polarization. A more detailed description is given in Ref. [149] and the references therein.

In Fig. 3.2, a schematic picture is shown of the target area. In this picture, hydrogen or deuterium molecules flow in from the left, where they first enter the Atomic Beam Source (ABS). In the ABS [150], the molecules are dissociated into atoms using a radio-frequency discharge within a pyrex tube. A cooled nozzle at the end of the tube and a collimator are used to form an atomic beam. The atomic beam passes a set of sextupole magnets, where the atoms are forced into hyperfine states according to the Stern-Gerlach mechanism. The magnets are used to select those atoms that are in hyperfine states with electron spin +1/2, whereas atoms with electron spin -1/2 are bent away from the atomic beam axis. The electron polarization of the atomic beam is changed into a nuclear polarization by interchanging hyperfine states using high-frequency transitions. This is done by a combination of weak field transitions (WFT), medium field transitions (MFT) and high field transitions (HFT). Using these high-frequency transitions, the nuclear polarization is reversed at 60–180 s time intervals. A second set of sextupole magnets is used to form a focussed atomic

beam with high nuclear polarization levels.

The nuclear-polarized atomic beam enters the storage cell through an injection tube on the side, as indicated in Fig. 3.2. The storage cell [151] is a 40 cm long tube with open ends on both sides, mounted inside the beam pipe. It is typically cooled to a temperature of 100 K in order to minimize recombination and depolarization effects of the injected atoms and to increase the target density.

The target cell is surrounded by either the longitudinal or the transverse target magnet. These magnets provide a homogeneous magnetic holding field for the nuclear polarization within the target cell. The magnetic field defines the polarization direction and prevents depolarization. An important difference between the longitudinal and transverse target magnets is that the orientation of the magnetic field of the latter causes the positron beam to be bent out of its orbit. In order to keep the beam in a stable orbit, two dipole magnets, installed in front and behind the target magnet, redirect the beam.

A sample of the target gas diffuses out of the target cell through the sample tube into the target gas analyzer (TGA) or the Breit-Rabi polarimeter (BRP). The TGA and BRP analyze the target gas in order to determine the target polarization P_T. The TGA [152] measures the relative fraction of atoms and molecules in the target gas using a quadrupole mass spectrometer (QMS). A chopper in between the sample tube and the QMS rotates at a frequency of 5.5 Hz periodically blocking the flow of gas from the target cell into the QMS. It allows a background subtraction of the molecular and atomic content of the residual gas in the TGA.

The BRP [151] determines the relative population of the hyperfine states of the atoms in the target gas. In combination with the value of the field strength of the target magnet, this information is used to calculate the degree of nuclear polarization. The setup of the BRP is comparable to that of the ABS, i.e., employing radio-frequency transitions and a set of sextupole magnets. The atoms in hyperfine states with electron polarization +1/2 are focussed towards the BRP beam axis and are detected by a quadrupole mass spectrometer (QMS), whereas atoms with electron polarization -1/2 are deflected away from the beam axis.

Finally, the target polarization P_T as seen by the electron beam can be calculated [149] by combining the measurement of the nuclear polarization in the atoms by the BRP and the measument of the relative fraction of atoms and molecules by the TGA

$$P_T = \alpha_0\alpha_r P_a + \alpha_0(1-\alpha_r)\beta P_a, \tag{3.1}$$

where α_0 represents the initial fraction of atomic nucleons (instead of molecular) produced in the ABS, α_r denotes the fraction of nucleons in atoms that did not recombine in the cell, and $\beta = P_m/P_a$ represents the ratio of the nuclear polarization of the molecules P_m produced by recombination relative to the nuclear polarization of the atoms P_a.

With the setup described here, the HERMES experiment reached an average luminosity-weighted transverse target polarization of 0.75 ± 0.05 (syst.) in the period 2002–2004 using target densities of the order of 10^{14} nucleons/cm^2 (see Ref. [149] for a specification of the various contributions to the systematic uncertainty).

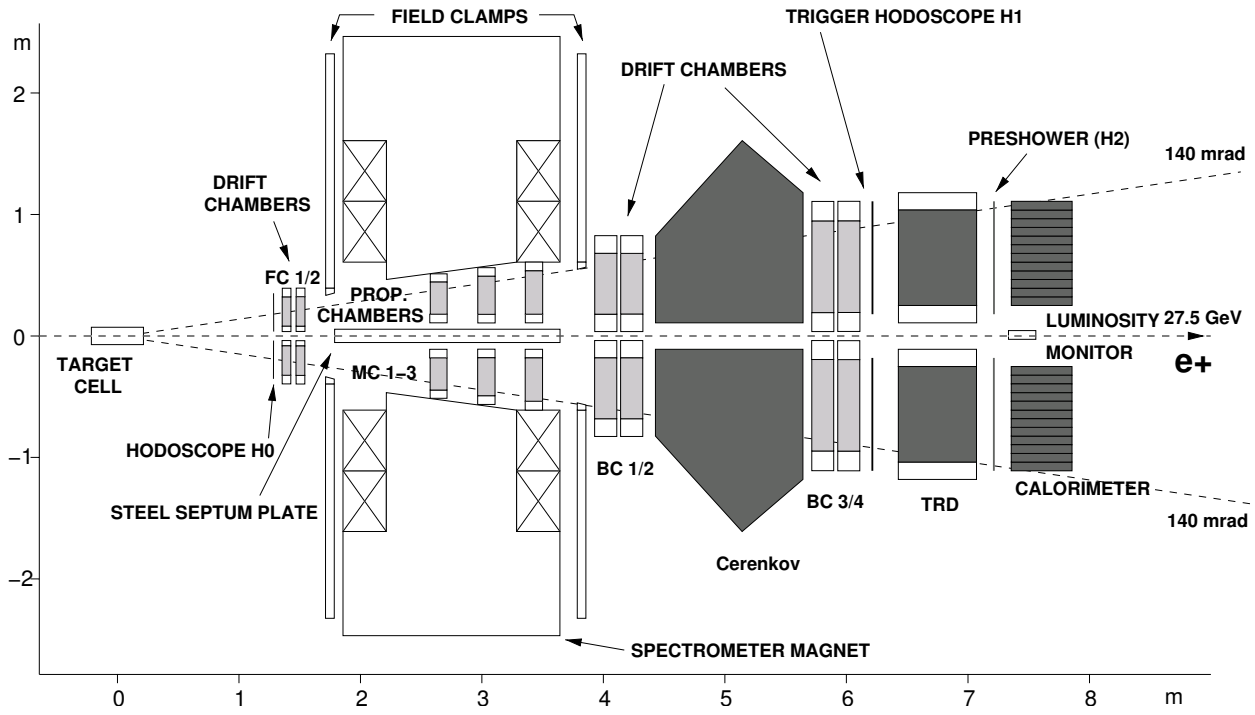

Figure 3.3: *Side view of the HERMES spectrometer. The axes indicate the position of the various components with respect to the target. Tracking detectors and particle identification detectors are indicated in light and dark grey, respectively.*

3.2 The spectrometer

The HERMES experiment uses a forward-angle spectrometer [153], shown schematically in Figure 3.3. It is symmetric around the horizontal plane, with a gap in between the two detector halves, which allows for both HERA beams to pass through. A septum plate shields the beams from the magnetic field of the spectrometer magnet. The spectrometer consists mainly of two types of detectors, i.e., tracking detectors and particle identification (PID) detectors, which are indicated in the figure in light and dark grey, respectively.

The tracking detectors can be divided into three groups: the Front Chambers (FC 1–2), the Magnet Chambers (MC 1–3) and the Back Chambers (BC 1–4). The Front Chambers [154] are located right before the spectrometer magnet and are used to reconstruct the trajectory of detected particles right after the scattering process took place (front tracks). Behind the front chambers, charged particles are deflected by the spectrometer magnet, after which their trajectory is reconstructed by the Back Chambers [155] (back tracks). This deflection, reconstructed from the combination of the front and back tracks, is used to calculate the particle's momentum. The Magnet Chambers [156] in the spectrometer magnet gap are used to reconstruct the tracks of low momentum (charged) particles that are strongly deflected by the spectrometer magnet and therefore do not pass through the Back Chambers. These low momentum particles are not identified, because all particle identification detectors are located behind the spectrometer magnet. Therefore, these

particles are not included in the present analysis. The Drift Vertex Chamber (DVC) is a tracking detector that for the present work is only used to calculate a small correction to the particle trajectories due to the influence of the transverse target magnet, as is discussed in Sec. 4.6.2.

The Ring Imaging Cherenkov (RICH) detector, the Transition Radiation Detector (TRD), the Pre-shower detector (H2) and the Calorimeter are the particle identification detectors. The combination of these four detectors is used to distinguish between leptons and hadrons. The RICH detector is furthermore used to identify hadrons as pions, kaons or (anti)protons.

Apart from the tracking detectors and the PID detectors, Fig 3.3 also shows the HERMES luminosity detector [157]. It is used to determine the luminosity of the experiment during a given data taking period, an essential parameter in order to measure absolute cross sections, and used as well to weight several data sets obtained during different data taking periods. The luminosity determination is based on elastic scattering of beam positrons off electrons in the target gas (Bhabha scattering) and the subsequent annihilation of these pairs into photons, for which the cross sections are well known (equivalently, Möller scattering is used when HERA runs with electrons instead of positrons). The detector uses two small crystal calorimeters for photon detection.

The geometrical acceptance of the spectrometer is 40 mrad $\leq |\theta_y| \leq$ 140 mrad in the vertical direction and $|\theta_x| \leq$ 170 mrad horizontally. In practice, the charge and momentum dependence of the acceptance caused by the bending due to the spectrometer magnet, also needs to be accounted for, as is discussed in Sec. 4.3.

In the following subsections the tracking detectors and PID detectors are described in some detail.

3.2.1 Tracking

The tracking chambers used in the experiment are either proportional chambers (MC 1–3) or drift chambers (DVC, FC 1–2 and BC 1–4).

The proportional chambers [156] are multi-wire chambers that consist of a set of thin, equally spaced anode wires placed in the middle of two cathode planes. The space between the cathode planes is filled with gas. A particle, traversing the chamber, ionizes the gas and an applied electric field will make the freed electrons drift towards an anode wire. This causes an avalanche of electrons near the wire, resulting in a current signal, which reveals the position of the particle. In practice, several sets of wires, tilted with respect to each other, are combined to obtain a good spatial resolution.

The drift chambers [154, 155] are also multi-wire chambers. With these chambers, spatial resolution is obtained by measuring the time electrons need to reach the anode wire, measured from the moment the ionizing particle traversed the detector. This typically results in a higher resolution than can be obtained with multi-wire proportional chambers. The reason that proportional chambers were used for MC 1–3 instead of drift chambers, is that proportional chambers can be operated more easily inside the strong magnetic field of the target magnet.

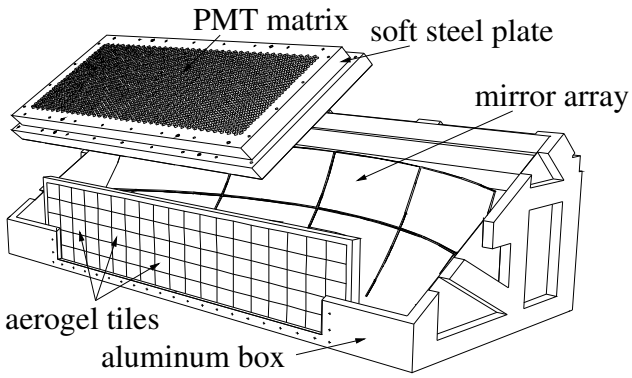

Figure 3.4: *Schematic picture of the RICH detector at HERMES. Charged particles traversing the RICH detector produce one or two Cherenkov cones when they pass through the radiators, i.e., the aerogel tiles and the C_4F_{10} gas behind it. The Cherenkov cones are projected onto a matrix of photomultiplier tubes (PMT's) by a spherical mirror.*

Using these tracking detectors, a momentum resolution $\Delta p/p \leq 2.6\%$, and an angular resolution $\Delta\theta \leq 1.8$ mrad [38] is obtained with the HERMES spectrometer (depending on particle type and momentum).

3.2.2 Particle identification

Particle identification detectors exploit various physics processes in order to distinghuish between particle types. In this section, these processes are briefly explained for each of the PID detectors used in the HERMES spectrometer.

The RICH detector. When a charged particle traverses a dielectric medium it radiates Cherenkov radiation if its velocity v is larger than the speed of light in this material (the *radiator*), that is, if $v > \frac{c}{n}$, with n the refractive index of the radiator. A RICH detector measures the opening angle of the cone of the emitted Cherenkov radiation, which determines the velocity of the radiating particle. The opening angle is given by $\cos\theta_c = c/(nv)$. Combined with a determination of the momentum of the particle, the velocity measurement yields the mass of the particle.

The RICH detector at HERMES [158] is of the dual-radiator type, meaning that a particle traverses *two* radiators: a wall of silica aerogel tiles and a volume of C_4F_{10}, a heavy fluorocarbon gas. As shown in Fig. 3.4, the Cherenkov cones are focussed by a spherical mirror onto a grid of photomultipliers, where they produce two concentric rings. The radius of a ring is proportional to the Cherenkov angle. In Fig. 3.5, the Cherenkov angle θ_c is shown versus the particle momentum for pions, kaons and (anti)protons for both radiators. Combined, the two radiators enable hadron identification in the momentum range 2–15 GeV for pions, kaons and (anti)protons. Pions can be identified in the momentum range 1–2 GeV as well [159, 160].

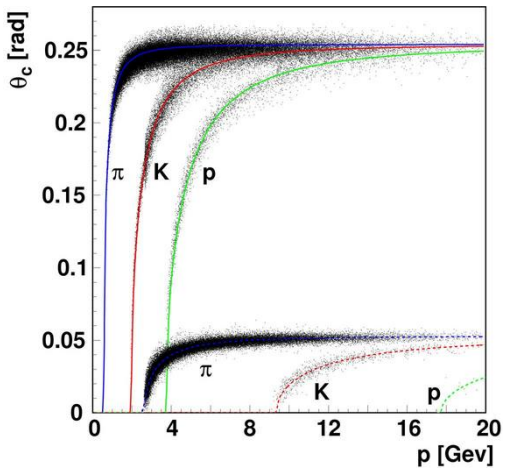

Figure 3.5: *The Cerenkov angle θ_c versus hadron momentum for the aerogel (upper band) and C_4F_{10} gas radiators (lower band). The data shown are based on a Monte-Carlo simulation.*

The transition radiation detector. Transition radiation detectors (TRD's) measure the electromagnetic radiation (X-rays) emitted by highly relativistic charged particles (Lorentz factor $\gamma > 1000$) that cross a boundary between two dielectric media (see for example [161]). The radiated energy is proportional to the Lorentz factor of the radiating particles. This offers the possibility of hadron-lepton separation, since leptons have a much higher Lorentz factor as compared to hadrons of the same energy. For example, positrons with an energy of 5 GeV have $\gamma \approx 10^4$, whereas pions of the same energy have $\gamma \approx 36$. This example also illustrates that in the energy domain accessed by the HERMES experiment, transition radiation is only produced by positrons and not by hadrons. The radiation is emitted at a very small angle $\theta \sim 1/\gamma$ such that it is not possible to separate the transition radiation from other processes by which the positron looses energy in the detector (mostly Bremsstrahlung). Because only a very small number of photons is radiated if a positron crosses a boundary, a TRD consists of several layers in order to make the transition radiation detectable.

The HERMES TRD [153] consists of 6 modules that each contain a radiator and proportional wire chamber, optimized to detect X-ray photons. One radiator is 6.35 cm thick and consists on average of 267 dielectric layers. As shown in Fig. 3.6, the TRD provides a clear lepton-hadron separation.

The pre-shower detector. Hadrons traversing matter loose energy mostly through inelastic collisions, causing excitations and ionizations of the atoms. On the contrary, due to their lower mass, high energy positrons ($E \gtrsim 10$ MeV) loose energy mostly through the radiation of Bremsstrahlung, resulting in electromagnetic showers [162]. Through this process, positrons loose energy much faster when traversing matter than hadrons and this difference is exploited by the pre-shower detector at HERMES [153] in order to separate detected particles into positrons and hadrons (see Fig. 3.6).

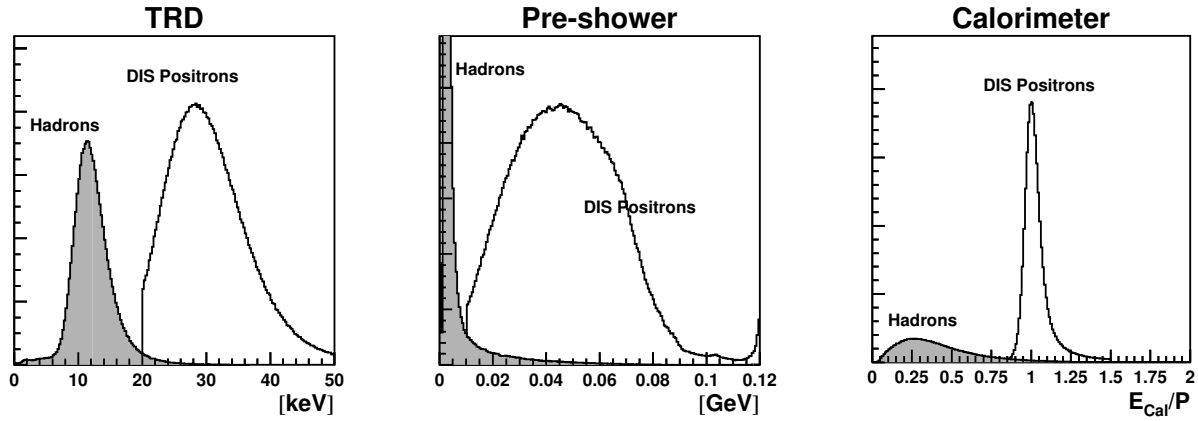

Figure 3.6: *Energy deposition by DIS positrons (cf. Sec. 4.2.3) and hadrons in three of the PID detectors, obtained by a Monte-Carlo simulation [164].*

The pre-shower detector consists of a hodoscope (H2) with, in front of it, an 11 mm thick lead plate (2 radiation lengths) sandwiched between two 1.3 mm steel plates. The hodoscope itself consists of 42 vertically mounted scintillator modules.

The calorimeter. The HERMES calorimeter [163] exploits the same basic physics principle as the pre-shower detector in order to separate hadrons and leptons. The calorimeter is composed of a wall of lead-glass blocks. Positrons loose almost all their energy in the 50 centimeters of lead-glas composite of the calorimeter (18 radiation lengths). Positrons and hadrons are separated using the E/p distribution, where E is the deposited energy in the calorimeter blocks and p is the momentum of the particles as derived from the track curvature in the spectrometer. In this distribution, positrons appear as a sharp peak around $E/p = 1$, while the hadron peak shows up at a much lower energy (see Fig. 3.6).

Fig. 3.6 shows the energy deposition of hadrons and positrons in the TRD, pre-shower detector and the Calorimeter according to a Monte-Carlo simulation of the detector responses [164]. How the PID detectors are used in the present analysis as well as the efficiency obtained for particle identification is discussed in Sec. 4.2.2.

3.3 The trigger system

The main purpose of the HERMES trigger system [153] is to distinguish relevant physics events from background signals and to initiate readout and digitization of detector signals for those events. Two main physics triggers have been set up at HERMES, one for the selection of inclusive deep-inelastic scattering events (the DIS trigger; see also Sec. 2.1) and one for the selection of photoproduction events (producing hadrons like the K, ρ, J/ψ and Λ^0), where typically the beam leptons are scattered at such small angles that they are outside of the spectrometer acceptance (see Fig. 3.3).

Recently, a trigger was set up especially for the detection of the pentaquark [144]. The DIS trigger, used in the present analysis, requires a coincidence of the hodoscopes H0, H1 and H2 as well as an energy deposit E in two adjacent columns of the calorimeter above a certain threshold ($E > 1.4$ GeV for the present analysis). Of all events that are recorded as the result of a DIS trigger, about 4–6% are identified as DIS events in the offline analysis [116].

3.4 Data production chain

The data production chain at HERMES starts with the data acquisition (DAQ) system, responsible for digitization and fast readout of the detector signals whenever a trigger occurs [153]. It is based on Fastbus, VME, and CAMAC electronics and produces raw data files of about 450 MB each stored in the EPIO format [165], containing per event one record with all detector readings. The dead time of the DAQ system during standard running is typically well below 10%, at total trigger rates of up to 300 Hz [38]. In the offline analysis [166] the data are processed by the HERMES decoder (HDC). It takes into account calibrations of the detectors and relates hardware channels to the physical position of the detector components in the experiment. The output of HDC is stored in ADAMO tables [167]. The data are further processed by the HERMES reconstruction (HRC) code, which reconstructs particle tracks from the signals registered by the tracking detectors.

In parallel with the fast readout by the DAQ system, a slow control system reads out hardware that monitors relatively slowly changing detector information, like pressures, temperatures, high voltages, etc. This readout is carried out every 10 seconds. These 10 second time periods are referred to as *bursts*. Finally, the output of HRC is combined with these slow control files into μDST (data summary tape) files. These files are the starting point for the data analysis, which is described in the following chapter.

4

Measurement of single-spin asymmetries

The dihadron transverse single-spin asymmetry and the associated azimuthal amplitude are extracted from deep-inelastic scattering measurements obtained at HERMES using an analysis chain, discussed in this chapter. The analysis chain can be divided into three main steps. The first step, discussed in Sec. 4.1, is to construct from the measurements a data set only containing high-quality events. This implies, selecting those events that were measured at times when the target, the beam and all detectors used in the analysis were working properly. At this stage, the data sample still contains events corresponding to several different scattering processes, of which the deep-inelastic scattering (DIS) events only make up a subset. Therefore, the next step is to select the DIS events and from those events the small subset of semi-inclusive DIS events containing two oppositely charged pions. This is the topic of Sec. 4.2. The remainder and main part of this chapter discusses how to construct the transverse single-spin asymmetry from those semi-inclusive DIS events (Sec. 4.3), and subsequently how to extract its azimuthal moment (Sec. 4.4). In particular, in Sec. 4.4.2 some corrections are introduced to the standard extraction method that are important when the azimuthal moment is extracted from a statistics-limited data sample, as is the case for the present data sample.

An important topic in the determination of the azimuthal amplitude is the investigation of systematic effects that can influence its value. The main contribution to the resulting systematic

uncertainty comes from so-called detector acceptance effects, which are discussed in detail in Sec. 4.5. The method used to extract the azimuthal amplitude from the HERMES measurements has been chosen such as to minimize these acceptance effects. Various other possible systematic effects have been investigated as well (Sec. 4.6) and most of them turn out to have a negligible influence on the extracted value of the azimuthal amplitude. The measured values of the main observables studied in this thesis are presented in Sec. 4.5 and the interpretation of these data is discussed in detail in Chapter 5. The present chapter is concluded with a brief summary.

4.1 Data quality

The analysis presented in this chapter is based on measurements that were performed during the years 2002–2004. These measurements are processed and stored on disc in μDST files (see Sec. 3.4) as was described in Sec. 3.4. These files are the starting point for all of the various physics analyses performed at HERMES. Depending on the type of analysis, information from some part of the experiment can be ignored. Because the μDST files also contain events measured at times when some detectors were not working properly, the first stage of the analysis is to select those events for which all parts of the entire experimental set-up that are used in the present analysis were operating according to a pre-defined set of criteria.

All information about the performance of the detectors, which is stored at the *burst* level, is combined by the data quality group at HERMES into burst lists. These lists contain bit patterns (of 32 bits) for each burst for both detector halves, where each bit corresponds to a detector (or some other part of the experiment) and is set (1) if this detector was operating properly. For the analysis presented here, all bits were required to be equal to one, except for bit number 1, which requires the beam polarization to be in between 20% and 80%. This requirement is left out, as the present analysis does not require a polarized beam. The most important data quality requirements imposed by using these burst lists are:

- good performance of the PID detectors, the tracking detectors and the luminosity monitor: a gain monitoring system (GMS) [168] continuously monitors the response of all individual scintillator blocks of hodoscope H2 and the calorimeter blocks of the Calorimeter and the Luminosity monitor. One dead block is allowed in the Calorimeter in the year 2002, which was shown not to influence SSA's of charged hadrons in semi-inclusive DIS [169]. Furthermore, it is verified that no high voltage trips occurred in any of the detectors.

- good target performance: it is verified that the hydrogen atoms injected by the ABS in the target cell are nuclear polarized (instead of electron polarized), and that the polarization state determined by the TGA/BRP is consistent with the state injected by the ABS (see also Ref. [170]).

- reasonable beam current (2 mA $\leq I_B \leq$ 50 mA).

- reasonable luminosity rate (1 Hz $\leq L \leq$ 50 Hz).
- recent measurement of the beam polarization: the most recent measurement of the beam polarization has to be less than 5 minutes ago for all events. Although the present analysis requires an unpolarized beam, the beam polarization needs to be measured in order to be able to construct a data set for which the average beam polarization is essentially zero (see Sec. 4.2.4).
- DAQ dead time smaller than 50%.

More detailed information about these data quality criteria can be found on the website of the HERMES data quality group [170].

4.2 Event selection

Following the data quality selection, performed at the burst level, many further requirements are imposed at the event level. The events that pass all requirements, constitute the data set that is used in the analysis. In this section, the various additional selection criteria are discussed, in the same order as they are applied in the analysis chain.

4.2.1 Geometric requirements

First, all tracks in each event are required to satisfy several geometric requirements:

- the origin of the reconstructed tracks has to lie within the boundaries of the target cell;
- the reconstructed tracks have to pass through the fiducial volume of the spectrometer and they should not pass through the field clamps or the septum plate.

These geometric selection criteria are quantified in Table 4.1. These cuts provide a few mm clearance from the boundaries of various apertures to guarantee a decent tracking resolution.

4.2.2 Particle identification

Lepton-hadron separation

The next step is to identify the particle type of each track. This is done using the PID detectors, which were introduced in Chapter 3.

First, the particle sample is separated into hadrons and leptons, using all four PID detectors, i.e., the calorimeter, the pre-shower detector, the TRD and the RICH detector. Each of these detectors separately is used to calculate the likelihood $\mathcal{L}^i(p,\theta,\xi)$ that a particle of type i with momentum p and polar angle θ causes a detector response ξ. For the RICH detector, ξ corresponds

	front partial track	back partial track
vertex position	$\|z\| < 18$ cm	
front field clamp ($z = 172$ cm)	$\|x\| \leq 31$ cm	
septum plate ($z = 181$ cm)	$\|y\| \leq 7$ cm	
rear field clamp ($z = 383$ cm)	$\|y\| \leq 54$ cm	$\|y\| \leq 54$ cm, $\|x\| \leq 100$ cm
calorimeter ($z = 738$ cm)		$\|x\| \leq 175$ cm, 30 cm $\leq \|y\| \leq 108$ cm

Table 4.1: *Geometric requirements for all tracks used in the analysis (see also Fig. 3.3 for the position of the various components of the spectrometer). The requirements on the values of x and y refer to the x and y position of tracks at the z positions indicated in the first column.*

to the Cerenkov angle θ_c and for the other three detectors it corresponds to the energy deposit E in these detectors. These likelihoods are intrinsic properties of the PID detectors. They are evaluated for one detector by analyzing its response for a clean sample of leptons or hadrons. These samples are constructed using the other three PID detectors, selecting kinematic regions where these detectors can identify leptons with a low hadron contamination and vice versa where they can identify hadrons with a low lepton contamination.

For each detector these likelihoods are used to calculate the probability $P^i(p, \theta, \xi)$ that a track, with momentum p, polar angle θ and detector response ξ corresponds to a particle type i:

$$P^i(p, \theta, \xi) = \frac{\phi^i(p, \theta)\mathcal{L}^i(p, \xi)}{\sum_j \phi^j(p, \theta)\mathcal{L}^j(p, \xi)}, \tag{4.1}$$

where ϕ^i is the particle flux for incident particles of type i. These probabilities are then used to calculated the PID′ value:

$$PID' \equiv \log_{10} \frac{P^l}{P^h} = \log_{10} \frac{\mathcal{L}^l}{\mathcal{L}^h} - \log_{10} \Phi \equiv PID - \log_{10} \Phi, \tag{4.2}$$

which is the logarithmic ratio of the probabilities that a track corresponds to a lepton (P^l) or to a hadron (P^h). The ratio $\Phi \equiv \phi^l/\phi^h$ of the incident lepton and hadron fluxes is called the *flux factor*. For the present analysis, the flux factor is not taken into account, as it represents a negligible correction to the PID value for semi-inclusive analyses [171]. Hence, in this case the log-likelihood ratios are equal to the log-probability ratios.

In order to obtain an optimal separation, the log-likelihood ratios of the PID detectors are combined:

$$PID_3 = \log_{10} \frac{\mathcal{L}^e_{\text{CAL}}\mathcal{L}^e_{\text{RICH}}\mathcal{L}^e_{\text{PRE}}}{\mathcal{L}^h_{\text{CAL}}\mathcal{L}^h_{\text{RICH}}\mathcal{L}^h_{\text{PRE}}}, \qquad PID_5 = \log_{10} \frac{\mathcal{L}^e_{\text{TRD}}}{\mathcal{L}^h_{\text{TRD}}}, \tag{4.3}$$

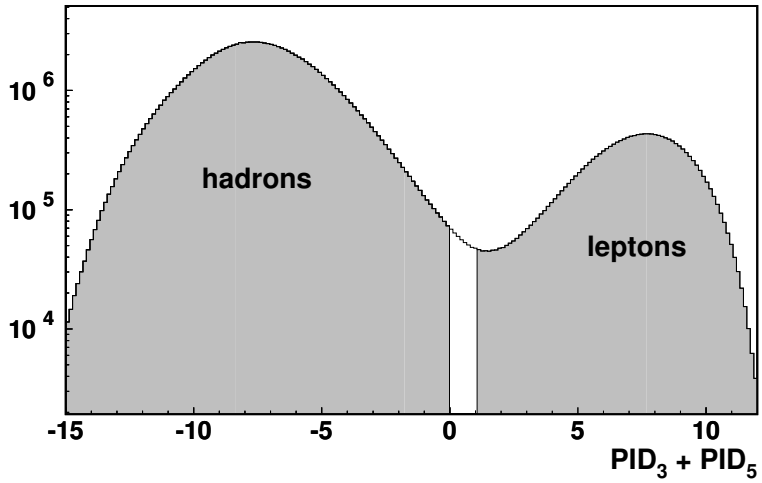

Figure 4.1: *Distribution of the values of the quantity $PID_3 + PID_5$, which combines the information of all four PID detectors, for all tracks associated with DIS trigger events. The tracks with PID values to the right of the gap are identified as leptons, those to the left as hadrons.*

where the names PID_3 and PID_5 are internal HERMES conventions. The following criteria were applied to separate the data into leptons and hadrons:

$$\text{leptons}: \quad PID_3 + PID_5 > 1, \tag{4.4}$$

$$\text{hadrons}: \quad PID_3 + PID_5 < 0. \tag{4.5}$$

This way, hadrons and leptons are identified with efficiencies larger than 98% and cross contaminations smaller than 1% [164, 171, 172]. In Fig. 4.1 the distribution is shown of PID_3+ PID_5 for all tracks resulting from DIS triggers for the entire data sample used in the analysis. More detailed information on the subject of particle identification at HERMES can be found for example in Ref. [171].

Hadron-type identification

The hadron identification is accomplished using the RICH detector (see Sec. 3.2.2). It can distinguish between pions, kaons and protons. Depending on the particle type and momentum, each of these particles produces one or two Cerenkov cones as it moves through the RICH detector. In order to determine the Cerenkov angles θ_c for all tracks in an event from the pattern of Cerenkov photons striking the matrix of PMT's, an algorithm called the indirect ray tracing (IRT) algorithm is used [173]. The algorithm gives for each track a logarithmic ratio of likelihoods called the RICH quality parameter (rQp):

$$rQp = \log_{10} \frac{\mathcal{L}^{h_1}}{\mathcal{L}^{h_2}}, \tag{4.6}$$

which is similar to the PID values discussed above for the lepton-hadron separation. The difference is that the RICH detector distinguishes between three different hadron types. Therefore, this ratio

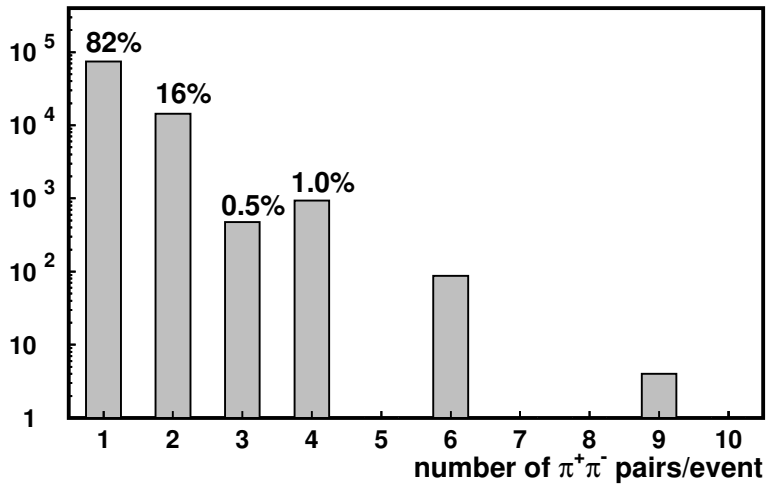

Figure 4.2: *Distribution of the number of $\pi^+\pi^-$ pairs per event for the final data set.*

is defined as the likelihood for having observed a particle of type h_1 with the largest likelihood to that of a particle of type h_2 with the second largest likelihood. Pions are selected, e.g., by requiring for any tracks for which $\mathcal{L}^\pi$ is the largest likelihood:

$$rQp > 0, \tag{4.7}$$

$$p > 1 \text{ GeV}. \tag{4.8}$$

The requirement on the pion momentum is needed in order to select the momentum range in which the RICH detector is able to identify pions (cf. Sec. 3.2.2). The efficiency of the RICH detector is a combination of detection efficiency (the probability that a particle produces a signal in the detector) and identification efficiency (the probability that a hadron of type h is correcly identified as type h). The *detection* efficiency is monitored in the online run-by-run data quality of the RICH detector for electrons/positrons and is typically 85–95%. The efficiency of hadron *identification* and the related contamination of the pion sample with kaons and (anti)protons is process type dependent. Averaged over the selected sample of $\pi^+\pi^-$ pairs, the identification efficiency of $\pi^+\pi^-$ pairs is 85% and the contamination by different hadron pair combinations is 6%. How these last two numbers are obtained and what the effect can be of the contamination on the extracted asymmetry is discussed in detail in Sec. 4.6.4.

4.2.3 Process selection

After all tracks in each event have been separated into lepton and hadron tracks and the hadron type has been identified, the next step in the analysis chain is the selection of those events that correspond to the relevant scattering process. Hence, the events must contain a beam lepton that scattered deep-inelastically off a target nucleon and at least one $\pi^+\pi^-$ pair.

Inclusive deep-inelastic scattering. Prior to making any selection based on the process type, the event sample contains events that were registered as a result of various different triggers, active during data taking. Therefore the first step towards selecting a clean sample of inclusive deep-inelastic scattering events, is to select those events that were registered as a result of a DIS trigger (cf. Sec. 3.3). Of these DIS trigger events, the sample of true DIS events, for which the scattered beam lepton is actually detected, is still a small subset since most of the DIS trigger events contain only hadrons and no leptons [116].

The deep-inelastic scattering events are selected by requiring that a DIS trigger event contains a lepton, which has to satisfy the following constraints:

$$Q^2 > 1\ \mathrm{GeV}^2\,, \qquad 0.1 < y < 0.85\,, \tag{4.9a}$$

$$W^2 > 4\ \mathrm{GeV}^2\,, \qquad x > 0.023. \tag{4.9b}$$

The cuts on W^2 and Q^2 are used to exclude the nucleon resonance region and to ensure that Bjorken scaling of the distribution functions holds. The upper limit on y removes events that may be affected by higher order QED radiation effects. As all these selections are correlated, the lower limits on y and x approximately correspond to the region accessible by the HERMES experiment after applying the other DIS cuts.

Semi-inclusive deep-inelastic scattering. In addition to the requirements described above, and in order to select the semi-inclusive process of interest, the DIS events have to contain at least one $\pi^+\pi^-$ pair that satisfies the following constraints:

$$\Delta E \equiv (M_X^2 - M_p^2)/2M_p > 2\ \mathrm{GeV}, \tag{4.10}$$

$$2m_\pi < M_{\pi\pi} < 2\ \mathrm{GeV}, \tag{4.11}$$

with M_X the missing mass, M_p the proton mass, m_π the pion mass and $M_{\pi\pi}$ the two-pion invariant mass. The cut on ΔE avoids contributions from exclusive two-pion production, for which factorization in distribution functions and fragmentation functions cannot be assumed. The two-pion invariant mass range corresponds to the range accessible to the HERMES experiment. All possible combinations of detected $\pi^+\pi^-$ pairs were included for each event. If more than one combination is possible, these pairs are treated as separate semi-inclusive events in the analysis. Fig. 4.2 shows a distribution of the number of $\pi^+\pi^-$ pairs per event for the final event sample used in the analysis. It indicates, for instance, that for 16% of the total event sample two $\pi^+\pi^-$ pairs (from three different pions) can be constructed per event. In Table 4.2, the total number of selected inclusive and semi-inclusive events are given.

4.2.4 Beam polarization balancing

During standard operation, the HERA lepton beam is tuned such as to obtain as high a beam polarization as possible. The beam helicity is typically reversed once a month or once every couple

process type	inclusive DIS	semi-inclusive $\pi^+\pi^-$ pairs
no. of events	3475368	108919

Table 4.2: *Total number of inclusive DIS events and semi-inclusive $\pi^+\pi^-$ events for the final data set used in the analysis. These events were extracted from the data collected in the years 2002–2004.*

of months. Only during the year 2002 HERA operated without optimizing the beam polarization as it was starting up after a major upgrade [145].

However, for the measurement of the transverse single-spin asymmetry A_{UT}, one needs an unpolarized (U) lepton beam. Using a polarized lepton beam, the numerator and denominator of the ratio used to extract a value of A_{UT} could be influenced by the cross section differences σ_{LT} and σ_{LU} [105, 108][1], respectively. However, at leading twist and integrated over the transverse momentum $\boldsymbol{P}_{h\perp}$, both of these cross section differences are zero [105]. At subleading twist, integrated over $\boldsymbol{P}_{h\perp}$, both cross section differences contain terms that could be nonzero and therefore could contribute to A_{UT}. Still, these terms cannot contribute to the extracted value of the amplitude $A_{UT}^{\sin(\phi_{R\perp}+\phi_S)\sin\theta}$ as they appear with different dependencies on the azimuthal angles $\phi_{R\perp}$ and ϕ_S which do not contribute to the integral performed to extract $A_{UT}^{\sin(\phi_{R\perp}+\phi_S)\sin\theta}$ (cf. Eq. 2.72). Therefore, even if the beam polarization is nonzero, it is not expected that this influences the extracted amplitude. Indeed, the extracted amplitude was found to be the same for both beam helicities [174].

Even if the beam polarization could somehow influence the extracted value of A_{UT} (for instance due to contributions of even higher twist), this effect would vanish for the total semi-inclusive data set used in the present analysis, as the average beam polarization for these data is negligible, i.e., 0.3% (see Fig. 4.3).

4.3 Transverse single-spin asymmetry

The transverse single-spin asymmetry, as defined in Eq. 2.67 is extracted from the measured events using the following expression:

$$A_{UT} \equiv \frac{\mathrm{d}\sigma_{UT}}{\mathrm{d}\sigma_{UU}} = \frac{1}{|\boldsymbol{P}_T|}\frac{N^{\uparrow}/N_{\mathrm{i}}^{\uparrow} - N^{\downarrow}/N_{\mathrm{i}}^{\downarrow}}{N^{\uparrow}/N_{\mathrm{i}}^{\uparrow} + N^{\downarrow}/N_{\mathrm{i}}^{\downarrow}}. \tag{4.12}$$

Here, $N^{\uparrow(\downarrow)}$ is the number of semi-inclusive $\pi^+\pi^-$ pair events detected while the target is either polarized upwards ($\uparrow$) or downwards ($\downarrow$). Both these numbers are normalized to the corresponding numbers of inclusive DIS events $N_{\mathrm{i}}^{\uparrow(\downarrow)}$. The quantity $|\boldsymbol{P}_T|$ in Eq. 4.13 represents the luminosity-weighted target polarization.

[1] These cross section differences are defined similarly to σ_{UL} and σ_{UT}, defined in Sec. 2.4, i.e., they select a part of the cross section related to the beam/target polarization.

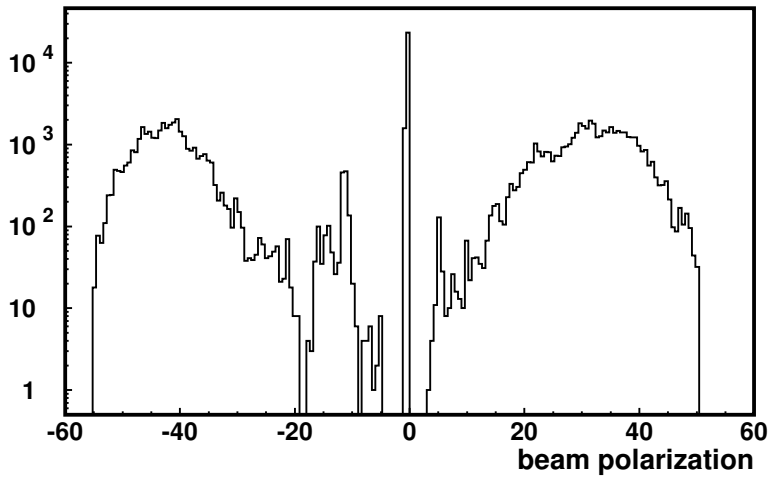

Figure 4.3: *Distribution of the beam polarization for all semi-inclusive $\pi^+\pi^-$ events used in the analysis of the selected three years of data taking. The huge peak at zero corresponds to the beam polarization for the year 2002, when the beam was not tuned to be polarized (during part of this period the polarization was not measured at all, but just set to zero).*

As mentioned in Sec. 2.4, one of the main reasons to measure an asymmetry instead of the polarized cross section itself, is that the detector acceptance of HERMES does not have a full 4π coverage. This directly influences the measured cross section, whereas to a large extent the asymmetry remains unaffected. As an example of the relevance of this difference, the left plot in Fig. 4.4 shows the two-dimensional distribution of the azimuthal angles $\phi_{R\perp}$ versus ϕ_S (defined in Secs. 2.3.1 and 2.1.1, respectively), two kinematic variables that A_{UT} directly depends on. For this distribution, the events for both target polarization states are summed, such that the contribution from σ_{UT} cancels (see Eq. 2.68). At leading twist, also the unpolarized cross section σ_{UU} (Eq. 2.69) is independent of both $\phi_{R\perp}$ and ϕ_S. Therefore, the complicated patterns visible in this distribution can be entirely attributed to the limited geometrical spectrometer acceptance, i.e., using a 4π detector this distribution would have been homogeneous. The gaps in the distribution and the diagonal patterns are due to the gap in the acceptance between the top and bottom parts of the spectrometer. The large difference in the number of events in the two encircled parts of the distribution is related to the effect of the spectrometer magnet on the particle tracks. The schematic picture of the HERMES spectrometer on the right in Fig. 4.4 explains this effect. It shows that, depending on both $\phi_{R\perp}$ and ϕ_S, the spectrometer magnet either bends both particles towards each other or away from each other. In the first situation one or both of the pions can be bent into the detector acceptance, in the latter situation one or both can be bent out of the detector acceptance. This example illustrates that in order to measure the $\phi_{R\perp}$ and ϕ_S dependence of the cross section, one needs to evaluate a complicated acceptance correction, whereas for asymmetry measurements the effect of the acceptance mostly cancels.

The following section explains how the amplitude $A_{UT}^{\sin(\phi_{R\perp}+\phi_S)\sin\theta}$ is extracted from the single-spin asymmetry A_{UT}. Subsequently, it is explained in Sec. 4.5 that in practice even such an az-

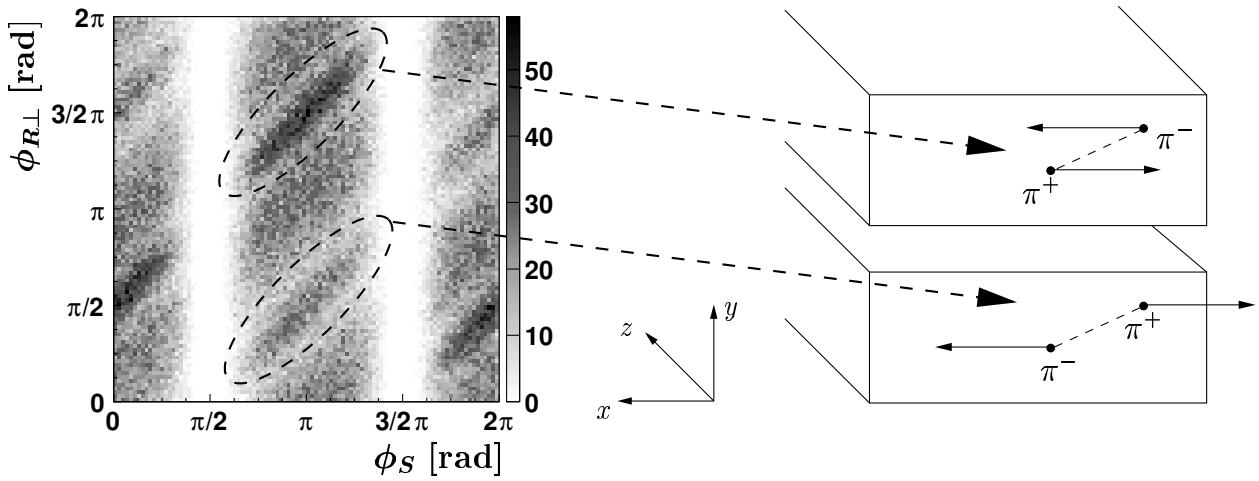

Figure 4.4: *On the left, the measured distribution of the azimuthal angles $\phi_{R\perp}$ versus ϕ_S for the transversely polarized hydrogen data is shown. On the right, a simplified picture of the HERMES acceptance is shown with the beam or z-direction going into the paper. It shows two possible configurations of the $\pi^+\pi^-$-pair. It explains that when the π^- is to the left (right) of the π^+ there is an enlarged probability that one or both of the pions are bent out of (into) the HERMES acceptance. The magnetic field of the spectrometer magnet is pointing in the positive y-direction.*

imuthal amplitude can be affected by remaining detector acceptance effects. The possible size of such effects is investigated and an extraction method is introduced that limits the size of these effects.

4.4 Extraction of azimuthal moments

4.4.1 Least-squares fitting and the statistical uncertainty

To extract the azimuthal moment $A_{UT}^{\sin(\phi_{R\perp}+\phi_S)\sin\theta}$ from the measured asymmetry a binned χ^2 fit was used. This is a method that is easy to implement and was originally used within HERMES as an extraction method that cannot be influenced by acceptance effects (discussed in Sec. 4.5). Here, the extraction method is explained for the case of a one-dimensional fit. The method can be easily extended to a multi-dimensional fit. Assume an asymmetry given by:

$$A(\phi) = a\sin(\phi) = \frac{N^{\uparrow}(\phi) - N^{\downarrow}(\phi)}{N^{\uparrow}(\phi) + N^{\downarrow}(\phi)}, \tag{4.13}$$

with $N^{\uparrow}$ and $N^{\downarrow}$ the measured number of events for two different spin states of the target, both depending on some variable ϕ. The value of a can be extracted by fitting the function $f(\phi) = a\sin(\phi)$ to the measured asymmetry using the least squares method, i.e., minimizing χ^2:

$$\chi^2 = \sum_i^{N_b} \frac{(A_i - f(\langle\phi\rangle_i))^2}{\Delta A_i^2}, \tag{4.14}$$

where the summation is over the ϕ bins with N_b the total number of bins, A_i the measured asymmetry in bin i, $f(\langle\phi\rangle_i))$ the value of the fit function evaluated at the average value of ϕ in bin i, and ΔA_i the statistical uncertainty of the measured asymmetry in bin i. For the statistical uncertainty on the measured number of events one can use

$$\Delta N^{\uparrow(\downarrow)} = \sqrt{N^{\uparrow(\downarrow)}}, \tag{4.15}$$

which is valid for large N ($N \gtrapprox 10$) where the Poisson distribution approximates a Gaussian distribution with standard deviation $\sqrt{N}$. Standard error propagation can be used to calculate the uncertainty ΔA giving

$$\Delta A = \frac{2\sqrt{N^{\uparrow}N^{\downarrow}(N^{\uparrow}+N^{\downarrow})}}{(N^{\uparrow}+N^{\downarrow})^2}. \tag{4.16}$$

Two corrections are introduced to improve the extraction method if only statistically-limited data sets are available. These corrections are discussed in the following subsection.

4.4.2 Low-statistics corrections

Correction to ΔA. In Eq. 4.15 an estimator is given of the uncertainty on a measured number of events. The real uncertainty on a measured number of events is given by $\Delta N = \sqrt{N_{\text{av}}}$, where N_{av} is the average of the (unknown) Poisson distribution from which N was drawn. Using $\Delta N = \sqrt{N}$ introduces a bias towards small values of N. This can easily be seen if one repeats such a counting experiment many (i) times. The weighted average of N would be at $\sum_i \frac{N_i}{(\Delta N_i)^2} / \sum_i \frac{1}{(\Delta N_i)^2} < N_{\text{av}}$. This bias increases with decreasing values for N, i.e., small event samples. A better estimate of the uncertainties can be obtained in an iterative procedure using the results of the fit:

- Calculate the asymmetry using the measured number of events $N^{\uparrow(\downarrow)}(\phi)$ and fit the asymmetry with the functional shape given by Eq. 4.13 using $\sqrt{N^{\uparrow(\downarrow)}(\phi)}$ as the statistical uncertainty (with a as a free parameter).
- Using the fit result, calculate $N^{\uparrow}_{\text{av}}$ and $N^{\downarrow}_{\text{av}}$. These numbers are better estimates of the averages of the distributions from which $N^{\uparrow}$ and $N^{\downarrow}$ originate. As one fits the asymmetry and not the distributions of $N^{\uparrow}$ and $N^{\downarrow}$ separately, one needs an extra constraint to solve this equation for $N^{\uparrow}_{\text{av}}$ and $N^{\downarrow}_{\text{av}}$. Here the assumption is made that $(N^{\uparrow}+N^{\downarrow}) = (N^{\uparrow}_{\text{av}}+N^{\downarrow}_{\text{av}})$ in each bin.
- Iterate the previous two steps using $\sqrt{N^{\uparrow(\downarrow)}_{\text{av}}}$ as the uncertainty (typically, one iteration is sufficient). The uncertainty ΔA is again calculated from these uncertainties using standard error propagation.

Correction to χ^2. If the fit function is nonlinear one has to account properly for nonlinear behavior within the bins. This can be done by redefining χ^2 as

$$\chi^2 = \sum_i^{N_b} \frac{(A_i - \langle f_i(\phi)\rangle)^2}{\Delta A_i^2}, \qquad \langle f_i(\phi)\rangle = \frac{1}{N_i}\sum_{n=1}^{N_i} f(\phi_{i,n}), \tag{4.17}$$

where the fit function $f_i(\phi)$ is averaged over the bin i using the measured number of events N_i in this bin. Instead, it is also possible to calculate analytically the integral of the fit function to obtain $\langle f_i(\phi)\rangle$. The disadvantage of such an approach is that it does not apply in case of nonuniform event distributions within the bin, which Eq. 4.17 takes into account naturally.

For the situation where both the numerator (N) and the denominator (D) of the asymmetry depend on ϕ, the average of the fit function needs to be calculated as:

$$\langle f_i(\phi)\rangle \equiv \frac{\langle f_{\mathrm{N},i}(\phi)\rangle}{\langle f_{\mathrm{D},i}(\phi)\rangle} = \frac{\sum_{n=1}^{N_i} f_{\mathrm{N}}(\phi_{i,n})}{\sum_{n=1}^{N_i} f_{\mathrm{D}}(\phi_{i,n})} \neq \frac{1}{N_i}\sum_{n=1}^{N_i} f(\phi_{i,n}), \tag{4.18}$$

due to the convention that any integral of a measured asymmetry over one of the relevant kinematic variables it depends on is performed separately for the numerator and the denominator (σ_{UT} and σ_{UU}, respectively) in practice. It has been verfied that the proposed extraction method with the corrections described above works well, as discussed in Appendix C.

4.5 Acceptance effects

The fully differential asymmetry for two-hadron semi-inclusive deep-inelastic scattering depends on 9 kinematic variables: x, y, z, $M_{\pi\pi}$, $|\boldsymbol{P}_{\boldsymbol{h}\perp}|$, $\phi_{R\perp}$, ϕ_S, ϕ_h, and θ, as defined in Chapter 2. Due to the limited statistics, it is not possible to determine the amplitudes $A_{UT}^{\sin(\phi_{R\perp}+\phi_S)\sin\theta}$ of the asymmetry fully differentially in all relevant variables. Combined with the restriction that the HERMES spectrometer does not have a full 4π acceptance, this implies that the measured number of events is always convoluted with the experimental acceptance ϵ, i.e.,

$$\begin{aligned} N^{\uparrow(\downarrow)}(\phi_{R\perp},\phi_S,\theta,M_{\pi\pi}) \propto \int \mathrm{d}x\,\mathrm{d}y\,\mathrm{d}z\,\mathrm{d}^2\boldsymbol{P}_{\boldsymbol{h}\perp}\,\epsilon(x,y,z,\boldsymbol{P}_{\boldsymbol{h}\perp},\phi_{R\perp},\phi_S,\theta,M_{\pi\pi}) \\ \times\,\sigma_{U\uparrow(\downarrow)}(x,y,z,\boldsymbol{P}_{\boldsymbol{h}\perp},\phi_{R\perp},\phi_S,\theta,M_{\pi\pi}), \end{aligned} \tag{4.19}$$

such that ϵ does not necessarily drop out of the expression for the asymmetry (Eq. 4.13). This implies that one might not be able to directly compare the results measured at HERMES to results measured in a detector with full 4π coverage or equivalently to a theoretical prediction that does not take the HERMES acceptance into account. Therefore, in this section the influence of the limited HERMES acceptance on the results presented in this thesis is investigated (and in the present work, any such influence is referred to as an *acceptance effect*).

In the following subsection, a technique is explained that can be used to introduce a model for A_{UT} into an unpolarized Pythia Monte-Carlo simulation [175]. In subsection 4.5.2, this technique is used to implement a model for the amplitude $A_{UT}^{\sin(\phi_{R\perp}+\phi_S)\sin\theta}$ and it is discussed how one can best compare the extracted values for $A_{UT}^{\sin(\phi_{R\perp}+\phi_S)\sin\theta}$ as measured within the HERMES acceptance to a model prediction. After that, subsections 4.5.3 and 4.5.4 discuss the influence of the acceptance for some specific variables, on which the asymmetry depends, i.e., the angles ϕ_h and θ.

It is noted that the final values obtained from the present analysis for $A_{UT}^{\sin(\phi_{R\perp}+\phi_S)\sin\theta}$ are also shown in this section (Fig. 4.13), but a full discussion of these results is only presented in Chapter 5.

4.5.1 Introducing spin dependence into an unpolarized Monte-Carlo

In order to investigate the influence of the HERMES acceptance on the extracted value of A_{UT} and its azimuthal amplitudes, one needs a Monte-Carlo simulation that has an expression implemented both for σ_{UU} and for σ_{UT}. However, as it is beyond the scope of this work to write a new Monte-Carlo code, a different method is used. Starting point is a version of the Pythia Monte-Carlo code [175] that does not have σ_{UT} implemented. Specifically, a version of Pythia was used where the cross sections of all implemented processes were tuned to HERMES data [137].

In Fig. 4.5, a comparison is shown for all kinematic variables that the asymmetry depends on, between the distributions extracted from the present experimental polarized hydrogen data (summing events of both target polarization states) and the Pythia Monte-Carlo simulation mentioned above. The various experimental distributions are well reproduced by the Monte-Carlo simulation. Only for the ϕ_h distribution considerable differences are observed, which are discussed specifically in Sec. 4.5.3. The two peaks in the $M_{\pi\pi}$ invariant-mass distribution correspond to the ρ^0 ($M_{\pi\pi} = 775.5$ MeV) resonance and the K^0_s ($M_{\pi\pi} = 497.6$ MeV) resonance.

The target polarization dependence is introduced in the Monte-Carlo code by assigning target spin states for each event according to an expression for A_{UT}. It reads, written in a C-like fashion:

$$spin = (random < 0.5\,(1 + A_{UT}(x, y, z, M_{\pi\pi}, |\boldsymbol{P}_{h\perp}|, \phi_{R\perp}, \phi_S, \phi_h, \theta))), \tag{4.20}$$

where $0 < random < 1$. For each event a random number is drawn resulting in $spin$ = true for target spin up and $spin$ = false for target spin down. It is thus possible, for a given model of A_{UT}, to generate a sample of DIS data with a realistic spin distribution.

4.5.2 Reconstructing the amplitude $A_{UT}^{\sin(\phi_{R\perp}+\phi_S)\sin\theta}$

To be able to perform acceptance studies a model prediction for $A_{UT}^{\sin(\phi_{R\perp}+\phi_S)\sin\theta}$ needs to be implemented in the Monte-Carlo code. For the implementation it was assumed that there are no other contributions to the asymmetry, i.e.,

$$\begin{aligned} A_{UT} &= \sin(\phi_{R\perp}+\phi_S)\sin\theta\, A_{UT}^{\sin(\phi_{R\perp}+\phi_S)\sin\theta} \\ &= -\sin(\phi_{R\perp}+\phi_S)\sin\theta \frac{B(y)}{A(y)} \sqrt{1-4\left(\frac{M_\pi}{M_{\pi\pi}}\right)^2} \frac{\sum_q e_q^2 h_1^q(x) H_{1,q}^{\sphericalangle,sp}(M_{\pi\pi}, z)}{\sum_q e_q^2 f_1^q(x) D_{1,q}(M_{\pi\pi}, z)}, \end{aligned} \tag{4.21}$$

where Eq. 2.72 was used. For the dihadron fragmentation functions $D_{1,q}(M_{\pi\pi}, z)$ and $H_{1,q}^{\sphericalangle,sp}(M_{\pi\pi}, z)$, parametrizations were taken from Ref. [122]. For the distribution functions $f_1^q(x)$ and $h_1^q(x)$, parametrizations were taken from Ref. [176] and Ref. [117], respectively (corresponding to the dashed line in Fig. 2.18). As the model from Ref. [122] for the two dihadron fragmentation functions is the only model available that gives a full parametrization of these functions, this is presently the best way the target spin dependence can be introduced in a Monte-Carlo simulation.

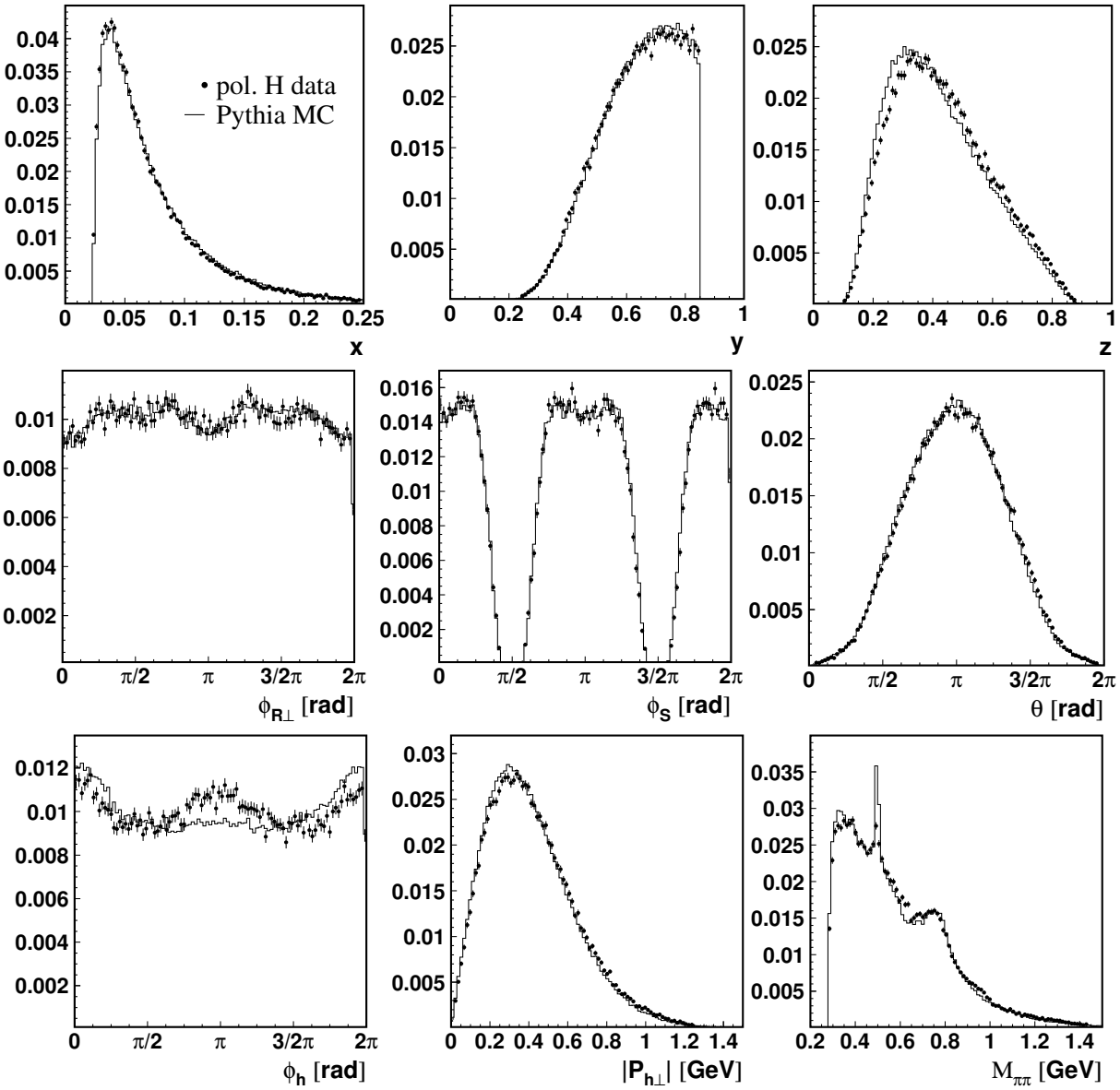

Figure 4.5: *Normalized event distributions for semi-inclusive $\pi^+\pi^-$ production in deep-inelastic lepton-nucleon scattering for all nine independent kinematic variables that the asymmetry A_{UT} depends on. The data points represent the distributions extracted from the polarized hydrogen data (summing the events of both target polarization states) used in the analysis, and the histograms represent the results of the Pythia Monte-Carlo simulation, taking into account the HERMES acceptance.*

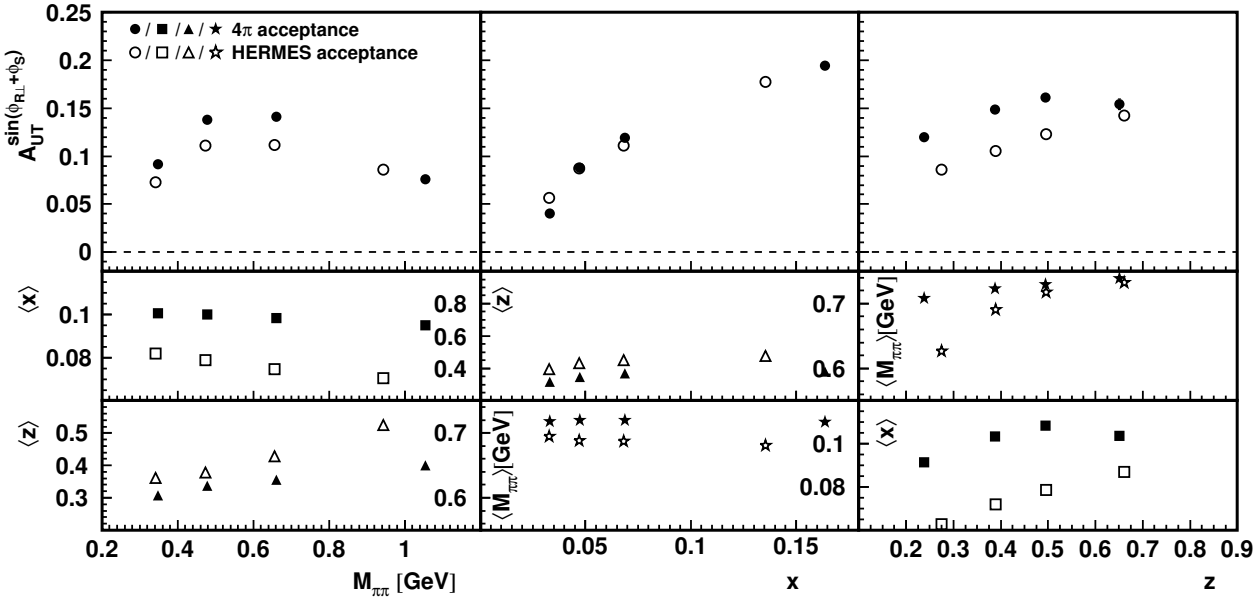

Figure 4.6: *The azimuthal amplitude $A_{UT}^{\sin(\phi_{R\perp}+\phi_S)}$ as a function of $M_{\pi\pi}$, x and z as evaluated with the model prediction of Ref. [122]. The simulations in a 4π acceptance (closed symbols) are compared to those in the HERMES acceptance (open symbols). The bottom panels indicate for each data point the corresponding average values $\langle M_{\pi\pi}\rangle$, $\langle x\rangle$ and $\langle z\rangle$.*

A comparison of the simulated results generated in the HERMES geometric acceptance to the same model simulated in a 4π acceptance are shown in Fig 4.6. The figure shows that for the $M_{\pi\pi}$ dependence and for the z dependence there is a clear difference in the values of the extracted amplitudes. This can be caused by the fact that the average values of the variables that are integrated over[2] are different for the two data sets (especially the difference in the average values of x for the $M_{\pi\pi}$ dependence and for the z dependence is significant). In principle, one could make an acceptance correction to the HERMES data based on this model. However, this has not been done, because the model itself has quite large inherent uncertainties.

Instead of applying acceptance corrections to the data, it is possible to compare the measured amplitudes to the simulated model prediction evaluated at the average kinematics of the data. This is a good method, as long as the predicted amplitude is linearly dependent on all variables in the range that it is integrated over. The result of such a comparison is shown in Fig. 4.7. Although slightly better for some data points than what was shown in Fig. 4.6, this comparison still doesn't show a good agreement. This is due to the highly nonlinear dependence of $A_{UT}^{\sin(\phi_{R\perp}+\phi_S)\sin\theta}$ on the invariant mass in this model, with strong peaks at $M_{\pi\pi} \approx 0.5$ GeV and at the ρ^0 mass ($M_{\pi\pi} = 0.78$ GeV), as shown in Fig. 2.18. Even for the invariant-mass dependence itself, there is a large difference between the two methods, which is a reflection of the non-linearity of the model within

[2]Note that if an asymmetry is integrated over certain variables x_i, it is generally meant that the numerator and denominator of the asymmetry are integrated separately, e.g. $A(x_1) = \frac{\int \mathrm{d}x_2\,\mathrm{d}x_3\ldots\sigma_{UT}(x_1,x_2,x_3,\ldots)}{\int \mathrm{d}x_2\,\mathrm{d}x_3\ldots\sigma_{UU}(x_1,x_2,x_3,\ldots)}$.

these invariant-mass bins. Finer invariant-mass bins would make this effect smaller. However, for the x and z dependence, one integrates over a much larger invariant-mass range (0.5 to 1 GeV) and in order to reduce the difference between the two methods for these dependencies, one would also need to evaluate these dependences in separate $M_{\pi\pi}$ bins. This is not possible with the current amount of statistics available, i.e., the data acquired in the years 2002-2004.

Figs. 4.6 and 4.7 show that at HERMES acceptance effects can influence the extraction of the azimuthal amplitude $A_{UT}^{\sin(\phi_{R\perp}+\phi_S)\sin\theta}$. This complicates direct comparisons of the HERMES data to model predictions. The best way such comparisons can still be made is by taking the HERMES acceptance into account for each model prediction individually. This can be done for instance by using a Monte-Carlo code that simulates the effect of the HERMES acceptance, as was shown for the model of Ref. [122] in Figs. 4.6 and 4.7. The comparison of this model to the HERMES data is discussed in Chapter 5.

A different method of dealing with these acceptance effects, is to estimate a systematic uncertainty that accounts for these effects. In principle, both comparisons shown in Figs. 4.6 and 4.7 can be used for such an estimate. However, the latter comparison, using the model evaluated at the average kinematics of the data, is not well suited for this, because this estimate would be very sensitive to the exact shape of the invariant-mass dependence in the model, and as a consequence the estimated systematic uncertainty would be highly model dependent. A systematic uncertainty based on the comparison made in Fig. 4.6 is more robust. This can be explained from the origin of the observed differences between the two simulations in Fig. 4.6. As was mentioned above, these differences can be attributed to the differences in the average x values. Hence, a systematic uncertainty based on this comparison is dependent on the chosen model for the transversity distribution function $h_1(x)$, because $h_1(x)$ represents the only unknown part of the x dependence of $A_{UT}^{\sin(\phi_{R\perp}+\phi_S)\sin\theta}$ (cf. Eq. 4.21). Combined with the fact that most models for $h_1(x)$, are approximately linear in the x range accessed by the HERMES experiment, it is concluded that this (relative) systematic uncertainty is less model dependent than a systematic uncertainty based on the comparison shown in Fig. 4.7. It is thus possible to give one overall estimate of the systematic uncertainty for each of the dependencies, making use of the comparison shown in Fig. 4.6. This results in an underestimate of up to 26% of the measured amplitude for the $M_{\pi\pi}$ dependence, a negligeable effect for the x dependence and an up to 41% underestimate for the z dependence[3].

4.5.3 Dependence on the azimuthal angle ϕ_h

As was shown in Sec. 2.3.3, the polarized cross section can be integrated over the transverse momentum of the pion pair $\boldsymbol{P}_{h\perp}$ while remaining sensitive to transversity. However, experimentally this requires a full coverage of the detector in $\boldsymbol{P}_{h\perp}$, or equivalently in both ϕ_h and $|\boldsymbol{P}_{h\perp}|$. If

[3]Using the final extraction method, as discussed in Sec. 4.5.4, these numbers are slightly bigger, i.e., an underestimate up to 32% for the $M_{\pi\pi}$ dependence, a negligeable effect for the x dependence and an underestimate up to 44% for the z dependence.

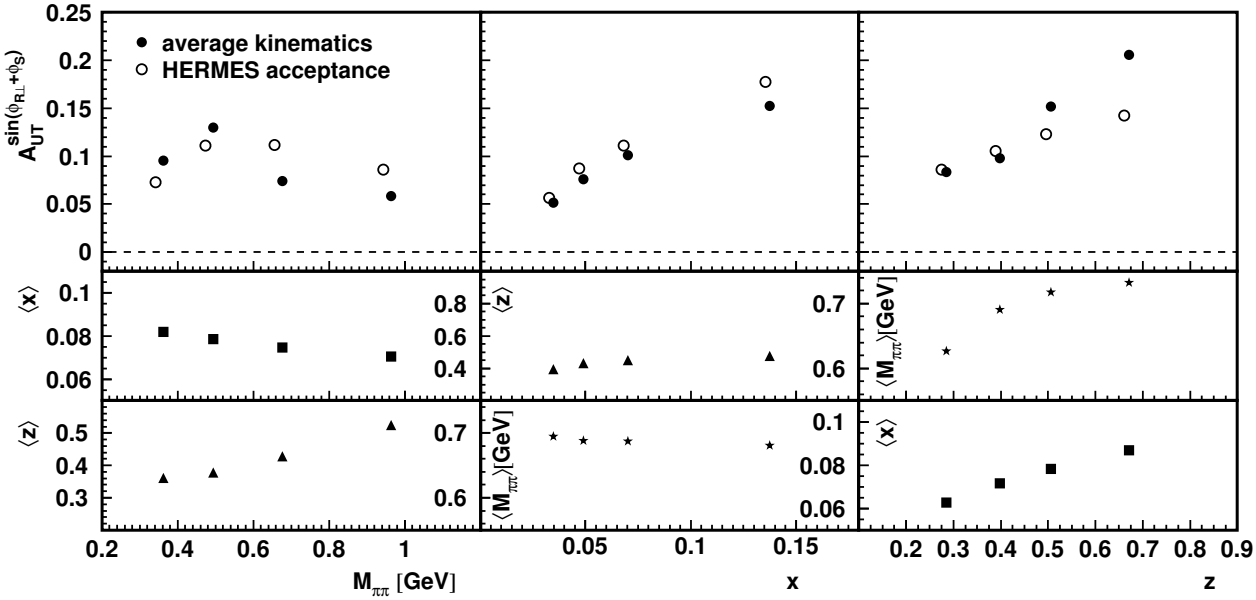

Figure 4.7: *The azimuthal amplitude $A_{UT}^{\sin(\phi_{R\perp}+\phi_S)}$ as a function of $M_{\pi\pi}$, x and z as evaluated with the model prediction of Ref. [122]. A comparison is shown between the model prediction evaluated at the average kinematics of the HERMES data (closed symbols) to the model prediction evaluated with a Monte-Carlo simulation that takes the HERMES acceptance into account. (Note that the statistical uncertainties are smaller than the symbol size.)*

the coverage in $\boldsymbol{P_{h\perp}}$ is not complete, one may get many unwanted contributions to the measured asymmetry. This can be seen in Appendix B, where the leading-twist expressions for the polarized and unpolarized cross sections, unintegrated over $\boldsymbol{P_{h\perp}}$ are listed, as derived in Ref. [106]. These extra terms can directly influence the extraction of the term of interest. Consider for example the third term in Eq. B.2. It depends on the angles ϕ_h, ϕ_R and ϕ_S through the factor $\sin(2\phi_h - \phi_R - \phi_S)$, which can be rewritten as:

$$\sin(2\phi_h - \phi_R - \phi_S) = \sin(2\phi_h)\cos(\phi_R + \phi_S) - \cos(2\phi_h)\sin(\phi_R + \phi_S). \tag{4.22}$$

Therefore in case of an incomplete integration over ϕ_h, the $\cos(2\phi_h)$ term will not vanish, but instead gives a contribution to the asymmetry proportional to $\sin(\phi_R + \phi_S)$. Apart from such contributions, also combinations of ϕ_h-dependent terms in the numerator to ϕ_h-dependent terms in the denominator can give rise to a $\sin(\phi_R + \phi_S)$ dependence. Finally, an incomplete integration can influence the overall size of the denominator, resulting in a scaling of the extracted $\sin(\phi_R + \phi_S)$ dependence.

Fig. 4.8 shows that indeed the ϕ_h coverage in the HERMES acceptance is not complete. It shows distributions of the angle ϕ_h for measured events, summing both target polarization states, for four different invariant-mass bins. Superimposed are the same distributions from a Pythia Monte-Carlo simulation, taking into account the HERMES acceptance. The Monte-Carlo simulation has no explicit ϕ_h dependence implemented; hence its ϕ_h distributions are flat in a 4π accep-

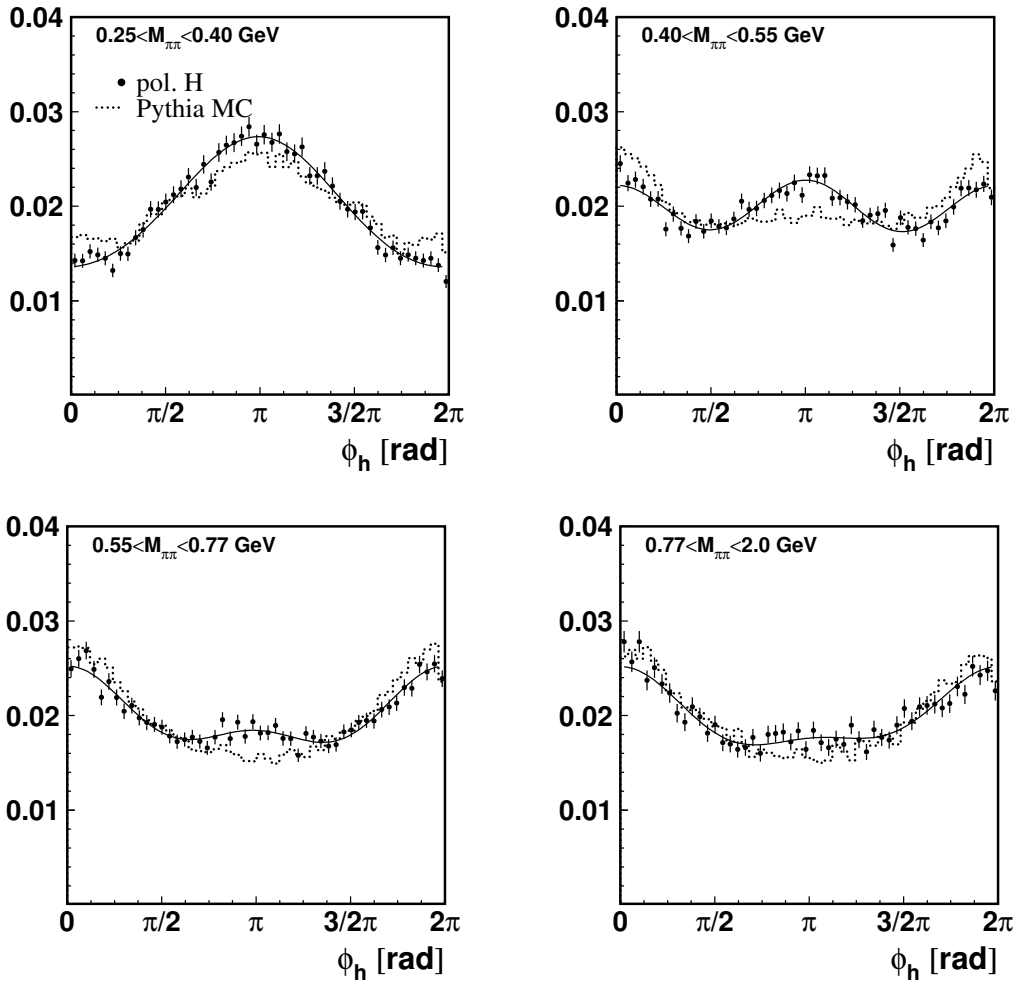

Figure 4.8: *Normalized event distributions of the azimuthal angle ϕ_h for four different bins in the invariant mass $M_{\pi\pi}$ as indicated. The data points represent the polarized hydrogen data (summing the events of both target polarization states), the solid curves result from a fit with a Fourier Series to the data and the dotted histogram represents the simulated events of the Pythia Monte-Carlo simulation, taking into account the HERMES acceptance.*

tance. The level of agreement between the Monte-Carlo simulation and the measurements clearly demonstrates that the ϕ_h dependence is strongly influenced by the HERMES detector acceptance, and that this influence depends on the invariant mass $M_{\pi\pi}$. The differences between the data and the Monte-Carlo simulation could be due to a ϕ_h dependence in the unpolarized cross section (not present in the Monte-Carlo code) or due to remaining acceptance effects.

In order to assign a systematic uncertainty to this acceptance effect one needs model predictions for the size and dependencies of all these ϕ_h-dependent terms. However, no such information exists, e.g., most of the involved distribution functions and fragmentation functions are as yet completely unknown. In order to still be able to estimate a systematic uncertainty, a very general model was used in which the size and dependencies of these terms are varied between reasonable bounds. The effect on the extracted value of $A_{UT}^{\sin(\phi_{R\perp}+\phi_S)\sin\theta}$ is then used to estimate the corresponding contribution to the systematic uncertainty. Below, this procedure and the results it generates are described in detail.

The starting point is again the unpolarized Pythia Monte-Carlo code where spin states are assigned to the semi-inclusive events according to an asymmetry A_{UT} using the procedure described in Sec. 4.5.1. For the term of interest in the numerator (containing the product $h_1 H_1^{\sphericalangle}$) and for the unpolarized cross section, integrated over $\boldsymbol{P_{h\perp}}$, the model of Ref. [122] was used (and the same model for $h_1(x)$ and $f_1(x)$ as before). As the model predicts these terms *integrated* over $\boldsymbol{P_{h\perp}}$, for this study a Gaussian Ansatz was used for the $|\boldsymbol{P_{h\perp}}|$ dependence of both terms:

$$\mathcal{I}[f_1(x,\boldsymbol{p_T}^2) D_1(z,\zeta,M_h^2,\boldsymbol{k_T}^2,\boldsymbol{k_T}\cdot\boldsymbol{R_T})] = f_1(x)\, D_1(z,\zeta,M_h^2)\frac{1}{\pi\langle \boldsymbol{P}_{\boldsymbol{h\perp}}^2\rangle} e^{-\boldsymbol{P}_{\boldsymbol{h\perp}}^2/\langle \boldsymbol{P}_{\boldsymbol{h\perp}}^2\rangle}, \tag{4.23}$$

and the same $\boldsymbol{P_{h\perp}}$ dependence was introduced for the convolution integral $\mathcal{I}[h_1 H_1^{\sphericalangle}]$.

Subsequently, the ϕ_h-dependent terms were implemented such that the corresponding azimuthal amplitudes depend on z, x, and $\boldsymbol{P_{h\perp}}$ according to[4]:

$$\begin{aligned}\frac{1}{2}A_{UT}^{\sin(a\phi_h+b\phi_{R\perp}+c\phi_S+\frac{d}{2}\pi)} &\equiv \frac{\int\int\int \mathrm{d}\phi_h\,\mathrm{d}\phi_{R\perp}\,\mathrm{d}\phi_S\,\sin(a\phi_h+b\phi_{R\perp}+c\phi_S+\frac{d}{2}\pi)\,\mathrm{d}^9\sigma_{UT}}{\int\int\int \mathrm{d}\phi_h\,\mathrm{d}\phi_{R\perp}\,\mathrm{d}\phi_S\,\mathrm{d}^9\sigma_{UU}} \\ &= C_N\, z^{\alpha_N}\, x^{\beta_N}\, f_N(|\boldsymbol{P_{h\perp}}|),\end{aligned} \tag{4.24}$$

with N identifying the various terms in the polarized cross section given in Eqs. B.1 or B.2, C_N a constant scaling factor, $\alpha_N, \beta_N \in [0.1, 3]$ and a, b, c and d are either zero or integers depending on N. Similarly, azimuthal amplitudes $A_{UU}^{\sin(a\phi_h+b\phi_{R\perp}+c\phi_S+\frac{d}{2}\pi)}$ were introduced for the ϕ_h-dependent parts of the unpolarized cross section. Apart from the fact that these terms increase nonlinearly with increasing x and z, the choices for α_N and β_N are quite arbitrary, but were found not to influence the final conclusions. All amplitudes were chosen to be independent of θ. How to properly handle the θ-dependence of the asymmetry in the extraction of the amplitude will be discussed in the next section.

[4] For those terms containing either $h_1(x)$ or $H_1^{\sphericalangle}(z, M_h)$, the x dependence, and the z and M_h dependencies were used as given by the models of Ref. [176] and Ref. [122], respectively.

Two different approaches were used to model the $|\boldsymbol{P}_{h\perp}|$ dependence ($f_N(|\boldsymbol{P}_{h\perp}|)$) of the asymmetry. In the first approach (I), it is assumed that all terms in the cross section have the same Gaussian $|\boldsymbol{P}_{h\perp}|$ dependence as given in Eq. 4.23, resulting in no $|\boldsymbol{P}_{h\perp}|$ dependence for the amplitudes $A_{UT}^{\sin(\cdots)}$ of Eq. 4.24 ($f_N(|\boldsymbol{P}_{h\perp}|) = 1$ for all N).[5] In the second approach (II), a Gaussian Ansatz was used for the distribution and fragmentation functions themselves:

$$g_{1T}(x, \boldsymbol{p}_T^2) = \frac{1}{\pi\langle \boldsymbol{p}_T^2\rangle} e^{-\boldsymbol{p}_T^2/\langle \boldsymbol{p}_T^2\rangle} g_{1T}(x), \tag{4.25}$$

$$G_1^{\perp}(z, \zeta, M_h^2, \boldsymbol{k}_T^2, \boldsymbol{k}_T \cdot \boldsymbol{R}_T) = \frac{1}{\pi\langle \boldsymbol{k}_T^2\rangle} e^{-\boldsymbol{k}_T^2/\langle \boldsymbol{k}_T^2\rangle} G_1^{\perp}(z, \zeta, M_h^2), \tag{4.26}$$

with the same $\boldsymbol{p}_T^2$ and $\boldsymbol{k}_T^2$ dependence implemented for all other distribution and fragmentation functions. Within this assumption, one can evaluate all convolution integrals appearing in Eqs. B.1 and B.2. Due to the fact that no $\boldsymbol{k}_T \cdot \boldsymbol{R}_T$ dependence is taken into account for the fragmentation functions, about half of the convolution integrals are zero, thus simplifying the expressions for $\mathrm{d}^9\sigma_{UU}$ and $\mathrm{d}^9\sigma_{UT}$ to those given in Eqs. B.5 and B.6. Within approach II, the $|\boldsymbol{P}_{h\perp}|$ dependence of these expressions was used for $f_N(|\boldsymbol{P}_{h\perp}|)$.

The values of the scaling factors C_N in Eq. 4.24 were derived from the averaged amplitudes, which were randomly chosen in the range [-0.1,0.1], i.e.,

$$\frac{\int A_{UU/T}^{\sin(a\phi_h + b\phi_{R\perp} + c\phi_S + \frac{d}{2}\pi)} \, \mathrm{d}^9\sigma_{UU}}{\int \mathrm{d}^9\sigma_{UU}} \equiv R_N \in [-0.1, 0.1], \tag{4.27}$$

where the chosen range for R_N is based on the Ansatz that the single-spin asymmetries related to these terms do not exceed $|R_N| = 0.1$. The integral is performed over all 9 dimensions and the following integration ranges were used (based on the selections used in the analysis of the experimental data):

$$\begin{aligned} M_{\pi\pi} &\in [0.5, 1]\ \text{GeV}, \\ |\boldsymbol{P}_{h\perp}| &\in [0, \infty]\ \text{GeV}, \\ y &\in [0.10, 0.85], \\ z &\in [0.1, 1.0], \\ x &\in [Q^2_{\min}/(y(s - M^2)), 0.4] = [1/(y(s - M^2)), 0.4]. \end{aligned} \tag{4.28}$$

Each resulting parametrization of A_{UT} had to satisfy the positivity limit $|A_{UT}| < 1$. If this is not the case, then the values of R_N were randomly scaled down one by one until this constraint was met. A typical distribution of simulated values for R_N is shown in Fig. 4.9. The distributions for the other terms are of similar shape. The fact that the width of these distributions is quite small indicates

[5] Within this approach, the first two terms in Eq. B.2 were not taken into account, as they would not vanish when integrated over $\boldsymbol{P}_{h\perp}$, as is required.

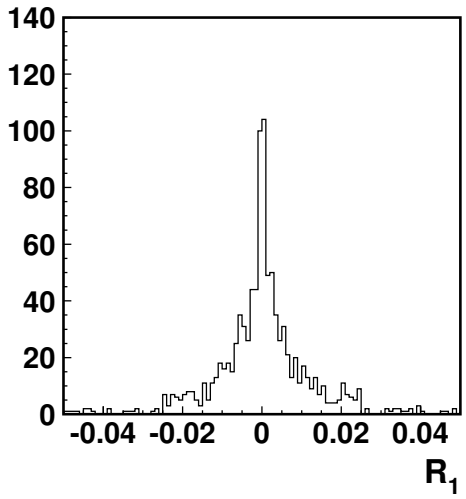

Figure 4.9: *Typical distribution of simulated values for R_N. Here, R_N is shown for $N = 1$ (with $f_N(|\boldsymbol{P_{h\perp}}|) = 1$ for all N), corresponding to the amplitude proportional to* $\sin(2\phi_h - \phi_R - \phi_S)$*. The distribution contains 1000 entries, corresponding to the amount of simulations that were performed in order to estimate the uncertainty due to the incomplete integration of the cross section over ϕ_h (see text). All other distributions R_N (N=2,3,...) are of similar shape.*

that, given the general expression for the amplitudes of Eq. 4.24, only a few amplitudes can be of the same order of magnitude as $A_{UT}^{\sin(\phi_{R\perp}+\phi_S)\sin\theta}$ [6].

In order to estimate the systematic uncertainty, the amplitude $A_{UT}^{\sin(\phi_{R\perp}+\phi_S)\sin\theta}$ was extracted from the same simulated data set 1000 times, but each time with different values for α_N, β_N and R_N for each of the ϕ_h-dependent terms. The obtained distribution was compared with a distribution of extracted amplitudes, for which only $A_{UT}^{\sin(\phi_{R\perp}+\phi_S)\sin\theta}$ was implemented. The results are shown for four x bins in Fig. 4.10. As can be seen the influence of the ϕ_h-dependent terms on the extracted amplitude is very small.

In Table 4.3 and 4.4 the results of this study are given for approach I and II for the binning in $M_{\pi\pi}$, z, and x. The tables list the averages of the simulated distribution of $A_{UT}^{\sin(\phi_{R\perp}+\phi_S)\sin\theta}$ values ($\langle a\rangle$ and $\langle a'\rangle$), their widths (σ and σ'), the ratios of those widths and the averages of the calculated statistical uncertainty ($\langle\Delta a\rangle$, cf. Eq. 4.16). The latter should be equal to σ.

The averages $\langle a\rangle$ and $\langle a'\rangle$ are equal within the statistical uncertainty ($\frac{\sigma}{\sqrt{N}}$), which is small compared to the statistical uncertainty on a itself (Δa). Within approach I, also the widths of the distributions are equal within the statistical uncertainty. Within approach II, σ' is on average 10% larger than σ. Compared to the systematic effect discussed in the previous section, and compared to the statistical uncertainty, this is a small effect, since it inflates the statistical uncertainty on the amplitude (which is not small) by only 10%.

[6] To allow for more nonzero ϕ_h-dependent amplitudes, in this study the implemented amplitude $A_{UT}^{\sin(\phi_{R\perp}+\phi_S)\sin\theta}$ was scaled down by a factor 0.4 to make it comparable to the data.

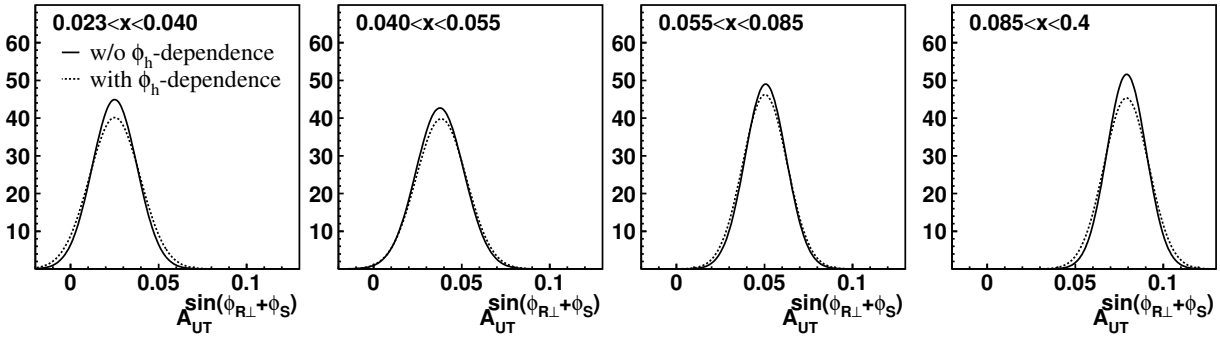

Figure 4.10: *Gaussian fits to the distributions of simulated values of $A_{UT}^{\sin(\phi_{R\perp}+\phi_S)}$ without (solid histograms) and with (dashed histograms) a contribution of ϕ_h-dependent terms to A_{UT}. The distributions themselves are not shown in order to be able to distinguish between the two fits. The reduced χ^2 values of the fits are in the range 0.50–1.1. The fits shown here, result from the simulations for which the ($|\boldsymbol{P}_{h\perp}|$) dependence according to Eqs. B.5 and B.6 was used (approach II). The different panels correspond to different x bins as indicated.*

4.5.4 Dependence on the polar angle θ

In the previous two sections, the θ dependence in the expression for A_{UT} was ignored. This is justified by the expressions for $A_{UT}^{\sin(\phi_{R\perp}+\phi_S)}$ given in Eqs 2.74 and 2.75, which indicate that this amplitude is sensitive to transversity through the fragmentation function $H_1^{\sphericalangle,sp}$ even if the numerator and the denominator of the asymmetry are first integrated over $\cos\theta$. However, as with the ϕ_h dependence, this holds only if one has a full acceptance coverage for this angle, which is not the case at HERMES. This can easily be understood if one realizes that the angle θ is defined in the center-of-mass system of the two pions (see Fig. 2.10). As a consequence this angle is directly related to the relative magnitude of the pion momenta. (For instance, the regions $\theta < \frac{\pi}{2}$ and $\theta > \frac{\pi}{2}$ correspond to $|\boldsymbol{P_1}|/|\boldsymbol{P_2}| > 1$ and $|\boldsymbol{P_1}|/|\boldsymbol{P_2}| < 1$, respectively.) As the HERMES spectrometer can only identify pions with momenta larger than 1 GeV (see Sec. 3.2.2), the acceptance coverage at HERMES for the angle θ is incomplete. In Fig. 4.11 the θ distribution is shown for various lower limits on the pion momentum as obtained from a Monte-Carlo simulation. (It is noted that the same Monte-Carlo simulation is used that was shown to be in agreement with the data in Fig. 4.5.) Fig. 4.11 shows that indeed the θ distribution is highly sensitive to this lower limit [7]. Therefore,

[7] It should be noted that the incomplete acceptance coverage for the angle θ is not a specific draw-back of the HERMES spectrometer. In general, existing spectrometers have a lower limit larger than zero for the pion momentum, which affects the acceptance coverage for the angle θ. This is typically due to the nonzero material budget of any detector, the geometrical acceptance for low-momentum pions and/or the momentum acceptance of particle identification detectors. The COMPASS spectrometer, e.g., can only identify pions with momenta larger than 2 GeV [77].

	$\langle a \rangle$	$\langle a' \rangle$	$\langle a \rangle / \langle a' \rangle$	σ	σ'	σ'/σ	$\langle \Delta a \rangle$
$0.250 < M_{\pi\pi} < 0.400$	0.0346	0.0346	1.00	0.0095	0.0094	0.98 ± 0.04	0.0093
$0.400 < M_{\pi\pi} < 0.550$	0.0502	0.0506	0.99	0.0077	0.0085	1.10 ± 0.04	0.0085
$0.550 < M_{\pi\pi} < 0.770$	0.0494	0.0498	0.99	0.0085	0.0087	1.02 ± 0.04	0.0087
$0.770 < M_{\pi\pi} < 2.00$	0.0382	0.0386	0.99	0.0105	0.0102	0.97 ± 0.03	0.0102
$0.100 < z < 0.340$	0.0375	0.0375	1.00	0.0115	0.0115	0.99 ± 0.04	0.0119
$0.340 < z < 0.440$	0.0474	0.0465	1.02	0.0127	0.0127	1.00 ± 0.04	0.0125
$0.440 < z < 0.560$	0.0558	0.0534	1.04	0.0125	0.0127	1.02 ± 0.04	0.0133
$0.560 < z < 1.000$	0.0653	0.0639	1.02	0.0135	0.0137	1.02 ± 0.04	0.0137
$0.023 < x < 0.040$	0.0246	0.0251	0.98	0.0123	0.0126	1.02 ± 0.04	0.0132
$0.040 < x < 0.055$	0.0383	0.0380	1.01	0.0138	0.0134	0.97 ± 0.04	0.0138
$0.055 < x < 0.085$	0.0498	0.0502	0.99	0.0120	0.0123	1.02 ± 0.04	0.0124
$0.085 < x < 0.400$	0.0790	0.0791	1.00	0.0117	0.0116	0.99 ± 0.04	0.0120

Table 4.3: *Results of the study of the possible influence of the ϕ_h-dependent terms within the HERMES acceptance, within the assumptions of approach I (see text). Here $\langle a \rangle$ ($\langle a' \rangle$) is the average of the distribution of extracted values of $A_{UT}^{\sin(\phi_{R\perp}+\phi_S)\sin\theta}$ without (with) the implementation of such terms, σ (σ') is the corresponding width of this distribution and $\langle \Delta a \rangle$ is the calculated average uncertainty on a.*

when the numerator and the denominator of the asymmetry A_{UT} are integrated over θ within the HERMES acceptance, one can still get contributions from all terms in Eqs. 2.68 and 2.69, in contrast to Eq. 2.72, which is valid for a detector with a complete acceptance for the angle θ. According to the boundaries given in Ref. [106], the fragmentation functions D_1^{sp} and $D_{1,ll}^{pp}$, which appear in Eq. 2.69, can be of the same order of magnitude as D_1.

The effect of these θ-dependent terms can be quite large as is shown in Fig 4.12. The figure compares two distributions of $A_{UT}^{\sin(\phi_{R\perp}+\phi_S)\sin\theta}$ for which different θ dependencies were simulated, similar to what was presented in the previous section for the ϕ_h dependence. For the solid histogram, only the term of interest is included, i.e., the first term of Eq. 2.68, again according to the model prediction of Ref. [122]. For the dashed histogram, also the other terms in Eqs. 2.68 and 2.69 are included. The amplitude $A_{UT}^{\sin(\phi_{R\perp}+\phi_S)\sin 2\theta}$ related to the fragmentation function $H_1^{\sphericalangle,pp}$ was modeled as:

$$A_{UT}^{\sin(\phi_{R\perp}+\phi_S)\sin 2\theta} = C\, z^{\alpha}\, \frac{\sum_q e_q^2 h_1^q(x)}{\sum_q e_q^2 f_1^q(x)}, \tag{4.29}$$

where C was varied in accordance with all limits expressed by Eq. 4.28. The values of the

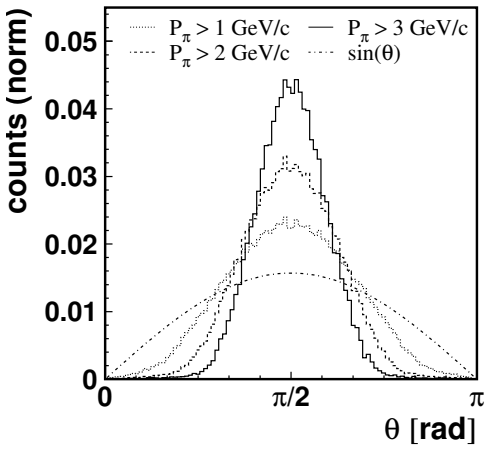

Figure 4.11: *Simulated histograms of the polar angle θ for different lower momentum cuts as indicated in the figure. The dash-dotted curve shows the distribution one would obtain if no θ-dependence is present in the data. Each histogram was normalized to unity.*

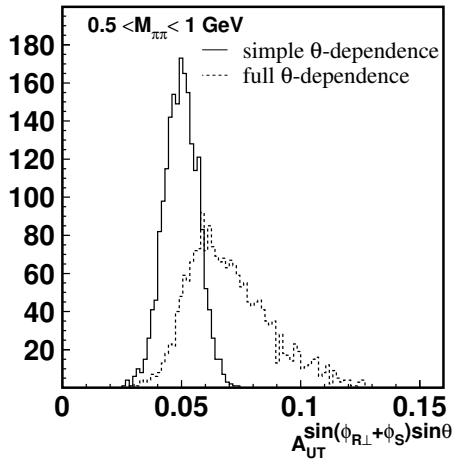

Figure 4.12: *Distributions of simulated values of $A_{UT}^{\sin(\phi_{R\perp}+\phi_S)\sin\theta}$ without (solid line) and with (dashed line) θ-dependent contributions of the fragmentation functions D_1^{sp}, D_1^{pp} and $H_1^{\sphericalangle,sp}$ to A_{UT}.*

	$\langle a \rangle$	$\langle a' \rangle$	$\langle a \rangle / \langle a' \rangle$	σ	σ'	σ'/σ	$\langle \Delta a \rangle$
$0.250 < M_{\pi\pi} < 0.400$	0.0344	0.0343	1.01	0.0097	0.0093	0.96 ± 0.04	0.0093
$0.400 < M_{\pi\pi} < 0.550$	0.0502	0.0505	0.99	0.0078	0.0095	1.22 ± 0.04	0.0085
$0.550 < M_{\pi\pi} < 0.770$	0.0496	0.0496	1.00	0.0083	0.0091	1.09 ± 0.04	0.0087
$0.770 < M_{\pi\pi} < 2.000$	0.0387	0.0386	1.00	0.0098	0.0107	1.09 ± 0.04	0.0102
$0.100 < z < 0.340$	0.0382	0.0367	1.04	0.0120	0.0112	0.94 ± 0.03	0.0119
$0.340 < z < 0.440$	0.0464	0.0473	0.98	0.0122	0.0132	1.08 ± 0.04	0.0125
$0.440 < z < 0.560$	0.0563	0.0550	1.02	0.0123	0.0142	1.15 ± 0.05	0.0133
$0.560 < z < 1.000$	0.0643	0.0651	0.99	0.0132	0.0149	1.13 ± 0.05	0.0137
$0.023 < x < 0.040$	0.0250	0.0251	1.00	0.0127	0.0144	1.14 ± 0.04	0.0132
$0.040 < x < 0.055$	0.0376	0.0383	0.98	0.0136	0.0143	1.05 ± 0.04	0.0138
$0.055 < x < 0.085$	0.0507	0.0503	1.01	0.0117	0.0126	1.08 ± 0.04	0.0124
$0.085 < x < 0.400$	0.0792	0.0791	1.00	0.0111	0.0127	1.14 ± 0.04	0.0120

Table 4.4: *Same as Table 4.3, but for approach II (see text).*

fragmentation functions D_1^{sp} and D_1^{pp} were varied randomly, within the following boundaries:

$$-\frac{3}{2} \leq D_1^{sp}/D_1 \leq \frac{3}{2}\,, \tag{4.30}$$

$$-1 \leq D_1^{pp}/D_1 \leq 2\,. \tag{4.31}$$

These boundaries are needed to ensure positivity of the cross section. Finally, for each chosen set of values a scan was made to ensure that they also satisfy the constraint $|A_{UT}| < 1$. The two histograms in Fig. 4.12 are obviously very different: not only is the dashed distribution much broader, it is also shifted.

As the possible influence of θ-dependent terms is large, it was decided not to account for it by assigning a systematic uncertainty to the extracted value of $A_{UT}^{\sin(\phi_{R\perp}+\phi_S)\sin\theta}$. Instead, the measured asymmetry is binned in θ as well as in $(\phi_{R\perp}+\phi_S)$ and the θ-dependent terms are taken into account in a two-dimensional χ^2 fit of the form:

$$A_{UT}(\phi_{R\perp}+\phi_S,\theta) = \sin(\phi_{R\perp}+\phi_S)\frac{a_1\sin\theta + a_2\sin(2\theta)}{1 + a_3\cos\theta + a_4\frac{1}{4}(3\cos^2\theta - 1)}\,, \tag{4.32}$$

where the a_i are free parameters of the fit and $a_1 \equiv A_{UT}^{\sin(\phi_{R\perp}+\phi_S)\sin\theta}$ and $a_2 \equiv A_{UT}^{\sin(\phi_{R\perp}+\phi_S)\sin 2\theta}$.

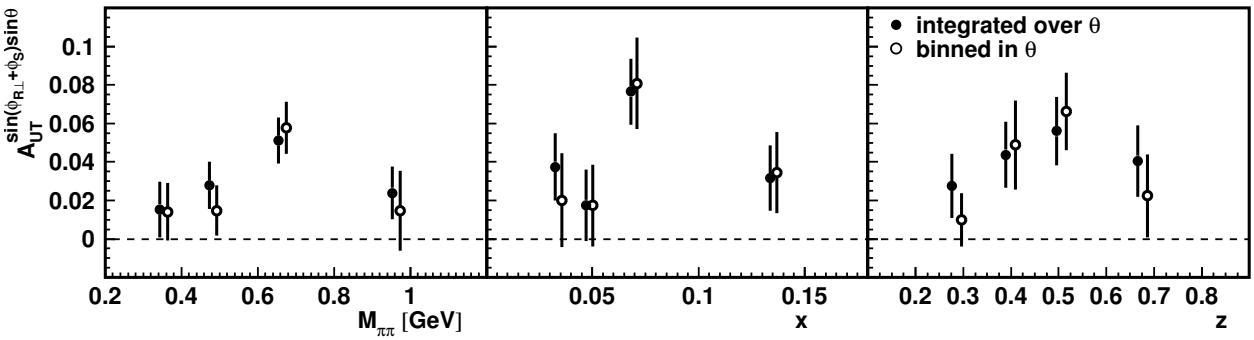

Figure 4.13: *The azimuthal amplitude $A_{UT}^{\sin(\phi_{R\perp}+\phi_S)\sin\theta}$ as a function of $M_{\pi\pi}$, x and z as extracted from the HERMES data collected in the years 2002–2004. The two results shown are based on the same data, but have used a different method to account for the θ dependence. For the closed symbols, the numerator and denominator of the asymmetry were integrated over θ; for the open symbols, the asymmetry was binned in θ and the fit function of Eq. 4.33 was used. The results of the latter method represent the main result of the present work, which is discussed in more detail in Chapter 5.*

Due to the extra number of free parameters in the fit, the statistical uncertainties increase compared to the method where one integrates over θ. In order to decrease the number of free parameters again, the binning in θ was antisymmetrized around $\theta = \pi/2$, such that one can use the following fit function:

$$A_{UT}(\phi_{R\perp}+\phi_S,\theta') = \sin(\phi_{R\perp}+\phi_S)\frac{a_1\sin\theta'}{1+a_4\frac{1}{4}(3\cos^2\theta'-1)}\,, \tag{4.33}$$

with θ' defined as $\theta' \equiv ||\theta-\pi/2|-\pi/2|$ in the range $\theta' \in [0,\frac{\pi}{2}]$. In this expression, all contributions to σ_{UU} and σ_{UT} that are odd with respect to $\theta = \pi/2$ cancel. The fit is performed using a nonequidistant binning in θ', as the θ distribution is strongly peaked around $\theta = \pi/2$. The bin boundaries are chosen such that each two-dimensional bin used in the fit contains approximately the same number of events. This has the advantage that one can use a finer binning where there are more events.

In Fig. 4.13, $A_{UT}^{\sin(\phi_{R\perp}+\phi_S)\sin\theta}$ is shown using both this method, as well as the method where the numerator and denominator of A_{UT} are integrated over θ. The resulting values are obtained from the present HERMES data. The data shown in this figure represent the main results of this thesis, which are discussed in more detail in Chapter 5, in particular regarding the interpretation of the data. The figure shows an inflation of the statistical uncertainty of the data for some of the points. The inflation strongly depends on the corresponding value of a_4, because the fitted values of a_1 and a_4 have correlation coefficients up to 0.9.

Since Eq. 4.33 represents a highly nonlinear function of θ, simulations have been performed to check if the fitting procedure extracts the correct value of $A_{UT}^{\sin(\phi_{R\perp}+\phi_S)\sin\theta}$ with the correct statistical uncertainty. The procedure works properly with sufficient statistics. If the event sample becomes too small, the fit has a tendency to end up at values of a_4 for which the denominator of Eq. 4.33 is zero. In this case, neither the extracted value nor the calculated uncertainties on a_1 and a_4

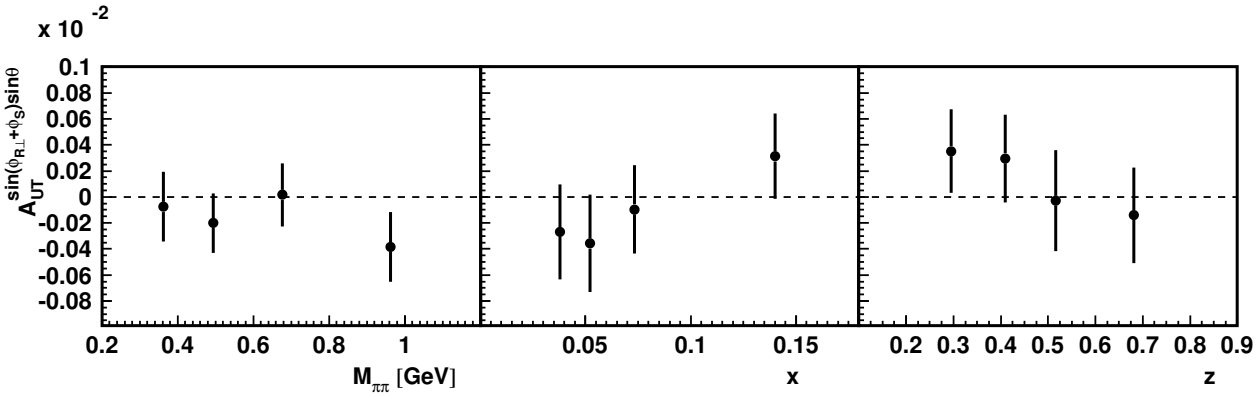

Figure 4.14: *Amplitudes $A_{UT}^{\sin(\phi_{R\perp}+\phi_S)\sin\theta}$ as a function of $M_{\pi\pi}$, x, and z, extracted from a Monte-Carlo data set without any target spin dependence implemented, i.e., $A_{UT} = 0$. The HERMES detector acceptance was taken into account in the simulation. Note the small vertical scale.*

are correct anymore. With the current data set, this limits the maximum number of bins to 4 corresponding to what has been shown in Fig. 4.13.

Note that a_2 in Eq. 4.32 is related to $h_1 H_1^{\sphericalangle,pp}$. As was mentiond in Sec. 2.3.4, both fragmentation functions $H_1^{\sphericalangle,sp}$ and $H_1^{\sphericalangle,pp}$ can be used to access transversity. However, from Eq. 4.32 it can be seen that $H_1^{\sphericalangle,pp}$ appears with a prefactor $\sin 2\theta$, whereas $H_1^{\sphericalangle,sp}$ appears with a prefactor $\sin\theta$. Because of the stronger θ dependence connected to $H_1^{\sphericalangle,pp}$, it is more difficult to isolate this term from a statistically limited data set. With a larger data set, the antisymmetrization leading to Eq.. 4.33 is not needed and the contributions related to $H_1^{\sphericalangle,sp}$ and $H_1^{\sphericalangle,pp}$ could have been extracted simultaneously.

4.5.5 Zero asymmetry test

In order to verify the validity of the developed extraction method, the amplitudes were extracted from Monte-Carlo data obtained from simulations where no target spin dependence was implemented, i.e., $A_{UT} = 0$ (but again taking into account the HERMES acceptance). The results are shown in Fig. 4.14. The extracted amplitudes are consistent with zero to within 0.04% (note the small scale on the y axis). For this test the fit parameter a_4 (see Eq. 4.33) was fixed to zero. These results also indicate that the limited detector acceptance of HERMES cannot generate nonzero asymmetries. The acceptance effects, as studied in Secs. 4.5.2–4.5.4, always occur due to a convolution of the limited detector acceptance with a truely nonzero asymmetry (cf. Eq. 4.19).

4.6 Systematic uncertainties

4.6.1 Angular resolution

The momenta and scattering angles of leptons and hadrons are determined in the HERMES spectrometer with a very good resolution, i.e., $\Delta p/p < 0.03$ and $\Delta\theta_{x/y} < 1.5$ mrad. The resolution of $\boldsymbol{k}$,

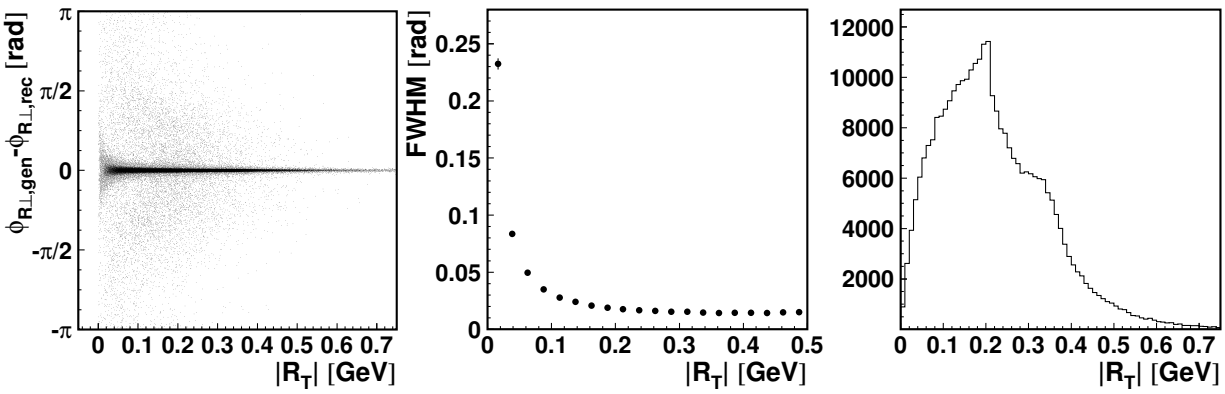

Figure 4.15: *Plots related to the study of the resolution of the angle $\phi_{R\perp}$. The plot on the left shows the difference $\Delta\phi_{R\perp} \equiv \phi_{R\perp,\mathrm{gen}} - \phi_{R\perp,\mathrm{rec}}$ between the azimuthal angle $\phi_{R\perp}$ for generated events ($\phi_{R\perp,\mathrm{gen}}$) and for reconstructed events ($\phi_{R\perp,\mathrm{rec}}$) versus $|\boldsymbol{R_T}|$, the middle plot shows the corresponding resolution of $\Delta\phi_{R\perp}$ and the plot on the right shows the event distribution versus $|\boldsymbol{R_T}|$. These plots were obtained using a Pythia Monte-Carlo simulation.*

representing the 27.5 GeV beam particle, is typically even better than this[8]. The resolution of the angles ϕ_S, $\phi_{R\perp}$ and θ that enter in the extraction of $A_{UT}^{\sin(\phi_{R\perp}+\phi_S)\sin\theta}$ are directly related to these resolutions, i.e., to the resolution of $\boldsymbol{k}$, $\boldsymbol{k'}$, $\boldsymbol{P_1}$ and $\boldsymbol{P_2}$ (see Eq. 2.8, Eq. 2.38 and Fig. 2.10, respectively). As a result, similarly good resolutions on ϕ_S and θ are obtained.

However, the azimuthal angle $\phi_{R\perp}$ is constructed from the vectors $\boldsymbol{k}$, $\boldsymbol{q}$ and $\boldsymbol{R_T}$ (Eq. 2.38), where the vector $\boldsymbol{R_T}$ is constructed from the *difference* $\boldsymbol{R}$ of the momenta of two detected pions (cf. Eqs. 2.33 and 2.36). The consequence is that the (relative) resolution of $|\boldsymbol{R_T}|$ increases with decreasing $|\boldsymbol{R_T}|$ (with $|\boldsymbol{R_T}| \equiv \sin\theta|\boldsymbol{R}| = \sin\theta\frac{1}{2}\sqrt{M_h^2 - 4m_\pi^2}$). Fig. 2.9 indicates that if $|\boldsymbol{R_T}|$ becomes small and the reduced resolution is large, the uncertainties on $\phi_{R\perp}$ are large[9]. This effect and the resulting effect on the extracted values of $A_{UT}^{\sin(\phi_{R\perp}+\phi_S)\sin\theta}$ were investigated, using a Pythia Monte-Carlo simulation (using the same production as was used for the studies described in Sec. 4.5).

In Fig. 4.15 the plot on the left shows the difference $\Delta\phi_{R\perp} = \phi_{R\perp,\mathrm{gen}} - \phi_{R\perp,\mathrm{rec}}$ versus $|\boldsymbol{R_T}|$. Here $\phi_{R\perp,\mathrm{gen}}$ is the true value of $\phi_{R\perp}$, constructed from events as they are *generated* from the Monte-Carlo simulation, and $\phi_{R\perp,\mathrm{rec}}$ is the value of $\phi_{R\perp}$ determined from events as they are *reconstructed* in the HERMES spectrometer, taking into account the detector resolution. The plot shows that the difference $\Delta\phi_{R\perp}$ reaches all possible values in the range from $\Delta\phi_{R\perp} = -\pi$ to $\Delta\phi_{R\perp} = \pi$, especially at low values of $|\boldsymbol{R_T}|$. The corresponding resolution was determined by fitting the $\Delta\phi_{R\perp}$ distribution with a Lorentz curve. The full-width at half-maximum (FWHM) obtained from the fit was used as an estimate for the resolution. The middle plot in Fig. 4.15 shows this resolution versus $|\boldsymbol{R_T}|$. It indicates very clearly that the resolution becomes worse at small $|\boldsymbol{R_T}|$ values.

[8] However, the installation of the transverse target magnet in 2001 slightly deteriorated this resolution.

[9] Analogously, the uncertainty on ϕ_h is strongly influenced by $|\boldsymbol{P_{h\perp}}|$.

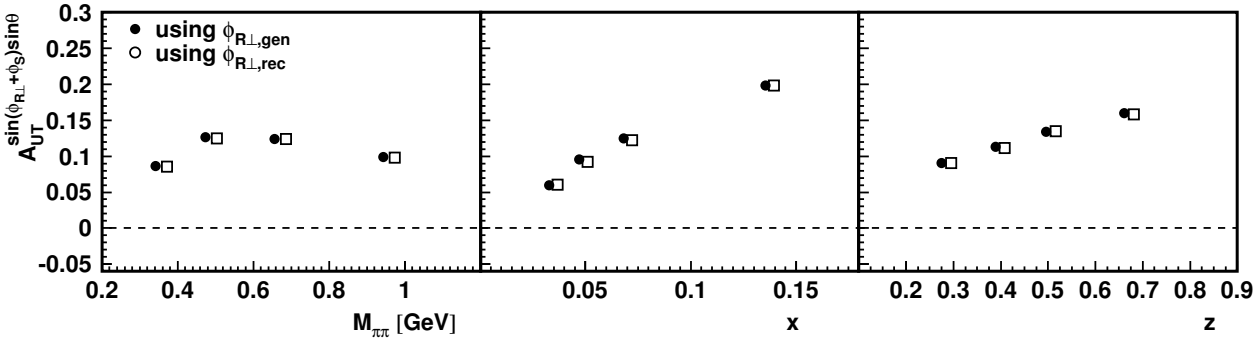

Figure 4.16: *Comparison of the value of the amplitudes $A_{UT}^{\sin(\phi_{R\perp}+\phi_S)\sin\theta}$ determined using either the generated Monte-Carlo events or the reconstructed Monte-Carlo events to calculate $\phi_{R\perp}$, i.e., using $\phi_{R\perp,\mathrm{gen}}$ or $\phi_{R\perp,\mathrm{rec}}$, respectively. The open symbols (based on $\phi_{R\perp,\mathrm{rec}}$) are shifted with respect to the closed symbols (based on $\phi_{R\perp,\mathrm{gen}}$) along the x-axis in order to be able to distinguish overlapping points.*

In principle, for the analysis one could decide to use only those events with $|\boldsymbol{R_T}| \gtrapprox 0.05$. The right plot in Fig. 4.15 shows the event distribution versus $|\boldsymbol{R_T}|$, which indicates that such an event selection would only have a minor effect on the total number of events. However, it was decided not to make such an additional event selection, as it directly effects the size of the extracted amplitude (cf. Eq. 2.72) in a nontrivial way, complicating a comparison to model predictions for the amplitude.

The influence of the relatively poor resolution of $\phi_{R\perp}$ at small values of $|\boldsymbol{R_T}|$ on $A_{UT}^{\sin(\phi_{R\perp}+\phi_S)\sin\theta}$ is automatically included in the study of the acceptance effects described in Sec. 4.5. However, in order to get an idea of the absolute magnitude of the effect on the extracted value of $A_{UT}^{\sin(\phi_{R\perp}+\phi_S)\sin\theta}$, this was studied separately as well using the same Monte-Carlo simulation and model for A_{UT} as described in Sec. 4.5.2. The amplitudes were extracted twice: first using $\phi_{R\perp,\mathrm{gen}}$ and then using $\phi_{R\perp,\mathrm{rec}}$. The difference between the extracted amplitudes of both methods can be used as an estimate of the systematic uncertainty introduced by the angular resolution of $\phi_{R\perp}$. The extracted values of $A_{UT}^{\sin(\phi_{R\perp}+\phi_S)\sin\theta}$ are shown in Fig. 4.16. The figure shows no significant systematic effect. Thus, any remnant systematic effect has to be smaller than the statistical uncertainty of this Monte-Carlo study, i.e., smaller than 0.001 (absolute).

4.6.2 Target magnet correction

The transverse target magnet has been installed in the year 2001. Before that time, the HERMES experiment was operated with a target magnet with its magnetic field oriented along the lepton beam. Because of its orientation, the effect of the magnetic field on the 3-momentum of both the beam leptons and the detected particles was negligibly small. However, for the transverse target magnet, this effect is much larger as the magnetic deflections of the particles are in a direction which is mostly transverse with respect to their direction of motion. For the analysis one needs to know the track parameters (the polar angle θ, the azimuthal angle ϕ, the position and the mo-

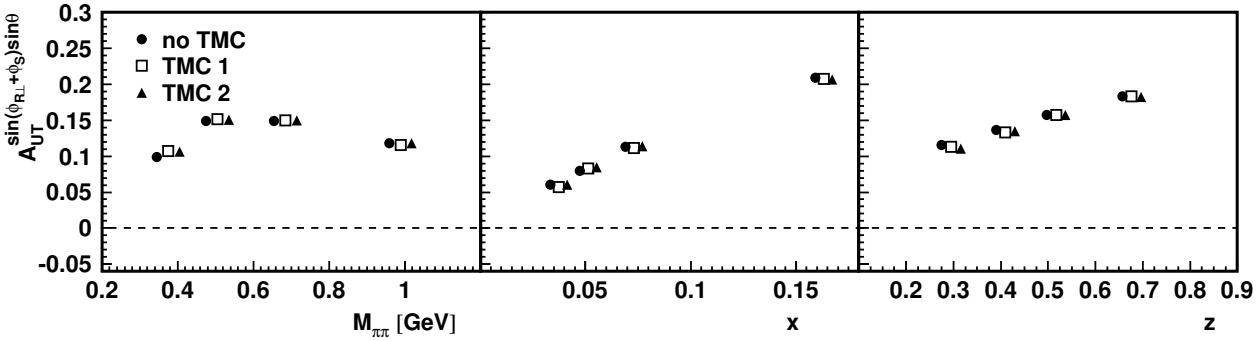

Figure 4.17: *Comparison of the azimuthal amplitudes $A_{UT}^{\sin(\phi_{R\perp}+\phi_S)\sin\theta}$ as a function of $M_{\pi\pi}$, x and z using two different methods (TMC-1 and TMC-2, see text) to correct for the effect of the target magnet. Also shown are the extracted amplitudes in case no correction is made for the effect of the target magnet at all. The statistical uncertainties of these simulated results are smaller than the symbol size.*

mentum) of each track at the interaction point, i.e., before the tracks are deflected by the magnetic field of the target magnet. These track parameters can be calculated from the measurements using either of two algorithms. The first algorithm, Target Magnet Correction 1 (TMC-1), calculates the trajectories through the magnetic field for a set of reference particles, of which the track parameters at the interaction point are varied. Using these reference tracks a mapping file is created that relates the track parameters at the interaction point to the track positions in the DVC and FC2 (see Fig. 3.3). These drift chambers are outside the range where the magnetic field of the target magnet deflects the tracks. The second algorithm, Target Magnet Correction 2 (TMC-2), also calculates a set of reference tracks. It is assumed that a measured track, close to a reference track at the DVC and FC2, is also close to the reference track at the interaction point. The difference between the reference track and the actual track at the interaction point can be related to the difference between the reference track and the actual track at the DVC and FC2 by a Taylor series expansion. The coefficients of this expansion are calculated using the reference tracks. A detailed description and comparison of both methods is given in Ref. [177].

The corrections to the track parameters, calculated by TMC-1/2, directly influence the kinematic variables that the asymmetry A_{UT} depends on. To investigate the influence of the correction to the extracted value of the amplitude $A_{UT}^{\sin(\phi_{R\perp}+\phi_S)\sin\theta}$ a Monte-Carlo simulation was performed. A comparison was made between the extracted value of $A_{UT}^{\sin(\phi_{R\perp}+\phi_S)\sin\theta}$ either without applying a target magnet correction or with the use of TMC-1 or TMC-2. For this study, the DIS Monte-Carlo simulation was used with the same model for A_{UT} that was described in Sec. 4.5.2. The results, shown in Fig. 4.17, indicate that the effect of the target magnet correction on $A_{UT}^{\sin(\phi_{R\perp}+\phi_S)\sin\theta}$ is very small, a statistically significant influence is only observed for the lowest $M_{\pi\pi}$ bin and the the lowest z bin. The difference between the results obtained using either TMC-1 or TMC-2 can be used as an estimate for a possible systematic effect related to the correction method. As the results obtained using the two correction methods are consistent within the statistical uncertainty, any such effect has to be smaller than 0.002 (absolute).

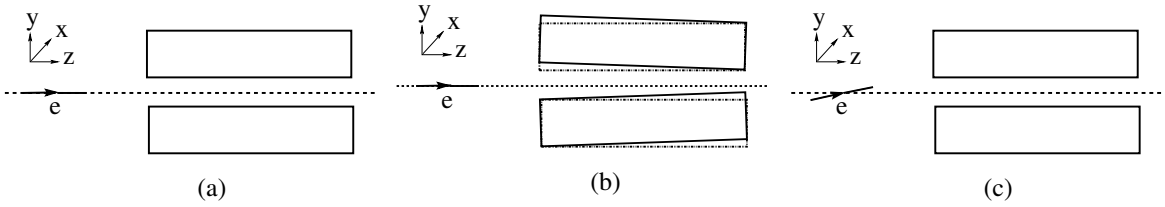

Figure 4.18: *Schematic picture of the misalignment of the spectrometer and of the beam: (a) the spectrometer and the beam in their ideal places; (b) misalignment of the two spectrometer halves; (c) misalignment of the beam.*

2002–2004	x-slope (mrad)	y-slope (mrad)	x-offset (cm)	y-offset (cm)
top spectrometer	-0.18	-0.62	0.30	-0.08
bottom spectrometer	-0.42	0.49	0.29	0.11
positron beam	-0.035	-0.42	0.0165	0.16

Table 4.5: *The measured misalignment of the spectrometer [178] and the beam [179] during the years 2002-2004, with respect to the alignment used in the track reconstruction code.*

4.6.3 Misalignment of the detector and of the beam

Another possible source of systematic uncertainties is a misalignment of the HERMES spectrometer or of the HERA beam. The alignments of HERA and HERMES can change over the years. In case of the spectrometer, this happens for example due to maintenance on the detectors in shutdown periods during which the entire spectrometer is moved away from the beam position. In the case of the beam, this happens for example after a switch from using electrons to using positrons or vice versa. The misalignments are small. The translations (offsets) are typically fractions of centimeters and the rotations (slopes) fractions of millirads, both for the spectrometer halves and for the beam at the HERMES interaction point. For the period 2002–2004, these misalignments are given in Refs. [178, 179]. The results are listed in Table 4.5. Fig. 4.18 shows a schematic picture of the effect of these misalignments.

Because the spectrometer halves have alignments that are independent of each other, one cannot construct a relative alignment of the beam with respect to the spectrometer as a whole.

The effect of these misalignments is twofold. Firstly, these misalignments affect the size and shape of the HERMES acceptance. Secondly, the misalignments can affect all reconstructed kinematic variables, because they are not taken into account in the track reconstruction. In order to do this appropriately, the misalignment of all individual detectors and detector frames needs to be taken into account, but this information is not available. In principle, both these effects can influence the amplitude $A_{UT}^{\sin(\phi_{R\perp}+\phi_S)\sin\theta}$.

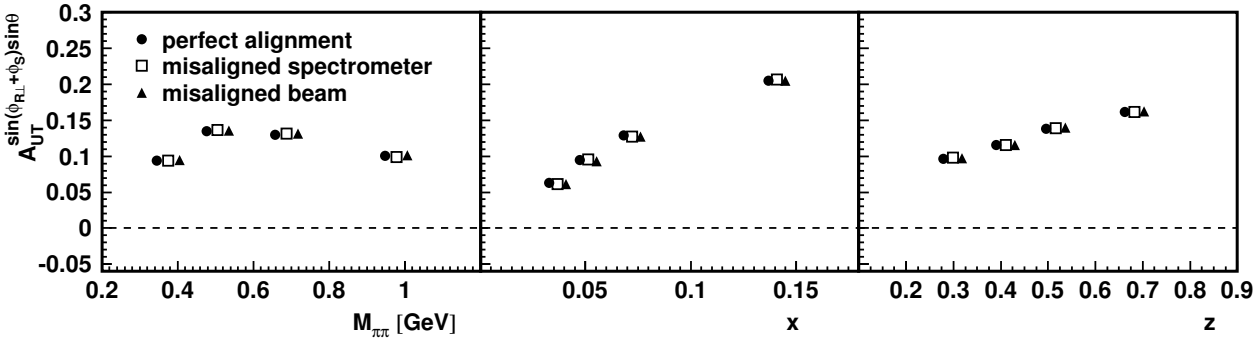

Figure 4.19: *Comparison of the amplitudes $A_{UT}^{\sin(\phi_{R\perp}+\phi_S)\sin\theta}$ as a function of $M_{\pi\pi}$, x and z extracted from simulations using either a perfectly aligned spectrometer and beam (solid circles), a misaligned spectrometer (open squares) or a misaligned beam (solid triangles). The differences are observed to be negligible.*

The effect of the spectrometer misalignment at HERMES was found to produce a $\cos\phi_h$ modulation in the hadron yield [180]. However, in Ref. [116] the resulting effect on the extracted Sivers and Collins amplitudes was investigated and found to be negligible. Also, in the analysis of beam-spin and beam-charge asymmetries in DVCS, both the effect of the spectrometer misalignment and the effect of the beam misalignment was found to be small [179]. Similar studies are repeated here as the effect is likely to be different depending on the type of process considered and quantity extracted.

In order to study the effect of the misalignments on the value of the amplitude $A_{UT}^{\sin(\phi_{R\perp}+\phi_S)\sin\theta}$ extracted from HERMES data, three different Pythia Monte-Carlo productions were used. One production was used where both the spectrometer and the beam are perfectly aligned, i.e., without any deviations with respect to their ideal positions. Secondly, another Monte-Carlo production was created where a misaligned spectrometer was used in the Monte-Carlo simulation according to the values given in Table 4.5. The third production takes into account the misalignment of the beam. For this production, only the x-slope θ_x and the y-slope θ_y were taken into account. This was done by using $\boldsymbol{k}/|\boldsymbol{k}| = (\sin\theta_x, \sin\theta_y, \sqrt{1-\sin^2\theta_x-\sin^2\theta_y})$ instead of $\boldsymbol{k}/|\boldsymbol{k}| = (0,0,1)$ for the beam momentum $\boldsymbol{k}$, which influences most of the kinematic variables that the amplitude depends on. For all three productions, the same model for the asymmetry A_{UT} was implemented as was discussed in the previous sections.

The results of the three simulations are shown in Fig. 4.19 and are consistent within the statistical uncertainty. In fact, according to the present simulations any systematic effect due to misalignment of the spectrometer or the beam on the extracted amplitudes has to be smaller than 0.002 (absolute).

4.6.4 Hadron misidentification

In general, pions are identified by the RICH detector with high efficiency and low contaminations from other particle types by requiring that the RICH quality parameter is larger than zero ($rQp > 0$,

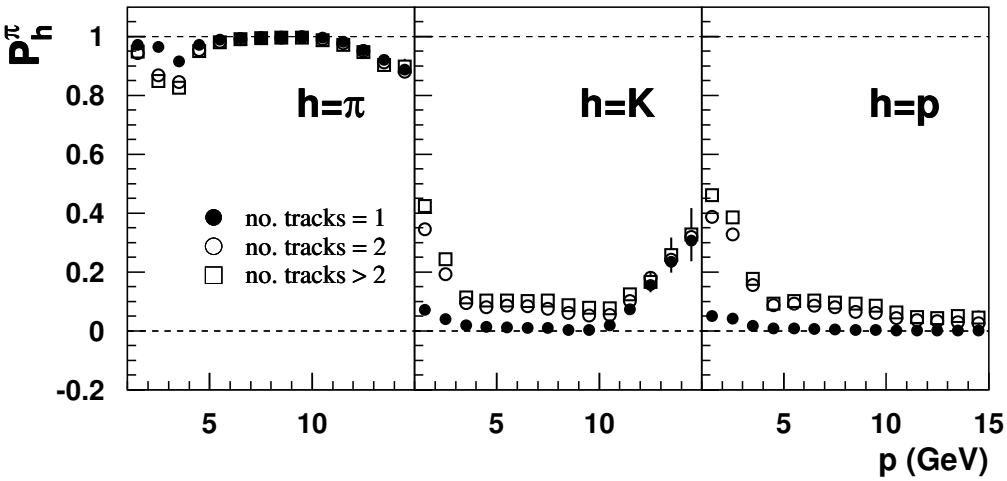

Figure 4.20: *The probabilities that the RICH detector identifies a pion as a pion (left plot), a kaon as a pion (middle plot) or a proton as a pion (right plot). The probabilities are given as a function of the track momentum p and they are shown separately for the situation where either one, two or three tracks were detected at the same time in one detector half. These numbers were obtained using a MC simulation.*

cf. Sec. 4.2.2). In the left plot of Fig. 4.20, the efficiency of *single*-pion identification is shown, i.e., the probability P_π^π that a pion is also identified as a pion by the RICH detector. These numbers were obtained from a Monte-Carlo simulation of the detector. The momentum dependence of this probability is directly related to the momentum dependence of the Cerenkov angle Θ_c shown in Fig. 3.5. The probabilities are given separately for the situation that one, two or more than two tracks are detected per detector half. As can be seen in the figure, a larger number of tracks per detector half results in a lower efficiency. This is caused by the increased difficulty of reconstructing the Cerenkov angle when the Cerenkov cones of different particles are overlapping at the position of the photomultiplier tubes in the RICH detector.

The other two plots in Fig. 4.20 give the probabilities P_K^π and P_p^π that a kaon or a proton is misidentified as a pion, respectively. But, whereas the identification efficiency is purely a detector property given by P_π^π, the contamination of the pion sample by kaons or protons is a combination of P_K^π and P_p^π together with their relative flux with respect to the pion flux. Thus, unlike the efficiencies, the contaminations are process-type dependent.

In principle, the particle fluxes can be taken into account in Eq. 4.6 in order to arrive at a flux-corrected ratio of probabilities, similar to the role of the flux factor in Eq. 4.2 for lepton-hadron separation. However, the calculation of a correction for the particle fluxes is more involved in this case, as there may be cross contaminations between the 3 particle types, instead of just cross contaminations between two particle types, i.e., leptons and hadrons. The proper evaluation of the correction for the particle fluxes requires the use of a so-called unfolding procedure [181]. In practice this is not feasible for the process considered here, for the following reason: In order to correctly take into account the contamination of the sample of $\pi^+\pi^-$ pairs by kaons and (anti)protons, one needs to be able to identify all hadrons. However, the RICH detector can identify pions above 1

GeV, while for kaons and (anti)protons, the identification only works for momenta above 2 GeV Selecting $\pi^+\pi^-$ pairs where both pions have momenta above 2 GeV instead of above 1 GeV would reduce the total event sample by 39%.

Alternatively, one could take into account the effect of hadron contamination on the azimuthal amplitude $A_{UT}^{\sin(\phi_{R\perp}+\phi_S)\sin\theta}$ using the target-polarized cross sections for the semi-inclusive production of π^+K^-, $\pi^+\bar{p}$, $K^+\pi^-$, $p\pi^-$, $p\bar{p}$, K^+K^-, pK^- and $K^+\bar{p}$ pairs. However, these cross sections are unknown, i.e., they have not been measured by any experiment and no model predictions exist for them. Note that these processes do not necessarily act as a dilution of the measured asymmetry. For instance, πK production close to the K^{*0} resonance (m = 896 MeV) and KK production close to the ϕ resonance (m = 1019 MeV) are also considered as possible candidates to measure transversity [118]. The convolution of transversity with the fragmentation functions for these processes contributes to the transverse-target-spin asymmetry through the same angular dependence as for $\pi^+\pi^-$ production.

Instead of adopting an unfolding procedure, the contamination C_h of misidentified hadron pairs in the sample of identified $\pi^+\pi^-$ pairs is calculated and this number is used to estimate a contribution to the systematic uncertainty of the final result. Using the probabilities shown in Fig. 4.20, the number $I_{\pi^+\pi^-}$ of identified pion pairs can be related to the true number $N_{h^+h^-}$ of detected hadron pairs by

$$\begin{aligned} I_{\pi^+\pi^-}(p_1,p_2) &\approx (P_\pi^\pi)^2 N_{\pi^+\pi^-}(p_1,p_2) \\ &+ \sum_{h=K^-,\bar{p}} P_\pi^\pi P_h^\pi N_{\pi^+h}(p_1,p_2) + \sum_{h=K^+,p} P_\pi^\pi P_h^\pi N_{h\pi^-}(p_1,p_2). \end{aligned} \tag{4.34}$$

The efficiency with which $\pi^+\pi^-$ pairs are identified can be written as $\epsilon = (P_\pi^\pi)^2$, and the contamination C_h can be written as

$$C_h(p_1,p_2) = \frac{\sum_{h=K^-,\bar{p}} P_\pi^\pi P_h^\pi N_{\pi^+h}(p_1,p_2) + \sum_{h=K^+,p} P_\pi^\pi P_h^\pi N_{h\pi^-}(p_1,p_2)}{I_{\pi^+\pi^-}(p_1,p_2)}. \tag{4.35}$$

In these equations, the contribution from pairs where both pions are misidentified is not taken into account as their incident flux is relatively small (see Table 4.6) and they enter with small misidentification probabilities. Because the true yields $N_{h^+h^-}$ are unknown, the calculation of the contamination assumes that $N_{h^+h^-} = I_{h^+h^-}$. In this way the efficiency is estimated to be larger than 0.72 and the efficiency[10] averaged over the entire event sample is $\langle\epsilon\rangle = 0.85$. The contamination, using Eq. 4.35 is always smaller than 0.11, and $\langle c\rangle = 0.06$.

The contribution of the contamination to the measured asymmetry can be easily calculated using

$$A_{UT} = A_{UT}^{\pi^+\pi^-}(0.94 + 0.06\, A_{UT}^X / A_{UT}^{\pi^+\pi^-}), \tag{4.36}$$

[10]Note that although the efficiency itself is process type independent, the efficiency averaged over the event sample strongly depends on the considered process type.

type	$\pi^+\pi^-$	π^+K^-	$\pi^+\bar{p}$	π^-K^+	π^-p	K^+K^-	$K^+\bar{p}$	K^-p	$p\bar{p}$
number of events	108919	9558	3114	14473	8056	3860	930	1377	1101
fraction of the total (%)	71.9	6.3	2.1	9.6	5.3	2.5	0.6	0.9	0.7

Table 4.6: *Number of identified hadron pairs (second row) as identified according to the information provided by the RICH detector. For each possible combination the number of pairs is also listed as the fraction with respect to the total number of identified hadron pairs (third row), These hadrons (data) passed all semi-inclusive selections and for all identified hadrons it was required that $rQp > 0$.*

where A_{UT}^X represents the asymmetry for hadron pairs other than $\pi^+\pi^-$. If $|A_{UT}^X/A_{UT}^{\pi^+\pi^-}| \leq 2$, then this leads to an estimate of the (asymmetric) systematic uncertainty of $[-6\%, +22\%]$ (relative) on the amplitude $A_{UT}^{\sin(\phi_{R\perp}+\phi_S)\sin\theta}$. This systematic uncertainty most likely gives an overestimate for this effect. An asymmetry originating from a different production channel than $\pi^+\pi^-$ is also expected to peak around the invariant mass of a resonance. As the calculated invariant mass for the hadron pairs containing misidentified hadrons is wrong, such an asymmetry will be smeared over a large invariant mass range within the sample of identified $\pi^+\pi^-$ pairs.

4.7 Summary

In this chapter it has been discussed how a high quality data sample containing $\pi^+\pi^-$ semi-inclusive DIS events has been selected from measurements performed by the HERMES collaboration during the years 2002–2004. Subsequently it has been discussed how the transverse single-spin asymmetry A_{UT} and its azimuthal amplitude $A_{UT}^{\sin(\phi_{R\perp}+\phi_S)\sin\theta}$ have been extracted from this data sample. The main part of the chapter has been devoted to discussing possible systematic effects that can influence the extracted value of the amplitude and its margin of uncertainty. All contributions to the total systematic uncertainty discussed in this chapter are listed in Table 4.7. Almost all of these contributions depend on the model used for A_{UT}. In particular, the estimated systematic uncertainty associated with acceptance effects is strongly model dependent. Also, the estimate of the systematic uncertainty due to hadron misidentification by the RICH detector is directly related to the assumption on the size of the asymmetry for misidentified hadron pairs. The latter two systematic effects give the main contributions to the total systematic uncertainty. The only systematic uncertainty that is independent of model predictions for A_{UT} is the scale uncertainty coming from the target polarization P_T. The final results for the azimuthal amplitude $A_{UT}^{\sin(\phi_{R\perp}+\phi_S)\sin\theta}$ are given in Fig. 4.13 (open symbols). In the next chapter these results are discussed and interpreted in detail.

source of uncertainty	reference section	size [lower limit, upper limit]
acceptance effects (1)	Sec. 4.5.2	$[0\%, \leq 44\%]$ (relative)
acceptance effects (2)	Sec. 4.5.3	$[-0.01, 0.01]$ (absolute)
RICH hadron misidentification	Sec. 4.6.4	$[-6\%, 22\%]$ (relative)
spectrometer/beam misalignment	Sec. 4.6.3	$[-0.002, 0.002]$ (absolute)
target-magnet correction	Sec. 4.6.2	$[-0.002, 0.002]$ (absolute)
angle resolution	Sec. 4.6.1	$[-0.001, 0.001]$ (absolute)
uncertainty on P_T	Sec. 3.1	$[-6.6\%, 6.6\%]$ (relative)

Table 4.7: *Size of systematic uncertainties on the azimuthal amplitude $A_{UT}^{\sin(\phi_{R\perp}+\phi_S)\sin\theta}$ for all investigated sources. The actual size of the systematic uncertainties depend on the kinematics and is properly shown in the corresponding figures, in the sections indicated in the second column.*

5

Results

As was discussed extensively in Chapter 2, semi-inclusive deep-inelastic scattering off a transversely polarized hydrogen target, producing two oppositely charged pions has been proposed [83, 84] as one of the most promising probes to study the transversity distribution function. The HERMES collaboration is the first ever to study this process and the results are presented in the present work. The observable $A_{UT}^{\sin(\phi_{R\perp}+\phi_S)\sin\theta}$ has been extracted from HERMES measurements using an analysis chain that was described in the previous chapter. In this chapter these results are discussed.

The results are presented in Sec. 5.1, and compared to model predictions in Sec. 5.2. In Sec. 5.3, the present results, which were obtained on a transversely polarized hydrogen target, are compared with earlier results, where transversity was studied through two-hadron fragmentation using a *longitudinally* polarized deuterium target [182]. In Sec. 5.4, preliminary results are discussed from the COMPASS collaboration for two-hadron fragmentation using a transversely polarized LiD target [77], after which the chapter ends with conclusions and an outlook in Sec. 5.5.

5.1 Discussion of results

The values of $A_{UT}^{\sin(\phi_{R\perp}+\phi_S)\sin\theta}$ extracted from measurements performed in the years 2002-2004 by the HERMES collaboration are presented in Fig. 5.1. The figure shows the $M_{\pi\pi}$ dependence, as well as the x, and z dependence of the amplitude. Excluding the dependencies considered in the

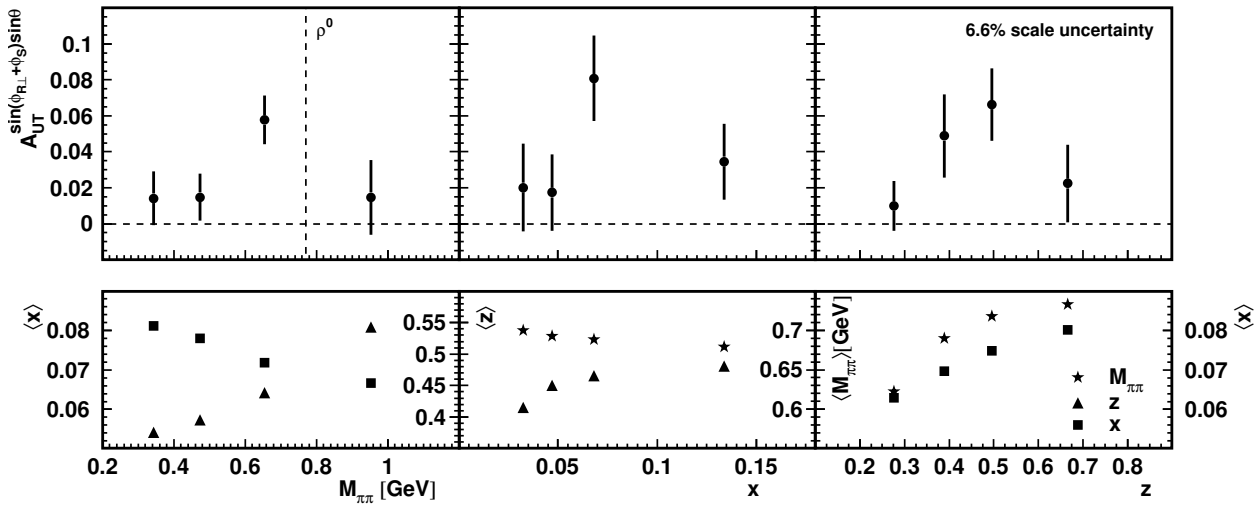

Figure 5.1: *The top panels show the experimental values of* $A_{UT}^{\sin(\phi_{R\perp}+\phi_S)\sin\theta}$ *versus* $M_{\pi\pi}$*, x, and z (which are the same as the open symbols in Fig. 4.13). The bottom panels show the average values of the variables that were integrated over. For the dependence on x and z,* $M_{\pi\pi}$ *was constrained to the range* $0.5 < M_{\pi\pi} < 1.0$ *GeV. The bin boundaries for the* $M_{\pi\pi}$ *dependence are at 0.25, 0.40. 0.55, 0.77, and 2.0 GeV, for x at 0.023, 0.04, 0.055, 0.085, and 0.4, and for z at 0, 0.34, 0.44, 0.56, and 1.0. The error bars represent the statistical uncertainty only. A relative scale uncertainty of 6.6% arises from the uncertainty in the target polarization.*

figure, the amplitude is integrated over all other variables it depends on. Thus, for example for the invariant mass dependence shown on the left, the amplitude is integrated over x, y, and z (actually, as mentioned before, the numerator and the denominator of the asymmetry, from which the amplitude is extracted, are integrated separately over these variables). The results presented in Fig. 5.1 differ from those presented in Refs. [183, 184] where the dihadron fragmentation functions D_1^{sp} and D_1^{pp} in the denominator were ignored in the extraction of the amplitude, i.e., they were assumed to be equal to zero. However, the differences between the results obtained with either method are small with respect to the statistical uncertainties.

The error bars in Fig. 5.1 represent the statistical uncertainties only. As most of the systematic uncertainties are highly model dependent, they are not shown in the figure. An overview of the possible influence of the various systematic effects is given in Table 4.7. Only the indicated 6.6% scale uncertainty, which is due to the uncertainty in the value of the target polarization, is independent of the models employed in the previous chapter. For the x and z dependencies the amplitude was considered in a slightly restricted range of the invariant mass, i.e., $0.5 < M_{\pi\pi} < 1.0$ GeV, in order to select the invariant mass region close to the mass of the ρ^0 (0.78 GeV; indicated in Fig. 5.1 by a dashed vertical line), where it is most likely that the amplitude could be nonzero. The bottom panels in Fig. 5.1 show the average values $\langle M_{\pi\pi} \rangle$, $\langle x \rangle$, and $\langle z \rangle$, corresponding to the data points shown in the top panels.

The values of the amplitude shown in the figure differ significantly from zero. In order to determine the significance of the data, the amplitude was extracted from events summed over the

entire experimental acceptance, i.e., $0.023 < x < 0.4$, $0.5 < M_{\pi\pi} < 1.0$ GeV and $0 < z < 1$. The mean values of the kinematic variables corresponding to this kinematic region are $\langle x \rangle = 0.07$, $\langle y \rangle = 0.64$, $\langle Q^2 \rangle = 2.35$ GeV^2, $\langle z \rangle = 0.43$, and $\langle |\boldsymbol{P}_{h\perp}| \rangle = 0.42$ GeV. The extracted mean value of $A_{UT}^{\sin(\phi_{R\perp}+\phi_S)\sin\theta}$ is 0.043 ± 0.012 (stat.). Thus, the amplitude in this range deviates by more than 3 σ from zero. If, instead of the mean value, the normalized integral of the data shown in Fig. 5.1 is computed, one also obtains values that are 3–4 σ above zero.

This result implies that both the transversity distribution function h_1 and the two-hadron fragmentation function $H_1^{\sphericalangle,sp}$ are very likely to be nonzero, and therefore that semi-inclusive production of oppositely charged pions on a transversely polarized hydrogen target can be used, in combination with an independent measurement of $H_1^{\sphericalangle,sp}$, to extract transversity. There exists already some evidence that the transversity distribution could be nonzero (see Chapter 2), but the present measurements provide the first indication ever that the two-hadron fragmentation function $H_1^{\sphericalangle,sp}$ is nonzero as well (at the 3–4 σ level).

The dependence of the amplitude $A_{UT}^{\sin(\phi_{R\perp}+\phi_S)\sin\theta}$ on x shown in Fig. 5.1 can be directly related to the x dependence of the two distribution functions involved, $h_1(x)$ and $f_1(x)$ (see Eq. 2.72). On the other hand, the dependence of the amplitude on $M_{\pi\pi}$ and z can be directly related to the $M_{\pi\pi}$ and z dependence of the dihadron fragmentation functions $H_1^{\sphericalangle,sp}(z, M_{\pi\pi}^2)$ and $D_1(z, M_{\pi\pi}^2)$. These dependencies are discussed in some detail when discussing the model predictions in the following section (Sec. 5.2). It should be noted, though, that due to the limited HERMES spectrometer acceptance and the applied kinematic selections, the dependencies shown in Fig. 5.1 are correlated with each other, as indicated by the simultaneous dependencies on the other variables illustrated in the bottom panels of Fig. 5.1.

One aspect that the models for the fragmentation function $H_1^{\sphericalangle,sp}$ discussed in Sec. 2.7.3 have in common is that they all predict that this function could be nonzero in the vicinity of the ρ^0 mass. The relatively large value of the amplitude of the third data point in the top left panel in Fig. 5.1 provides support for this expectation. In order to explore a possible sensitivity to resonances, in Fig. 5.2 the invariant mass distribution is shown for the $\pi^+\pi^-$ semi-inclusive DIS events used in the present analysis, and compared to a Monte-Carlo simulation. The main resonances contributing to this spectrum are identified separately in the figure. The various resonances involved are the η (548 MeV), η' (958 MeV), K_s^0 (498 MeV), ρ^0 (776 MeV) and the ω (783 MeV) [185]. However, only the peaks corresponding to the ρ^0, the K_s^0 and the very small peak from the ω result from a decay process into a $\pi^+\pi^-$ pair (without producing any other decay products). Thus, only these peaks appear at the invariant masses corresponding to the nominal values given above. The peaks from the η, the η' and the broad peak of the ω around 500 MeV appear at lower values than their nominal values, because for these resonances the $\pi^+\pi^-$ pair represents only part of the decay products. From Fig. 5.2, it can be seen that the ρ^0 is the main resonance contributing in the invariant mass region corresponding to the third data point in the left top panel of Fig. 5.1, i.e., $0.55 < M_{\pi\pi} < 0.77$ GeV.

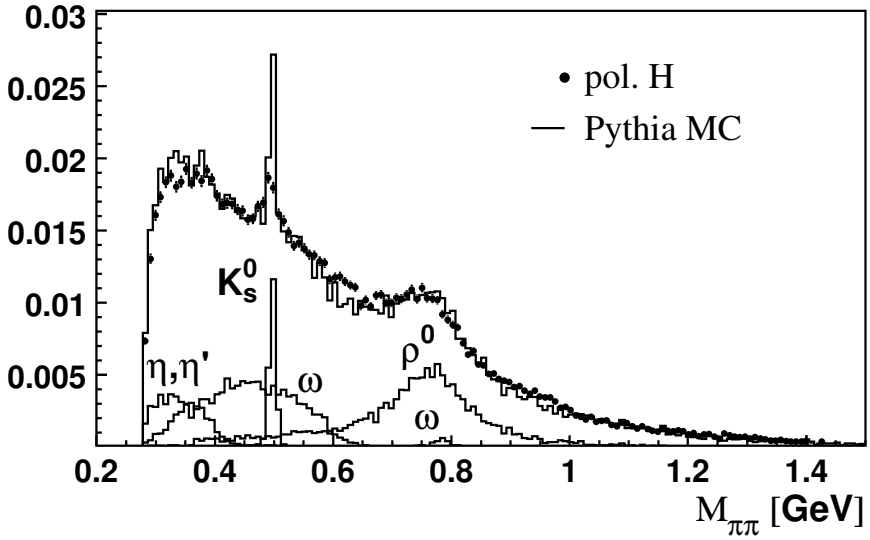

Figure 5.2: *Yield distribution (normalized to unity) of the invariant mass of the $\pi^+\pi^-$ pairs used in the present analysis (data points), compared to a Pythia Monte-Carlo simulation (histogram) taking into account the effect of the HERMES spectrometer acceptance. The contributions of the most important resonances in this invariant mass range are indicated separately as well.*

5.2 Comparison with model predictions

The model of Refs. [118, 119] predicts a sign change of the dihadron fragmentation function $H_1^{\sphericalangle,sp}$ approximately at the ρ^0 mass, and consequently that the amplitude $A_{UT}^{\sin(\phi_{R\perp}+\phi_S)\sin\theta}$ would show such a sign change as well (see Sec. 2.7.3 and Fig. 2.16(a)). Such a distinct prediction can easily be verified with high accuracy, even with the current amount of data for the invariant mass dependence of the amplitude and with the present uncertainties. This was done by fitting the following function to the data:

$$\begin{aligned} A_{UT}^{\sin(\phi_{R\perp}+\phi_S)\sin\theta}(M_{\pi\pi}) &= c\,\frac{|\boldsymbol{R}|}{M_{\pi\pi}}\sin\delta_0\sin\delta_1\sin(\delta_0-\delta_1), \\ &= c\,\sqrt{1-4\left(\frac{M_\pi}{M_{\pi\pi}}\right)^2}\sin\delta_0\sin\delta_1\sin(\delta_0-\delta_1), \end{aligned} \tag{5.1}$$

where δ_0 and δ_1 are $M_{\pi\pi}$ dependent phases of the pion pair in a relative s or p-wave, as introduced in Sec. 2.7.3. In order to obtain a practical description of the invariant-mass behavior of the fit function (Eq. 5.1), the phase factor $\sin\delta_0\sin\delta_1\sin(\delta_0-\delta_1)$ itself was first fitted with a function chosen to yield a smooth description of the data, shown in Fig. 5.3(a). The factor $|\boldsymbol{R}|/M_{\pi\pi}$ is taken along in the fit using Eq. 2.72 for the amplitude, and c is a free parameter in the fit, which reflects that in Refs. [118, 119] no prediction was given for the size or sign of the amplitude. It should be noted that this fit assumes that the phase factor is the only invariant-mass dependent part of the dihadron fragmentation function $H_1^{\sphericalangle,sp}$ (cf. Eq. 2.79). Also, the invariant-mass dependence of the unpolarized dihadron fragmentation function D_1 is ignored. However, it is not likely that these

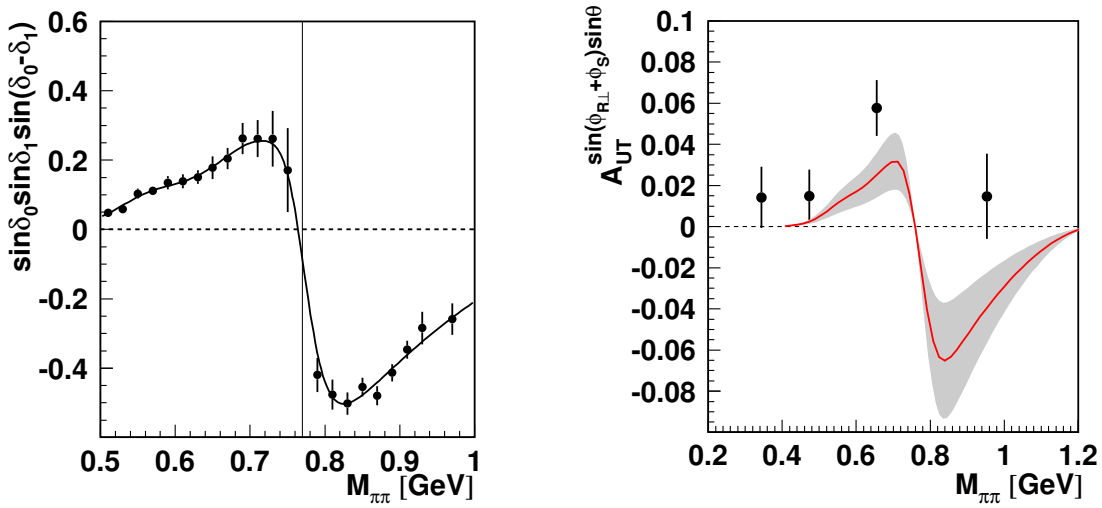

(a) (b)

Figure 5.3: *On the left, the quantity* $\sin\delta_0 \sin\delta_1 \sin(\delta_0 - \delta_1)$ *is shown, where the s- and p-wave phases* (δ_0 *and* δ_1*, respectively) were obtained from pion-nucleon scattering experiments [126]. This quantity represents the invariant mass dependence of* $H_1^{\sphericalangle,sp}(M_{\pi\pi}, z)$ *according to Ref. [118, 119]. The curve in the figure results from a fit to these data, where the shape of the function is chosen such that it smoothly describes the data. On the right, the invariant mass dependence of the amplitude* $A_{UT}^{\sin(\phi_{R\perp}+\phi_S)\sin\theta}$ *of the 2002-2004 HERMES data is shown. The figure includes the result of a fit to these data with the function given by Eq. 5.1. The shaded area indicates the uncertainty of the fit.*

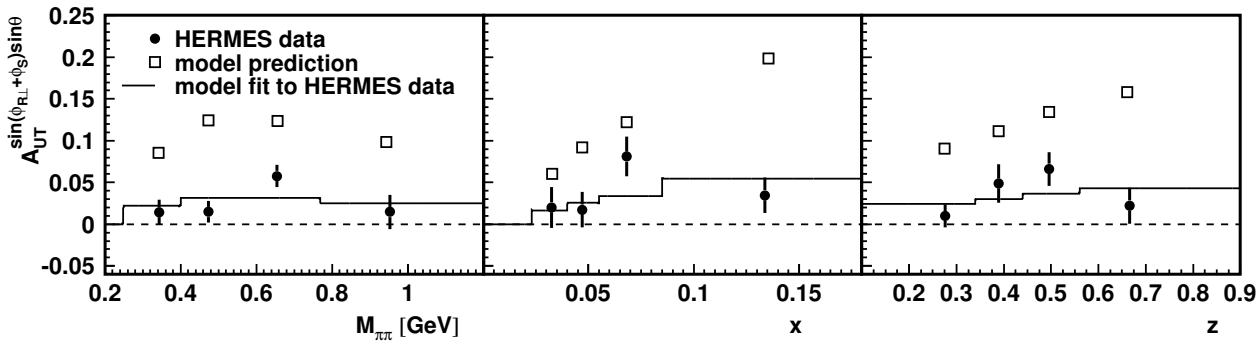

Figure 5.4: *The amplitude $A_{UT}^{\sin(\phi_{R\perp}+\phi_S)\sin\theta}$ as extracted from the HERMES data (closed symbols, which are identical to those shown in Fig. 5.1). Included is the prediction of Ref. [122], taking into account the HERMES acceptance using the Monte-Carlo simulation described in Sec. 4.5.2 (open symbols). Also shown is a fit of this model with a free scaling factor (solid line). The obtained values for this scaling factor are listed in Table 5.1*

simplifications influence the predicted sign change and therefore the use of the fit function given by Eq. 5.1 is well justified. The result of the fit is shown in Fig. 5.3(b). Because the phase factor is given for the invariant mass range $0.51 < M_{\pi\pi} < 0.97$ GeV, the data point of the lowest invariant mass was omitted from the fit and the fit function shown in Fig. 5.3(a) was extrapolated in order to include the full invariant mass range corresponding to the remaining three data points.

The fit (which takes into account possible nonlinear behavior within the bins according to Eq. 4.17) gives a χ^2/d.f. of 14.6/2, which excludes with high significance (with a probabilty $P > 0.999$) the predicted sign change of Refs. [118, 119].

The model of Ref. [122] gives a quantitative prediction for the full kinematic dependence of both dihadron fragmentation functions $H_1^{\sphericalangle,sp}$ and D_1 that are needed to calculate the amplitude $A_{UT}^{\sin(\phi_{R\perp}+\phi_S)\sin\theta}$ (see Sec. 2.7.3). As was discussed in Sec. 4.5.2, the best way this model can be compared to the data, is by evaluating the predicted amplitude with a Monte-Carlo simulation taking into account the detector acceptance. The result of such a comparison is shown in Fig. 5.4. In Ref. [122], a prediction for the amplitude evaluated at the kinematics of the HERMES experiment was given as well, which is shown in Fig. 2.18. The model shown in Fig. 2.18 and the (same) model evaluated in Fig. 5.4 differ in two ways. Most importantly, the prediction shown in Fig. 5.4 accounts for acceptance effects. Another difference is that the prediction shown here, takes into account the momentum requirement for the identified pions, $P > 1$ GeV, which was ignored for the amplitude shown in Fig. 2.18. In the Monte-Carlo simulation, for which the results are shown in Fig. 5.4, this requirement was taken into account, as it introduces correlations between kinematic variables, like y and z, and can therefore have a nontrivial influence on the amplitude. Note also that in Fig. 2.18 the amplitude $A_{UT}^{\sin(\phi_{R\perp}+\phi_S)}$ is shown, whereas Fig. 5.4 presents the amplitude $A_{UT}^{\sin(\phi_{R\perp}+\phi_S)\sin\theta}$, which differs by a factor $\pi/4$ according to Eq. 2.75 (within a 4π acceptance). For the amplitudes of Fig. 5.4, the model for the transversity distribution function of Ref. [117] was used, which corresponds to the dashed curve in Fig. 2.18.

dependence	scale factor	χ^2/d.f.
$M_{\pi\pi}$	0.25 ± 0.06	5.97/3
x	0.28 ± 0.08	5.01/3
z	0.27 ± 0.08	4.83/3

Table 5.1: *Results from fits of the model prediction of Ref. [122] as shown in Fig. 5.4 to the HERMES data. The only free parameter in these fits was an overall scale factor. These fits indicate that the shape of the model with respect to $M_{\pi\pi}$, x, and z describes the data well, but that the model overestimates the data by approximately a factor 4.*

Fig. 5.4 shows that the model of Ref. [122] overestimates the HERMES data. It should also be noted that this model does not predict the sign of the amplitude, as the sign of the amplitude from the present HERMES data is used as input. In order to estimate how much the amplitude is overestimated and to compare the shape of the amplitude as a function of $M_{\pi\pi}$, x, and z, the model was fitted to the data, taking one overall scaling factor as a free parameter. This fit was performed separately for the three kinematic dependencies and the result is included in the figure. The fits describe all three dependencies well. The extracted values for the scaling factor as well as the χ^2 values corresponding to the fits are given in Table 5.1. The extracted scaling factors for the three dependencies are consistent with each other, they indicate that the model overestimates the data by a factor of 4. In Refs. [122, 186] it was argued that the model probably overestimates the effect of interferences, that is, the model overestimates the dihadron fragmentation function $H_1^{\sphericalangle,sp}$.

5.3 Comparison with HERMES results for A_{UL}

A first attempt to access transversity using dihadron semi-inclusive deep-inelastic scattering was presented by the HERMES collaboration in 2005 [182]. This work was based on data collected in the years 1998–2000. At that time, HERMES did not have a transversely polarized target yet and was operated with a longitudinally polarized deuterium targets instead. As was discussed in Sec. 2.4, also a target that is polarized longitudinally with respect to the beam, can be used to study transverse-spin effects. In this case, the numerator of the asymmetry A_{UL}^{ℓ} (see Eq. 2.56), i.e., the polarized cross section difference $\mathrm{d}^7\sigma_{UL}^{\ell}$ is given, at subleading twist, by [187]:

$$\mathrm{d}^7\sigma_{UL}^{\ell} = -\sum_q \frac{\alpha^2 e_q^2}{2\pi s x y^2} \sin\phi_R \sin\theta \left\{ |S_L|\, V(y)\, \frac{|\boldsymbol{R}|}{Q} \left[\frac{Mx}{M_h}\, h_L\, H_1^{\sphericalangle} + \frac{1}{z}\, g_1\, \widetilde{G}^{\sphericalangle} \right] - S_T\, B(y)\, \frac{|\boldsymbol{R}|}{M_h}\, h_1\, H_1^{\sphericalangle} \right\}, \tag{5.2}$$

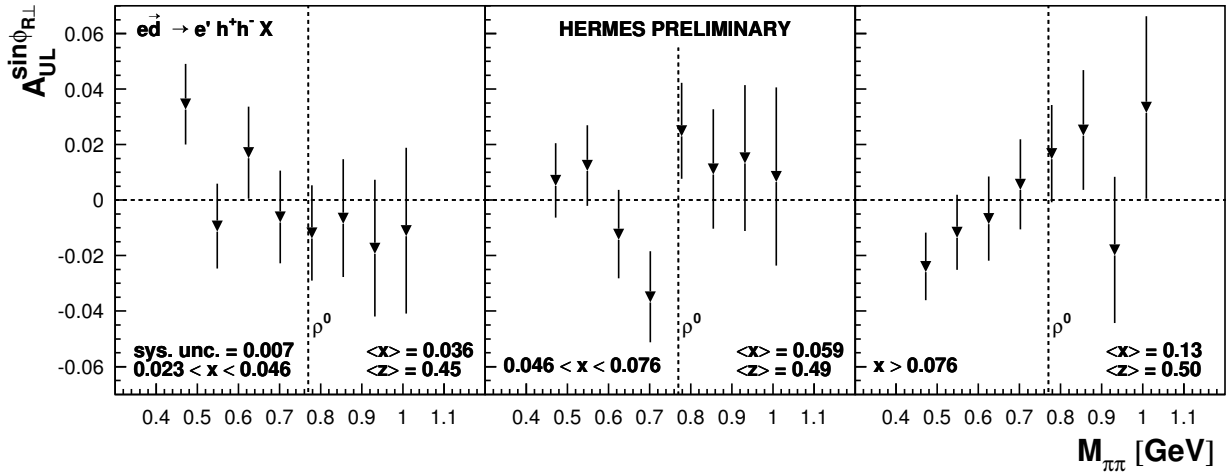

Figure 5.5: *The amplitude $A_{UL}^{\sin\phi_{R\perp}}$ versus the invariant mass $M_{\pi\pi}$ as obtained from the 1998-2000 HERMES data, using a deuterium target. The amplitude is shown in three panels of increasing x, as indicated. The quoted systematic uncertainty of 0.007 is a scale uncertainty due to the uncertainty in the target polarization. The dashed vertical lines indicate the mass of the ρ^0 resonance (0.78 GeV).*

and the unpolarized cross section $\mathrm{d}^7\sigma_{UU}$ is the same as before (see Eq. 2.69 for the leading-twist expression, or Ref. [108] for the subleading-twist expression). Eq. 5.2 is split into a part proportional to the longitudinal polarization S_L ($S_L = \cos\theta_\gamma P_L \approx P_L$) and a part proportional to the transverse polarization S_T, which is related to the longitudinal polarization as $S_T \approx \sin\theta_\gamma |S_L|$. The distribution function h_L, which is directly related to h_1 [99, 188], and the fragmentation function $\widetilde{G}^\sphericalangle$ both contribute only at subleading twist, such that at leading twist the only contribution of Eq. 5.2 to the asymmetry A_{UL}^{ℓ} comes from the term containing the product $h_1 H_1^\sphericalangle$. (The expression for the latter term can easily be derived from the expression given in Eq. 2.68 for $\mathrm{d}^7\sigma_{UT}$ using the relation between A_{UL}^{ℓ} and $A_{UT}^{\gamma^*}$ given by Eq. 2.57.) The product $h_1 H_1^\sphericalangle$ can be obtained experimentally by evaluating the amplitude $A_{UL}^{\sin\phi_{R\perp}} = \frac{\pi}{4} A_{UL}^{\sin\phi_{R\perp}\sin\theta}$. This amplitude is shown in Fig. 5.5 and 5.6 as a function of $M_{\pi\pi}$ in panels representing several bins in x and z, respectively, for pairs of unidentified oppositely charged hadrons. These results were obtained using a longitudinally polarized deuterium target, with an average target polarization $|P_L|$ of 0.84 ± 0.04. For all panels, the amplitude is consistent with zero given the size of the statistical uncertainties. The amplitude shown in these figures, can be related at leading twist to the amplitude $A_{UT}^{\sin(\phi_{R\perp}+\phi_S)\sin\theta}$ according to:

$$A_{UL}^{\sin\phi_{R\perp}\sin\theta} = -\sin\theta_\gamma A_{UT}^{\sin(\phi_{R\perp}+\phi_S)\sin\theta}. \tag{5.3}$$

Given the fact that the amplitude $A_{UT}^{\sin(\phi_{R\perp}+\phi_S)\sin\theta}$ shown in Fig. 5.1 is smaller than 0.1 and that $\langle\sin\theta_\gamma\rangle < 0.09$ in the HERMES acceptance, this means that the part of the amplitude $A_{UL}^{\sin\phi_{R\perp}\sin\theta}$ proportional to S_T has to be smaller than 0.009. This is consistent with the results shown in Fig. 5.5 and 5.6. Because of the relatively large statistical uncertainties and the small value of the amplitude

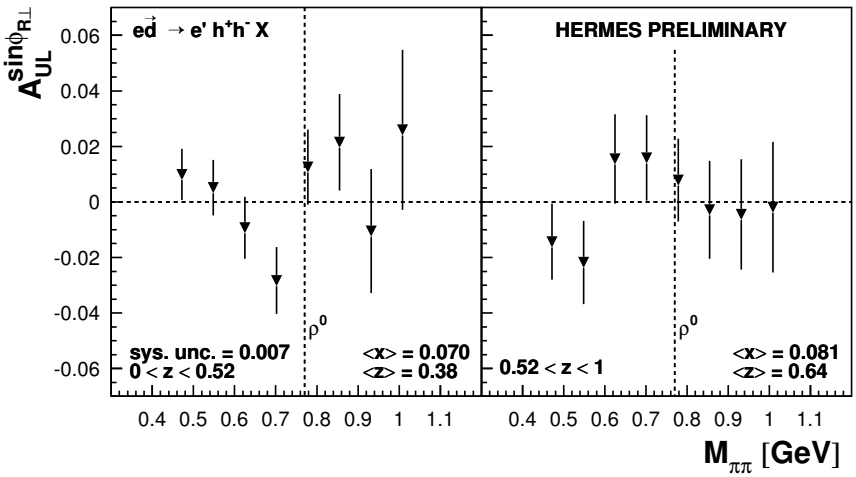

Figure 5.6: *The amplitude $A_{UL}^{\sin\phi_{R\perp}}$ versus the invariant mass $M_{\pi\pi}$, as in Fig. 5.5, but here shown in two panels of increasing z.*

shown in these figures, these results are of relatively little added value compared to the results for $A_{UT}^{\sin(\phi_{R\perp}+\phi_S)\sin\theta}$ shown in Fig. 5.1. However, these results do indicate that up to subleading twist the contribution of $A_{UL}^{\gamma^*}$ to A_{UT}^{ℓ} and therefore to $A_{UT}^{\sin(\phi_{R\perp}+\phi_S)\sin\theta}$ is insignificant, that is, smaller than about 0.001 (see Eq. 2.58). As a final remark, it should be noted though that for the HERMES $A_{UL}^{\sin\phi_{R\perp}}$ data no pion identication was required, which complicates the interpretation, and that a deuteron target was used, for which the expected asymmetries are significantly smaller [122] (see also Sec. 5.4).

5.4 Comparison with COMPASS results

Recently, preliminary results for the amplitude $A_{UT}^{\sin(\phi_{R\perp}+\phi_S)}$ on a transversely polarized ^{6}LiD target were presented by the COMPASS collaboration [77, 189] obtained from their 2002-2004 data taking period. The COMPASS collaboration uses a slightly different convention for the asymmetry [189–191]. They consider the asymmetry A_{RS}, defined as:

$$A_{RS} = \frac{A_{UT}^{\sin(\phi_{RS})}}{D_{NN} f P} = \frac{-A_{UT}^{\sin(\phi_R+\phi_S)}}{D_{NN}}, \tag{5.4}$$

where f (≈ 0.4) is the target dilution factor, P (≈ 0.50) is the target polarization and D_{NN} is the y-dependent depolarization factor $D_{NN} = (1-y)/(1-y+y^2/2)$. The angle ϕ_{RS} is defined as $\phi_{RS} \equiv \phi_R + \phi_S - \pi$ and the asymmetry $A_{UT}^{\sin(\phi_{RS})}$ is defined as $A_{UT}^{\sin(\phi_{RS})} \equiv f P A_{UT}^{\sin(\phi_R+\phi_S-\pi)}$. The value of A_{RS} is shown in Fig. 5.7 in bins of x, $M_{\pi\pi}$, and z. The amplitude is consistent with zero in the entire range of all three dependencies. This is not inconsistent with the HERMES results, as the

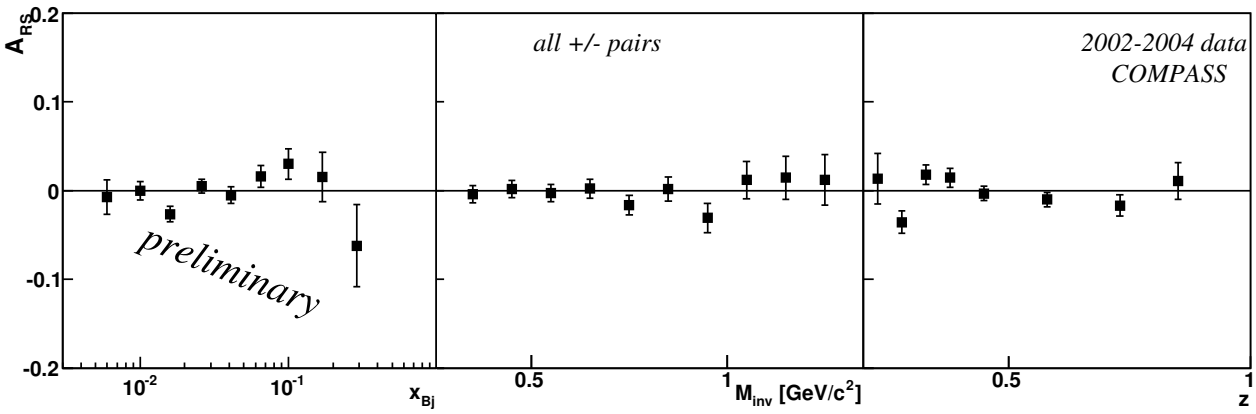

Figure 5.7: *The two-hadron asymmetry amplitude $A_{\phi_{RS}}$ $(= -A_{UT}^{\sin(\phi_{R\perp}+\phi_S)}/D_{NN})$ versus the kinematic variables x, $M_{\pi\pi}$, and z as measured by the COMPASS collaboration [77, 189]. The error bars represent the statistical uncertainty only. The average Q^2 for these measurements is 2.4 GeV^2.*

results from the two collaborations cannot be directly compared. Firstly, the COMPASS collaboration measured the amplitude $A_{UT}^{\sin(\phi_{R\perp}+\phi_S)}$ using a deuteron target. This can result in much smaller asymmetries compared to those measured on a proton target, due to cancellation effects between the transversity distribution of u quarks and d quarks. For example, within the model of Ref. [122] about a 10 times smaller value is predicted for the amplitude $A_{UT}^{\sin(\phi_{R\perp}+\phi_S)}$ at COMPASS kinematics on a deuteron target compared to the same amplitude at HERMES kinematics on a proton target. This observation is also consistent with the small Collins asymmetry measured by the COMPASS collaboration on a deuteron target [76]. Secondly, the COMPASS collaboration measured the amplitude for unidentified h^+h^- pairs, which cannot be directly compared to the amplitude for $\pi^+\pi^-$ pairs, as determined in the present experiment and discussed in Sec. 4.6.4. Finally, the COMPASS collaboration extracted the amplitude using a linear ϕ_{RS}-dependent fit [189], thereby integrating both the numerator and the denominator over θ and as such ignoring the complicated θ dependence present in the denominator of the asymmetry. There is no justification for such an integration, since in the COMPASS analysis the requirement is made that both $z_1 > 0.1$ and $z_2 > 0.1$, which influences the coverage in the angle θ (as was discussed in detail for HERMES kinematics in Sec. 4.5.4).

The COMPASS collaboration is planning to extract the amplitude using pion identification as well as using a transversely polarized hydrogen target [189], both of which facilitate the comparison with the present HERMES results.

5.5 Conclusions and Outlook

The main results of the present work were discussed in Sec. 5.1: the first ever measurement of the dihadron transverse single-spin asymmetry A_{UT} and its azimuthal amplitude $A_{UT}^{\sin(\phi_{R\perp}+\phi_S)\sin\theta}$. This amplitude is significantly nonzero, i.e., at the 3–4 σ level, which implies that both transversity

and the two-hadron fragmentation function $H_1^{\sphericalangle,sp}$ are very likely nonzero as well. This finding also directly implies that two-hadron semi-inclusive deep-inelastic scattering on a transversely polarized hydrogen target can indeed be used to determine transversity. It should be noted, though, that detector acceptance effects can be large and the corresponding systematic uncertainties are model dependent, as was discussed in Sec. 4.5.

In Sec. 5.2, the comparisons with two model predictions were discussed and it was shown that the present HERMES data exclude with a probability $P > 0.999$ a sign change of the fragmentation function $H_1^{\sphericalangle,sp}$ at the ρ^0 mass as predicted in Refs. [118, 119]. The model of Ref. [122] fails to properly describe the size of the HERMES data as well, but after appropriate scaling the predicted shape of the $M_{\pi\pi}$, x, and z dependence of the amplitude $A_{UT}^{\sin(\phi_{R\perp}+\phi_S)\sin\theta}$ is consistent with the present HERMES data. In Sec. 5.3, it was shown that the previously obtained HERMES results for the azimuthal amplitude $A_{UL}^{\sin\phi_{R\perp}}$ are consistent with the results for $A_{UT}^{\sin(\phi_{R\perp}+\phi_S)\sin\theta}$. Finally, in Sec. 5.4, the HERMES results were compared with preliminary data presented by the COMPASS collaboration. The results from the two collaborations are not inconsistent, but the anticipated higher-precision results from the COMPASS collaboration using pion identification are required for a more quantitative comparison.

In the near future, the final results for the amplitude $A_{UT}^{\sin(\phi_{R\perp}+\phi_S)\sin\theta}$ extracted from the total data taking period during which HERMES was operated with a transversely polarized hydrogen target (2002–2005) are expected. This will decrease the statistical uncertainty by a factor of 1.5 approximately. With this final data set, possibly the influence of detector acceptance effects can be reduced as well, by decreasing bin sizes. In combination with the anticipated measurement of the dihadron fragmentation function $H_1^{\sphericalangle,sp}$ by the BELLE collaboration [85], this will allow the extraction of the transversity distribution function.

A

Notation and conventions

In this thesis the Jaffe-Ji-Mulders notation [99, 192] is used for distribution functions and fragmentation functions as well as for the quark-quark correlators. For two-hadron fragmentation functions the notation is followed as introduced in [105]. For the notation and definition of azimuthal angles, single-spin asymmetries and moments of these asymmetries, the Trento Conventions [121, 193] are followed. Two different representations are used for four-vectors:

$$a^\mu = (a^0, a^1, a^2, a^3) = (a^0, \boldsymbol{a}),$$
$$a^\mu = (a^-, a^+, a^1, a^2) = (a^-, a^+, \boldsymbol{a_T}).$$

In the first equation, a is written in terms of standard Cartesian coordinates, whereas in the second equation light-cone coordinates are used (with $a^2 = (a^0)^2 - \boldsymbol{a}^2 = 2a^+a^- - \boldsymbol{a_T}^2$). The two representations are related to each other according to $a^\pm = (a^0 \pm a^3)/\sqrt{2}$. Like in this example, four-vectors are written in normal print, whereas two-vectors and three-vector are written in bold typesetting, i.e., $a = (a^0, \boldsymbol{a})$. Furthermore, the speed of light is taken equal to one, i.e., $c = 1$. The metric tensor used in the present work is defined as

$$g^{00} = 1 = -g^{11} = -g^{22} = -g^{33},$$
$$g^{\mu\nu} = 0 \quad \text{for} \quad \mu \neq \nu.$$

The antisymmetric Levi-Civita tensor is normalised so that $\epsilon^{0123} = -\epsilon_{0123} = 1$.

B

Cross section with transverse momentum

The fully differential single-spin asymmetry A_{UT} for two-hadron semi-inclusive DIS (cf. Eqs. 2.53 and 2.67) depends on 9 kinematic variables: x, y, z, ϕ_R, ϕ_S, θ, M_h and $\boldsymbol{P}_{h\perp}$ ($\mathrm{d}\boldsymbol{P}_{h\perp} = |\boldsymbol{P}_{h\perp}|\,\mathrm{d}|\boldsymbol{P}_{h\perp}|\,\mathrm{d}\phi_h$). The expressions for the full kinematic dependence of the numerator $\mathrm{d}\sigma_{UT}$ and the denominator $\mathrm{d}\sigma_{UU}$ of the asymmetry (at leading twist) are given in Refs. [96, 106]. These expressions, explicitly used in the study of detector acceptance effects (see Sec. 4.5.3), are given by

$$
\begin{aligned}
\mathrm{d}^9\sigma_{UU} = \sum_q \frac{\alpha^2 e_q^2}{2\pi s x y^2} \Bigg\{ & A(y)\, \mathcal{I}\left[f_1\, D_1\right] - B(y)\, \frac{|\boldsymbol{R_T}|}{M_h}\, \cos(\phi_h + \phi_R)\, \mathcal{I}\left[\frac{\boldsymbol{p_T}\cdot\hat{\boldsymbol{P}}_{h\perp}}{M}\, h_1^\perp\, H_1^{\sphericalangle\prime}\right] \\
& - B(y)\, \frac{|\boldsymbol{R_T}|}{M_h}\, \sin(\phi_h + \phi_R)\, \mathcal{I}\left[\frac{\hat{\boldsymbol{P}}_{h\perp}\wedge\boldsymbol{p_T}}{M}\, h_1^\perp\, H_1^{\sphericalangle\prime}\right] \\
& - B(y)\, \cos(2\phi_h)\, \mathcal{I}\left[\frac{2(\boldsymbol{p_T}\cdot\hat{\boldsymbol{P}}_{h\perp})(\boldsymbol{k_T}\cdot\hat{\boldsymbol{P}}_{h\perp}) - \boldsymbol{p_T}\cdot\boldsymbol{k_T}}{M M_h}\, h_1^\perp\, H_1^\perp\right] \\
& - B(y)\, \sin(2\phi_h)\, \mathcal{I}\left[\frac{(\boldsymbol{p_T}\cdot\hat{\boldsymbol{P}}_{h\perp})(\hat{\boldsymbol{P}}_{h\perp}\wedge\boldsymbol{k_T}) + (\boldsymbol{k_T}\cdot\hat{\boldsymbol{P}}_{h\perp})(\hat{\boldsymbol{P}}_{h\perp}\wedge\boldsymbol{p_T})}{M M_h}\, h_1^\perp\, H_1^\perp\right]\Bigg\},
\end{aligned}
\tag{B.1}
$$

$$
\begin{aligned}
\mathrm{d}^9\sigma_{UT} = \sum_q \frac{\alpha^2 e_q^2}{2\pi s x y^2}\ |\boldsymbol{S}_T|\ A(y) \Bigg\{ & \frac{-|\boldsymbol{R_T}|}{M_h}\ \sin(\phi_R - \phi_S)\ \mathcal{I}\left[\frac{\boldsymbol{p_T}\cdot\boldsymbol{k_T}}{2MM_h} g_{1T}\, G_1^\perp\right] \\
& - \frac{|\boldsymbol{R_T}|}{M_h}\ \cos(\phi_R - \phi_S)\ \mathcal{I}\left[\frac{(\boldsymbol{p_T}\cdot\hat{\boldsymbol{P}}_{\boldsymbol{h\perp}})(\hat{\boldsymbol{P}}_{\boldsymbol{h\perp}}\wedge\boldsymbol{k_T}) - (\boldsymbol{k_T}\cdot\hat{\boldsymbol{P}}_{\boldsymbol{h\perp}})(\hat{\boldsymbol{P}}_{\boldsymbol{h\perp}}\wedge\boldsymbol{p_T})}{2MM_h} g_{1T}\, G_1^\perp\right] \\
& + \frac{|\boldsymbol{R_T}|}{M_h}\ \sin(2\phi_h - \phi_R - \phi_S)\ \mathcal{I}\left[\frac{2(\boldsymbol{p_T}\cdot\hat{\boldsymbol{P}}_{\boldsymbol{h\perp}})(\boldsymbol{k_T}\cdot\hat{\boldsymbol{P}}_{\boldsymbol{h\perp}}) - \boldsymbol{p_T}\cdot\boldsymbol{k_T}}{2MM_h}\, g_{1T}\, G_1^\perp\right] \\
& - \frac{|\boldsymbol{R_T}|}{M_h}\ \cos(2\phi_h - \phi_R - \phi_S)\ \mathcal{I}\left[\frac{(\boldsymbol{p_T}\cdot\hat{\boldsymbol{P}}_{\boldsymbol{h\perp}})(\hat{\boldsymbol{P}}_{\boldsymbol{h\perp}}\wedge\boldsymbol{k_T}) + (\boldsymbol{k_T}\cdot\hat{\boldsymbol{P}}_{\boldsymbol{h\perp}})(\hat{\boldsymbol{P}}_{\boldsymbol{h\perp}}\wedge\boldsymbol{p_T})}{2MM_h}\, g_{1T}\, G_1^\perp\right] \\
& - \sin(\phi_h - \phi_S)\ \mathcal{I}\left[\frac{\boldsymbol{p_T}\cdot\hat{\boldsymbol{P}}_{\boldsymbol{h\perp}}}{M} f_{1T}^\perp\, D_1\right] + \cos(\phi_h - \phi_S)\ \mathcal{I}\left[\frac{\hat{\boldsymbol{P}}_{\boldsymbol{h\perp}}\wedge\boldsymbol{p_T}}{M} f_{1T}^\perp\, D_1\right]\Bigg\} \\
& + \sum_q \frac{\alpha^2 e_q^2}{2\pi s x y^2}\ |\boldsymbol{S}_T|\ B(y) \Bigg\{ - \sin(\phi_h + \phi_S)\ \mathcal{I}\left[\frac{\boldsymbol{k_T}\cdot\hat{\boldsymbol{P}}_{\boldsymbol{h\perp}}}{M_h} h_1\, H_1^\perp\right] \\
& + \cos(\phi_h + \phi_S)\ \mathcal{I}\left[\frac{\hat{\boldsymbol{P}}_{\boldsymbol{h\perp}}\wedge\boldsymbol{k_T}}{M_h} h_1\, H_1^\perp\right] - \frac{|\boldsymbol{R_T}|}{M_h}\ \sin(\phi_R + \phi_S)\ \mathcal{I}\left[h_1\, H_1^{\sphericalangle\prime}\right] - \sin(3\phi_h - \phi_S) \\
& \times \mathcal{I}\left[\frac{4(\boldsymbol{p_T}\cdot\hat{\boldsymbol{P}}_{\boldsymbol{h\perp}})^2(\boldsymbol{k_T}\cdot\hat{\boldsymbol{P}}_{\boldsymbol{h\perp}}) - 2(\boldsymbol{p_T}\cdot\hat{\boldsymbol{P}}_{\boldsymbol{h\perp}})(\boldsymbol{p_T}\cdot\boldsymbol{k_T}) - \boldsymbol{p_T}^2(\boldsymbol{k_T}\cdot\hat{\boldsymbol{P}}_{\boldsymbol{h\perp}})}{2M^2M_h} h_{1T}^\perp\, H_1^\perp\right] \\
& + \cos(3\phi_h - \phi_S)\ \mathcal{I}\Bigg[\Bigg(\frac{2(\boldsymbol{p_T}\cdot\hat{\boldsymbol{P}}_{\boldsymbol{h\perp}})^2(\hat{\boldsymbol{P}}_{\boldsymbol{h\perp}}\wedge\boldsymbol{k_T}) + 2(\boldsymbol{k_T}\cdot\hat{\boldsymbol{P}}_{\boldsymbol{h\perp}})(\boldsymbol{p_T}\cdot\hat{\boldsymbol{P}}_{\boldsymbol{h\perp}})(\hat{\boldsymbol{P}}_{\boldsymbol{h\perp}}\wedge\boldsymbol{p_T})}{2M^2M_h} \\
& - \frac{\boldsymbol{p_T}^2(\hat{\boldsymbol{P}}_{\boldsymbol{h\perp}}\wedge\boldsymbol{k_T})}{2M^2M_h}\Bigg) h_{1T}^\perp\, H_1^\perp\Bigg] - \frac{|\boldsymbol{R_T}|}{M_h}\ \sin(2\phi_h + \phi_R - \phi_S)\ \mathcal{I}\left[\frac{2(\boldsymbol{p_T}\cdot\hat{\boldsymbol{P}}_{\boldsymbol{h\perp}})^2 - \boldsymbol{p_T}^2}{2M^2} h_{1T}^\perp\, H_1^{\sphericalangle\prime}\right] \\
& + \frac{|\boldsymbol{R_T}|}{M_h}\ \cos(2\phi_h + \phi_R - \phi_S)\ \mathcal{I}\left[\frac{(\boldsymbol{p_T}\cdot\hat{\boldsymbol{P}}_{\boldsymbol{h\perp}})(\hat{\boldsymbol{P}}_{\boldsymbol{h\perp}}\wedge\boldsymbol{p_T})}{2M^2} h_{1T}^\perp\, H_1^{\sphericalangle\prime}\right]\Bigg\},
\end{aligned}
\tag{B.2}
$$

using the shorthand notation $\boldsymbol{a_T}\wedge\boldsymbol{b_T} = a_\mu \epsilon^{03\mu\nu} b_\nu$. The convolution integrals denoted by $\mathcal{I}$ appearing in these expressions can be computed if one makes an assumption for the $\boldsymbol{p_T}$ dependence of the distribution functions as well as for the $\boldsymbol{k_T}$ dependence of the fragmentation functions. If one makes the following simple Gaussian Ansatz for both these dependencies (the same for all distribution and fragmentation functions),

$$
g_{1T}(x, \boldsymbol{p_T}^2) = \frac{1}{\pi\langle \boldsymbol{p_T}^2\rangle} e^{-\boldsymbol{p_T}^2/\langle \boldsymbol{p_T}^2\rangle} g_{1T}(x) \tag{B.3}
$$

$$
G_1^\perp(z, \zeta, M_h^2, \boldsymbol{k_T}^2, \boldsymbol{k_T}\cdot\boldsymbol{R_T}) = \frac{1}{z^2\pi\langle \boldsymbol{k_T}^2\rangle} e^{-\boldsymbol{k_T}^2/\langle \boldsymbol{k_T}^2\rangle} G_1^\perp(z, \zeta, M_h^2), \tag{B.4}
$$

then about half of the terms appearing in $\mathrm{d}^9\sigma_{UU}$ and $\mathrm{d}^9\sigma_{UT}$ drop out. (This is caused by the fact that no $\boldsymbol{k_T}\cdot\boldsymbol{R_T}$ dependence is taken into account.) The resulting expressions for $\mathrm{d}^9\sigma_{UU}$ and $\mathrm{d}^9\sigma_{UT}$

are:

$$
\begin{aligned}
\mathrm{d}^9\sigma_{UU} = \sum_q \frac{\alpha^2 e_q^2}{2\pi^2 s x y^2} \Bigg\{ & A(y)\, \frac{1}{\langle \boldsymbol{P}_{\boldsymbol{h}\perp}^2 \rangle} f_1\, D_1 - B(y)\, \frac{|\boldsymbol{R}_T|}{M_h}\, \cos(\phi_h + \phi_R)\, z\, \frac{\langle \boldsymbol{p}_T^2 \rangle\, |\boldsymbol{P}_{\boldsymbol{h}\perp}|}{M \langle \boldsymbol{P}_{\boldsymbol{h}\perp}^2 \rangle^2} h_1^\perp\, H_1^{\sphericalangle\prime} \\
& + B(y)\, \cos(2\phi_h)\, z^4 \frac{\langle \boldsymbol{p}_T^2 \rangle\, \langle \boldsymbol{k}_T^2 \rangle\, |\boldsymbol{P}_{\boldsymbol{h}\perp}|^2}{M M_h \langle \boldsymbol{P}_{\boldsymbol{h}\perp}^2 \rangle^3}\, h_1^\perp\, H_1^\perp \Bigg\} e^{-\boldsymbol{P}_{\boldsymbol{h}\perp}^2 / \langle \boldsymbol{P}_{\boldsymbol{h}\perp}^2 \rangle},
\end{aligned}
\tag{B.5}
$$

$$
\begin{aligned}
\mathrm{d}^9\sigma_{UT} = \sum_q \frac{\alpha^2 e_q^2}{2\pi^2 s x y^2}\, |\boldsymbol{S}_T|\, A(y) \Bigg\{ & \frac{-|\boldsymbol{R}_T|}{M_h}\, \sin(\phi_R - \phi_S)\, z^4\, \frac{\langle \boldsymbol{p}_T^2 \rangle\, \langle \boldsymbol{k}_T^2 \rangle \left[\langle \boldsymbol{P}_{\boldsymbol{h}\perp}^2 \rangle - |\boldsymbol{P}_{\boldsymbol{h}\perp}|^2 \right]}{2 M M_h \langle \boldsymbol{P}_{\boldsymbol{h}\perp}^2 \rangle^3}\, g_{1T}\, G_1^\perp \\
& - \frac{|\boldsymbol{R}_T|}{M_h}\, \sin(2\phi_h - \phi_R - \phi_S)\, z^4\, \frac{\langle \boldsymbol{p}_T^2 \rangle\, \langle \boldsymbol{k}_T^2 \rangle\, |\boldsymbol{P}_{\boldsymbol{h}\perp}|^2}{2 M M_h \langle \boldsymbol{P}_{\boldsymbol{h}\perp}^2 \rangle^3}\, g_{1T}\, G_1^\perp \\
& - \sin(\phi_h - \phi_S)\, z\, \frac{\langle \boldsymbol{p}_T^2 \rangle\, |\boldsymbol{P}_{\boldsymbol{h}\perp}|}{M \langle \boldsymbol{P}_{\boldsymbol{h}\perp}^2 \rangle^2}\, f_{1T}^\perp\, D_1 \Bigg\} e^{-\boldsymbol{P}_{\boldsymbol{h}\perp}^2 / \langle \boldsymbol{P}_{\boldsymbol{h}\perp}^2 \rangle} \\
+ \sum_q \frac{\alpha^2 e_q^2}{2\pi^2 s x y^2}\, |\boldsymbol{S}_T|\, B(y) \Bigg\{ & + \sin(\phi_h + \phi_S)\, z\, \frac{\langle \boldsymbol{k}_T^2 \rangle\, |\boldsymbol{P}_{\boldsymbol{h}\perp}|}{M_h \langle \boldsymbol{P}_{\boldsymbol{h}\perp}^2 \rangle^2}\, h_1\, H_1^\perp \\
& - \frac{|\boldsymbol{R}_T|}{M_h}\, \sin(\phi_R + \phi_S)\, \frac{1}{\langle \boldsymbol{P}_{\boldsymbol{h}\perp}^2 \rangle}\, h_1\, H_1^{\sphericalangle\prime} + \sin(3\phi_h - \phi_S) z^{11}\, \frac{\langle \boldsymbol{p}_T^2 \rangle^2\, \langle \boldsymbol{k}_T^2 \rangle\, |\boldsymbol{P}_{\boldsymbol{h}\perp}|^3}{2 M^2 M_h \langle \boldsymbol{P}_{\boldsymbol{h}\perp}^2 \rangle^4}\, h_{1T}^\perp\, H_1^\perp \\
& - \frac{|\boldsymbol{R}_T|}{M_h}\, \sin(2\phi_h + \phi_R - \phi_S)\, z^4\, \frac{\langle \boldsymbol{p}_T^2 \rangle^2\, |\boldsymbol{P}_{\boldsymbol{h}\perp}|^2}{2 M^2 \langle \boldsymbol{P}_{\boldsymbol{h}\perp}^2 \rangle^3}\, h_{1T}^\perp\, H_1^{\sphericalangle\prime} \Bigg\} e^{-\boldsymbol{P}_{\boldsymbol{h}\perp}^2 / \langle \boldsymbol{P}_{\boldsymbol{h}\perp}^2 \rangle},
\end{aligned}
\tag{B.6}
$$

where it was used that $\langle \boldsymbol{P}_{\boldsymbol{h}\perp}^2 \rangle / z^2 = \langle \boldsymbol{p}_T^2 \rangle + \langle \boldsymbol{k}_T^2 \rangle$.

C

Testing the fitting method

The low-statistics corrections to the binned fit (see Sec. 4.4.1) were tested with a simple simulation. Asymmetries were generated of the form $A = a \sin\phi$. The value of ϕ was chosen randomly in the range $[0, 2\pi]$. The spin states were assigned using the Monte Carlo method described in Sec. 4.5.1. An experiment was simulated with 400 events using an arbitrary constant value for a as input ($a = 0.4$). From these events a was extracted using the binned fit and χ^2 was calculated, defined as $\chi^2 = (0.4 - a)^2/\Delta a^2$. This experiment was repeated 10000 times in order to calculate the averages $\langle\chi^2\rangle$, $\langle a\rangle$ and σ, the width of the distribution of extracted values of a. Subsequently, this was done for a varying number of ϕ-bins. In the situation that both spin states are empty for a certain bin, this bin was ignored in the fit. In the situation that only one of the spin states is empty, the uncertainty on the asymmetry (cf. Eq. 4.16) was calculated using $N = 0.25$ for this spin state, which gives a much more reasonable estimate of the uncertainty, since using $N = 0$ would result in $\Delta A = 0$.

The results are given in Fig. C.1, which indicate that the extraction method works very well. The fact that σ is larger for large bins is due to the information loss inherent in binned fitting. This cannot be corrected for. However, the fact that both $\langle\chi^2\rangle$ and $\langle a\rangle$ are still determined very precisely indicates that such information loss is compensated for by correspondingly larger statistical uncertainties. The fact that still $\langle\chi^2\rangle$ is not exactly 1 and $\langle a\rangle$ is not exactly 0.4 could be due to one or more of the assumptions that were made, as described above and in Section 4.4.1. In principle improvements to the extraction method are still possible, but not needed in view of the size of the statistical uncertainty on A_{UT}. In Fig. C.2 the same results are shown for the situation that one of the corrections, the correction to the statistical uncertainty ΔA, is not applied. The comparison of

both figures clearly indicates the importance of the correction in case of a small number of events per bin.

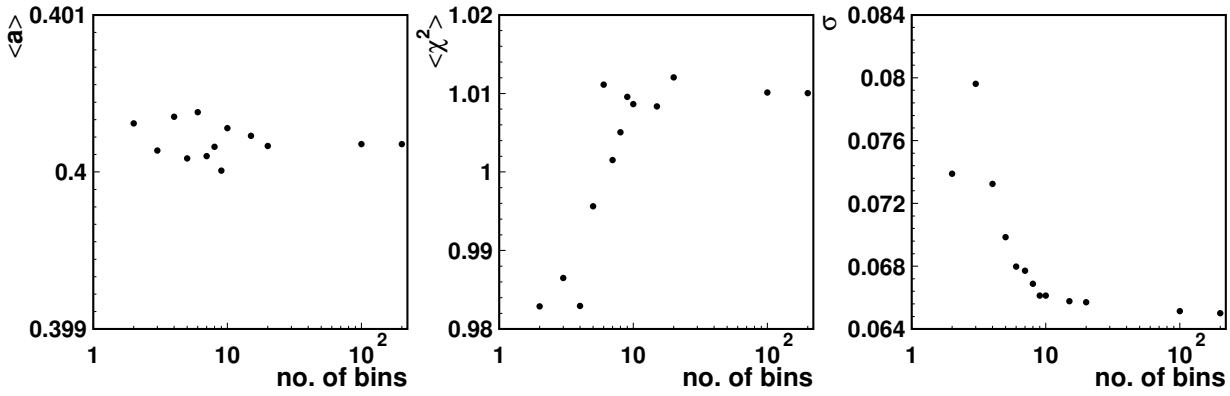

Figure C.1: *The averages $\langle a \rangle$ and $\langle \chi^2 \rangle$ and σ extracted from 10000 simulated experiments with each 400 events.*

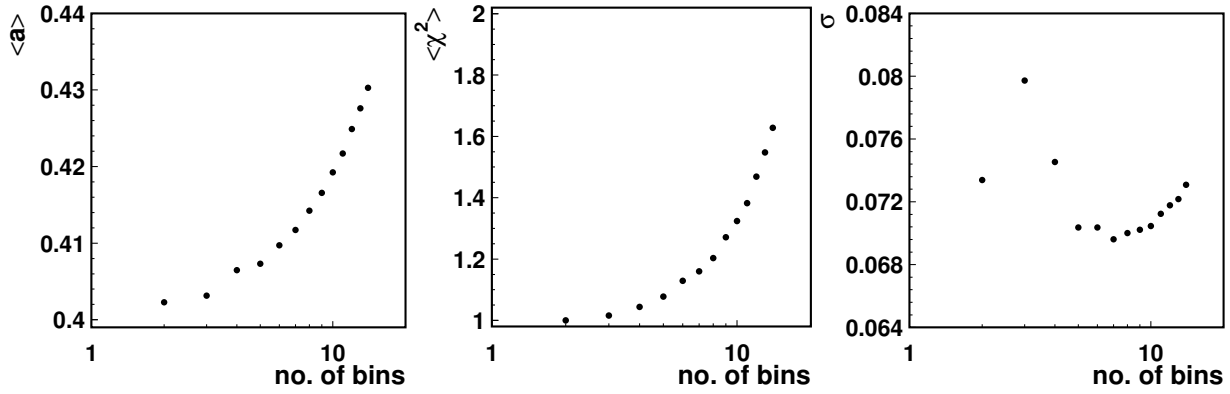

Figure C.2: *Same plots as in Fig. C.1, here without applying the correction to the statistical uncertainty ΔA.*

D

Calculation of the angle ϕ_R

Figure D.1 shows a possible configuration of the two-hadron semi-inclusive deep-inelastic scattering process, which helps to understand the calculation of the azimuthal angle ϕ_R. In this example $\boldsymbol{q}$, $\boldsymbol{q} \times \boldsymbol{k}$, $\boldsymbol{P}_h$ and the normal to the scattering plane, $\boldsymbol{P}_h \times \boldsymbol{R}_T$, are all lying within the same plane. Because the normal to the two-hadron plane also lies within the same plane, this configuration corresponds to $\phi_R = 0$ (see also Fig. 2.9).

The angle ϕ_R corresponds to the angle between the normal to the two-hadron plane and the vector $\boldsymbol{n}$. Where $\boldsymbol{n}$ is the vector perpendicular to $\boldsymbol{P}_h$ lying in the plane defined by $\boldsymbol{q} \times \boldsymbol{k}$ and $\boldsymbol{P}_h$, as indicated in the figure.

The vector $\boldsymbol{n}$ is calculated in the following way:

$$\hat{\boldsymbol{n}} = \hat{\boldsymbol{a}} \cos\delta + \hat{\boldsymbol{b}} \sin\delta, \tag{D.1}$$

where

$$\delta = \frac{1}{2}\pi - \arccos \frac{(\boldsymbol{q} \times \boldsymbol{k}) \cdot \boldsymbol{P_h}}{|\boldsymbol{q} \times \boldsymbol{k}| \cdot |\boldsymbol{P_h}|}, \tag{D.2}$$

$$\hat{\boldsymbol{a}} = \frac{\boldsymbol{q} \times \boldsymbol{k}}{|\boldsymbol{q} \times \boldsymbol{k}|}, \tag{D.3}$$

and

$$\hat{\boldsymbol{b}} = (\hat{\boldsymbol{P}}_h \times \hat{\boldsymbol{a}}) \times \hat{\boldsymbol{a}}. \tag{D.4}$$

Using this definition ϕ_R can be calculated as in Eq. 2.37.

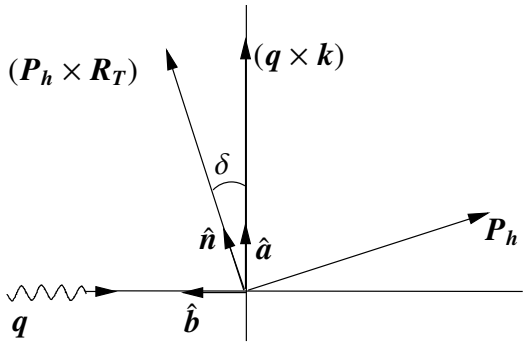

Figure D.1: *Example of a configuration of a two-hadron semi-inclusive DIS event, indicating the vector involved in the calculation of the azimuthal angle ϕ_R.*

E

Tables of results

In this appendix, the final results are listed in tables corresponding to the data shown in Fig. 5.1. The tables E.1, E.2, and E.3 give the amplitude $A_{UT}^{\sin(\phi_{R\perp}+\phi_S)\sin\theta}$ for the $M_{\pi\pi}$ dependence, the x dependence, and the z dependence, respectively. Apart from the amplitude and the average kinematics for each bin, the tables also list the normalized χ^2 for the fits that were used to extract the amplitude from the single-spin asymmetry A_{UT}.

$\langle M_{\pi\pi}\rangle$ [GeV]	$\langle x\rangle$	$\langle y\rangle$	$\langle z\rangle$	$\langle Q^2\rangle$ [GeV^2]	χ^2/d.f.	$A_{UT}^{\sin(\phi_{R\perp}+\phi_S)\sin\theta}$	stat. unc.
0.344	0.081	0.615	0.376	2.42	0.83	0.014	0.015
0.473	0.078	0.626	0.395	2.39	1.10	0.015	0.013
0.655	0.072	0.651	0.439	2.31	0.95	0.058	0.014
0.954	0.067	0.679	0.543	2.26	1.32	0.015	0.021

Table E.1: *The amplitude $A_{UT}^{\sin(\phi_{R\perp}+\phi_S)\sin\theta}$ in bins of the invariant mass $M_{\pi\pi}$. The bin boundaries are at 0.25, 0.40, 0.55, 0.77, and 2.0 GeV. Also included are the average values of the kinematic variables x, y, z, and Q^2. The listed normalized χ^2 corresponds to the fits used to extract the amplitude from the single-spin asymmetry A_{UT} (see Eq. 4.33).*

$\langle M_{\pi\pi}\rangle$ [GeV]	$\langle x\rangle$	$\langle y\rangle$	$\langle z\rangle$	$\langle Q^2\rangle$ [GeV^2]	χ^2/d.f.	$A_{UT}^{\sin(\phi_{R\perp}+\phi_S)\sin\theta}$	stat. unc.
0.700	0.033	0.734	0.415	1.23	0.76	0.020	0.024
0.693	0.047	0.655	0.450	1.59	0.83	0.017	0.021
0.688	0.068	0.618	0.466	2.18	1.09	0.081	0.024
0.679	0.134	0.574	0.481	3.97	0.91	0.035	0.021

Table E.2: *The amplitude $A_{UT}^{\sin(\phi_{R\perp}+\phi_S)\sin\theta}$ in bins of x. The bin boundaries are at 0.023, 0.04, 0.055, 0.085, and 0.4.*

$\langle M_{\pi\pi}\rangle$ [GeV]	$\langle x\rangle$	$\langle y\rangle$	$\langle z\rangle$	$\langle Q^2\rangle$ [GeV^2]	χ^2/d.f.	$A_{UT}^{\sin(\phi_{R\perp}+\phi_S)\sin\theta}$	stat. unc.
0.622	0.063	0.689	0.276	2.30	1.29	0.010	0.014
0.690	0.070	0.643	0.390	2.35	0.77	0.049	0.023
0.718	0.075	0.615	0.496	2.36	1.21	0.066	0.020
0.733	0.080	0.593	0.666	2.39	0.81	0.022	0.022

Table E.3: *The amplitude $A_{UT}^{\sin(\phi_{R\perp}+\phi_S)\sin\theta}$ in bins of z. The bin boundaries are at 0, 0.34, 0.44, 0.56, and 1.0.*

Bibliography

[1] H. Geiger and E. Marsden, *On a diffuse reflection of the α-particles*, Proc. Roy. Soc. **A82**, 495 (1909).

[2] E. Rutherford, *The scattering of α and β particles by matter and the structure of the atom*, Phil. Mag. **21**, 669 (1911).

[3] S. Weinberg, *The discovery of subatomic particles*, Cambridge, UK: Univ. Pr. (2003).

[4] E. D. Bloom *et al.*, *High-energy inelastic $e-p$ scattering at 6° and 10°*, Phys. Rev. Lett. **23**, 930 (1969), [SPIRES].

[5] J. I. Friedman, *Deep inelastic scattering: Comparisons with the quark model*, Rev. Mod. Phys. **63**, 615 (1991), [SPIRES].

[6] G. Miller *et al.*, *Inelastic electron-proton scattering at large momentum transfers*, Phys. Rev. **D5**, 528 (1972), [SPIRES].

[7] J. D. Bjorken, *Asymptotic sum rules at infinite momentum*, Phys. Rev. **179**, 1547 (1969), [SPIRES].

[8] EMC, J. Ashman *et al.*, *A measurement of the spin asymmetry and determination of the structure function g_1 in deep-inelastic muon proton scattering*, Phys. Lett. **B206**, 364 (1988), [SPIRES].

[9] EMC, J. Ashman *et al.*, *An investigation of the spin structure of the proton in deep-inelastic scattering of polarized muons on polarized protons*, Nucl. Phys. **B328**, 1 (1989), [SPIRES].

[10] E142, P. L. Anthony *et al.*, *Deep inelastic scattering of polarized electrons by polarized ^{3}He and the study of the neutron spin structure*, Phys. Rev. **D54**, 6620 (1996), hep-ex/9610007, [SPIRES].

[11] E154, K. Abe *et al.*, *Precision determination of the neutron spin structure function* g_1^n, Phys. Rev. Lett. **79**, 26 (1997), hep-ex/9705012, [SPIRES].

[12] Spin Muon, B. Adeva *et al.*, *A next-to-leading order QCD analysis of the spin structure function* g_1, Phys. Rev. **D58**, 112002 (1998), [SPIRES].

[13] Spin Muon, B. Adeva *et al.*, *Spin asymmetries* A_1 *of the proton and the deuteron in the low* x *and low* Q^2 *region from polarized high energy muon scattering*, Phys. Rev. **D60**, 072004 (1999), [SPIRES].

[14] Spin Muon, B. Adeva *et al.*, *Spin asymmetries* A_1 *of the proton and the deuteron in the low* x *and low* Q^2 *region from polarized high energy muon scattering*, Phys. Rev. **D62**, 079902 (2000).

[15] E143, K. Abe *et al.*, *Measurements of the proton and deuteron spin structure functions* g_1 *and* g_2, Phys. Rev. **D58**, 112003 (1998), hep-ph/9802357, [SPIRES].

[16] E155, P. L. Anthony *et al.*, *Measurements of the* Q^2 *dependence of the proton and neutron spin structure functions* g_1^p *and* g_1^n, Phys. Lett. **B493**, 19 (2000), hep-ph/0007248, [SPIRES].

[17] COMPASS, E. S. Ageev *et al.*, *Measurement of the spin structure of the deuteron in the DIS region*, Phys. Lett. **B612**, 154 (2005), hep-ex/0501073, [SPIRES].

[18] HERMES, A. Airapetian *et al.*, *Precise determination of the spin structure function* g_1 *of the proton, deuteron, and neutron*, Phys. Rev. **D75**, 012007 (2007), [SPIRES].

[19] Durham Database Group (UK), *HEPDATA - The Durham HEP Databases*, http://www.slac.stanford.edu/spires/hepdata, http://durpdg.dur.ac.uk/HEPDATA/PDF.

[20] R. L. Jaffe, *Where does the proton really get its spin?*, Phys. Today **48N9**, 24 (1995), [SPIRES].

[21] X. Ji, *Gauge invariant decomposition of nucleon spin*, Phys. Rev. Lett. **78**, 610 (1997), hep-ph/9603249, [SPIRES].

[22] H1, C. Adloff *et al.*, *Measurement of deeply virtual Compton scattering at HERA*, Phys. Lett. **B517**, 47 (2001), hep-ex/0107005, [SPIRES].

[23] ZEUS, S. Chekanov *et al.*, *Measurement of deeply virtual Compton scattering at HERA*, Phys. Lett. **B573**, 46 (2003), hep-ex/0305028, [SPIRES].

[24] H1, A. Aktas *et al.*, *Measurement of deeply virtual Compton scattering at HERA*, Eur. Phys. J. **C44**, 1 (2005), hep-ex/0505061, [SPIRES].

[25] CLAS, S. Stepanyan *et al.*, *First observation of exclusive deeply virtual Compton scattering in polarized electron beam asymmetry measurements*, Phys. Rev. Lett. **87**, 182002 (2001), hep-ex/0107043, [SPIRES].

[26] CLAS, S. Chen *et al.*, *Measurement of deeply virtual Compton scattering with a polarized proton target*, Phys. Rev. Lett. **97**, 072002 (2006), hep-ex/0605012, [SPIRES].

[27] M. Garcon, *Deeply virtual Compton scattering and nucleon structure*, AIP Conf. Proc. **870**, 93 (2006), [SPIRES].

[28] HERMES, A. Airapetian *et al.*, *The beam-charge azimuthal asymmetry and deeply virtual Compton scattering*, Phys. Rev. **D75**, 011103 (2007), hep-ex/0605108, [SPIRES].

[29] HERMES, A. Airapetian *et al.*, *Measurement of azimuthal asymmetries in exclusive electroproduction of real photons on a transversely polarized hydrogen target*, in preparation.

[30] HERMES, A. Airapetian *et al.*, *Measurement of the spin asymmetry in the photoproduction of pairs of high-p_T hadrons at HERMES*, Phys. Rev. Lett. **84**, 2584 (2000), hep-ex/9907020, [SPIRES].

[31] Spin Muon (SMC), B. Adeva *et al.*, *Spin asymmetries for events with high p_T hadrons in DIS and an evaluation of the gluon polarization*, Phys. Rev. **D70**, 012002 (2004), hep-ex/0402010, [SPIRES].

[32] COMPASS, C. Bernet, *The gluon polarization $\Delta G/G$ at COMPASS*, (2004), hep-ex/0405073, [SPIRES].

[33] COMPASS, C. Bernet, *Recent measurement of Delta(G)/G at COMPASS*, AIP Conf. Proc. **792**, 1011 (2005), hep-ex/0507049, [SPIRES].

[34] J. R. Ellis and M. Karliner, *Direct estimate of the gluon polarization in the nucleon*, Mod. Phys. Lett. **A21**, 721 (2006), hep-ph/0501115, [SPIRES].

[35] M. Karliner, *Goodbye to large ΔG? Direct estimate of gluon polarization in the nucleon*, Nucl. Phys. Proc. Suppl. **161**, 116 (2006), [SPIRES].

[36] W. Vogelsang, *Gluon polarization in the nucleon*, AIP Conf. Proc. **842**, 318 (2006), [SPIRES].

[37] R. L. Jaffe, *Spin, twist and hadron structure in deep inelastic processes*, (1996), hep-ph/9602236, [SPIRES], Proceedings of the Ettore Majorana International School on the Spin Structure of the Nucleon, Erice, Italy, 3-10 Aug 1995.

[38] HERMES, A. Airapetian *et al.*, *Quark helicity distributions in the nucleon for up, down, and strange quarks from semi-inclusive deep-inelastic scattering*, Phys. Rev. **D71**, 012003 (2005), hep-ex/0407032, [SPIRES].

[39] V. Barone, A. Drago, and P. G. Ratcliffe, *Transverse polarisation of quarks in hadrons*, Phys. Rept. **359**, 1 (2002), hep-ph/0104283, [SPIRES].

[40] R. L. Jaffe and N. Saito, *QCD selection rules in polarized hadron collisions*, Phys. Lett. **B382**, 165 (1996), hep-ph/9604220, [SPIRES].

[41] P. G. Ratcliffe, *QCD evolution of transversity in leading and next-to- leading order*, Czech. J. Phys. **53**, B27 (2003), hep-ph/0211222, [SPIRES].

[42] B. L. G. Bakker, E. Leader, and T. L. Trueman, *A critique of the angular momentum sum rules and a new angular momentum sum rule*, Phys. Rev. **D70**, 114001 (2004), hep-ph/0406139, [SPIRES].

[43] E. Leader, P. J. Mulders, and O. V. Teryaev *et al.*, Trieste meeting on the transverse spin nucleon sum rule, http://www.ts.infn.it/eventi/transversitySR, 24 Nov 2006.

[44] O. Teryaev, B. Pire, and J. Soffer, *Sum rules and positivity constraints on nucleon spin structure*, (1998), hep-ph/9806502, [SPIRES].

[45] P. G. Ratcliffe, *Theory of spin effects in hard hadronic reactions*, (1998), hep-ph/9811348, [SPIRES].

[46] S. Aoki, M. Doui, T. Hatsuda, and Y. Kuramashi, *Tensor charge of the nucleon in lattice QCD*, Phys. Rev. **D56**, 433 (1997), hep-lat/9608115, [SPIRES] 9608115.

[47] A. A. Khan *et al.*, *Axial and tensor charge of the nucleon with dynamical fermions*, Nucl. Phys. Proc. Suppl. **140**, 408 (2005), hep-lat/0409161, [SPIRES].

[48] A. Bacchetta, M. Boglione, A. Henneman, and P. J. Mulders, *Bounds on transverse momentum dependent distribution and fragmentation functions*, Phys. Rev. Lett. **85**, 712 (2000), hep-ph/9912490, [SPIRES].

[49] J. Soffer, *Positivity constraints for spin-dependent parton distributions*, Phys. Rev. Lett. **74**, 1292 (1995), hep-ph/9409254, [SPIRES].

[50] L. Dick *et al.*, *Spin effects in the inclusive reactions* $\pi^{\pm} + p^{\uparrow} \to \pi^{\pm} + X$ *at 8 GeV/c*, Phys. Lett. **B57**, 93 (1975), [SPIRES].

[51] R. D. Klem *et al.*, *Measurement of asymmetries of inclusive pion production in proton-proton interactions at 6 GeV/c and 11.8 GeV/c*, Phys. Rev. Lett. **36**, 929 (1976), [SPIRES].

[52] W. H. Dragoset *et al.*, *Asymmetries in inclusive proton-nucleon scattering at 11.75 GeV/c*, Phys. Rev. **D18**, 3939 (1978), [SPIRES].

[53] D. Aschman *et al.*, *Spin dependence of inclusive reactions from proton-proton collisions at 7.9 GeV/c*, Nucl. Phys. **B142**, 220 (1978), [SPIRES].

[54] S. Saroff *et al.*, *Single-spin asymmetry in inclusive reactions* $p^{\uparrow} + p \to \pi^{+} + X, \pi^{-} + X$, *and* $p + X$ *at 13.3 GeV/c and 18.5 GeV/c*, Phys. Rev. Lett. **64**, 995 (1990), [SPIRES].

[55] FNAL-E704, D. L. Adams *et al.*, *Analyzing power in inclusive* π^{+} *and* π^{-} *production at high* x_F *with a 200 GeV polarized proton beam*, Phys. Lett. **B264**, 462 (1991), [SPIRES].

[56] E581, D. L. Adams *et al.*, *Large-*x_F *spin asymmetry in* π^0 *production by 200 GeV polarized protons*, Z. Phys. **C56**, 181 (1992), [SPIRES].

[57] STAR, J. Adams *et al.*, *Cross sections and transverse single-spin asymmetries in forward neutral-pion production from proton collisions at* $\sqrt{s} = 200$ *GeV*, Phys. Rev. Lett. **92**, 171801 (2004), hep-ex/0310058, [SPIRES].

[58] BRAHMS, F. Videbaek, *Single-spin asymmetries in the BRAHMS experiment*, AIP Conf. Proc. **842**, 401 (2006), nucl-ex/0601008, [SPIRES] 0601008.

[59] PHENIX, S. S. Adler *et al.*, *Measurement of transverse single-spin asymmetries for mid-rapidity production of neutral pions and charged hadrons in polarized p+p collisions at* $\sqrt{s} = 200$ *GeV*, Phys. Rev. Lett. **95**, 202001 (2005), hep-ex/0507073, [SPIRES].

[60] J. C. Collins, *Fragmentation of transversely polarized quarks probed in transverse momentum distributions*, Nucl. Phys. **B396**, 161 (1993), hep-ph/9208213, [SPIRES].

[61] D. W. Sivers, *Hard scattering scaling laws for single-spin production asymmetries*, Phys. Rev. **D43**, 261 (1991), [SPIRES].

[62] M. Anselmino, M. Boglione, U. D'Alesio, E. Leader, and F. Murgia, *Parton intrinsic motion: Suppression of the Collins mechanism for transverse single-spin asymmetries in* $p^{\uparrow} p \to \pi X$, Phys. Rev. **D71**, 014002 (2005), hep-ph/0408356, [SPIRES].

[63] J. P. Ralston and D. E. Soper, *Production of dimuons from high-energy polarized proton-proton collisions*, Nucl. Phys. **B152**, 109 (1979), [SPIRES].

[64] G. Bunce, N. Saito, J. Soffer, and W. Vogelsang, *Prospects for spin physics at RHIC*, Ann. Rev. Nucl. Part. Sci. **50**, 525 (2000), hep-ph/0007218, [SPIRES].

[65] V. Barone, T. Calarco, and A. Drago, *Double-spin transverse asymmetries in Drell-Yan processes*, Phys. Rev. **D56**, 527 (1997), hep-ph/9702239, [SPIRES].

[66] O. Martin, A. Schafer, M. Stratmann, and W. Vogelsang, *Tranverse double-spin asymmetries for muon pair production in pp collisions*, Phys. Rev. **D60**, 117502 (1999), hep-ph/9902250, [SPIRES].

[67] PAX, V. Barone *et al.*, *Antiproton-proton scattering experiments with polarization*, (2005), hep-ex/0505054, [SPIRES].

[68] M. Anselmino, V. Barone, A. Drago, and N. N. Nikolaev, *Accessing transversity via J/ψ production in polarized $p^\uparrow \bar{p}^\uparrow$ interactions*, (2004), hep-ph/0403114, [SPIRES].

[69] A. V. Efremov, K. Goeke, and P. Schweitzer, *Transversity distribution function in hard scattering of polarized protons and antiprotons in the PAX experiment*, Eur. Phys. J. **C35**, 207 (2004), hep-ph/0403124, [SPIRES].

[70] N. N. Nikolaev and F. F. Pavlov, *Spin filtering in storage rings*, (2006), hep-ph/0601184, [SPIRES].

[71] M. Contalbrigo, *PAX: Polarized antiproton experiments*, prepared for international workshop on transverse polarization phenomena in hard processes (Transversity 2005), Villa Olmo, Como, Italy, 7-10 Sep 2005.

[72] D. Boer, *Investigating the origins of transverse spin asymmetries at RHIC*, Phys. Rev. **D60**, 014012 (1999), hep-ph/9902255, [SPIRES].

[73] SMC, A. Bravar, *Transverse spin asymmetries in $p^\uparrow p \to \pi^\pm + X$ and $lp^\uparrow \to l' + \pi^\pm + X$*, Nucl. Phys. **A666**, 314 (2000), [SPIRES].

[74] HERMES, A. Airapetian *et al.*, *Single-spin asymmetries in semi-inclusive deep-inelastic scattering on a transversely polarized hydrogen target*, Phys. Rev. Lett. **94**, 012002 (2005), hep-ex/0408013, [SPIRES].

[75] COMPASS, V. Y. Alexakhin *et al.*, *First measurement of the transverse spin asymmetries of the deuteron in semi-inclusive deep-inelastic scattering*, Phys. Rev. Lett. **94**, 202002 (2005), hep-ex/0503002, [SPIRES].

[76] COMPASS, E. S. Ageev *et al.*, *A new measurement of the Collins and Sivers asymmetries on a transversely polarised deuteron target*, (2006), hep-ex/0610068, [SPIRES].

[77] A. Martin, *COMPASS results on transverse single-spin asymmetries*, (2007), hep-ex/0702002, [SPIRES].

[78] The Jefferson Lab Hall A collaboration, *Measurement of single-target-spin asymmetry in semi-inclusive pion electroproduction on a transversely polarized ^{3}He target*, http://hallaweb.jlab.org/experiment/transversity, 2006, The E06-010 and E06-011 experiments (approved).

[79] CLAS, H. Avakian, P. Bosted, V. Burkert, and L. Elouadrhiri, *Studies of transverse spin effects at JLAB*, prepared for international workshop on transverse polarization phenomena in hard processes (Transversity 2005), Villa Olmo, Como, Italy, 7-10 Sep 2005.

[80] S. Corneliussen, *CEBAF set to double energy*, CERN Courier, vol. 44, no. 10, 2004, http://cerncourier.com/main/article/44/10/15.

[81] Belle, K. Abe *et al.*, *Measurement of azimuthal asymmetries in inclusive production of hadron pairs in e^+e^- annihilation at Belle*, Phys. Rev. Lett. **96**, 232002 (2006), hep-ex/0507063, [SPIRES].

[82] M. Anselmino *et al.*, *Transversity and Collins functions from SIDIS and e+ e- data*, Phys. Rev. **D75**, 054032 (2007), hep-ph/0701006, [SPIRES].

[83] J. C. Collins, S. F. Heppelmann, and G. A. Ladinsky, *Measuring transversity densities in singly polarized hadron-hadron and lepton-hadron collisions*, Nucl. Phys. **B420**, 565 (1994), hep-ph/9305309, [SPIRES].

[84] J. C. Collins and G. A. Ladinsky, *On $\pi - \pi$ correlations in polarized quark fragmentation using the linear sigma model*, (1994), hep-ph/9411444, [SPIRES].

[85] D. Gabbert, M. Grosse Perdekamp, R. Seidl, A. Ogawa, and K. Hasuko, *Spin-dependent fragmentation functions at BELLE*, prepared for 16th international spin physics symposium (SPIN 2004), Trieste, Italy, 10-16 Oct 2004.

[86] X. Artru and M. Mekhfi, *What can we learn from unpolarized and polarized electroproduction of fast baryons?*, Nucl. Phys. **A532**, 351 (1991), [SPIRES].

[87] X. Artru, *Proposals for measuring transversity distributions in deep- inelastic electron scattering and a model for E-704 asymmetries*, (1993), hep-ph/9310323, [SPIRES].

[88] R. L. Jaffe, *Polarized Λ's in the current fragmentation region*, Phys. Rev. **D54**, 6581 (1996), hep-ph/9605456, [SPIRES].

[89] COMPASS, F. Bradamante, *Transversity physics at COMPASS*, (2006), hep-ex/0602013, [SPIRES].

[90] COMPASS, A. Ferrero, *Lambda asymmetries*, prepared for international workshop on transverse polarization phenomena in hard processes (Transversity 2005), Villa Olmo, Como, Italy, 7-10 Sep 2005.

[91] M. Demey, *The polarization of Λ^0 hyperons in quasi-real photoproduction*, PhD thesis, Universiteit van Amsterdam (UvA), 2007, DESY-HERMES-07-05.

[92] X. Ji, *Chiral-odd and spin-dependent quark fragmentation functions and their applications*, Phys. Rev. **D49**, 114 (1994), hep-ph/9307235, [SPIRES].

[93] M. Anselmino, M. Boglione, J. Hansson, and F. Murgia, *Polarized inclusive leptoproduction, $\ell N \to hX$, and the hadron helicity density matrix $\rho(h)$: Possible measurements and predictions*, Phys. Rev. **D54**, 828 (1996), hep-ph/9512379, [SPIRES].

[94] A. Bacchetta and P. J. Mulders, *Deep-inelastic leptoproduction of spin-one hadrons*, Phys. Rev. **D62**, 114004 (2000), hep-ph/0007120, [SPIRES].

[95] A. Bacchetta and P. J. Mulders, *Positivity bounds on spin-one distribution and fragmentation functions*, Phys. Lett. **B518**, 85 (2001), hep-ph/0104176, [SPIRES].

[96] A. Bacchetta, *Probing the transverse spin of quarks in deep inelastic scattering*, PhD thesis, Vrije Universiteit Amsterdam, 2002, hep-ph/0212025.

[97] A. Bacchetta and M. Radici, *Dihadron interference fragmentation functions in proton-proton collisions*, Phys. Rev. **D70**, 094032 (2004), hep-ph/0409174, [SPIRES].

[98] M. Diehl and S. Sapeta, *On the analysis of lepton scattering on longitudinally or transversely polarized protons*, Eur. Phys. J. **C41**, 515 (2005), hep-ph/0503023, [SPIRES].

[99] P. J. Mulders and R. D. Tangerman, *The complete tree-level result up to order $1/Q$ for polarized deep-inelastic leptoproduction*, Nucl. Phys. **B461**, 197 (1996), hep-ph/9510301, [SPIRES], Erratum-ibid. **B484** (1997) 538.

[100] W. Melnitchouk, R. Ent, and C. Keppel, *Quark-hadron duality in electron scattering*, Phys. Rept. **406**, 127 (2005), hep-ph/0501217, [SPIRES].

[101] M. Boglione and P. J. Mulders, *Time-reversal odd fragmentation and distribution functions in pp and ep single-spin asymmetries*, Phys. Rev. **D60**, 054007 (1999), hep-ph/9903354, [SPIRES].

[102] A. Bacchetta *et al.*, *Semi-inclusive deep inelastic scattering at small transverse momentum*, (2006), hep-ph/0611265, [SPIRES].

[103] D. Boer, R. Jakob, and P. J. Mulders, *Angular dependences in electroweak semi-inclusive leptoproduction*, Nucl. Phys. **B564**, 471 (2000), hep-ph/9907504, [SPIRES].

[104] A. M. Kotzinian and P. J. Mulders, *Probing transverse quark polarization via azimuthal asymmetries in leptoproduction*, Phys. Lett. **B406**, 373 (1997), hep-ph/9701330, [SPIRES].

[105] A. Bianconi, S. Boffi, R. Jakob, and M. Radici, *Two-hadron interference fragmentation functions. I: General framework*, Phys. Rev. **D62**, 034008 (2000), hep-ph/9907475, [SPIRES].

[106] A. Bacchetta and M. Radici, *Partial-wave analysis of two-hadron fragmentation functions*, Phys. Rev. **D67**, 094002 (2003), hep-ph/0212300, [SPIRES].

[107] M. Radici, R. Jakob, and A. Bianconi, *Accessing transversity with interference fragmentation functions*, Phys. Rev. **D65**, 074031 (2002), hep-ph/0110252, [SPIRES].

[108] A. Bacchetta and M. Radici, *Two-hadron semi-inclusive production including subleading twist*, Phys. Rev. **D69**, 074026 (2004), hep-ph/0311173, [SPIRES].

[109] M. Diefenthaler, *Transversity measurements at HERMES*, AIP Conf. Proc. **792**, 933 (2005), hep-ex/0507013, [SPIRES].

[110] HERMES, M. Diefenthaler, *HERMES measurements of Collins and Sivers asymmetries from a transversely polarised hydrogen target*, (0600), arXiv:0706.2242 [hep-ex], [SPIRES].

[111] A. V. Efremov, K. Goeke, and P. Schweitzer, *Collins effect in semi-inclusive deeply inelastic scattering and in e^+e^- annihilation*, (2006), hep-ph/0603054, [SPIRES].

[112] V. Barone, *Understanding transversity: Present and future*, (2005), hep-ph/0502108, [SPIRES].

[113] X. Artru, J. Czyzewski, and H. Yabuki, *Single-spin asymmetry in inclusive pion production, Collins effect and the string model*, Z. Phys. **C73**, 527 (1997), hep-ph/9508239, [SPIRES].

[114] A. Schafer and O. V. Teryaev, *Sum rules for the T-odd fragmentation functions*, Phys. Rev. **D61**, 077903 (2000), hep-ph/9908412, [SPIRES].

[115] N. Makins, *Summary talk*, (2004), Talk delivered at the transversity workshop, Trento, Italy, 13-18 June 2004, http://www.lnf.infn.it/conference/transversity04/Talks/ summary.pdf.

[116] U. Elschenbroich, *Transverse spin structure of the proton studied in semi-inclusive DIS*, PhD thesis, Universiteit Gent, 2006, DESY-THESIS-2006-004.

[117] P. Schweitzer *et al.*, *Transversity distributions in the nucleon in the large-N_c limit*, Phys. Rev. **D64**, 034013 (2001), hep-ph/0101300, [SPIRES].

[118] R. L. Jaffe, X. Jin, and J. Tang, *Interference fragmentation functions and the nucleon's transversity*, Phys. Rev. Lett. **80**, 1166 (1998), hep-ph/9709322, [SPIRES].

[119] R. L. Jaffe, X. Jin, and J. Tang, *Interference fragmentation functions and valence quark spin distributions in the nucleon*, Phys. Rev. **D57**, 5920 (1998), hep-ph/9710561, [SPIRES].

[120] A. Bianconi, S. Boffi, R. Jakob, and M. Radici, *Two-hadron interference fragmentation functions. II: A model calculation*, Phys. Rev. **D62**, 034009 (2000), hep-ph/9907488, [SPIRES].

[121] A. Bacchetta, U. D'Alesio, M. Diehl, and C. A. Miller, *Single-spin asymmetries: The Trento conventions*, Phys. Rev. **D70**, 117504 (2004), hep-ph/0410050, [SPIRES].

[122] A. Bacchetta and M. Radici, *Modeling dihadron fragmentation functions*, Phys. Rev. **D74**, 114007 (2006), hep-ph/0608037, [SPIRES].

[123] V. Barone and P. G. Ratcliffe, *Transverse Spin Physics* (World Scientific, River Edge, USA, 2003).

[124] J. Levelt and P. J. Mulders, *Time reversal odd fragmentation functions in semiinclusive scattering of polarized leptons from unpolarized hadrons*, Phys. Lett. **B338**, 357 (1994), hep-ph/9408257, [SPIRES].

[125] D. Amrath, A. Bacchetta, and A. Metz, *Reviewing model calculations of the Collins fragmentation function*, Phys. Rev. **D71**, 114018 (2005), hep-ph/0504124, [SPIRES].

[126] P. Estabrooks and A. D. Martin, *$\pi\pi$ phase shift analysis below the $K\overline{K}$ threshold*, Nucl. Phys. **B79**, 301 (1974), [SPIRES].

[127] M. Wakamatsu, *Chiral-odd distribution functions in the chiral quark soliton model*, Phys. Lett. **B509**, 59 (2001), hep-ph/0012331, [SPIRES].

[128] V. A. Korotkov, W. D. Nowak, and K. A. Oganessyan, *Transversity distribution and polarized fragmentation function from semi-inclusive pion electroproduction*, Eur. Phys. J. **C18**, 639 (2001), hep-ph/0002268, [SPIRES].

[129] J. Soffer, M. Stratmann, and W. Vogelsang, *Accessing transversity in double-spin asymmetries at the BNL-RHIC*, Phys. Rev. **D65**, 114024 (2002), hep-ph/0204058, [SPIRES].

[130] A. A. Sokolov and I. M. Ternov, *On polarization and spin effects in the theory of synchrotron radiation*, Phys. Dokl. **8**, 1203 (1964), [SPIRES].

[131] D. P. Barber *et al.*, *Longitudinal Positron Polarisation in HERA-II*, Presented at the 9th European Particle Accelerator Conference (EPAC 2004), Lucerne, Switzerland, 5-9 Jul 2004.

[132] HERMES, *A Proposal to measure the spin-dependent structure functions of the neutron and the proton at HERA*, HERMES-PROPOSAL.

[133] HERMES, K. Ackerstaff *et al.*, *Measurement of the neutron spin structure function g_1^n with a polarized ^{3}He internal target*, Phys. Lett. **B404**, 383 (1997), hep-ex/9703005, [SPIRES].

[134] HERMES, A. Airapetian *et al.*, *Measurement of the proton spin structure function g_1^p with a pure hydrogen target*, Phys. Lett. **B442**, 484 (1998), hep-ex/9807015, [SPIRES].

[135] HERMES, A. Airapetian *et al.*, *First measurement of the tensor structure function b_1 of the deuteron*, Phys. Rev. Lett. **95**, 242001 (2005), hep-ex/0506018, [SPIRES].

[136] A. Hellemans, *DESY puts the spin into gluons*, Science **284 no 5411**, 27 (1999), DOI: 10.1126/science.284.5411.27.

[137] P. Liebing, *Can the gluon polarization in the nucleon be extracted from HERMES data on single high-p_T hadrons?*, PhD thesis, Universität Hamburg, 2004, DESY-THESIS-2004-036.

[138] V. Mexner, *Determination of the gluon polarization in the nucleon*, PhD thesis, Universiteit van Amsterdam, 2005, DESY-HERMES-05-39.

[139] E. Aschenauer and I. Flegel, *HERMES looks for final pieces in nucleon-spin puzzle*, CERN Cour. **46N3**, 26 (2006), [SPIRES].

[140] K. Rith, *Spin asymmetries in deep-inelastic electron-nucleon scattering: Selected HERMES results*, Prog. Part. Nucl. Phys. **49**, 245 (2002), [SPIRES].

[141] D. Hasch, *Spin physics at HERMES*, prepared for 17th international spin physics symposium (SPIN06), Kyoto, Japan, 2-7 Oct 2006; HERMES-06-115.

[142] G. van der Steenhoven, *The HERMES experiment*, Prog. Part. Nucl. Phys. **55**, 181 (2005), [SPIRES].

[143] HERMES, A. Airapetian *et al.*, *Hadron formation in deep-inelastic positron scattering in a nuclear environment*, Eur. Phys. J. **C20**, 479 (2001), hep-ex/0012049, [SPIRES].

[144] HERMES, A. Airapetian *et al.*, *Evidence for a narrow $|S| = 1$ baryon state at a mass of 1528 MeV in quasi-real photoproduction*, Phys. Lett. **B585**, 213 (2004), hep-ex/0312044, [SPIRES].

[145] P. Folkerts, *HERA Hits New Heights: A report on the challenges faced by the HERA crew after the luminosity upgrade of 2001*, DESY Press Release, http://www.interactions.org, 2005, Interactions News Wire 23-05.

[146] HERMES, R. Kaiser, *The HERMES recoil detector*, AIP Conf. Proc. **842**, 1082 (2006), [SPIRES].

[147] W. Yu, *The HERMES recoil detector*, prepared for international conference on Quarks and Nuclear Physics (QNP06), Madrid, Spain, 5-10 Jun 2006, to be published; HERMES-06-095.

[148] E. Steffens, *The HERMES gas target: 10 years on*, CERN Cour. **46N3**, 30 (2006), [SPIRES].

[149] HERMES, A. Airapetian *et al.*, *The HERMES polarized hydrogen and deuterium gas target in the HERA electron storage ring*, Nucl. Instrum. Meth. **A540**, 68 (2005), physics/0408137, [SPIRES] 0408137.

[150] A. Nass *et al.*, *The HERMES polarized atomic beam source*, Nucl. Instrum. Meth. **A505**, 633 (2003), [SPIRES].

[151] C. Baumgarten *et al.*, *An atomic beam polarimeter to measure the nuclear polarization in the HERMES gaseous polarized hydrogen and deuterium target*, Nucl. Instrum. Meth. **A482**, 606 (2002), [SPIRES].

[152] C. Baumgarten *et al.*, *A gas analyzer for the internal polarized target of the HERMES experiment*, Nucl. Instrum. Meth. **A508**, 268 (2003), [SPIRES].

[153] HERMES, K. Ackerstaff *et al.*, *The HERMES spectrometer*, Nucl. Instrum. Meth. **A417**, 230 (1998), hep-ex/9806008.

[154] J. T. Brack *et al.*, *The HERMES forward tracking chambers: Construction, operation, and aging effects*, Nucl. Instrum. Meth. **A469**, 47 (2001), [SPIRES].

[155] S. Bernreuther *et al.*, *The HERMES back drift chambers*, Nucl. Instrum. Meth. **A416**, 45 (1998), hep-ex/9803005, [SPIRES].

[156] A. Andreev *et al.*, *Multiwire proportional chambers in the HERMES experiment*, Nucl. Instrum. Meth. **A465**, 482 (2001), [SPIRES].

[157] T. Benisch *et al.*, *The luminosity monitor of the HERMES experiment at DESY*, Nucl. Instrum. Meth. **A471**, 314 (2001), [SPIRES].

[158] HERMES, H. E. Jackson, *The HERMES dual radiator RICH: Performance and impact*, Nucl. Instrum. Meth. **A553**, 205 (2005), [SPIRES].

[159] HERMES, *The HERMES RICH detector*, http://www-hermes.desy.de/groups/richgrp/rich.

[160] H. Jackson, private communication.

[161] V. Egorychev, V. Savelev, and S. J. Aplin, *Particle identification via transition radiation and detectors*, Nucl. Instrum. Meth. **A453**, 346 (2000), [SPIRES].

[162] W. R. Leo, *Techniques for nuclear and particle physics experiments: a how-to approach*, Berlin, Germany: Springer (1994), 2nd edition, 378 p.

[163] H. Avakian *et al.*, *Performance of the electromagnetic calorimeter of the HERMES experiment*, Nucl. Instrum. Meth. **A417**, 69 (1998), hep-ex/9810004, [SPIRES].

[164] E. Garutti, *Nuclear effects in semi-inclusive deep-inelastic scattering off ^{84}Kr and other nuclei*, PhD thesis, Universiteit van Amsterdam, 2003, DESY-HERMES-03-02.

[165] CERN computing and networks division, *EPIO manual*, CERN program library long writeup I101, 1993.

[166] N. Makins, *Data analysis boot camp*, http://www-hermes.desy.de/analyse/bootcamp.

[167] CERN Programming Techniques Group, ECP Division, *ADAMO reference manual version 3.3*, 1993.

[168] H. Tanaka *et al.*, *A gain monitoring system with a Nd:YAG laser for the photomultipliers of the HERMES experiment*, Nucl. Instrum. Meth. **A515**, 725 (2003), [SPIRES].

[169] D. Hasch, *Effect of a dead calo block in the analysis of semi-inclusive asymmetries...*, Mailing list: offline-list@hermes.le.desy.de, April 24, 2003.

[170] HERMES data quality webpage, *offline data quality*, http://www-hermes.desy.de/groups/daqlgrp.

[171] J. Wendland, *Polarized parton distributions measured at the HERMES experiment*, PhD thesis, Simon Fraser University, 2003, DESY-THESIS-2003-032.

[172] P. B. van der Nat, *Hadronization at 12 GeV*, Master's thesis, Vrije Universiteit Amsterdam, 2002, DESY-HERMES-02-60.

[173] N. Akopov *et al.*, *The HERMES dual-radiator ring imaging Cerenkov detector*, Nucl. Instrum. Meth. **A479**, 511 (2002), physics/0104033, [SPIRES] 0104033.

[174] P. B. van der Nat and T. Kobayashi, *Interference fragmentation on a transversely polarised hydrogen target*, HERMES release report, http://www-hermes.desy.de/reports, 2005, Release meeting, April 21.

[175] T. Sjostrand, L. Lonnblad, S. Mrenna, and P. Skands, *PYTHIA 6.3: Physics and manual*, (2003), hep-ph/0308153, [SPIRES].

[176] M. Gluck, E. Reya, and A. Vogt, *Dynamical parton distributions revisited*, Eur. Phys. J. **C5**, 461 (1998), hep-ph/9806404, [SPIRES].

[177] W. Augustyniak, A. Miller, G. Schnell, S. Yen, and P. Zupranski, *TMC- vertex reconstruction in the presence of the HERMES transverse target magnet*, HERMES Internal Report, 2007, HERMES-07-008.

[178] A. Bruell and A. Kisselev, *Top/bottom misalignment for 1996-2003 data*, Mailing list: offline-list@hermes.le.desy.de, June 9, 2003.

[179] Z. Ye and E. Aschenauer, *Misalignment effects on the beam-spin and beam-charge asymmetries in DVCS*, HERMES Internal Report, 2005, HERMES-05-038.

[180] B. Maiheu, A. Hillenbrand, and E. Aschenauer, *Monte-Carlo study of the influence of possible moments on the HERMES acceptance function for hadrons*, HERMES Internal Report, 2005, HERMES-05-004.

[181] B. Hommez, *Hadron identification with the HERMES RICH*, Nucl. Instrum. Meth. **A502**, 294 (2003), [SPIRES].

[182] HERMES, P. B. van der Nat and K. Griffioen, *Two-hadron single target-spin asymmetries: First measurements by HERMES*, (2005), hep-ex/0501009, [SPIRES], Proceedings of 16th International Spin Physics Symposium (SPIN 2004), Trieste, Italy, 10-16 Oct 2004.

[183] HERMES, P. B. van der Nat, *First measurement of interference fragmentation on a transversely polarized hydrogen target*, (2005), hep-ex/0512019, [SPIRES], Proceedings of International Workshop on Transverse Polarization Phenomena in Hard Processes (Transversity 2005), Villa Olmo, Como, Italy, 7-10 Sep 2005.

[184] HERMES, P. B. van der Nat, *First measurement of interference fragmentation on a transversely polarized hydrogen target*, AIP Conf. Proc. **792**, 953 (2005), [SPIRES], Proceedings of the 13th International Workshop on Deep- Inelastic Scattering (DIS 2005), Madison, Wisconsin, U.S.A. 27 Apr - 1 May 2005.

[185] Particle Data Group, W. M. Yao *et al.*, *Review of particle physics*, J. Phys. **G33**, 1 (2006), [SPIRES].

[186] M. Radici, *Transversity and inclusive two-pion production*, (2007), hep-ph/0701183, [SPIRES].

[187] A. Bacchetta and M. Radici, *Single-spin asymmetries with two-hadron fragmentation functions*, (2004), hep-ph/0407345, [SPIRES], Proceedings of the 12th International Workshop on Deep- Inelastic Scattering (DIS 2004), Strbske Pleso, Slovakia, 14 - 18 Apr 2004.

[188] R. D. Tangerman and P. J. Mulders, *Polarized twist-three distributions g_T and h_L and the role of intrinsic transverse momentum*, (1994), hep-ph/9408305, [SPIRES].

[189] COMPASS, R. Joosten, *Transversity signals in two hadron correlation at COMPASS*, (2006), [SPIRES], Proceedings of 17th International Spin Physics Symposium (SPIN 2006), Kyoto, Japan, 2-7 Oct 2006; to be published.

[190] COMPASS, R. Joosten, *Transversity signals in two-hadron correlation at COMPASS*, Proceedings of 16th International Spin Physics Symposium (SPIN 2004), Trieste, Italy, 10-16 Oct 2004.

[191] COMPASS, R. Joosten, *Transversity signals in two-hadron correlation at COMPASS*, AIP Conf. Proc. **792**, 957 (2005), [SPIRES], Proceedings of the 13th International Workshop on Deep- Inelastic Scattering (DIS 2005), Madison, Wisconsin, U.S.A. 27 Apr - 1 May 2005.

[192] D. Boer and P. J. Mulders, *Time-reversal odd distribution functions in leptoproduction*, Phys. Rev. **D57**, 5780 (1998), hep-ph/9711485, [SPIRES].

[193] M. Radici and G. van der Steenhoven, *The new transversity council of Trento*, CERN Cour. **44N8**, 51 (2004).

[194] S. A. Goudsmit, *De ontdekking van de electronenrotatie*, Nederlands Tijdschrift voor Natuurkunde **37**, 386 (1971).

[195] H. C. Manoharan, *Applied physics: Spin spotting*, Nature **416**, 24 (2002).

[196] G. van der Steenhoven, *De nieuwe kernfysica. Een spel van quarks en gluonen*, Nederlands Tijdschrift voor Natuurkunde **67**, 322 (2001).

[197] K. Rith and A. Schafer, *The Mystery of Nucleon Spin*, Scientific American **281**, 42 (July 1999).

[198] S. D. Bass, *How Does the Proton Spin?*, Science **315**, 1672 (2007), [SPIRES].

[199] E. Gabathuler, *Where is the nucleon spin?*, Nature Phys. **2**, 303 (2006), [SPIRES].

Summary

The interaction between quarks and gluons is successfully described by the theory of Quantum Chromodynamics (QCD). However, this by no means implies that we understand how these particles behave inside the proton. In fact, we don't even know how the confinement of quarks in hadrons can be calculated within the framework of QCD. Another property of the proton that we do not yet fully understand is its spin. The proton has spin $\frac{1}{2}$ and it should be possible to describe this total proton spin in terms of the dynamics of its constituents. In the 80s we have learned that not only the spin of the quarks is responsible for the proton spin. At present, it is well-known that the proton has a rich internal structure and that also the spin of the gluons and the orbital angular momentum of both the quarks and the gluons can contribute to the spin of the proton, which is reflected in the helicity sum rule, Eq. 1.2. In this equation, the first term ($\frac{1}{2}\Delta\Sigma$) represents the helicity of the quarks, which account for about 30% of the proton spin, i.e., $\frac{1}{2}\Delta\Sigma \sim 30\%$. However, the size of the other contributions to the total proton spin, given in Eq. 1.2, is still largely unknown. This is caused by the fact that it is difficult to isolate these contributions experimentally.

The type of experiments that are used to study the internal spin structure of the proton are polarized deep-inelastic scattering experiments. By polarizing the proton and varying the polarization direction (longitudinally or transversely with respect to the lepton beam), the proton can be prepared in different ways, both giving different insights into its internal spin structure. The contributions to the helicity of the proton, expressed in Eq. 1.2, can be studied when the proton is longitudinally polarized. When the proton is transversely polarized, the contributions of the constituents to the total spin are reflected in the transverse-spin sum rule, Eq. 1.4. This equation clearly shows an advantage of studying the spin structure of a transversely polarized proton, as in this case there are less contributions to consider, i.e., there is no contribution from transversely polarized gluons to the total proton spin. Therefore, it is easier to disentangle the contributions to the proton spin when the proton is transversely polarized. The only contributions come from the angular momenta of the quarks and gluons and the quark transversity distribution function h_1.

The transversity distribution function (transversity) describes the distribution of transversely polarized quarks inside a transversely polarized proton. At leading order in M/Q, i.e., at leading twist, transversity is the only missing distribution function needed to describe the quark structure

of the nucleon. Also, the first moment of the transversity distribution function can be related to the tensor charge of the nucleon, for which predictions are available from Lattice QCD.

In this thesis, the spin structure of transversely polarized protons is investigated using two-pion semi-inclusive deep-inelastic scattering. This process was proposed in Refs. [83, 84] as a probe of the transversity distribution function h_1. The dependence of the cross section for two-pion semi-inclusive DIS on the relative momentum of the two hadrons can be related to h_1 times an unknown dihadron fragmentation function $H_1^{\sphericalangle}$. In this thesis, the azimuthal amplitude $A_{UT}^{\sin(\phi_{R\perp}+\phi_S)\sin\theta}$ of the transverse single-spin asymmetry A_{UT} is determined, which is directly proportional to the product of h_1 and $H_1^{\sphericalangle}$.

The main questions that have been addressed in this thesis are: is it feasible to measure two-pion semi-inclusive deep-inelastic scattering at an electron-proton scattering experiment like HERMES and, if so, is it possible to use this process to study transversity? It has been shown that indeed this process can be measured at HERMES. However, it was shown as well that these measurements are influenced by large detector acceptance effects. These effects can occur also for other processes measured at an experiment with a limited geometrical acceptance like HERMES, but can be particularly large in two-hadron semi-inclusive DIS, due to the combination of the relatively small cross section and the strong dependence of the cross section on the invariant mass of the pion pair. Also the second question has been answered positively. The present data indicate that the azimuthal amplitude $A_{UT}^{\sin(\phi_{R\perp}+\phi_S)\sin\theta}$ deviates with 3–4 σ (stat.) from zero, which implies that both transversity and the fragmentation function $H_1^{\sphericalangle}$ are likely to be nonzero, and thus that two-pion semi-inclusive deep-inelastic scattering can be used as a probe of transversity (the systematic uncertainties are listed in Table 4.7).

The measurements were compared with model predictions. It was found that the present data are inconsistent, with a probability of $P > 0.999$, with the model of Jaffe, Jin and Tang [118, 119], which describes the dihadron fragmentation function $H_1^{\sphericalangle}$ in terms of $\pi-\pi$ phase shifts measured in pion-nucleon scattering experiments. The model predicts a sign change of the azimuthal amplitude $A_{UT}^{\sin(\phi_{R\perp}+\phi_S)\sin\theta}$ at the invariant mass of the ρ^0. However, no such sign change is observed in the present data. The model of Bacchetta and Radici [122], describes the two-pion semi-inclusive deep-inelastic scattering process within the context of a spectator model. Their model prediction is consistent with the dependence of the data on the invariant mass, as well as with the dependence on x and z. However, this model does not predict the sign and overestimates the measured amplitude by about a factor of 4.

In this thesis, an effort was made to contribute to the understanding of the spin structure of the proton. The results can be used in combination with planned measurements by the BELLE collaboration of the dihadron fragmentation function $H_1^{\sphericalangle}$ to extract transversity. As the measured asymmetries are small and the corresponding uncertainties typically quite large, a high-precision determination of transversity will require a combined analysis of the results from various experiments.

Samenvatting

Spin? Wat is dat eigenlijk?

In de zomer van het jaar 1925 werd door twee Nederlandse promovendi, Samuel Goudsmit en George Uhlenbeck, de spin van het elektron ontdekt. Deze ontdekking werd mogelijk gemaakt door de formulering van het zogeheten 'uitsluitingsprincipe' door Wolfgang Pauli eerder dat jaar. Dit principe zegt dat twee identieke elementaire materiedeeltjes (fermionen) zich nooit op dezelfde plek kunnen bevinden. Hiermee kon Pauli verklaren waarom elektronen in schillen op verschillende afstand om de atoomkern heen draaien. Indirect verklaart dit uitsluitingsprincipe daarmee ook veel van de chemische eigenschappen van atomen. Goudsmit was goed op de hoogte van deze nieuwe ontwikkelingen en had een wiskundig formalisme bedacht waarmee de implicaties van het uitsluitingsprincipe voor het atoommodel eenvoudiger te begrijpen zijn. Toen hij dit aan Uhlenbeck uitlegde, merkte deze op: "Maar zie je niet wat dat betekent? Dat betekent dat er nog een vierde vrijheidsgraad van het elektron is[1]. Dat betekent eenvoudig een spin van het elektron, dat het roteert!" [194]

Sinds die ontdekking is spin niet meer uit de fysica weg te denken. Spin is een intrinsieke eigenschap van alle elementaire deeltjes, net zoals massa of elektrische lading. Maar vraag aan een natuurkundige om uit te leggen wat spin precies is en het antwoord zal enigszins vaag zijn, namelijk dat het een soort rotatie is, met de kanttekening dat dat eigenlijk een slechte metafoor is. Eén van de problemen met het beeld van spin als een soort rotatie wordt veroorzaakt doordat het elektron een elementair deeltje is, wat betekent dat we denken dat het elektron oneindig klein is. Maar als het elektron oneindig klein is, wat draait er dan en met welke snelheid? De spin van elementaire deeltjes neemt ook alleen specifieke waarden aan, zoals 0, $1/2$, en 1 (uitgedrukt in de eenheid $\hbar$). Voor elektronen is de spin $1/2$ en deze waarde kan niet veranderen. Je kunt bijvoorbeeld het elektron niet een duwtje geven om het sneller te laten draaien, wat wederom aangeeft dat spin geen alledaagse vorm van rotatie is.

[1] Naast de bekende vrijheidsgraden die de grootte, de vorm en de oriëntatie van de baan van het elektron om de atoomkern beschrijven.

Vrijwel alle materie die we op aarde tegenkomen bestaat uit protonen, neutronen, en elektronen en het is dan ook niet verwonderlijk dat de spin van deze deeltjes een prominente rol speelt in tal van toepassingen. Een bekend voorbeeld hiervan is de MRI scanner, tegenwoordig onmisbaar in ziekenhuizen. Wanneer de spinrichting van een proton in een magnetisch veld omklapt, zendt het proton een klein beetje elektromagnetische straling uit. Dit wordt bij MRI scanners gebruikt om een driedimensionaal plaatje te maken van de dichtheid van waterstofatomen in het menselijk lichaam. Een ander voorbeeld ligt op het gebied van de 'scanning tunneling' microscopie (STM), een techniek waarmee individuele atomen kunnen worden waargenomen. Bij recente ontwikkelingen wordt gebruik gemaakt van de spin van elektronen om de verandering in de tijd van de spinrichting van individuele atomen in een materiaal te kunnen observeren [195]. Een totaal andere toepassing van de spin van elektronen waar onderzoek naar wordt gedaan is de zogenoemde 'spintronica', waarmee men een nieuwe generatie computers van ongekende snelheid hoopt te kunnen maken. Bij deze techniek fungeert de oriëntatie van de spin van een elektron als een bit in een computer.

De spincrisis

Protonen, neutronen en elektronen zijn alle drie deeltjes met spin $1/2$. Toch bestaat er een wezenlijk verschil tussen de spin van elektronen en die van protonen en neutronen. Protonen en neutronen zijn namelijk geen elementaire deeltjes, maar bestaan beide uit drie quarks bijeengehouden door gluonen (van het Engelse 'glue'). Dit impliceert dat de spin van protonen en neutronen verklaard moet kunnen worden uit de eigenschappen van deze bouwstenen. Oorspronkelijk dacht men dat de drie quarks samen volgens een eenvoudige som verantwoordelijk zijn voor de totale spin van het proton en het neutron. Voor protonen zijn dit twee 'up' quarks die in dezelfde richting draaien als het proton en één 'down' quark dat in tegengestelde richting draait, zoals is aangegeven in de linker afbeelding in figuur S.1. Aangezien ook de quarks deeltjes zijn met spin $1/2$, is deze som: $2 \times 1/2 + 1 \times (-1/2)$, wat inderdaad $1/2$ oplevert.

De ontdekking op CERN, eind jaren tachtig, dat slecht 30% van de spin van het proton herleid kan worden tot de spin van deze drie quarks, leidde dan ook tot de zogeheten 'spincrisis'. Het betekent dat een groot gedeelte van de protonspin een andere oorsprong moet hebben. Hiervoor zijn verschillende mogelijkheden, zoals is aangegeven in de rechter afbeelding in figuur S.1. De figuur geeft aan dat ook de spin van gluonen (deeltjes met spin-1) een rol kan spelen. Daarnaast is er mogelijk ook een bijdrage van de spin van 'virtuele' quarks. Dat zijn quarks die in het proton continu ontstaan en na zeer korte tijd weer verdwijnen. Tot slot kan ook de rotatie van de quarks en gluonen om een gezamenlijk middelpunt, de zogeheten baanbeweging, een rol spelen. Om de spin van het proton beter te doorgronden is in het begin van de jaren negentig als reactie op de spincrisis het HERMES experiment gebouwd.

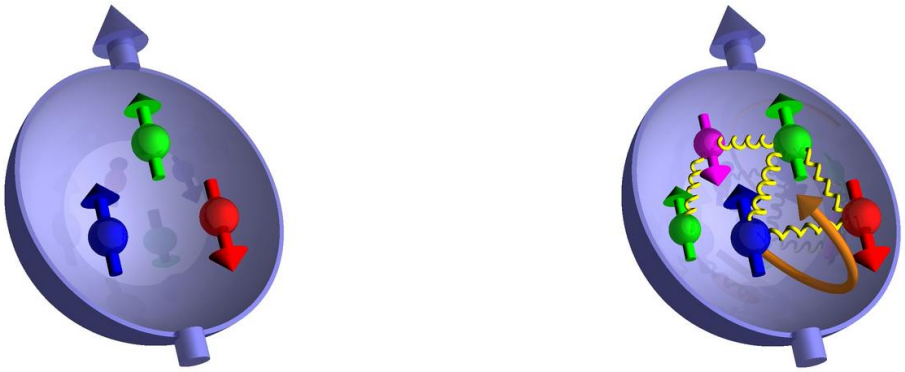

Figuur S.1: *Schematische afbeeldingen van de opbouw van de spin van het proton. De pijlen geven de spinrichting van het proton en de quarks weer. Links is aangegeven hoe men voor de spincrisis dacht dat de spin van het proton kon worden gerelateerd aan de spin van de quarks. De rechter afbeelding geeft ons huidige beeld weer, namelijk dat ook de spin van de gluonen (de gele 'veertjes'), de virtuele quarks (iets kleiner afgebeeld) en de baanbeweging van quarks en gluonen (aangegeven door de oranje pijl) een belangrijke bijdrage kunnen leveren aan de totale spin van het proton.*

HERMES

Het HERMES experiment staat in Hamburg, Duitsland, bij het onderzoeksinstituut DESY. Het experiment bestaat uit drie onderdelen: de deeltjesversneller, het target, en de spectrometer. De deeltjesversneller is een ring met een omtrek van 6 km waarin elektronen versneld worden totdat ze zo'n hoge snelheid bereikt hebben dat ze ongeveer 47000 rondjes per seconde door de versneller vliegen. Vervolgens botsen de elektronen op protonen in waterstofgas (het target). Met deze snelheid zijn de elektronen in staat een quark uit het proton weg te slaan. In de spectrometer worden vervolgens zoveel mogelijk eigenschappen gemeten van de brokstukken van de botsing, zoals elektrische lading, massa, snelheid en bewegingsrichting. Aan de hand van de eigenschappen van de brokstukken, kunnen bepaalde eigenschappen van de interne structuur van het proton gereconstrueerd worden. Deze 'brute force' methode is vooralsnog de enige manier waarop de structuur van materie op subatomaire schaal bestudeerd kan worden. In figuur S.2 is een foto te zien van het HERMES experiment. HERMES is een samenwerkingsverband tussen 33 instituten uit 12 landen, waar door de jaren heen meer dan 500 natuurkundigen aan meegewerkt hebben.

Spinfysica met HERMES

Het type proces dat met het HERMES experiment wordt onderzocht is geïllustreerd in figuur S.3. Het laat twee schematische afbeeldingen zien van een elektron (groen) dat met hoge snelheid op een quark in het proton botst. Deze botsing vindt plaats via de uitwisseling van een foton (γ^*, geel). Nu is het zo dat elektronen bij zeer hoge energie vrijwel alleen kunnen botsen met quarks met tegengestelde spinrichting. Hier wordt bij het HERMES experiment gebruik van gemaakt door

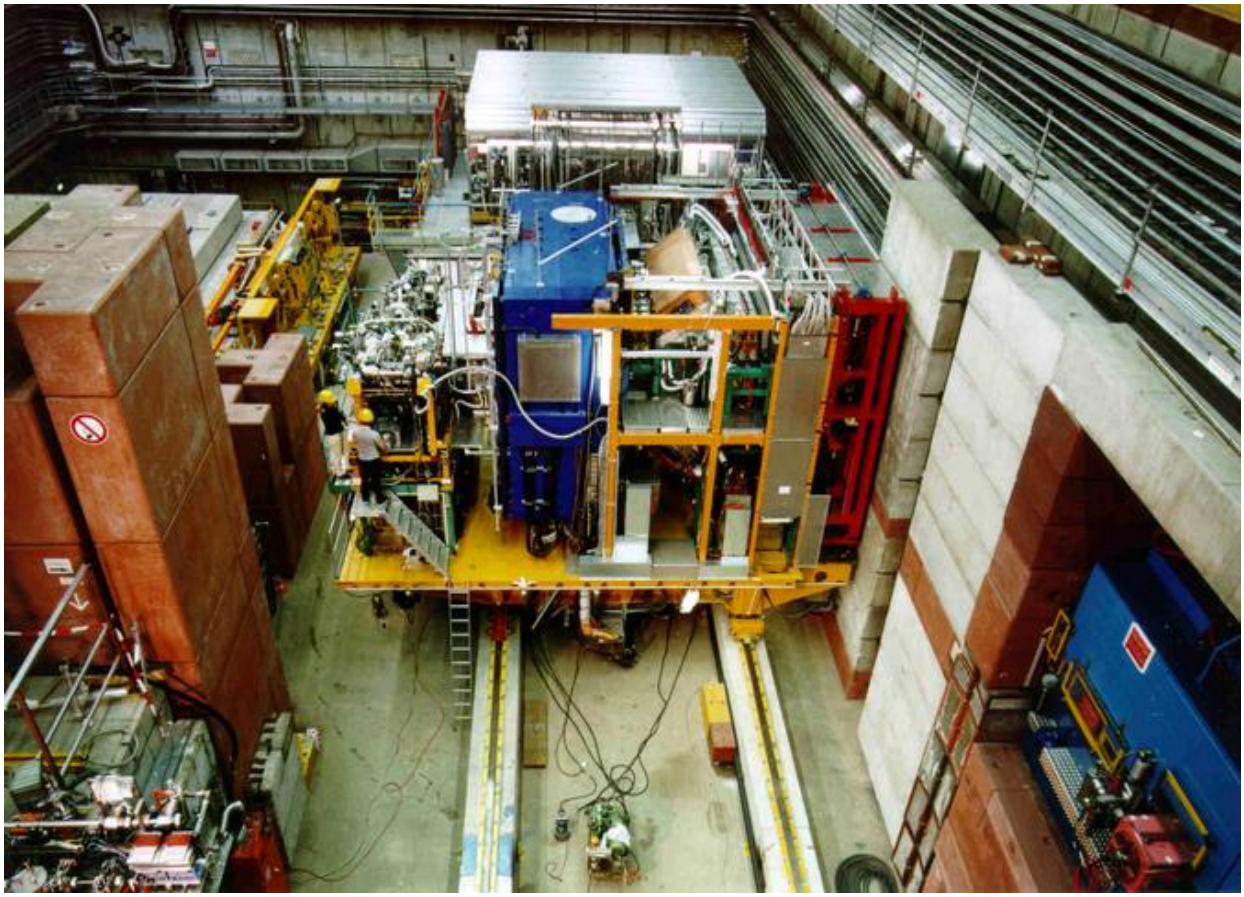

Figuur S.2: *Het HERMES experiment (HERA meting van spin). Op deze foto is te zien dat het target en de spectrometer op rails staan en uit de ring van de deeltjesversneller (HERA) gereden kunnen worden (zoals hier in 2001). Linksonder in de foto is een stuk buis van de versneller te zien waar de elektronen doorheen bewegen (naar rechts). De grote betonblokken worden om de versneller en het experiment heen gezet om mensen en elektronica tegen hoogenergetische foton- en neutronstraling te beschermen.*

de spinrichting van alle protonen in het waterstofgas in één richting vast te zetten (te *polariseren*) met behulp van een grote magneet die om het hele target heen staat. Wanneer de protonspinrichting wordt omgeklapt, botst het elektron met andere quarks, zoals is aangegeven in de twee afbeeldingen van figuur S.3. Door de botsingen voor deze twee oriëntaties te vergelijken, kan een goed beeld verkregen worden van het aantal quarks dat dezelfde spinrichting heeft als het proton en dus van de manier waarop de verschillende quarks bijdragen aan de spin van het proton.

Met behulp van dit soort metingen door het HERMES experiment is nu de bijdrage van de ‘up’ quarks en ‘down’ quarks aan de spin van het proton nauwkeurig bepaald. Een ander belangrijk resultaat van metingen bij HERMES is dat virtuele quarks niet of nauwelijks een bijdrage blijken te leveren. Dit betekent dat het grootste gedeelte van de spin van het proton geleverd wordt door een combinatie van de spin van gluonen en de baanbeweging van de quarks en/of gluonen.

De afbeeldingen in figuur S.3 corresponderen met een experimentele opstelling waarin het pro-

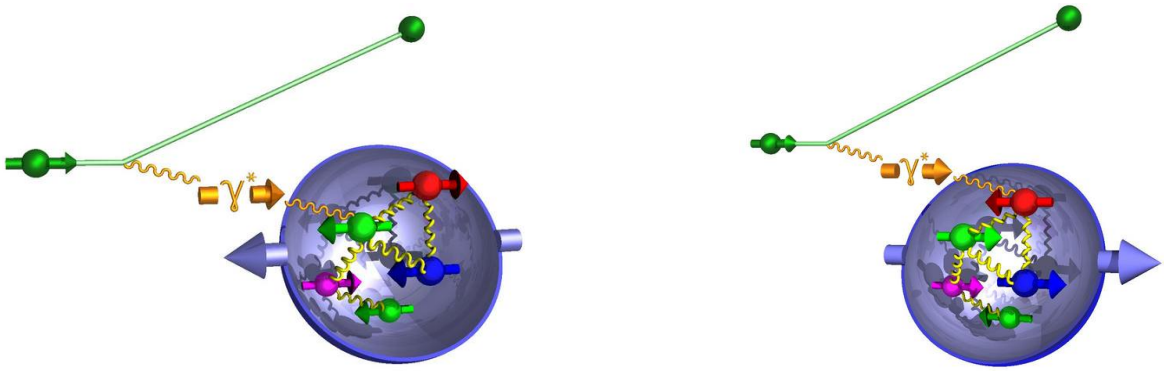

Figuur S.3: *Schematische afbeeldingen van een botsing tussen een elektron en een proton. In de linker afbeelding is de spinrichting van het proton tegengesteld aan die van het elektron en in de rechter afbeelding zijn de spinrichtingen van het proton en het elektron gelijk. Op welke quarks het elektron kan botsen is afhankelijk van de spinrichting van de quarks, zoals het verschil tussen de twee afbeeldingen laat zien (zie ook tekst).*

ton *longitudinaal* gepolariseerd is, wat wil zeggen dat het proton gepolariseerd is in dezelfde of tegengestelde richting als de richting waarin het elektron beweegt. Hiermee wordt een soort longitudinale doorsnede van de spinstructuur van het proton verkregen. Wanneer het proton *transversaal* wordt gepolariseerd (loodrecht op de richting waarin het elektron beweegt) kan een transversale doorsnede van de spinstructuur worden verkregen. Dat geeft niet alleen een complementair beeld van de spinstructuur van het proton, maar is ook interessant omdat in deze configuratie de spin van gluonen niet kan bijdragen. De transversale spin van quarks in een transversaal gepolariseerd proton heet ook wel 'transversaliteit'. Over deze grootheid is nog nauwelijks iets bekend. In dit proefschrift is een methode onderzocht om transversaliteit te meten.

Transversaliteit

Met het HERMES experiment kan transversaliteit op verschillende manieren worden onderzocht. Om dit te kunnen begrijpen moet iets beter uitgelegd worden hoe de botsing tussen een elektron en een quark in een proton in zijn werk gaat.

Zoals eerder gezegd, kan een elektron in het HERMES experiment met zoveel energie op een quark botsen dat die uit het proton schiet. Maar dit betekent niet dat we vervolgens een quark kunnen waarnemen in de spectrometer. Een eigenschap van quarks is namelijk dat ze nooit los voorkomen, maar alleen in paren en drietallen (deze deeltjes worden hadronen genoemd)[2]. Wat er gebeurt wanneer een quark uit een proton wordt geschoten is dat de energie van de botsing

[2]In 2003–2004 hebben wereldwijd een aantal experimenten, waaronder het HERMES experiment, aanwijzingen gevonden voor het bestaan van pentaquarks, deeltjes die bestaan uit vijf quarks. Of pentaquarks daadwerkelijk bestaan wordt op dit moment nader onderzocht.

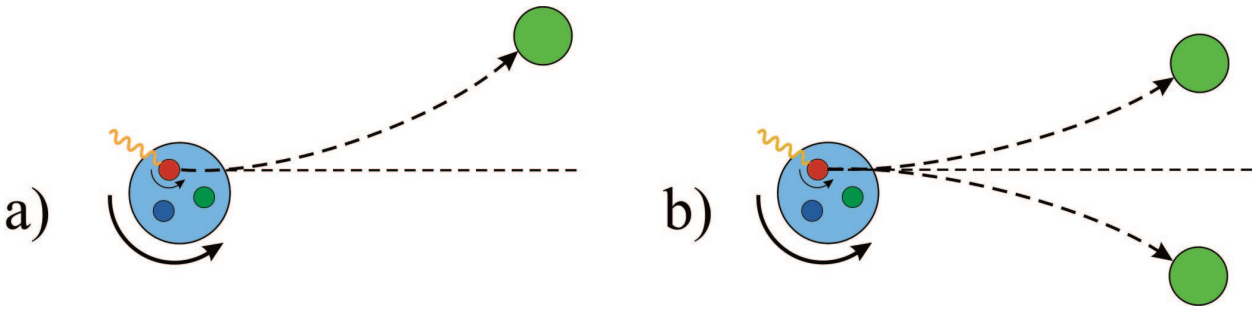

Figuur S.4: *Een schematische weergave van twee verschillende manieren waarop het proton kan 'breken', waarbij één of twee van de brokstukken (groen) eigenschappen hebben die gerelateerd kunnen worden aan de transversale spin van de quarks in een transversaal (loodrecht op het vlak van de tekening) gepolariseerd proton. Het foton dat een quark uit het proton wegslaat is in geel weergegeven.*

gedeeltelijk wordt omgezet in nieuwe quarks die samen met de getroffen quark een nieuw deeltje vormen (het vormen van zo'n nieuw deeltje heet 'fragmentatie'). Dit deeltje kan vervolgens door de spectrometer waargenomen worden en zo gebruikt worden om iets te leren over de structuur van het beschoten proton.

Wanneer je een bord tegen de muur gooit kan het op ontzettend veel verschillende manieren breken. Hetzelfde geldt voor het proton wanneer het kapot wordt geschoten door een elektron. Bij het onderzoek naar transversaliteit is één van de grootste uitdagingen om juist die brokstukken (nieuw gevormde deeltjes) te vinden die eigenschappen hebben die iets leren over de transversaliteit van de getroffen quark.

Bij HERMES worden verschillende soorten 'brokstukken' gebruikt om transversaliteit te onderzoeken. Eén van de mogelijkheden is dat een deeltje gevormd wordt dat tengevolge van de transversale spin van het getroffen quark weggeslingerd wordt, zoals is aangegeven in figuur S.4a. De mate van afbuiging is dan een maat voor de transversaliteit van de getroffen quarks. Dit is te vergelijken met een pingpongballetje dat tegen een ventilator aan wordt gegooid. Het balletje wordt weggeslingerd ten gevolge van de rotatie van de ventilator. Hoe ver het balletje wordt weggeslingerd is een maat voor de rotatiesnelheid van de ventilator. Deze methode om transversaliteit te meten is zeer succesvol gebleken en op basis van recente HERMES meetgegevens is het mogelijk gebleken transversaliteit voor 'up' quarks en 'down' quarks te bepalen. HERMES is het eerste experiment dat deze metingen heeft uitgevoerd, maar de onzekerheden in de bepaling van transversaliteit zijn nog wel vrij groot.

Om transversaliteit met grotere precisie te bepalen is het nodig om verschillende methoden te combineren. In dit proefschrift is daarom een alternatieve methode onderzocht, waarbij na de botsing twee hadronen gevormd worden die beide een tegengestelde kant op worden geslingerd, zoals is aangegeven in figuur S.4b. Eén van de belangrijkste resultaten van dit proefschrift is weergegeven in figuur S.5. De daarin getoonde variabele $A_{UT}^{\sin(\phi_{R\perp}+\phi_S)\sin\theta}$ is een maat voor het product van transversaliteit en de kans dat uit de getroffen quark twee hadronen gevormd worden. In de

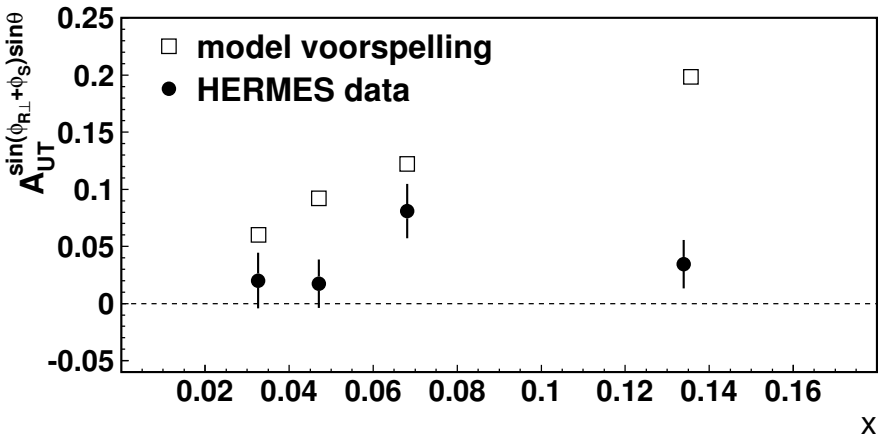

Figuur S.5: *Eén van de belangrijkste resultaten van dit proefschrift: de variabele* $A_{UT}^{\sin(\phi_{R\perp}+\phi_S)\sin\theta}$ *versus de impulsfractie x van het proton dat 'gedragen' wordt door het getroffen quark. De variabele* $A_{UT}^{\sin(\phi_{R\perp}+\phi_S)\sin\theta}$ *is een maat voor het product van transversaliteit en de waarschijnlijkheid dat twee hadronen uit het getroffen quark worden gevormd. Ook weergegeven is een voorspelling voor* $A_{UT}^{\sin(\phi_{R\perp}+\phi_S)\sin\theta}$ *uit een berekening door Alessandro Bacchetta en Marco Radici [122].*

grafiek staat $A_{UT}^{\sin(\phi_{R\perp}+\phi_S)\sin\theta}$ uitgezet tegen de fractie (x) van de impuls van het proton die 'gedragen' wordt door het getroffen quark. De gemeten waarden verschillen enerzijds duidelijk van nul (geen transversaliteit), maar zijn anderzijds kleiner dan een theoretische voorspelling [122]. In elk geval is dit de eerste meting ooit die aantoont dat fragmentatie naar twee hadronen inderdaad gebruikt kan worden om transversaliteit te bepalen, ook al zijn de foutenvlaggen nog relatief groot. Om deze resultaten te verkrijgen zijn meer dan 3 miljoen botsingen van een elektron en een proton onderzocht, waarvan ongeveer honderdduizend keer hadronparen gevormd werden die volgens het principe van figuur S.4b gebruikt zijn om de grootheid $A_{UT}^{\sin(\phi_{R\perp}+\phi_S)\sin\theta}$ te bepalen!

Om uiteindelijk de transversaliteit van quarks uit deze resultaten af te leiden is een onafhankelijke meting nodig van de genoemde kans om twee hadronen te vormen. Metingen van deze functie zijn in volle gang bij het BELLE experiment in Japan. Meer (toegankelijke) informatie over de spinstructuur van protonen is te vinden in Refs. [196–199].

Acknowledgements

It would not have been possible to write this thesis without the help of so many members of the HERMES collaboration. Thank you all very much! I really enjoyed my visits to Hamburg and especially the year that I have been living there (apart from the phone calls to the Λ-wheel mobile phone in the middle of the night!). I have learned a lot from the many different types of HERMES meetings and, in hindsight, I can even appreciate the release meetings, where people are subjected to third degree questioning on their analysis. From the many colleagues at DESY that I owe gratitude to for their help throughout the years, I would especially like to thank Gunar Schnell, Alessandro Bacchetta, Andy Miller, Elke Aschenauer, Ulrike Elschenbroich, Markus Diefenthaler, Riccardo Fabbri, Tomohiro Kobayashi, Ralf Seidl, Xiaorui Lu, Hal Jackson, Yoshi Miyachi, Delia Hasch, and Naomi Makins.

Special gratitude goes to my promotor Gerard van der Steenhoven, who inspired me to work on spin physics. One could hardly wish for a more enthousiastic supportive professor! I'm thankful as well to my co-promotor Louk Lapikás, with whom I could discuss the analysis in detail and who helped me a lot during the writing process.

The composition of the HERMES group at NIKHEF has changed a lot over the years and I need to thank many people for help with my analysis or, sometimes as important, for distraction. Special thanks to Jos Steijger and Henk Blok for many useful discussions. I would like to thank also Keith Griffioen, with whom I worked together on the analysis for some time. Keith, it was fun working with you! Then I would like to thank the proud new father Michiel Demey. Michiel, we are opposites in many ways, which made you a really valuable colleague to me. With the risk of forgetting people I would also like to thank Andreas Reischl, Vladas Tvaskis, Jeroen Dreschler, Vanessa Mexner, Martin van Beuzekom, Riccardo Fabbri, Willem Hesselink, Erika Garutti, Jan Visser, Armen Laziev, and David Heesbeen.

Many thanks go to Alessandro Bacchetta. Alessandro, if you would see the terrible state that my copy of your thesis is in, you would know how valuable your work has been to me. I really liked the close interplay between theory and experiment that we have going on with you in the transversity group.

Throughout the years I've received a lot of help from Gunar Schnell. Gunar, thank you for

everything, including the organization of a beautiful hiking trip and very interesting workshops in Tokyo and Gent!

I would also like to thank the members of drafting committee 64. Whether the meetings were face to face, over the telephone, using Skype or VRVS: I enjoyed our meetings and learned a lot from you guys. Andy, you are definitely the most thorough physicist I know!

The members of the reading committee, Piet Mulders, Keith Griffioen, Alessandro Bacchetta and Gunar Schnell, I would like to thank for many useful comments.

I would like to thank professor Shibata for hosting my stay in Tokyo and giving me the opportunity to work closely together with Tomo. Tomo, I enjoyed working with you and I won't easily forget the time that I entered the office in the morning and you were still there. Thanks to the entire group for a wonderful time!

The NIKHEF institute has been an ideal place to work and I would like to thank all colleagues for their support and the good atmosphere. Special thanks to the personel organisation for the festivities they always organize. I will for sure miss the yearly haring lunch. Mijn ganggenoten Ingrid, Carlijn, Peter, Esger, Jeroen, en Claud wil ik bedanken voor de gezellige lunches.

Tot slot wil ik al mijn vrienden en familie bedanken voor hun steun in de afgelopen jaren. Specifiek wil ik Willem bedanken voor het maken van de kaft (heel gaaf, dat je zo snel kon visualiseren wat ik in gedachten had!), Joost voor kommentaar op de tekst en Bram voor het beantwoorden van heel veel vragen over de opmaak en alle regeldingen rondom de promotie.

In het bijzonder wil ik tenslotte mijn paranimfen Hylke en Ingrid bedanken. Hylke, jij bedankt voor je hulp als mijn huistheoreet. Ik zal onze pauzes missen. Maar vooral wil ik jullie beiden bedanken voor de enorme steun die jullie voor me zijn geweest!